Backprojection for Synthetic Aperture Radar

Michael Israel Duersch

A dissertation submitted to the faculty of
Brigham Young University
in partial fulfillment of the requirements for the degree of

Doctor of Philosophy

David G. Long, Chair
Richard W. Christiansen
Brian D. Jeffs
Michael A. Jensen
D. J. Lee

Department of Electrical and Computer Engineering

Brigham Young University

June 2013

ABSTRACT

Backprojection for Synthetic Aperture Radar

Michael Israel Duersch
Department of Electrical and Computer Engineering
Doctor of Philosophy

Synthetic aperture radar (SAR) is a type of radar capable of high-resolution coherent imaging. In order to produce coherent imagery from raw SAR data, an image formation algorithm is employed. The various image formation algorithms have strengths and weaknesses. As this work shows, time-domain backprojection is one algorithm whose strengths are particularly well-suited to use at low-altitudes. This work presents novel research in three areas regarding time-domain backprojection.

The first key contribution of this work is a detailed analysis of SAR time-domain backprojection. The work derives a general form of backprojection from first principles. It characterizes the sensitivities of backprojection to the various inputs as well as error sources and performance characteristics. This work then shows what situations are particularly well-suited to use of the backprojection algorithm, namely regimes with turbulent motion and wide variation in incidence angle across the range swath (e.g., low-altitude, airborne SAR).

The second contribution of this work is an analysis of geometric signal correlation for multi-static, sometimes termed multiple-input and multiple-output (MIMO), imaging. Multi-static imaging involves forming multiple images using different combinations of transmitters and receivers. Geometric correlation is a measure of how alike observations of a target are from different aspect angles. This work provides a novel model for geometric correlation which may be used to determine the degree to which multi-static images are correlated. This in turn determines their applicable use: operating in the highly correlated regime is desirable for coherent processing whereas operating in a lower-correlation regime is desirable for obtaining independent looks.

The final contribution of this work is a novel algorithm for interferometry based on backprojected data. Because of the way backprojected images are formed, they are less suited to traditional interferometric methods. This work derives backprojection interferometry and compares it to the traditional method of interferometry. The sensitivity and performance of backprojection interferometry are shown, as well as where backprojection interferometry offers superior results. This work finds that backprojection interferometry performs better with longer interferometric baseline lengths or systems with large measurement error in the baseline length or angle (e.g., low-altitude, airborne SAR).

Keywords: synthetic aperture radar, backprojection, interferometry, geometric correlation

ACKNOWLEDGMENTS

This dissertation is dedicated to my wife, Michelle, whose support and encouragement made everything possible.

I would like to thank Dr. David Long for his advice and support throughout my graduate work and his years of mentoring and friendship. I could not have asked for a better advisor. I'm especially grateful to him for allowing me to monopolize his time during the writing of this dissertation.

I am thankful to Ryan Smith for allowing me to have a flexible work schedule so I could attend school full-time while still employed full-time. I'm also indebted to him for his vision of the possibility of miniature SAR.

Finally, I'm grateful to all of my family for their example and support. Particularly, I want to thank my parents and my children for all they have taught me.

Contents

List of Tables

List of Figures

Chapter 1

Introduction

1.1 Purpose

Synthetic aperture radar (SAR) is a type of radar designed to form high-resolution images. The distinguishing feature of SAR is the use of relative motion between the radar and its target in order to obtain the high resolution. Because of the need for motion, SAR sensors are typically placed on airborne or spaceborne platforms in order to perform remote sensing of the Earth.

Optical based imaging is limited in ways that SAR imaging is not. The pixel resolution of optical sensors is based on angles, meaning that as the distance from the sensor to the target is increased, the resolution becomes poorer. In SAR, the resolution is based on the nature of the signal and is independent of the range to the target. This means that a SAR sensor may be one hundred meters above the ground or one hundred kilometers above the ground and have the same pixel resolution. The frequencies of typical SARs allow the electromagnetic waves to pass through clouds, smoke, rain and other such obstacles unperturbed. Additionally, as a radar provides its own illumination, it may operate in complete darkness. Besides these differences, SAR is also a *coherent* sensor. A coherent sensor is able to measure the phase of the propagating wave in addition to its intensity. The ability to measure phase provides insight into the precise distance the wave has traveled. For these and other reasons, SAR technology has wide application in a variety of areas, both civilian and military.

The creation of SAR images requires the use of an *image formation algorithm*. An image formation algorithm takes the raw data (i.e., phase history measurements) received by the system, and through a step-by-step list of mathematical operations, calculates the pixels that form the output image. The earliest SARs produced analog images through a sophisticated network of optical lenses. Beginning in the late 70s, digital methods were employed. Since then, many imaging algorithms have been invented. The majority of those actually used in practice belong to a family known as *frequency domain algorithms*. Frequency domain methods perform calculations with respect to the *frequency* of a signal rather than the *timing* of the signal.

Frequency domain methods are advantageous because they are computationally efficient. Nevertheless, they have drawbacks. Performing calculations in the frequency domain requires making assumptions that do not hold in all types of imaging scenarios (e.g., low squint, spotlight mode geometry, narrow range swath, etc.) This means that frequency domain methods may need to be modified in order to suit a particular situation. Frequency domain methods also assume that the radar data have been sampled regularly. Because this is generally not the case, especially in airborne SAR, a step prior to image formation known as *motion compensation* is required. Motion compensation does well at meeting the sampling assumptions of frequency domain methods, however it is not able to account for it perfectly. Finally, frequency domain methods produce output images in what is called the *slant-plane*. The slant-plane is the line-of-sight plane that is implicit in the way radar observes a scene. In a slant-plane image, targets that are closer to the radar appear to be stretched longer than the actually are. Other imaging artifacts exist as well. In order to rectify this, a post-image formation step known as *orthorectification* or *georegistration* is performed to map the slant-plane image into the ground-plane. The ground-plane is the overhead view that resembles the point-of-view of satellite optical imagery.

There are other image formation algorithms besides the frequency domain methods. One such method, which is the focus of this dissertation, is *time domain backprojection*. As the name suggests, time domain backprojection does not form images in the frequency domain. Instead, backprojection forms images by matched filtering radar data according to what it expects to receive. In this way, backprojection may be considered an ideal matched-filter for

SAR. Backprojection doesn't suffer from the same limitations as the frequency domain methods. No separate motion compensation step is required because the backprojection algorithm handles non-ideal motion/sampling implicitly. Additionally, the same algorithm may be used for all imaging geometries. A more detailed comparison of frequency domain methods versus backprojection is given in Chapter 3. The downside to time-domain backprojection is that it is more computationally expensive than the frequency domain methods. This disadvantage has limited the widespread adoption of backprojection.

Perhaps due to the computational expense of backprojection, there is a dearth of analysis of backprojection in literature. This has often lead researchers to treating backprojection as a second-tier algorithm. However, because of backprojection's advantages, this author believes it deserves more interest. This is especially true because modern technology has vastly increased the ability to perform parallel computations, where multiple operations can execute simultaneously. Backprojection is highly parallelizable. Because of this, the computational expense of backprojection is becoming less relevant. This means that backprojection may be compared to frequency domain methods by its quality and merits rather than its computational efficiency.

This dissertation extends the body of knowledge of time-domain backprojection for synthetic aperture radar. The dissertation provides a generalized formulation of the backprojection algorithm and examines its strengths and weaknesses. Geometric correlation for multiple input and multiple output (MIMO) SAR is analyzed, which measures how alike multiple signals are when they observe the same target from different angles. The dissertation presents research into backprojection interferometry. Interferometry is a technique that uses superimposed waves to infer additional information about the waves. This dissertation also shows situations that are particularly fitted to backprojection. Specifically, it is seen that backprojection is well-suited for low-altitude use.

1.2 Contributions

This dissertation makes novel contributions to the field of synthetic aperture radar, particularly in regard to the backprojection algorithm. These contributions are organized into three primary categories: generalized time-domain backprojection fundamentals, multistatic geometric correlation, and interferometry.

The first main contribution of this dissertation is regarding the time-domain backprojection algorithm. The dissertation derives generalized time-domain backprojection from first principles. This derivation is novel in that it formulates backprojection in a more straightforward manner than currently exists in literature. The derivation introduces the concept of focusing errors caused when the *phase-center* of a scattering-cell is not the physical center of that cell, which means that from the point of view of the radar, the apparent center of a group of scatterers is not their actual center. If the phase-center is at the physical center (or similarly, if the exact location of the phase-center is known), then in principle it is possible to achieve perfect imaging. Additionally, the derivation introduces the idea of *nominal residual phase*, which is related to these focusing errors and is a symptom of the unknown location of the phase-center of each scattering-cell. In order to make later analysis tractable, the analysis uses an approximation for the hyperbolic range from the antennas to the target based on the Bakhshali approximation, which is novel for SAR. The dissertation performs an analysis of the various sensitivities of the backprojection algorithm to the radar and geometric parameters as well as an analysis of several performance characteristics of backprojection. Specifically, contributions are made showing the effects of height errors in the digital elevation map used in image formation. It also shows that there is a maximum useful azimuth antenna beamwidth for SAR due to the unknown phase-center of the scattering-cells. The contribution to this area concludes by showing that backprojection is not affected by antenna squint, something that particularly troubles frequency domain methods.

The second main contribution of the dissertation concerns multistatic geometric correlation. Multi-static, or MIMO, imaging denotes forming multiple images using different combinations of transmit and receive antennas. Because antennas cannot physically occupy the same space, they view an illuminated scene from different angles. The difference in view leads to a decrease in signal correlation. Multistatic geometric correlation is a measure of the degree to which multiple images of the same scene taken from different angles are coherent (i.e., have the same phase). While geometric correlation for SAR has been studied in the past, multiple models exist and there is no current work in literature that compares each of them to show which is most appropriate in a specific situation. Furthermore, each of the models from literature make assumptions that may not be appropriate in some scenarios. Using the backprojection foundations given, the dissertation presents a new model of geometric correlation that makes fewer assumptions than the originals. A key finding is that when taken on the average, the total number of scatterers inside a scattering-cell does not affect the correlation statistics: one random target behaves the same way as many. The dissertation finds that for practical imaging situations, when all antennas are placed on the same imaging platform, the resulting images are highly correlated.

The final contributions relate to backprojection interferometry. As stated above, SAR interferometry uses the superposition of multiple images to obtain more information and one practical application of it is the generation of height maps of an imaged surface. This dissertation derives a new method of SAR interferometry based on backprojected imagery. The matched filter used for backprojection makes backprojected images unsuited to traditional SAR interferometric methods, which necessitates a new method. The dissertation compares traditional interferometry to backprojection interferometry, followed by a comparison of their respective sensitivities to their input parameters. The comparison shows that despite both being based on the phase difference of two images, both perform quite differently. A key observation is that backprojection interferometry is insensitive to errors in measurement of the interferometric baseline–a matter that is critical in traditional interferometry. The analysis shows the minimum baseline length for which backprojection interferometry outperforms traditional interferometry. The backprojection interferometry analysis presented may be the largest contribution of this dissertation because it shows that low-altitude interferometry is feasible in situations where traditional interferometry is unsatisfactory.

1.3 Outline

This dissertation is organized as follows:

- Chapter 2 provides the background information and context necessary to understand the material presented in the subsequent chapters. This includes a discussion of target scattering and background of the SAR model. A simple algorithm for frequency domain image formation is presented.

- Chapter 3 provides a general derivation of time-domain backprojection. As the general form is extremely computationally expensive, a section showing when certain approximations may be made to simplify computation is included. Next, the chapter presents an analysis of backprojection's sensitivities to phase-center displacement, non-ideal motion, and the mean position of the imaging platform. This leads to an investigation of general performance characteristics of backprojection: elevation map errors, phase-center effects, antenna position estimates, and maximum azimuth beamwidth. The chapter ends with a discussion of which imaging conditions are especially befitting backprojection, as well as the navigational system requirements to achieve an acceptable level of performance for a given imaging geometry.

- In Chapter 4, an analysis is made of geometric pixel correlation for multistatic imaging. It begins with a discussion of the motivations for a new analysis of correlation. After that is a presentation of the possible multistatic imaging geometries. The chapter provides an analytic solution for the geometric correlation in the case of a single scatterer. The chapter then presents a numeric solution for the case of multiple scatterers. A comparison is made of the new analytic and numeric methods to the previous correlation models. The chapter concludes with a discussion of example multistatic geometries and their relative levels of correlation.

- Chapter 5 presents a novel interferometry algorithm based on backprojection image formation. First, it derives interferometry for backprojected images and compares the result to traditional interferometry. It is shown that the two methods differ in form and the traditional interferometry equations may not be applied directly to backprojected imagery. The chapter then performs a detailed sensitivity analysis of both methods to baseline length, baseline angle, range to target, and target displacement. Next, the chapter examines the performance of backprojection interferometry. It considers the effects of DEM and phase/baseline accuracy, and develops the notion of the transition baseline, which is the minimum baseline length where backprojection begins to perform better than traditional methods. The chapter ends with a discussion of which situations are particularly well-suited to backprojection interferometry.

- Chapter 6 concludes this dissertation. It gives a a summary of the results of the chapters and specifies the contributions made. It ends with a discussion of possible areas of future research.
- Appendix A details an autofocus algorithm well-suited for use with the backprojection algorithm.
- Appendix B derives range and azimuth compression for the range-Doppler algorithm.
- Appendix C provides some of the SAR figures of merit, including resolution and signal-to-noise ratios.

Chapter 2

Background

Synthetic aperture radar is an important tool in earth remote sensing. In conventional side-looking airborne radar (SLAR) systems, an antenna is mounted on the side of an aircraft and the radar observes a scene it illuminates while the platform is in motion. The along-track resolution of SLAR is dependent on the size of the illumination footprint. Synthetic aperture radar (SAR), on the other hand, uses the antenna motion to achieve much better resolution in the direction of motion than is possible by conventional means [1]. A SAR can be thought of as a system that uses motion to synthesize a uniform, linear antenna array and create a highly focused beam capable of achieving high azimuthal resolution.

High azimuth resolution is just one of many reasons that make SAR a popular imaging sensor. SAR provides its own illumination, can "see" through clouds and rain, has resolution that is independent of platform altitude, and modern systems have the ability to image at centimeter-level resolutions [2]. For these and other reasons, SAR is used in a variety of remote sensing applications.

In order to form images from a collection of pulses, SAR data must be combined in a *coherent* way (i.e., utilize both phase and magnitude of the data). The coherent processing does this by performing range and azimuth focusing or *compression*, which transforms the raw phase history data into a complex valued image. A particular method for creating an image is called an *image formation algorithm*. Many such algorithms are described in books and literature [3, 4, 5]. Several these algorithms are briefly discussed at the end of this chapter.

This chapter provides context for the research presented in the dissertation. It also describes the SAR background essential to understanding the research. First, the SAR geometry and definitions are presented. Next is a discussion of SAR compression from the viewpoint of the range-Doppler algorithm. Finally, a brief overview of several other common image formation algorithms are introduced.

2.1 Geometry

Several SAR operational modes exist. Much of this dissertation focuses on *stripmap* mode SAR, where the radar is attached to an aircraft or spacecraft which moves at a constant velocity and linear trajectory and the antenna maintains a boresight pointing orthogonal to the flight track. This mode of imaging is illustrated in Fig. 2.1. It is termed stripmap because the radar creates a continuous strip along the direction of travel.

In addition to stripmap mode imaging, a few of the other SAR modes are briefly mentioned for completeness: spotlight, scanning, squinted, and circular. In *spotlight* mode SAR, the antenna beam is steered to remain fixed on a given target. This means that the dwell time on the target is longer than for stripmap mode imaging. The result of a longer dwell time is both increased signal-to-noise ratio (SNR) as well as improved (finer) azimuth resolution. The cost is a reduction in spatial coverage. The analysis of spotlight mode SAR is similar to stripmap, except that some of the processing steps are simplified [4]. *Scanning* SAR steers the beam in range (i.e., elevation angle) in order to achieve greater spatial coverage in ground-range at the expense of azimuth resolution. *Squinted* SAR purposefully squints the antenna beam forward ahead of the platform in order to observe targets that are still some distance away (in azimuth). Generally, this mode is only used in airborne systems, particularly for military applications. Finally, *circular* SAR is the only mode where the platform does not travel in a straight line. Instead, the platform circles around a target and spotlights it. Because some targets appear differently at particular aspect angles, circular SAR allows for observing a more complete spectrum of the target's signature.

A few terms regarding the stripmap mode collection geometry shown in Fig. 2.1 are defined. The imaging surface is termed the *ground-plane*. The direction of travel is called the

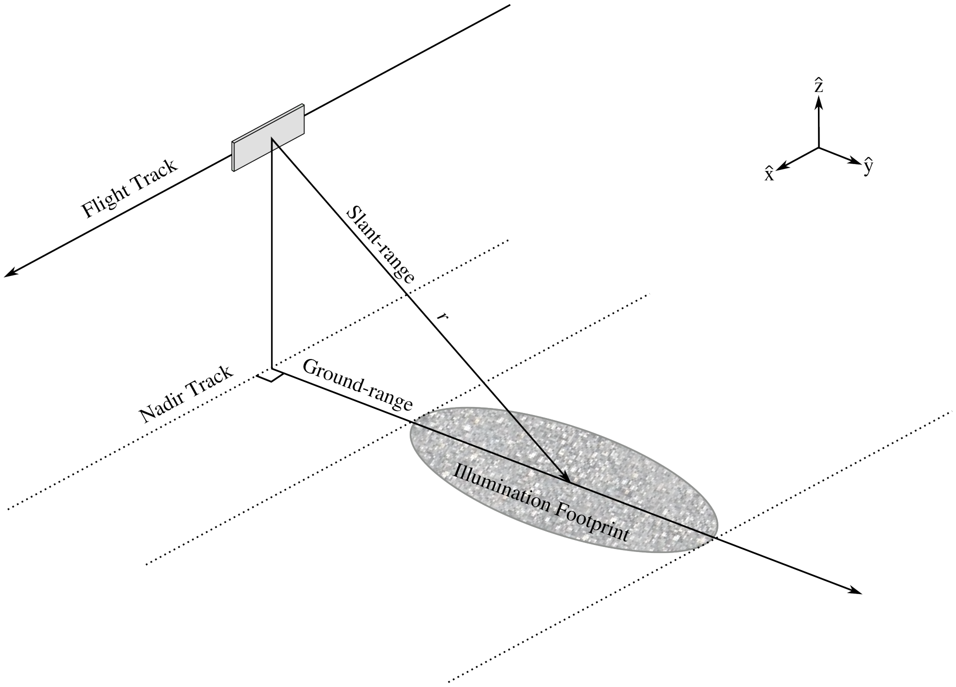

Figure 2.1: Side-looking SAR geometry. The coordinates $(\hat{x}, \hat{y}, \hat{z})$ refer to the along-track, ground-range, and elevation dimensions.

along-track, *azimuth*, or *slow-time* dimension and is denoted $\hat{x}$. On the ground-plane, perpendicular to the azimuth direction is the *ground-range*, or *fast-time* dimension and is denoted $\hat{y}$. The height or *elevation* dimension is perpendicular to the ground-plane and is denoted $\hat{z}$. Both $\hat{y}$ and $\hat{z}$ may be considered cross-track dimensions, though some refer to cross-track ambiguously as the ground-range dimension only.

Consider a target at position (x_0, y_0, z_0). The range from an antenna on the SAR platform to that target is given by

$$r = \sqrt{(x(t) - x_0)^2 + (y(t) - y_0)^2 + (z(t) - z_0)^2}, \tag{2.1}$$

where $x(t)$, $y(t)$, $z(t)$ are the coordinates of the antenna as a function of time. If the instantaneous velocity of the aircraft is always in the direction of the flight track, then the platform reaches the *point of closest approach* (PCA) when $x(t) = x_0$. For a given target, it is common to reference the PCA as occurring at time $t = 0$. Using this convention, $x(0) = x_0$. The range at the PCA is then

$$r_0 = \sqrt{(y(0) - y_0)^2 + (z(0) - z_0)^2}. \tag{2.2}$$

A flight track is considered to be ideal if it is a perfectly straight line. When this is the case, both $y(t)$ and $z(t)$ are constant and Eq. 2.2 may be substituting into Eq. 2.1 yielding

$$r = \sqrt{(x(t) - x_0)^2 + r_0^2}, \tag{2.3}$$

or

$$\frac{(x(t) - x_0)^2}{r^2} + \frac{r_0^2}{r^2} = 1, \tag{2.4}$$

which is a common expression for a hyperbola. Thus, an ideal, straight flight track leads to a hyperbolic *range-to-target*.

When the center of the antenna beam in azimuth illuminates a target at the same time the platform reaches the point of closest approach, then it is said there is zero *squint* at the PCA. An example of squint is given in Fig. 2.2. Squint is generally undesirable in SAR unless the imaging mode specifically demands it. In zero squint imaging, it may be assumed that the range and Doppler dimensions are orthogonal. When squint is non-zero, this assumption no longer holds. If the squint is significant then the imaging algorithm must specifically account for it or the resulting image quality suffers (e.g., distortion, de-focusing, misplacement, etc.)

One final note on geometry nomenclature is necessary. When the SAR utilizes a single antenna for both transmitting and receiving, it is termed *monostatic*. If the transmit and receive antennas are separated then it is *bistatic*. If distinct transmit and receive antennas are used, but are only separated by a small distance, then they may be termed *pseudo-monostatic*, as bistatic often implies widely separated antennas. Finally, *multistatic* refers to the use of multiple images from several monostatic and/or bistatic configurations.

2.2 Targets

A target is any illuminated object in a scene that reflects (scatters) transmitted energy toward a receive antenna. The received signal is a time-delayed copy of the transmit signal reflected by the target. Targets may be classified into two categories: *discrete* and *distributed*. Discrete targets, also called point targets, are small with respect to the resolution of the radar. For example, a corner reflector, a fence post, or even an aircraft are examples of discrete

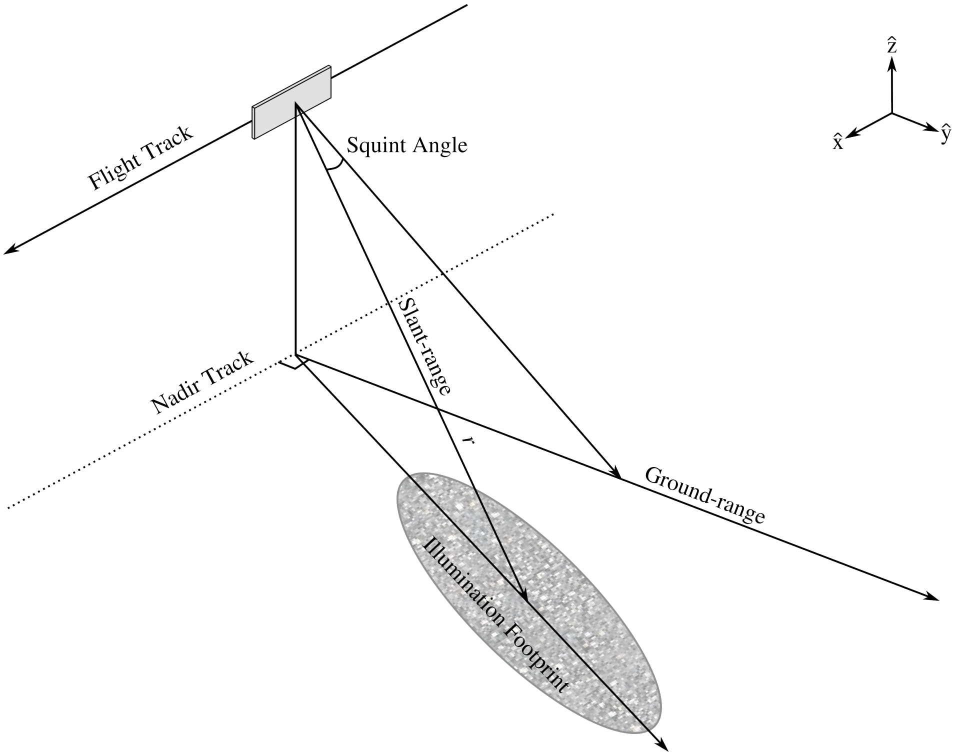

Figure 2.2: Squinted SAR geometry. The beam pointing in azimuth is not perpendicular to the direction of flight.

targets. Distributed targets, also called extended targets, are made up of many individual scatterers inside a resolution cell. For example, a field of grass or a dirt road are distributed targets.

This leads to the idea of a *scattering-cell*. A scattering-cell is a three dimensional volume that contains a group of scatterers that cannot be uniquely resolved (i.e., they are closer together than the resolution of the radar). All of the scatterers illuminated by the radar fall into a grid of scattering-cells. The exact dimensions of the cell are dependent on the resolution of the SAR and the imaging geometry. A depiction of a scattering-cell is shown in Fig. 2.3. The signals returned from the scattering-cells are resolved by the SAR into pixels in the output image. Note that throughout this dissertation the term *pixel* refers to the imaged signal and scattering-cell refers to the physical location being imaged.

Typically, the scattering-grid observed by the radar maps directly to the physical grid. There are exceptions to this, however, if the terrain slope is greater than the incidence angle, then taller objects appear closer than shorter objects because the taller ones are closer to the

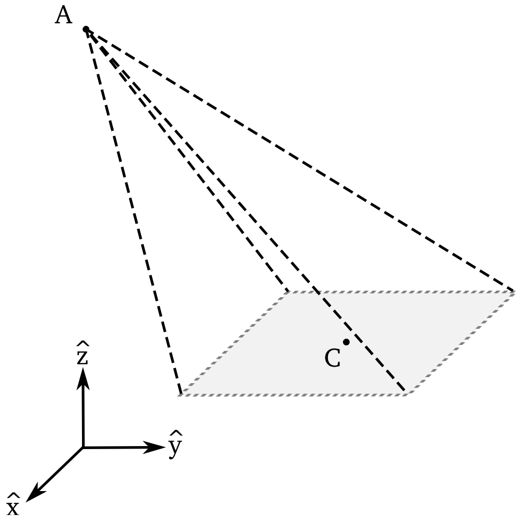

Figure 2.3: Illustration of a scattering-cell. Point A is the antenna position and point C is the center of the scattering-cell.

radar. This is known as *layover*. Likewise, if the terrain slope is less than the negative of the incidence angle then those targets fall within a radar “shadow” and are unobservable.

As the platform travels, many observations of the scattering-cells are made. Each observation is accomplished by a *pulse*. The rate at which pulses are transmitted is called the *pulse repetition frequency* (PRF). This leads to the concept of fast-time vs. slow-time. Fast-time refers to the timing inside each transmitted pulse and equivalently, the timing in which the pulse is sampled. Since the pulse propagates at the speed of light, this is fast time indeed. Slow-time, on the other hand, refers to timing on the order of multiple pulses. In other words, fast-time measures range-to-target and slow-time measures along-track distance. In fast-time, it is often assumed that the platform does not move significantly through the duration of a pulse.

In order to meet Nyquist sampling requirements in the along-track dimension, at least one pulse must be received for every distance covered that is equal to the along-track resolution of the radar (i.e., if the resolution is 1 m then a pulse must be received every 1 m that the platform moves along-track). SAR resolution is discussed in Appendix C.

When data are collected from the SAR, every target’s two-dimensional signature is spread in both the fast-time and slow-time. In order to form an image, the response of each target must be *compressed*. This compression process must be preformed in both the range direction and azimuth directions. There are many ways to consider SAR and its associated compression, the following sections present compression from the *range-Doppler* matched filter point of view, which is not only the most widely used method, but also the original digital method.

2.3 Range-Doppler Compression

This section describes the SAR transmit waveforms and an overview of range-Doppler compression [i.e, the range-Doppler algorithm (RDA)]. Several types of transmit waveforms may be used for the transmitted pulse. The waveform used most often is a linear frequency-modulated waveform (LFM). This type of waveform has properties that are particularly suited for use with radar, including the advantage of having a larger bandwidth while keeping the pulse duration short and having an envelope with constant magnitude [1, 6]. Additionally, small mismatches in Doppler do not change the general shape of the pulse nor reduce the amplitude significantly (although mismatches do shift the pulse in time). This is significant since radar typically involves relative motion of the sensor and/or targets. LFM is the most common signal type used in practical SAR applications [4].

An LFM chirp is a sinusoidal signal with linearly varying frequency. A complex LFM chirp can be written as $\exp(j\pi\beta t^2)$ where β is the chirp rate. The time derivative of this phase term gives the frequency $2\pi\beta t$: a linear function in time. Multiplying by a time-shifted copy of its conjugate (matched filtering) results in a signal with linear phase whose frequency is proportional to the time shift. This property is used in range compression, shown below.

There are two types of LFM transmit signals: pulsed and continuous-wave. An example of both is illustrated in Fig. 2.4. Pulsed radar transmits a single envelope then has a delay where nothing is transmitted before the next pulse is sent out again. This ensures that the radar is not transmitting during reception of the scattered signals. This means the same physical antenna may be used for both transmit and receive (i.e., monostatic). Continuous-wave radar has no (or very little) delay between pulses and is essentially always transmitting, even during reception of the scattered signals. Generally, this means the same antenna may not be used for transmit and receive in this case (i.e., pseudo-monostatic or bistatic).

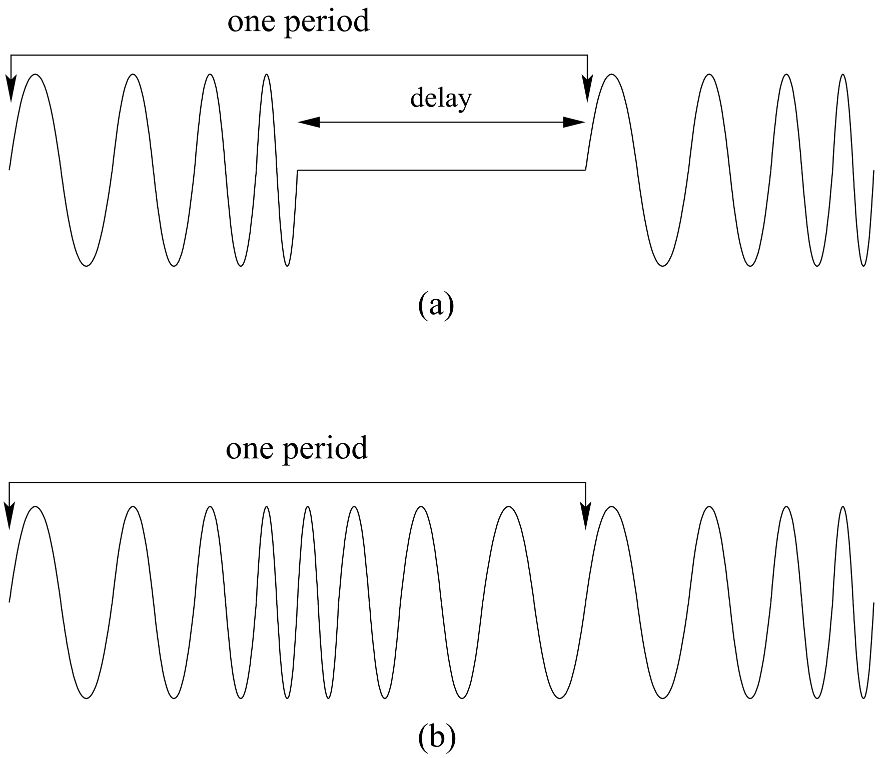

Figure 2.4: Example of linear frequency modulated waveforms. (a) Pulsed (b) Continuous-wave.

Most SAR systems employ pulsed signal transmission. Pulsed transmission involves transmitting a quick burst of electromagnetic radiation then receiving reflections off targets, and repeating the process. The term *pulse repetition interval* (PRI) refers to the elapsed time between pulse transmissions. PRF refers to the number of pulses transmitted per second, and is equivalent to the reciprocal of the PRI.

Linear frequency-modulation continuous-wave (LFM-CW) radar continuously and simultaneously transmits and receives. Although the signal is continually being transmitted in LFM-CW, it is possible to draw an analogy between pulsed and LFM-CW methods. As seen in Fig. 2.4, the frequency of the transmit signal increases, then decreases, then increases again and so on. The time interval it takes for the frequency oscillation to ramp up and back down is considered the PRI, and hence the number of up/down ramps per second is the PRF. Note that while the up-ramp and down-ramp periods are identical in the figure, in practice this may not be the case (e.g., the down-ramp period may be very short).

A key difference between the two transmit types is that pulsed radar generally mixes the received signal down to some intermediate frequency, then samples and stores the data, while LFM-CW radar mixes the received signal with the transmitting signal (essentially a delayed copy of itself), then samples. This process of mixing the received signal with the transmit signal is known as *dechirping* and has the advantage of requiring a lower sampling frequency at the expense of requiring a higher dynamic sampling range. LFM-CW radar also has the advantage of consuming less power than pulsed radar for a given SNR. This is because LFM-CW transmits pulses of much longer duration. The longer pulse length yields more energy contained in a single pulse.

The process of range compression for pulsed LFM involves matched filtering the received data with the transmit waveform. A derivation of this appears in Appendix B. The process of range compression for LFM-CW SAR is somewhat simpler than pulsed SAR, mostly due to the dechirped nature of the data. Dechirping allows data to be sampled at a much lower frequency and still meet the minimum Nyquist rate. This is due to the fact that most of the energy of each target's signature has already been compressed. There is a drawback, however. While pulsed SAR must be recorded at a high sampling rate because of its high frequency, it has low dynamic range and can be sampled using only a few bits. Because the signature of an LFM-CW signal has already been compressed in frequency, a higher sampling dynamic range is required and quantization noise becomes a factor. In general, wider dynamic sampling at a slower rate is less complicated, therefore simpler analog-to-digital (A/D) hardware can be utilized, resulting in an overall lower costing system. A derivation of range compression for dechirped, LFM-CW SAR appears in Sec. B.1.2.

Once range compression has been performed, the next step of image formation is to focus the target's signature spread in azimuth. This is known as *azimuth compression*. Azimuth compression may be accomplished similarly to pulsed range compression, i.e., matched filtering. The difference lies in the matched filter used. Whereas pulsed radar data are matched with the transmitted LFM chirp, the phase histories in azimuth are matched with the Doppler chirp corresponding to each range slice (i.e., the group of data in slow-time representing a given range-to-target). For ideal motion, this chirp is also LFM and is a result of the change in propagation phase of scattered signals as the platform travels in the along-track dimen-

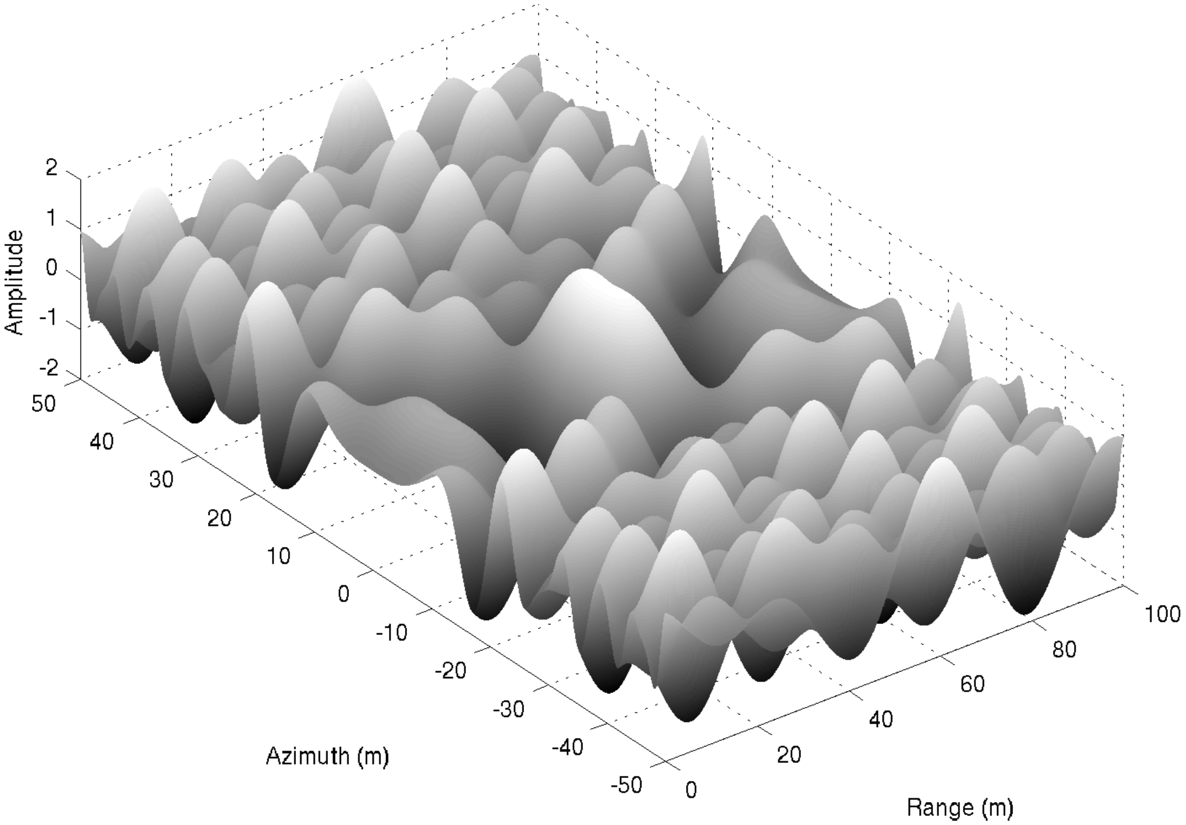

Figure 2.5: Example SAR raw waveform of two point targets. Because the energy of the targets has not been compressed, it is difficult to identify their location or magnitude.

sion. Based on the assumption of accurately known platform velocity and range-to-target, the Doppler chirp for each range slice can be calculated analytically. Azimuth compression is derived in Sec. B.2.

The following figures provide illustrations of SAR data before and after compression. Figure 2.5 shows an example of two point targets, each at position 0 m in azimuth, but at 40 m and 90 m in range. As evidenced by the figure, without processing, the individual signals from the targets are difficult to resolve. Figure 2.6 shows an example of range compression for the raw data. The energy of the two targets that was previously spread in the fast-time dimension is now compressed. The compression in range shows the sinc like behavior of the point-spread of LFM autocorrelation. In azimuth, the targets exhibit the the response of the Doppler chirp. Compression of the Doppler chirp (i.e., azimuth compression) is shown Figure 2.7.

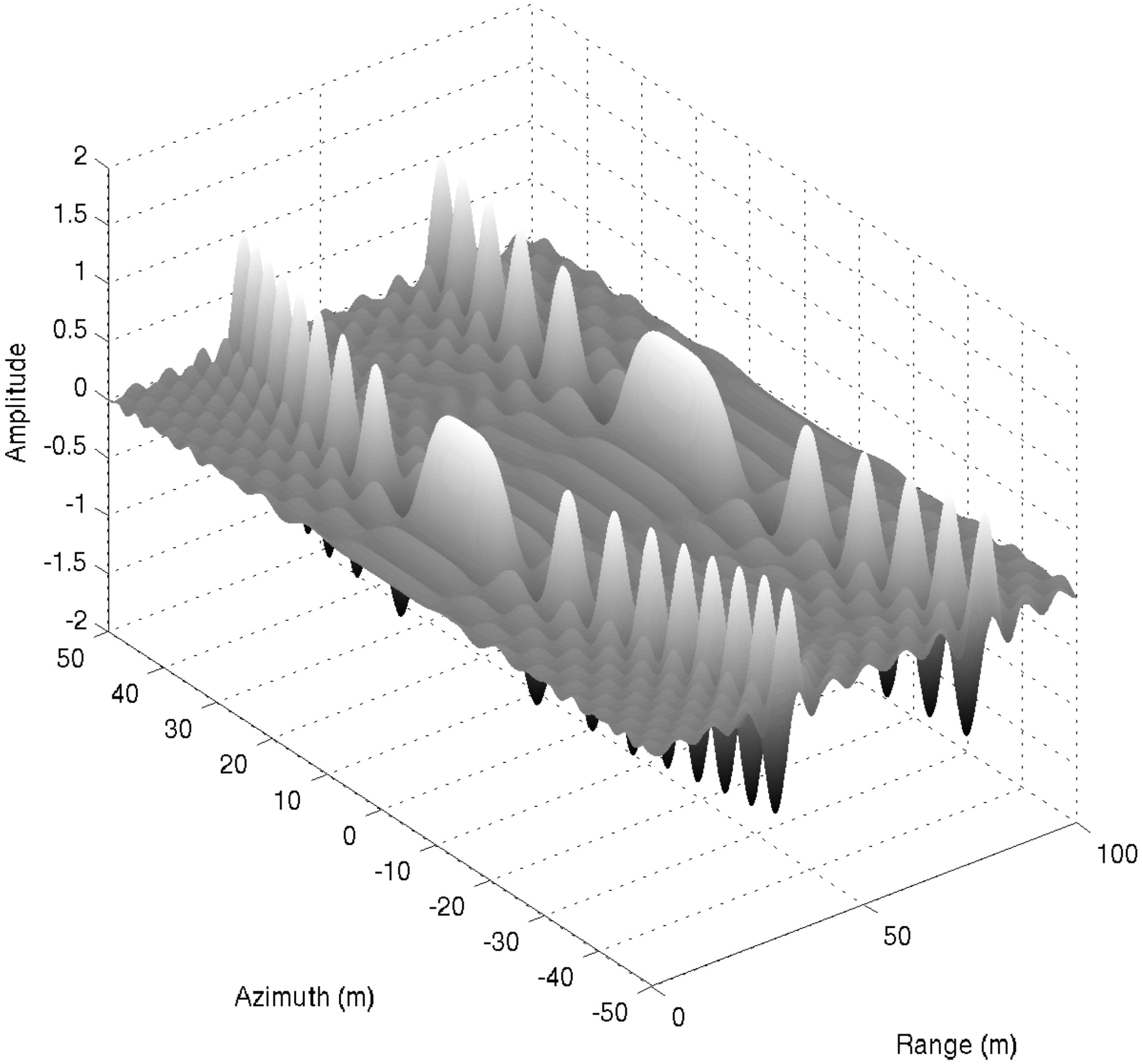

Figure 2.6: Example SAR range-compressed waveform corresponding to the raw data of Fig. 2.5. After compressing each pulse, two distinct phase histories corresponding to each of the point targets are visible at different ranges.

2.4 Introduction to More Frequency Domain Algorithms

The family of frequency domain algorithms are the primary methods of SAR image formation. The frequency domain methods share many of the same characteristics, including that they image in the slant-plane. The chief algorithms are range-Doppler, omega-k, chirp scaling, and polar formatting. These are briefly introduced below. A thorough treatment of them appears in [3, 7].

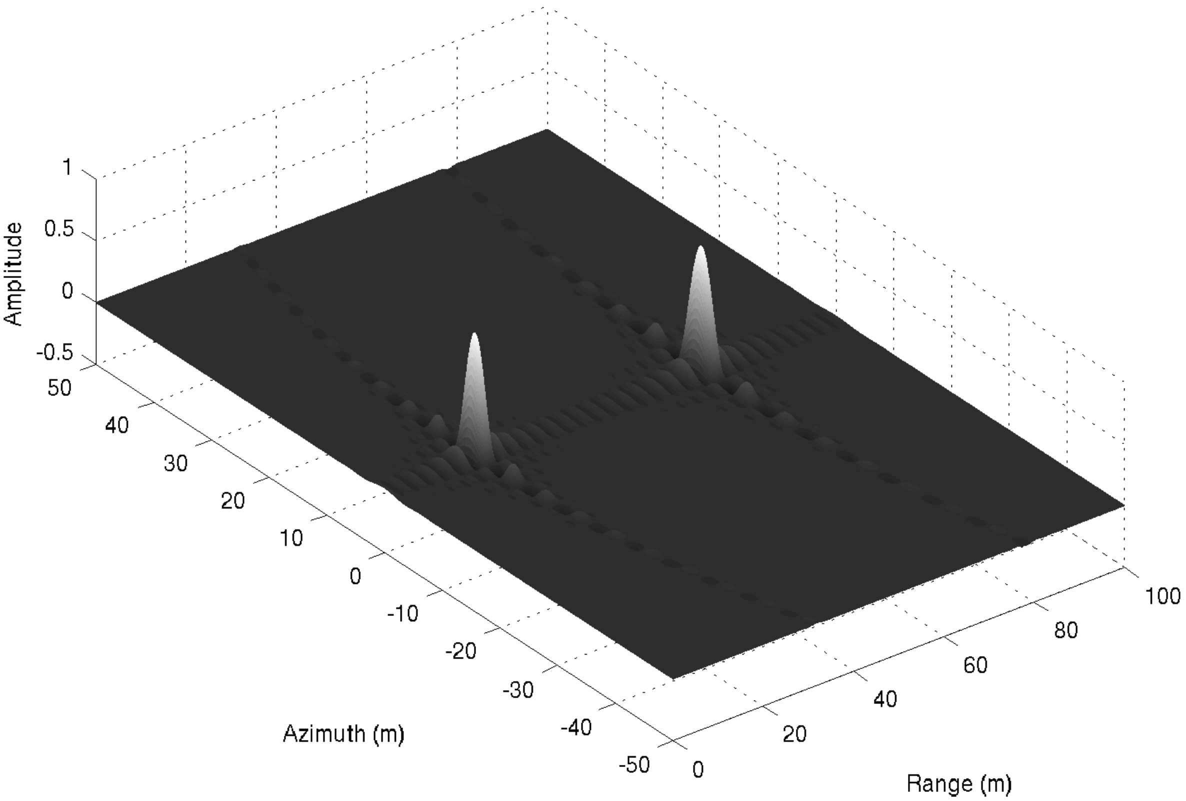

Figure 2.7: Example azimuth-compressed waveform from a SAR. The sinc response in range and azimuth is apparent.

The range-Doppler algorithm (RDA) was described in the previous section. The range-Doppler algorithm was the first digital algorithm used for focusing SAR phase history data. The algorithm is very robust and able to form images, though not perfectly, even when velocity and motion estimates are poor. The downside is that the formation is not perfect and extra processing steps are required to handle range cell migration and coupling of range and azimuth (i.e., squint). The handling of this coupling is performed by a step known as secondary range compression (SRC).

The omega-k algorithm is also called the range-migration algorithm or seismic processing. It comes from the field of seismic signal processing where geophones are placed linearly on the ground and acoustic waves are used to sense features below the surface. Rocca [8], in the late 80s, was the first to apply these seismic techniques to SAR. As the name implies, in omega-k the important aspects happen in the 2-D frequency domain (omega is range angular frequency and k is azimuth wavenumber). After transforming to the 2-D frequency domain, the data are multiplied by a reference function which performs compression but only perfectly at a single range. This step is known as bulk compression. Afterward, differential compression is performed to focus the surrounding data and is done by Stolt mapping, which is a one dimensional interpolation in the range frequency dimension. Omega-k is able to focus wide azimuth apertures and relatively high squint angles [3].

The chirp scaling algorithm was developed concurrently but independently in the early 1990s by Cumming and Wong at MacDonald Dettwiler and by Runge and Bamler in Oberpfaffenhofen at the German Aerospace Center (DLR). Chirp scaling may be viewed as an approximation of the omega-k solution, but without the Stolt interpolation. It performs operations in both the azimuth-frequency/range-time and the azimuth-frequency/range-frequency domains. Its main limitations are wide azimuth apertures and/or high squint. It is computationally more efficient than omega-k [3].

Finally, the polar formatting algorithm is a method of compressing spotlight mode SAR data. In it, the raw phase histories are sampled onto a polar grid, instead of a rectangular one. Polar formatting is unique in that under ideal circumstances, azimuth compression may be performed by a Fourier transform in azimuth [4].

In all of these algorithms, a preprocessing step known as *motion compensation* is typically used. Motion compensation involves correcting for motion errors due to deviations from the assumed straight line, constant heading, constant velocity movement of the platform. Motion compensation is essential to obtaining well-focused imagery when significant path non-idealities are present. Detailed specifics of motion compensation appear in [9, 10].

These algorithms share the common element that certain assumptions are made that allow for more computationally efficient processing of the data. These assumptions usually result in convolution processing, which is aided through use of a Fourier transform to the frequency domain. The drawback to this is that each algorithm has limits on which modes and geometries may be used with it. There is a more general method for SAR signal processing which places fewer requirements on imaging mode and geometry. This is the *backprojection* algorithm introduced in the next chapter.

Figure 2.8 shows example images created from SAR data [11]. Subfigure (a) shows an image formed by the range-Doppler algorithm and subfigure (b) shows the same data formed by backprojection. The images are of arctic sea ice taken by the CASIE SAR in July 2009. Notice that there is finer detail present in the backprojected image. Additionally, the RDA image has blurring in azimuth due to uncompensated motion.

After azimuth compression, the data are in complex form. Simple images are created by representing each pixel as the magnitude of each complex data point. Phase representations of the data are also possible. Once the SAR compression schemes are completed and processed images are available, other processing techniques can be performed. In order reduce speckle noise in SAR images, *multilook* averaging is often performed whereby the magnitude value of adjacent pixels are averaged in order to improve radiometric resolution at the expense of spatial resolution [3]. Another post-processing technique available when multiple receive channels are present is interferometry [12, 13].

Interferometry involves using target phase differences from multiple images to create a topographical height-map of an imaged landscape. Although the range-resolution of a radar is typically not fine enough to unambiguously recover the exact distance a propagation wave travels, through the use of two receive antennas, the *difference* in path length between the two can be determined with great precision. Interferometry uses this in order to obtain the height of a pixel's scattering-cell.

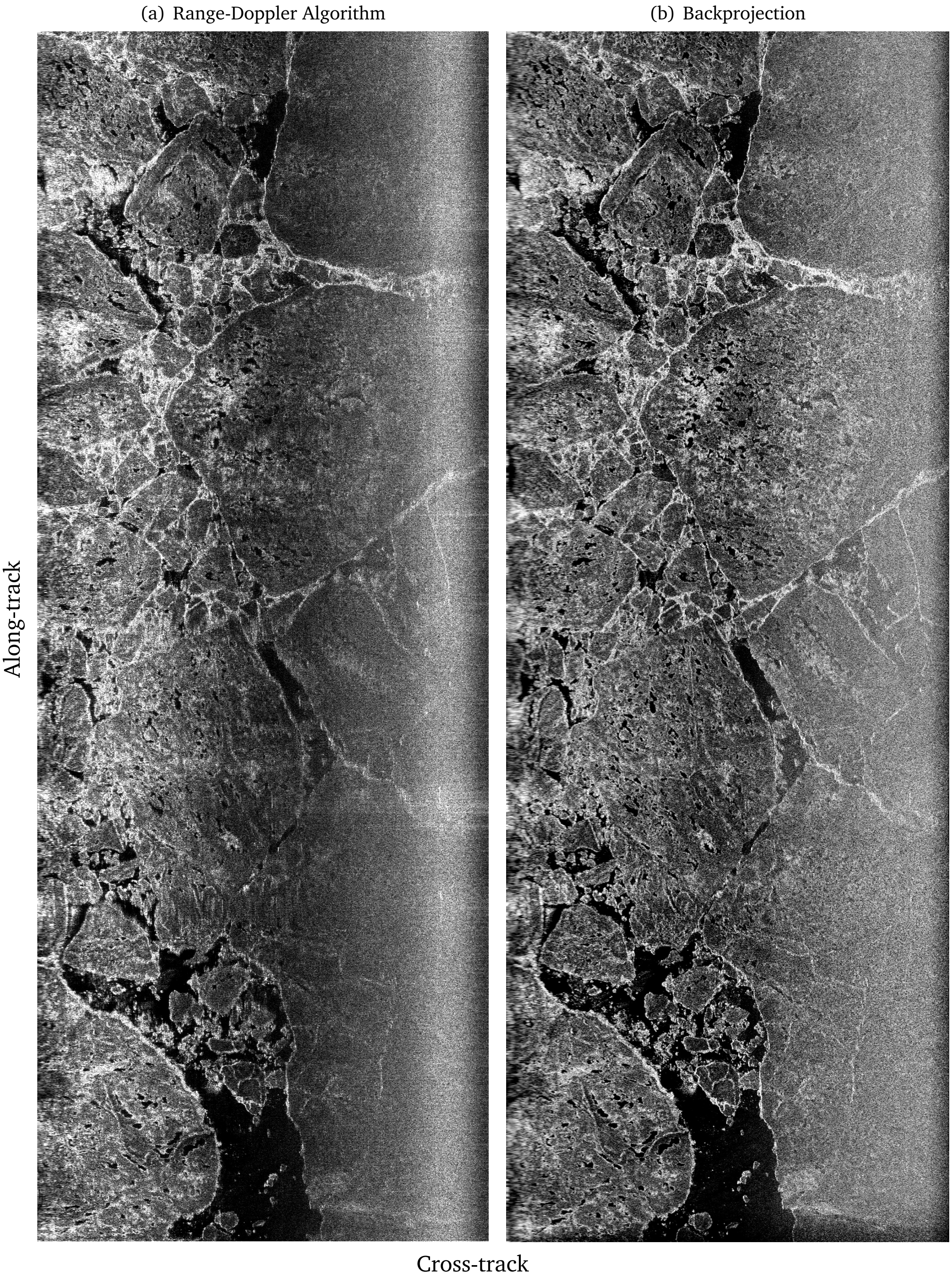

Figure 2.8: Image comparison of (a) the range-Doppler algorithm and (b) backprojection. The images are of arctic sea ice taken by the CASIE SAR in July 2009.

Chapter 3

Time-domain Backprojection

3.1 Introduction

Synthetic aperture radar (SAR) is a class of radar that utilizes platform motion to obtain finer resolution in the along-track dimension than that given by the along-track illumination footprint [3]. Researchers have developed many algorithms over the past several decades to form images from raw SAR phase history data [8, 14, 15, 16, 17, 18, 19]. Most SAR algorithms are founded on the use of frequency domain techniques and have been analyzed in great detail [3, 4, 20, 21, 22, 23, 24, 25]. However, time-domain backprojection is one class of image formation techniques that does not fall under the frequency domain category.

Frequency-domain methods make varying assumptions about squint, range curve migration, platform motion, point spread homogeneity, and others. Time-domain backprojection, on the other hand, makes few assumptions. The main assumption it makes is that the imaging geometry is known precisely. Because backprojection makes fewer assumptions and can model the ideal SAR matched filter, with respect to the frequency-domain methods it enjoys a number of advantages which are listed below. (Note: not all frequency domain methods share the same limitations, but all are limited in at least one of the following areas.)

- **Invariant to imaging mode.** Backprojection utilizes the same algorithm regardless of imaging mode. Frequency domain methods, on the other hand, typically require modification depending on the imaging mode and geometry. For example, a different algorithm is used for stripmap and spotlight modes. Many of the frequency domain methods require special processing steps when the illumination footprint has non-zero Doppler centroid or for highly squinted geometries.

- **Indifference to unambiguous aliasing in azimuth**. Ambiguous azimuth aliasing occurs when along-track frequencies exceed the Nyquist spatial sampling requirements. Unambiguous aliasing occurs in squinted geometries where the signal bandwidth does not exceed the sampling requirements but has undergone "spectral wrapping." Given the pulse repetition frequency (PRF) is high enough to avoid ambiguous signal aliasing in Doppler (i.e., azimuth), backprojection is insensitive to the number of spectral wraps that occur in squinted geometries.
- **Space/time matched filter**. Backprojection fully uses information about the imaging geometry to produce a pixel-by-pixel varying matched filter to approximate the expected return signal. This includes higher order effects such as antenna gain compensation (phase and magnitude) on an individual pulse basis. The frequency domain methods can only roughly compensate for higher order effects as they are convolution based and thus use the same response across the entire processing window.
- **Motion compensation**. Implicit in the backprojection algorithm is motion compensation that utilizes available ground information (see the previous point). This advantage becomes more significant at lower airborne altitudes.
- **Multi-static imaging**. Multi-static imaging geometries where transmit and receive antennas are widely separated with incongruous motion (e.g., two platforms moving in non-parallel paths) are incompatible with most traditional methods. Backprojection handles these situations gracefully (given the positions are known).
- **Ground-plane imaging**. Orthorectification is a process that maps slant-plane SAR imagery to the ground-plane. It is often a necessary post-image formation step to correct image perspective for human visualization. Backprojection explicitly images in the ground-plane making the orthorectification step unnecessary. Topography can be explicitly included, which reduces image artifacts due to terrain relief. Frequency domain

methods implicitly image the target scene in the slant-plane and therefore require orthorectification.

- **Swath width**. Backprojection places no fundamental limits on imaging swath other than those imposed by the geometry and physics of the radar (e.g. minimum PRF, etc.). Backprojection is able to handle geometries where the relative velocity between the antenna and the scene varies across the imaging swath. Frequency domain methods are commonly limited in these regards.

- **Pulses may be processed as they are received without buffering**. Frequency domain methods involve, as the name implies, performing a transform to the frequency domain and accordingly must buffer a certain amount of data. This may constitute a considerable amount of memory depending on the synthetic aperture length. Backprojection can process each pulse as it is received without the need for any additional buffering of the raw data.

- **Azimuth segmentation**. When convolving two signals where one is very long, the "overlap and save" method, also called azimuth segmentation, is often used which segments the longer signal and performs the convolution in steps, saving a portion of the result and discarding the rest. Not only does backprojection not require azimuth segmentation because the output image may be one continuous array (see the previous point), but this may also lead to better continuity between images when placed adjacently. As the frequency domain methods are convolution based they require azimuth segmentation.

- **Image subset**. Backprojection easily handles imaging a subset of a scene with great computational improvement (equivalent to the percentage of pixels not imaged). Frequency domain methods generally require all of the pixels contributing to the scene to be imaged simultaneously, or have limited computational savings when imaging a subset of the scene.

- **Simplicity**. Of all the SAR image formation algorithms, backprojection may have the simplest description of them all. With range-compressed data as the input, backprojection may be described with one equation denoted by the summation of two terms. Only the range-Doppler algorithm without motion compensation, range curvature migration compensation, or secondary range compression approaches this level of simplicity.

While the backprojection algorithm exhibits a remarkable number of advantages over the frequency domain methods, it has two main disadvantages: computational expense and the requirement for precise knowledge of imaging geometry. Computational complexity has traditionally been the limiting factor preventing the wide adoption of backprojection for SAR image formation. In recent years however, advancement in computational capabilities has rendered this disadvantage all but obsolete as current technology allows backprojection of images in real time [11, 26]. This leaves as the principle disadvantage to using backprojection the requirement of knowing precisely the imaging geometry.

Backprojection requires the time-varying position of the antenna(s) be known relative to the three-dimensional position of the imaged terrain in the ground-plane of the scene. The position of the antenna is usually estimated with an Inertial Navigation System (INS) while the height of the scatterers is satisfied through the use of a digital elevation map (DEM). In contrast, while frequency domain methods require knowledge of the antenna position for motion compensation and imaging (i.e., an INS is necessary), only the slant-plane projection of the position of the scatterers is needed, which is implicit in the radar data. Frequency domain processing thus can be done adequately without a DEM.

This chapter seeks to provide a more detailed analysis of the time-domain backprojection image formation algorithm than presently exists in literature, including characterization of the sensitivities of backprojection to its various input parameters. The chapter considers the sources of error and provides analysis of requirements to achieve a given level of performance. In order to facilitate this, we begin with a generalized derivation of the time-domain backprojection algorithm.

The chapter is organized as follows. Section 3.2 presents a general expression for backprojection image formation. Using these results, Section 3.3 presents an approximation of the residual range present in each backprojection term. This facilitates the investigation of performance and error sources in Section 3.4. Finally, Section 3.5 concludes with an analysis of the results.

3.2 Generalized Time-domain Backprojection

Many SAR image formation derivations begin with two implicit assumptions: that the radar point spread function is constant across the image and that image formation may be separated into two steps–range compression and azimuth compression [3, 20]. This equates to formulating the problem into one of convolution. In order to be more general, I explicitly avoid this assumption.

The following subsections provide a detailed derivation of the time-domain backprojection image formation algorithm. I begin with a general, time domain, uncompressed formulation and then progress to other forms through the use of various assumptions. These results are used in later sections as the basis for the backprojection analysis.

3.2.1 Derivation of General Form

The backprojection derivation begins with a generic linear frequency modulated (LFM) signal. The instantaneous frequency $f(t)$ of an LFM signal is

$$f(t) = f_0 + Kt, \tag{3.1}$$

where t is fast-time, f_0 is the center frequency, and K is the frequency modulation (FM) ramp-rate in Hz per second. Note that in this convention the signal is centered at time $t = 0$. The corresponding phase of Eq. 3.1 is the integral

$$\begin{aligned} \phi(t) &= 2\pi \int_0^t f(\tau) \mathrm{d}\tau \\ &= 2\pi \int_0^t \left(f_0 + K\tau\right) \mathrm{d}\tau \\ &= 2\pi \left(f_0 t + \frac{K}{2} t^2 + \phi_0\right), \end{aligned} \tag{3.2}$$

with ϕ_0 the initial phase. This leads to the LFM transmit signal

$$\begin{aligned} s^{\mathrm{tx}}(t) &= w\left(t\right) \exp\left\{j2\pi\phi(t)\right\} \\ &= w\left(t\right) \exp\left\{j2\pi f_0 t + j\pi K t^2 + j\phi_0\right\}, \end{aligned} \tag{3.3}$$

where $w(t)$ is the pulse envelope (e.g. $\mathrm{rect}(t/T) = 1$ over the domain $[-\frac{1}{2}, \frac{1}{2}]$, with T the pulse duration).

Consider a stationary, isotropic scatterer located in three-space. The round-trip propagation delay from transmitter to scatterer to receiver is t_n, where n is the slow-time pulse index. Note that t_n is implicitly a function of fast-time t, but for simplicity in notation this is neglected. From Eq. 3.3, the scattered received signal is an amplitude-adjusted, time-delayed copy of the transmit signal,

$$s_n^{\mathrm{rx}}(t) = A_n(t-t_n)\, G_n(t-t_n)\, w(t-t_n) \exp\left\{j2\pi f_0 (t-t_n) + j\pi K (t-t_n)^2 + j\phi_0\right\} + \eta. \quad (3.4)$$

Here, $A_n(t)$ is an amplitude term that depends on target area, random atmospheric effects, etc., $G_n(t)$ is an amplitude term that depends on antenna gains, propagation loss, system filters, etc., and η is additive noise. If the received signal is demodulated when received then this becomes

$$s_n^{\mathrm{rx}}(t) = A_n(t-t_n)\, G_n(t-t_n)\, w(t-t_n) \exp\left\{-j2\pi f_0 t_n + j\pi K (t-t_n)^2 + j\phi_0\right\} + \eta. \quad (3.5)$$

Examining this equation, the first term inside the exponential is termed the propagation phase and the second term inside the exponential is the LFM chirp.

As the energy of the received signal is spread in fast- and slow-times, it is desirable to focus this energy as narrowly as possible. This processes is called *compression*. Compression is typically performed with a matched filter since it maximizes SNR in the presence of additive noise [27] (although other types of filters could be used, e.g., a Wiener filter). In order to matched-filter Eq. 3.5, the filter reference function is

$$h_n^{\mathrm{C}}(t) = w\left(t-\widetilde{t}_n\right)\, G_n\left(t-\widetilde{t}_n\right) \exp\left\{-j2\pi f_0 \widetilde{t}_n + j\pi K \left(t-\widetilde{t}_n\right)^2\right\}, \quad (3.6)$$

where $\widetilde{t}_n$ is the delay parameterizing the matched filter. Ideally $\widetilde{t}_n$ is equal to t_n, but it is retained as a separate term to explore the results of mismatch.

Matched-filtering is customarily implemented through the use of correlation (i.e., sliding inner-product). However, this concept is not fully congruous with the concept of backprojection because there is no simple way of sliding slow/fast-time in the ground-plane. Since time-domain backprojection is not implemented using convolution methods (i.e., reduction in computation through use of the frequency domain), it makes sense to calculate only the peak of the matched filter for a given pixel. The point-spread response around the peak may be obtained by "imaging" the surrounding area in the ground-plane.

Neglecting the noise term for the sake of brevity, the result of matched filtering a single pixel is

$$\begin{aligned} I &= \sum_{n\in\mathcal{N}} \int s_n^{\mathrm{rx}}(\tau) h_n^{\mathrm{C}*}(\tau) \mathrm{d}\tau \qquad (3.7) \\ &= \sum_{n\in\mathcal{N}} \int A_n(\tau - t_n)\, G_n\left(\tau - t_n\right)\, w_n\left(\tau - t_n\right) \exp\left\{-j2\pi f_0 t_n + j\pi K \left(\tau - t_n\right)^2 + j\phi_0\right\} \\ &\qquad \cdot G_n\left(\tau - \widetilde{t}_n\right)\, w_n\left(\tau - \widetilde{t}_n\right) \exp\left\{j2\pi f_0 \widetilde{t}_n - j\pi K \left(\tau - \widetilde{t}_n\right)^2\right\} \mathrm{d}\tau, \qquad (3.8) \end{aligned}$$

where $\mathcal{N}$ is the set of all pulses contributing to the scattering-cell and I is the backprojected pixel value for the scattering-cell. The term *pixel* refers to the imaged signal and *scattering-cell* refers to the physical area being imaged. Note the lack of a conjugation symbol $*$ on $G\left(\right)$ and $w\left(\right)$, which are assumed to be purely real-valued.

Several observations are in order. First, matched filtering in this manner handles both the propagation phase and the LFM chirp, thus simultaneously performing both azimuth and range compression, respectively. Second, as $G_n\left(t\right)$ and $w_n\left(t\right)$ are functions of fast-time and slow-time, this expression does not assume stationary/homogeneous gain terms since each may vary on a sample-by-sample and pulse-by-pulse basis. Third, Eq. 3.8 yields the value I for only a single scattering-cell: this process must be repeated for every scattering-cell in the desired image. Performing this process on an $n \times n$ image is extremely computationally expensive, on the order of $\mathcal{O}\left(n^4\right)$.

Finally, if $\widetilde{t}_n = t_n$ then the resulting pixel value is

$$I = \exp\left(j\phi_0\right) \sum_{n\in\mathcal{P}} \int A_n\left(\tau - t_n\right) G_n^2\left(\tau - t_n\right) w_n^2\left(\tau - t_n\right)\, \mathrm{d}\tau. \qquad (3.9)$$

With the assumption that the time-delay to the target is known exactly, the phase of the filter perfectly matches the phase of the signal at each pulse. For this assumption to hold, the target must be located at precisely the anticipated position; it is not sufficient to use the delay to the center of the scattering-cell, but rather the delay to the phase-center of the cell (for each pulse). In general, the precise phase-center of the scattering-cell is not the physical center and is not known. The implications of this concept are discussed both here and in following chapters.

If $t_n \neq \widetilde{t}_n$ then the complex exponentials in Eq. 3.8 no longer cancel out: a differential propagation phase $\exp\left\{j2\pi f_0 \left(\widetilde{t}_n - t_n\right)\right\}$ results. There is also an error $\phi_{\text{LFM error}}$ due to mismatch in the LFM chirp term. This results in

$$I = \sum_{n\in\mathcal{N}} \int (\cdots) \exp\left\{j2\pi f_0 \left(\widetilde{t}_n - t_n\right)\right\} \exp\left\{j\phi_{\text{LFM error}}\right\} \, \mathrm{d}\tau, \tag{3.10}$$

where the gain terms comprise the ellipsis and the starting phase is neglected. Comparing the derivation here with that of the range-Doppler algorithm (RDA) in Appendix B, it is seen that backprojection has a simpler form than RDA, which is the simplest of the frequency domain algorithms.

Examining the LFM chirp error, it is useful to understand the maximum error in $\widetilde{t}_n$. The radar has a slant-range resolution of $^1\!/_{2KT}$ in time. Therefore, $\widetilde{t}_n$ can differ from t_n by at most $\pm{}^1\!/_{4KT}$ (half the slant-range resolution). Examining the maximum LFM error, if

$$\widetilde{t}_n = t_n \pm \frac{1}{4KT}, \tag{3.11}$$

then

$$\phi_{\text{LFM error}} = \pi K \left[\left(\tau^2 - 2\tau t_n + t_n^2\right) - \left(\tau^2 - 2\tau \tilde{t}_n + \tilde{t}_n^2\right)\right]$$

$$
\begin{aligned}
&= \pi K \left[2\tau\left(\tilde{t}_n - t_n\right) + \left(t_n^2 - \tilde{t}_n^2\right)\right] \\
&= \pi K \left[2\tau\left(t_n \pm \frac{1}{4KT} - t_n\right) + \left(t_n^2 - \left(t_n^2 \pm \frac{t_n}{KT} + \frac{1}{(4KT)^2}\right)\right)\right] \\
&= \pi K \left[\pm\frac{\tau}{2KT} \mp \frac{t_n}{KT} - \frac{1}{(4KT)^2}\right] \\
&= \pm\frac{\pi}{T}\left(\frac{\tau}{2} - t_n\right) - \frac{\pi}{16KT^2}. \qquad (3.12)
\end{aligned}
$$

The first term vanishes in the integral in Eq. 3.10 and the second term $\pi/16KT^2$ is insignificant for practically any LFM SAR time-bandwidth product. Thus, the only significant phase term is the differential propagation phase [3] and is termed the *residual phase*. It is residual phase that is the heart of the backprojection analysis in later sections.

3.2.2 Compression Simplification

As stated above, performing compression according to Eq. 3.8 is computationally very expensive. However, under certain conditions compression can be broken into two separate steps (range and azimuth compression). A limiting factor preventing separation in the derivation above is the implicit dependence of t_n on fast-time. However, if the pulse duration T is short enough that the platform movement during propagation is insignificant then t_n may be considered stationary throughout the pulse duration (i.e., the *stop-and-hop* approximation). Note that this does not constrain the maximum distance to the target since a monostatic radar may be considered bistatic for purposes of calculating the range to the target (i.e., treat the antenna as being in one position during transmit and then in a different position during receipt).

Through use of this assumption, the matched filter may be modified to first perform range compression by using the reference function

$$h_n^{\mathrm{R}}(t) = w(t - t_n)\exp\left\{j\pi K (t - t_n)^2\right\}, \qquad (3.13)$$

which includes only the LFM chirp term. This leads to the matched filtered (range-compressed) signal $g_n\left(t\right)$:

$$\begin{aligned} g_n(t) &= \int s_n^{\mathrm{rx}}(\tau) h_n^{\mathrm{R}*}(\tau - t)\mathrm{d}\tau && (3.14) \\ &= \int A_n(\tau - t_n)\, G_n\left(\tau - t_n\right)\; w\left(\tau - t_n\right) \exp\left\{-j2\pi f_0 t_n + j\pi K \left(\tau - t_n\right)^2 + \phi\right\} \cdot \\ &\qquad\qquad w\left(\tau - t - \widetilde{t}_n\right) \exp\left\{-j\pi K \left(\tau - t - \widetilde{t}_n\right)^2\right\} \mathrm{d}\tau \\ &\approx A_n\left(t - t_n\right)\, G_n\left(t - t_n\right)\, T \operatorname{sinc}\left\{KT\left(t - \left(t_n^2 - \widetilde{t}_n^2\right)\right)\right\}\, \exp\left\{-j2\pi f_0 t_n + \phi\right\}, && (3.15) \end{aligned}$$

with $w(t) = \mathrm{rect}\left(t/T\right)$.

At this point it is useful to map this result from time coordinates to spatial coordinates. This is done by noting that the two-way delay is

$$t_n = \frac{r_n^{\mathrm{tx}} + r_n^{\mathrm{rx}}}{c}, \tag{3.16}$$

with r_n^{tx} and r_n^{rx} the transmitter and receiver range-to-target, respectively, and c the propagation speed (e.g., the speed of light). In the case of a monostatic radar, $r_n^{\mathrm{tx}} = r_n^{\mathrm{rx}}$. This expression is equivalent to

$$2\pi f_0 t_n = k\left(r_n^{\mathrm{tx}} + r_n^{\mathrm{rx}}\right), \tag{3.17}$$

where the wavenumber

$$k = 2\pi f_0/c = 2\pi/\lambda. \tag{3.18}$$

The two-way range to the target is

$$d_n = r_n^{\mathrm{tx}} + r_n^{\mathrm{tx}} \tag{3.19}$$

and the two-way range parameterizing the matched filter is $\widetilde{d}_n$. The difference between the two is the residual range

$$\Delta d_n = \widetilde{d}_n - d_n. \tag{3.20}$$

In the “worst case” scenario of maximum residual range, the phase-center may be in the corner of the scattering-cell. Thus, the maximum horizontal (i.e., ground range) displacement of a target in the scattering-cell is half the ground resolution cell width:

$$\delta_{\mathrm{y-max}} = \frac{R_y}{2} = \frac{R_{y,\mathrm{slant}}}{2\sin\theta}, \tag{3.21}$$

with $R_{y,\mathrm{slant}}$ the slant-range resolution, R_y the ground-range resolution, and θ the incidence angle. The maximum vertical displacement (at the center of the cell) is

$$\delta_{\mathrm{z-max}} = R_y \cos\theta. \tag{3.22}$$

The maximum azimuth displacement is half the azimuth resolution. Note that these give the worst-case scenario which is likely to occur only in the case of a point target. The expected position of the phase-center of distributed targets is near the cell's center.

Using this mapping, the range-compressed signal may be written as

$$g_n\left(l\right) = A_n\left(l - d_n\right)\, G_n\left(l - d_n\right)\, R\left(\Delta d_n\right)\, \exp\left\{-jkd_n\right\}, \tag{3.23}$$

where l is fast-time distance and $R()$ is the range-compressed impulse response centered at 0.

Azimuth compression of the range-compressed signal in Eq. 3.23 is then computed by matched filtering with the reference function

$$h_n^{\mathrm{A}}\left(t\right) = \exp\left(-jk\widetilde{d}_n\right). \tag{3.24}$$

This leads to the backprojected result

$$\begin{aligned} I &= \sum_{n\in\mathcal{N}} g_n\left(\widetilde{d}_n\right) \exp\left(jk\widetilde{d}_n\right) \\ &= \sum_{n\in\mathcal{N}} A_n\left(\widetilde{d}_n - d_n\right)\, G_n\left(\widetilde{d}_n - d_n\right)\, R\left(\Delta d_n\right) \exp\left(jk\Delta d_n\right). \end{aligned} \tag{3.25}$$

While a phase-only matched filter is used here, in practice, other terms (including the antenna gain) may be added. As before, the only remaining phase term is the residual propagation phase present at each pulse when $\Delta d_n \neq 0$. Performing range and azimuth separately in this manner leads to a computational complexity of $\mathcal{O}\left(n^3\right)$ for an $n \times n$ image. Further optimization, albeit with some loss of quality, may be obtained through fast-factorized backprojection [28, 29].

If the antennas do move significantly (on the order of a wavelength) through the duration of the pulse, range/azimuth compression is still separable if the platform velocity is constant. A derivation of this is shown in [30]. A modification for LFM-CW (continuous wave) operation is shown in [7].

3.3 Hyperbolic Range-to-target

One of the key parameters in the backprojection equation is the distance (or equivalently, time-delay) from the antenna(s) to the scattering-cell phase-center. For purposes of this chapter, the assumed distance to the scattering-cell is the distance from the antennas to the physical center of the scattering-cell (equivalent to the value parameterizing the backprojection matched filter). The actual distance is that from the antennas to the phase-center of the scattering-cell. It is the difference between the assumed and actual distances that leads to the residual distance Δd_n (and residual phase $k\Delta d_n$) discussed previously.

Consider the *nominal residual phase* for a given target to be the residual phase for the contribution at the mean position of the synthetic aperture (ideally the point of closest approach). Contributing samples from pulses transceived away from the mean position may have a different residual phase than the nominal. The difference between the residual phase at surrounding pulses and the nominal is *phase error*. In general, the phase error grows as the platform distance from the mean position grows. If the phase error becomes too large then the contributing sample that produced it sums destructively during backprojection summation. In order to facilitate later sensitivity and performance analysis of backprojection, I examine the residual range that leads to the residual phase.

With the dimensions x, y, z as along-track, cross-track and elevation, respectively, the one-way range r_n to the physical center of a scattering-cell is

$$\begin{aligned} r_n &= \sqrt{x_n^2 + y_n^2 + z_n^2} \\ &= \sqrt{(\bar{x} + \zeta_{\mathrm{x},n})^2 + (\bar{y} + \zeta_{\mathrm{y},n})^2 + (\bar{z} + \zeta_{\mathrm{z},n})^2} \\ &= \sqrt{(\bar{x}^2 + \bar{y}^2 + \bar{z}^2) + \zeta_{\mathrm{x},n}\,(2\bar{x} + \zeta_{\mathrm{x},n}) + \zeta_{\mathrm{y},n}\,(2\bar{y} + \zeta_{\mathrm{y},n}) + \zeta_{\mathrm{z},n}\,(2\bar{z} + \zeta_{\mathrm{z},n})}, \qquad (3.26) \end{aligned}$$

where n is the time index, $(x_n,\, y_n,\, z_n)$ is the three-dimensional range to the scattering-cell for each time index, $(\bar{x},\, \bar{y},\, \bar{z})$ is the mean range-to-target (e.g., $\bar{x}$ is zero for non-squinted geometry), and $(\zeta_{\mathrm{x},n},\, \zeta_{\mathrm{y},n},\, \zeta_{\mathrm{z},n})$ is the antenna displacement from the mean at time n.

The range to the phase-center $r_n^{'}$ is

$$\begin{aligned} r_n^{'} &= \sqrt{x_n^{'2} + y_n^{'2} + z_n^{'2}} \\ &= \sqrt{(\bar{x} + \zeta_{\mathrm{x},n} - \delta_\mathrm{x})^2 + (\bar{y} + \zeta_{\mathrm{y},n} - \delta_\mathrm{y})^2 + (\bar{z} + \zeta_{\mathrm{z},n} - \delta_\mathrm{z})^2} \\ &= \sqrt{(\bar{x}^2 + \bar{y}^2 + \bar{z}^2) + V_{\mathrm{x},n} + V_{\mathrm{y},n} + V_{\mathrm{z},n}}, \qquad (3.27) \end{aligned}$$

with the azimuth terms grouped into

$$V_{\mathrm{x},n} = \zeta_{\mathrm{x},n}^2 + \delta_\mathrm{x}^2 + 2\,(\bar{x}\zeta_{\mathrm{x},n} - \bar{x}\delta_\mathrm{x} - \zeta_{\mathrm{x},n}\delta_\mathrm{x}) \qquad (3.28)$$

and likewise $V_{\mathrm{y},n}$ and $V_{\mathrm{z},n}$ for the range and elevation terms.

Given the ranges defined above, the residual range is

$$\begin{aligned} \Delta r_n &= r_n - r_n^{'} \qquad (3.29) \\ &= \sqrt{x_n^2 + y_n^2 + z_n^2} - \sqrt{x_n^{'2} + y_n^{'2} + z_n^{'2}}. \qquad (3.30) \end{aligned}$$

The residual range leads to the phase term $\phi_n = 2k\Delta r_n$ present at each pulse summed in backprojection (assuming a monostatic radar). As a non-zero value for Δr_n results in residual phase, manipulating Eq. 3.29 is critical to analysis. Unfortunately, there is no simplification for this equation that results in an exact value for Δr_n. With certain assumptions, however, a close approximation may be made.

3.3.1 First-order Taylor Series Approximation

Suppose the mean range-to-target is

$$\bar{r} = \sqrt{\bar{x}^2 + \bar{y}^2 + \bar{z}^2}. \tag{3.31}$$

A first-order Taylor series approximation of the square root (where $a \gg b$)

$$\sqrt{a^2 + b} \approx a + \frac{b}{2a}, \tag{3.32}$$

can be used in Eqs. 3.26 and 3.27 to produce

$$\begin{aligned} r_n &\approx \bar{r} + \frac{\zeta_{\mathrm{x},n}\left(2\bar{x} + \zeta_{\mathrm{x},n}\right) + \zeta_{\mathrm{y},n}\left(2\bar{y} + \zeta_{\mathrm{y},n}\right) + \zeta_{\mathrm{z},n}\left(2\bar{z} + \zeta_{\mathrm{z},n}\right)}{2\bar{r}}, && (3.33) \\ r_n^{'} &\approx \bar{r} + \frac{V_{\mathrm{x},n} + V_{\mathrm{y},n} + V_{\mathrm{z},n}}{2\bar{r}}. && (3.34) \end{aligned}$$

With this approximation the residual range is

$$\boxed{\Delta r_n = \frac{\beta_n}{2\bar{r}}}, \tag{3.35}$$

where

$$\beta_n = 2\left[\delta_{\mathrm{x}}\left(\bar{x} + \zeta_{\mathrm{x},n}\right) + \delta_{\mathrm{y}}\left(\bar{y} + \zeta_{\mathrm{y},n}\right) + \delta_{\mathrm{z}}\left(\bar{z} + \zeta_{\mathrm{z},n}\right)\right] - \delta_{\mathrm{x}}^2 - \delta_{\mathrm{y}}^2 - \delta_{\mathrm{z}}^2. \tag{3.36}$$

A quick examination of this shows that if the phase-center of the scattering-cell is known (i.e., all δ in Eq. 3.36 are zero) then the residual range vanishes identically, as expected.

An important observation regarding the approximation of Eq. 3.35 is that for the case of ideal, linear motion, β_n is constant for all n (given that δ_x is zero). This leads to Δr_n and ϕ_n also being constant for all n. This, however, is not true since Δr_n is the difference of two hyperbolas with separate foci. This point illustrates the limitation of the first-order Taylor series approximation: since this approximation erroneously suggests ϕ_n is constant for all n, it likewise suggests there are no residual phase variations and thus no phase errors.

For small values of $\zeta_{\mathrm{x},n}$, the phase error is small so the approximation is warranted. Hence, the first-order Taylor series is a good approximation for narrow-beam antennas and near the point of closest approach. However, as $\zeta_{\mathrm{x},n}$ grows large, the approximation for the square root becomes invalid.

3.3.2 Bakhshali Approximation

In order to ameliorate the restrictions of the first-order Taylor series approximation above, I introduce the Bakhshali square root approximation [31]. The Bakhshali method of approximating the square root is equivalent to two iterations of the first-order Taylor series approximation,

$$\sqrt{a^2+b} \approx a + \frac{b}{2a} - \frac{b^2}{8a^3+4ab}. \tag{3.37}$$

The residual range is then:

$$\boxed{\Delta r_n \approx \frac{\beta_n}{2\bar{r}} - \frac{\gamma_n^2}{4\bar{r}\left(2\bar{r}^2+\gamma_n\right)} + \frac{\left(\gamma_n-\beta_n\right)^2}{4\bar{r}\left(2\bar{r}^2+\gamma_n-\beta_n\right)}}, \tag{3.38}$$

with β_n as in Eq. 3.36 and

$$\gamma_n \;=\; 2\left(\bar{x}\,\zeta_{\mathrm{x},n}+\bar{y}\,\zeta_{\mathrm{y},n}+\bar{z}\,\zeta_{\mathrm{z},n}\right)+\zeta_{\mathrm{x},n}^2+\zeta_{\mathrm{y},n}^2+\zeta_{\mathrm{z},n}^2. \tag{3.39}$$

Notice that the first term in Eq. 3.38 is precisely the result of the first-order Taylor series approximation in Eq. 3.35. Also as in the Taylor series approximation, when $\beta_n = 0$ the residual range vanishes.

A comparison of both methods along with the third-order Taylor series approximation

$$\sqrt{a^2+b} \approx a + \frac{b}{2a} - \frac{b^2}{8a^3} + \frac{b^3}{16a^5}, \tag{3.40}$$

is illustrated in Fig. 3.1. In this example, the phase-center of the scattering-cell is displaced in slant-range (i.e., both range and elevation) by 1 meter. Subfigures (a), (c), and (e) show the range residual for an antenna placed at 30°, 45°, and 60°, respectively. The solid curve shows the exact value of the residual range. The first-order Taylor series approximation is constant at all azimuth angles. The third-order Taylor and Bakhshali methods both exhibit hyperbolic shapes; however, the Bakhshali method is accurate over a much wider range of azimuth angles and requires fewer operations than the third-order Taylor series. The Bakhshali method becomes very useful when analyzing the effects of residual range on wide-beamed antennas.

Figures 3.1(b), (d), and (f) show the approximation error of each method. How much error can be tolerated depends on the radar wavelength and expected phase-center displacement. Radars with relatively fine resolution relative to the wavelength better tolerate phase-center displacement than those with coarse resolution. As is evident from the figure, antennas with up to a 20° azimuth beamwidth have about 1% range error when using the first-order Taylor series approximation. Many SAR antennas in practice have such a beamwidth or even narrower. Thus, for purposes of this chapter, an antenna with such a beamwidth is termed "narrow-beam." If accuracy across a wider beamwidth is required then the Bakhshali method is preferable as the error is still small at a 90° beamwidth.

Recall from Sec. 3.2.2 that these results bound the approximation error: distributed targets generally have small displacement from the scattering-cell center and are unlikely to have a phase-center near the corner of the scattering-cell.

3.3.3 Sensitivity

With the derived approximations in place for the square roots in the residual range formula, an examination of sensitivity is possible. The sensitivity of the residual range Δr_n is found by solving its partial derivative with respect to each of the constituent terms. The results are shown in Table 3.1. Note that while the partial derivative is taken with respect to only the azimuth dimension, the same results hold for the other dimensions by substituting x for y and z.

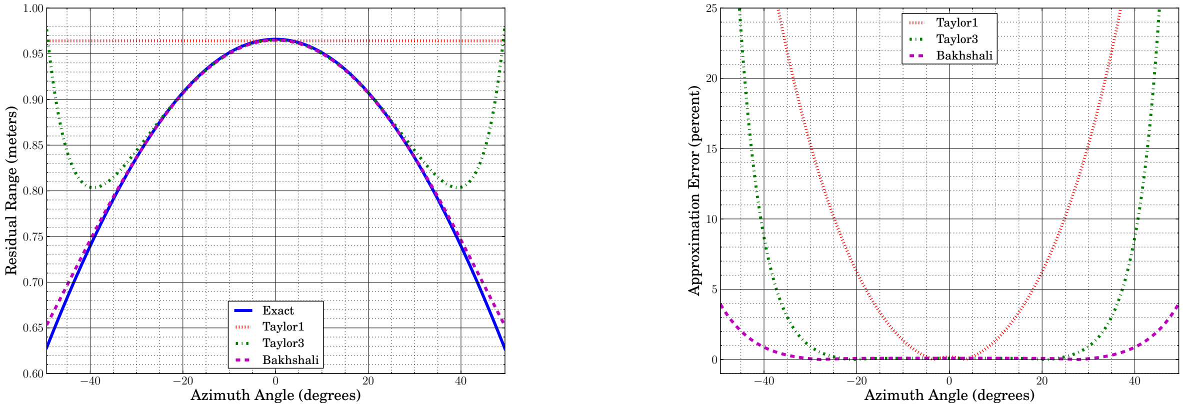

(a) $\theta = 30°$

(b) $\theta = 30°$

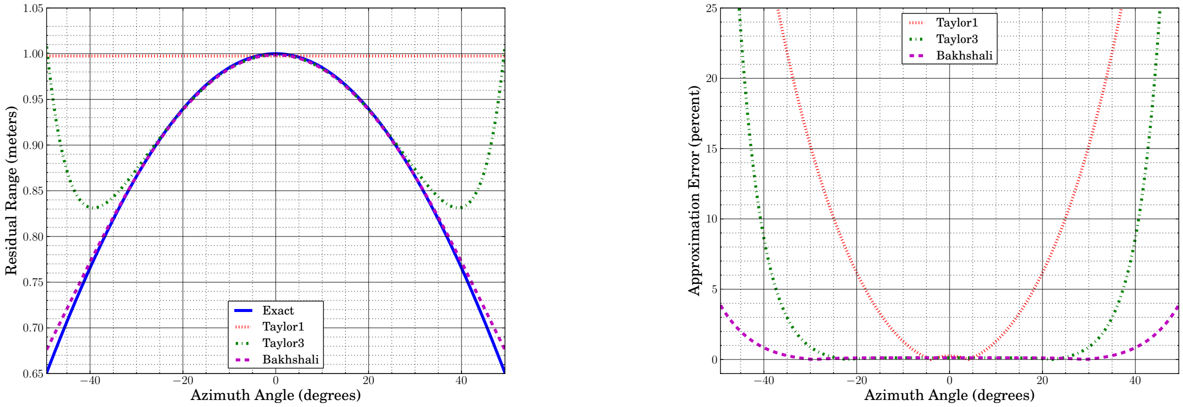

(c) $\theta = 45°$

(d) $\theta = 45°$

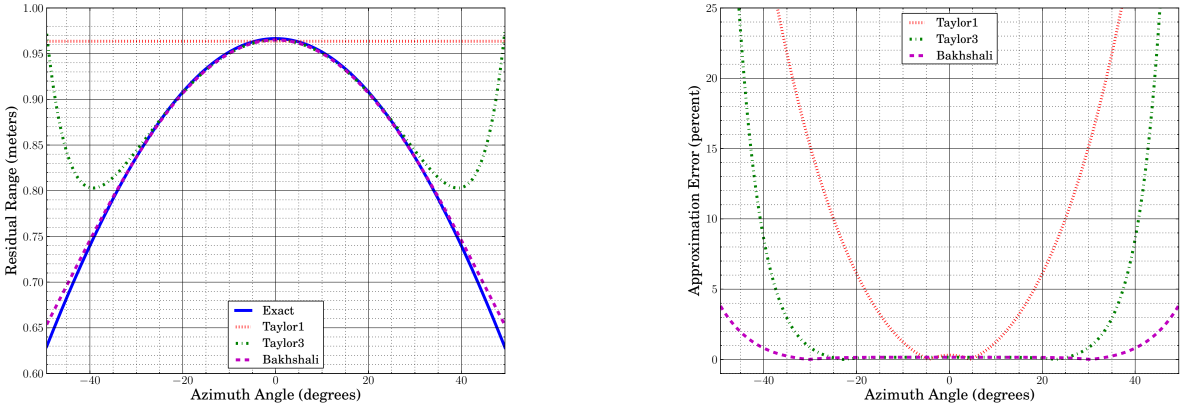

(e) $\theta = 60°$

(f) $\theta = 60°$

Figure 3.1: Comparison of the hyperbolic range residual approximations for varying azimuth angles-to-target with an incidence of $30°$, $45°$, and $60°$. Subfigures (a), (c), and (e) show the range residual where the solid curve represents the exact solution while the dashed/dotted curves are the approximations. Notice that the first-order Taylor series approximation is constant with azimuth angle. Subfigures (b), (d), and (f) show a comparison of the approximation error. Each of the approximations is accurate near $0°$ azimuth (the point of closest approach) but beyond that have varying degrees of accuracy at larger angles.

Table 3.1: Partial Derivatives for 1st-order Taylor Series and Bakhshali Approximations

	Taylor 1	Bakhshali
Δr_n	$\frac{\beta_n}{2\bar{r}}$	$\frac{\beta_n}{2\bar{r}} - \frac{\gamma_n^2}{4\bar{r}(2\bar{r}^2+\gamma_n)} + \frac{(\gamma_n-\beta_n)^2}{4\bar{r}(2\bar{r}^2+\gamma_n-\beta_n)}$
$\frac{\partial}{\partial\delta_{\mathrm{x}}}$	$\frac{\bar{x}+\zeta_{\mathrm{x},n}-\delta_{\mathrm{x}}}{\bar{r}}$	$\frac{\bar{x}+\zeta_{\mathrm{x},n}-\delta_{\mathrm{x}}}{\bar{r}} - \frac{2(\bar{x}+\zeta_{\mathrm{x},n}-\delta_{\mathrm{x}})(\gamma_n-\beta_n)}{2\bar{r}(2\bar{r}^2+\gamma_n-\beta_n)} + \frac{2(\bar{x}+\zeta_{\mathrm{x},n}-\delta_{\mathrm{x}})(\gamma_n-\beta_n)^2}{4\bar{r}(2\bar{r}^2+\gamma_n-\beta_n)^2}$
$\frac{\partial}{\partial\zeta_{\mathrm{x},n}}$	$\frac{\delta_x}{\bar{r}}$	$\frac{\delta_x}{\bar{r}} - \frac{(\bar{x}+\zeta_{\mathrm{x},n})\gamma_n}{\bar{r}(2\bar{r}^2+\gamma_n)} + \frac{(\bar{x}+\zeta_{\mathrm{x},n})\gamma_n^2}{2\bar{r}(2\bar{r}^2+\gamma_n)^2} + \frac{(\bar{x}+\zeta_{\mathrm{x},n}-\delta_{\mathrm{x}})(\gamma_n-\beta_n)}{\bar{r}(2\bar{r}^2+\gamma_n-\beta_n)} - \frac{(\bar{x}+\zeta_{\mathrm{x},n}-\delta_{\mathrm{x}})(\gamma_n-\beta_n)^2}{2\bar{r}(2\bar{r}^2+\gamma_n-\beta_n)^2}$
$\frac{\partial}{\partial\bar{x}}$	$\frac{\delta_x}{\bar{r}} - \frac{\bar{x}\beta_n}{2\bar{r}^3}$	$\frac{\delta_{\mathrm{x}}}{\bar{r}} - \frac{\bar{x}\beta_n}{2\bar{r}^3} - \frac{\zeta_{\mathrm{x},n}\gamma_n}{\bar{r}(2\bar{r}^2+\gamma_n)} + \frac{(2\bar{x}+\zeta_{\mathrm{x},n})\gamma_n^2}{2\bar{r}(2\bar{r}^2+\gamma_n)^2} + \frac{\bar{x}\gamma_n^2}{4\bar{r}^3(2\bar{r}^2+\gamma_n)}$ $+\frac{(\zeta_{\mathrm{x},n}-\delta_{\mathrm{x}})(\gamma_n-\beta_n)}{\bar{r}(2\bar{r}^2+\gamma_n-\beta_n)} - \frac{(2\bar{x}+\zeta_{\mathrm{x},n}-\delta_{\mathrm{x}})(\gamma_n-\beta_n)^2}{2\bar{r}(2\bar{r}^2+\gamma_n-\beta_n)^2} - \frac{\bar{x}(\gamma_n-\beta_n)^2}{4\bar{r}^3(2\bar{r}^2+\gamma_n-\beta_n)}$

Several insights may be gained by examining the sensitivity of the Taylor series terms:

1. **Phase-center displacement**. Referring to the first unshaded row in Table 3.1:

$$\frac{\partial \Delta r_n}{\partial \delta_{\mathrm{x}}} = \frac{\bar{x} + \zeta_{\mathrm{x},n} - \delta_{\mathrm{x}}}{\bar{r}}. \tag{3.41}$$

- The sensitivity to phase-center displacement is small for a given dimension if the mean range $\bar{x}$ and displacement $\zeta_{\mathrm{x},n}$ in that dimension is small compared to the total mean range (i.e., $(\bar{x} + \zeta_{\mathrm{x},n})/\bar{r}$ is small). For example, the residual range is not very sensitive to phase-center displacement in azimuth when the platform is near the point of closest approach. Likewise, the residual range is most sensitive to phase-center displacement in whichever dimension has the largest range-to-target. At shallow incidence angles this is elevation and at large incidence angles this is ground-range.
- Particularly applicable in the along-track dimension, when the antenna is located far away from the mean (i.e., $\zeta_{\mathrm{x},n} \gg \bar{x}$) then that separation from the mean begins to dominate. In other words, at larger azimuth angles the sensitivity to azimuth

displacement of the phase-center increases. Because this effect is only significant for wide-beamed antennas, it is actually more appropriate to use the sensitivity with respect to the Bakhshali approximation (see the last column in Table 3.1). While not immediately obvious due to the complexity of the equation, this leads to an even larger sensitivity to azimuth displacement of the phase-center.

2. **Non-ideal motion**. Examining the second unshaded row in Table 3.1:

$$\frac{\partial \Delta r_n}{\partial \zeta_{\mathrm{x},n}} = \frac{\delta_x}{\bar{r}}. \tag{3.42}$$

   - Sensitivity to non-ideal motion is less than sensitivity to phase-center displacement, by a factor of $\bar{x}/\delta_x$.
   - Sensitivity to non-ideal motion grows in a given dimension as the phase-center displacement in that dimension grows (i.e., $\delta_{\mathrm{x}}/\bar{r}$ grows larger). For example, if the SAR has very coarse range resolution (thus increasing the possible values for δ_x) then the residual range is more sensitive to any motion outside the linear track.
   - On the other hand, a large range-to-target mitigates this effect. Thus at longer ranges non-ideal motion becomes less of an issue, especially for fine resolutions.

3. **Mean position**. Referring to the last row in Table 3.1:

$$\frac{\partial \Delta r_n}{\partial \bar{x}} = \frac{\delta_x}{\bar{r}} - \frac{\bar{x}\beta_n}{2\bar{r}^3}. \tag{3.43}$$

   - Sensitivity to mean position is the least significant of the sensitivity terms. The elements dominating the residual range are from Eqs. 3.41 and 3.42 above.
   - If $\bar{x}$ is small (or zero) then $\frac{\partial}{\partial \bar{x}} \approx \frac{\delta_x}{\bar{r}}$, which is the same sensitivity as $\frac{\partial}{\partial \zeta_{\mathrm{x},n}}$ above. This is applicable mostly in the azimuth dimension.
   - For the range and elevation dimensions, the second term $\bar{x}\beta_n/2\bar{r}^3$ significantly reduces the impact of any phase-center displacement in the first term $\delta_x/\bar{r}$. Thus, the sensitivity due to the magnitude of the mean position is insignificant.

With general concepts of sensitivity in place, the performance of time-domain backprojection is explored in greater detail in the next section.

3.4 Performance Considerations

The following subsections analyze various factors that affect the performance of time-domain backprojection: digital elevation map (DEM) accuracy, antenna position accuracy, azimuth beamwidth, squint, and interpolation of the range-compressed signal. The key concept throughout is that variations in residual phase cause phase errors that lead to reduced performance.

As previously noted, the physical center and phase-center of a scattering-cell are not collocated in general. This leads to a residual phase when the matched filter is set as the range to the center of the cell. As seen in the previous section, if the antenna's azimuth beamwidth is sufficiently narrow then the residual phase due to phase-center displacement does not vary significantly with pulse number so the net phase error is small. However, if DEM height errors, non-linear platform motion, or antenna position measurement errors exist, then the phase error grows.

3.4.1 Digital Elevation Map

This subsection describes how the accuracy of the digital elevation map affects the backprojected image. The effects vary based on the nature of the platform motion and any uncertainty in knowledge of the platform positions. The case of ideal, linear platform motion is presented first, followed by more complex models.

Ideal, Linear Path

The backprojection formula requires, for every contributing pulse, knowing the range from antenna to scattering-cell at every pixel in the image. Assuming the platform positions are already known, one way to calculate the range is through knowledge of the scattering-cell's three dimensional location. A priori knowledge of the cell's vertical position is provided via a DEM of the terrain. Knowledge of the lateral position comes from the platform position data. A height offset (i.e., a bias error) in the elevation map results in varying effects on the output image depending on the SAR collection geometry.

For the simplest case, assume that a non-squinted SAR platform has a straight and level flight track. In this scenario, all platform motion is in the along-track direction (i.e., there is no deviation from the linear path in elevation or cross-track). Recall from Eq. 3.26 that the range to a scattering-cell is $r_n = \sqrt{x_n^2 + y_n^2 + z_n^2}$. Considering the motion to be ideal, y_n and z_n are constant. Let $\bar{r}^2 = \bar{y}_n^2 + \bar{z}_n^2$, which is also constant. Thus,

$$r_n = \sqrt{x_n^2 + \bar{r}^2}, \tag{3.44}$$

which is only variable in slow-time by azimuth position x_n. Given a slant-range r_n and azimuth position x_n, the ground-range distance y and elevation distance z cannot be uniquely determined. This means that while the slant-range from the SAR to a point on the ground is unique, the potential values for ground-range and elevation of the target are not: the possible solutions to these parameters lie on a hyperbolic curve, any point on which provides a correct solution of the slant-range-to-target. Hence, each range/elevation pair produces an equally well focused pixel in the backprojected image. However, the elevation offset causes the position of the target in the output image to be translated (i.e., shifted). This is illustrated in Fig. 3.2, where three DEM heights and the respective lateral shift of the target are shown.

A positive vertical offset in the elevation map places the ground-plane closer to the SAR in elevation. As the slant-range solution for a target is constant, this causes the focused target to appear imaged farther away in ground-range. In the same way, lowering the elevation map causes the focused target to appear imaged closer to the SAR in ground-range. Thus, unless the elevation map specifies the correct terrain height, imaged targets are erroneously shifted in range. It is important to remember, however, that regardless of the shift in range, the target's focus is essentially unaffected so long as the motion is ideal. Since the along-track dimension is orthogonal to the slant-range dimension, an offset in the elevation map does not affect the azimuth position of the target in the backprojected image.

Offsetting the apparent height of the target adds approximately a constant range residual at every pulse, and thus approximately the same phase (i.e., little phase error). This is seen

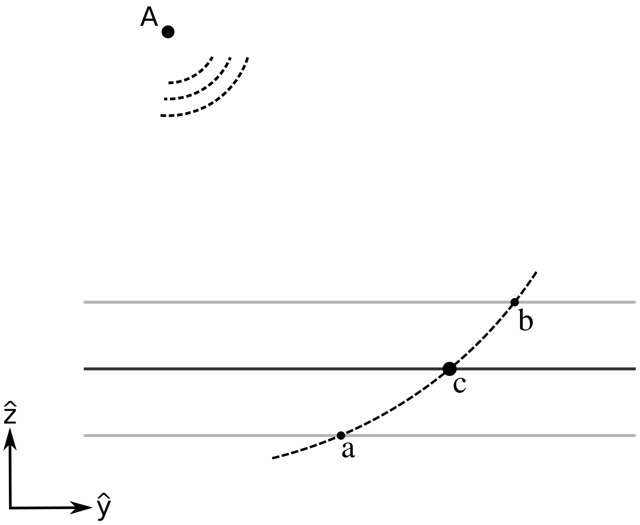

Figure 3.2: Illustration of lateral shift caused by DEM height offset. An antenna is located at point A and the true DEM height is given by the dark middle line. The dashed curve represents a portion of the solution space of an equal slant-range-to-target. The upper and lower gray lines indicate a shift in the height of the DEM, with the associated shift in the target position (shown by an intersecting dot).

in Eq. 3.36. Given that $\bar{z} \gg \zeta_{\mathrm{z},n}$ and $\bar{z} \gg \delta_{\mathrm{z}}$, then the change in Δr_n is approximately the same for every pulse. As the phase added is roughly constant, it has little effect on compression. However, as the DEM errors grow, the approximation no longer holds and the compression suffers significantly. This is not surprising since backprojection requires at least a coarse idea of the height of the scatterers.

An example of the effects of DEM offset on the azimuth impulse response for an ideal path is illustrated in Fig. 3.3, which shows the azimuth impulse response of a simulated point target. The parameters used in simulation are 0.3 m wavelength, 8.6° azimuth antenna beamwidth (corresponding to 1 m azimuth resolution), and 45° incidence angle. The SAR platform moves in an ideal, linear fashion. In subfigure (a) the point target is placed at the center of the scattering-cell while in subfigure (b) the target is placed the maximal distance away according to Eqs. 3.21 and 3.22. Each subfigure has three curves: zero vertical displacement of the DEM and ± 10 m vertical displacement of the DEM (i.e., DEM height error). Examining both plots, the DEM offset has little effect on the azimuth response for the reasons detailed above (all solutions are equally valid). Likewise there is no effect in the

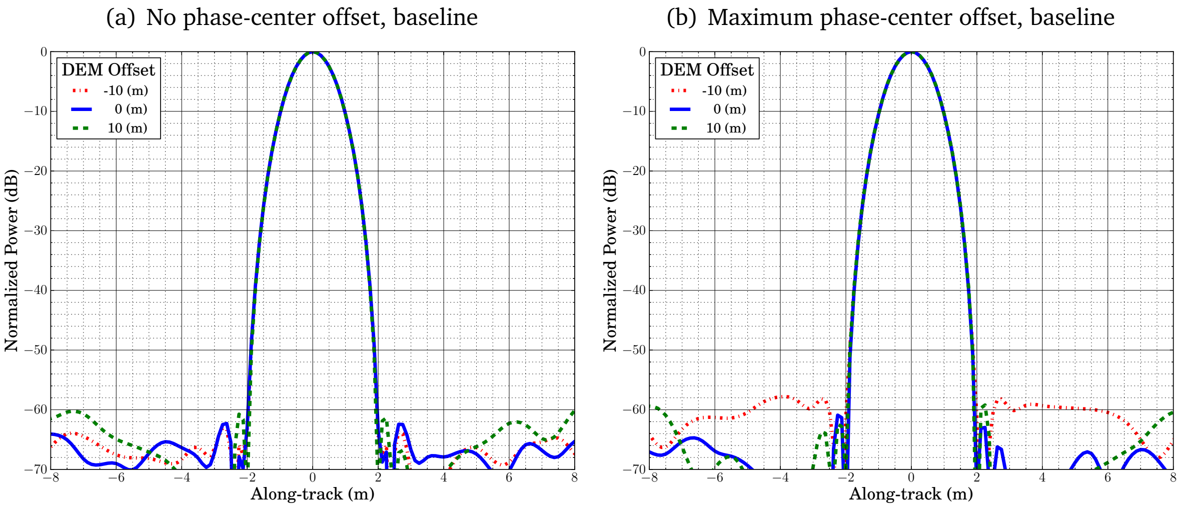
(a) No phase-center offset, baseline

(b) Maximum phase-center offset, baseline

Figure 3.3: Baseline azimuth impulse response plots. The antenna positions are known exactly on an ideal, linear flight path. Three curves are shown representing different DEM height offsets.

range response (not shown). While not visible in the figures (because the curves show a slice through the peak), the imaged target positions are shifted in range between the various height curves because the target solution in ground-range changes in order to maintain a constant slant-range-to-target.

Known, Non-ideal Motion

For the case above, all platform motion is assumed to be in the along-track direction. If any motion occurs in the cross-track or elevation directions then the solution for the imaged target position becomes more constrained. If the correct height is not used in processing and there is non-ideal motion, then the target's compression suffers. However, this effect is small for small height errors.

Figure 3.4 demonstrates the effects of non-ideal platform motion. Here, the simulation is set up the same as in Fig. 3.3 except that a zero-mean, Gaussian perturbation of standard deviation σ_{ant} is added to the antenna positions in range and elevation (the antenna positions are known exactly). The three rows in the figure correspond to position perturbation with a standard deviation of 1, 2.5 and 5 wavelengths. While this distribution of platform positions is not likely to occur in practice, it does show how a given magnitude of non-ideal motion affects performance. The first column gives the azimuth response where the point target is at the physical center of the scattering-cell and the second column gives the response where it is maximally displaced, as before. Again, the DEM is offset zero and ± 10 m in elevation. All plots have been normalized to the same peak power in order to compare magnitude effects among the plots.

When a target is placed at the physical center of the cell (first column of subplots) and the DEM offset is zero (the solid curves), there is little difference between the responses (except for a slight raising of the sidelobes at larger position-perturbation variances). This is not so when the DEM is offset. In the case where $\sigma_{\text{ant}} = 1\lambda$, the peak power is barely affected but the sidelobes raise almost 30 dB. At $\sigma_{\text{ant}} = 5\lambda$ there is a significant decrease in the peak power and an increase in sidelobe power. At $\sigma_{\text{ant}} = 10\lambda$ the mainlobe becomes indistinguishable from the sidelobes. This underscores the powerful effect a DEM offset has when the path motion is non-ideal, even for relatively small amounts of movement.

In the case of non-ideal motion, displacing the target to the edge of the cell has a noticeable effect on all azimuth impulse response curves. The peak-to-sidelobe ratio decreases slightly more than the previous case; however, for the offset DEM cases, there is a significant decrease in the peak-to-sidelobe ratio. It is interesting to note that this is primarily due to raising sidelobe levels; there is little loss in peak power.

3.4.2 Antenna Position Estimate

DEM uncertainties are not the only sources of geometry error. Unfortunately, the position estimates of the antenna are also subject to error. In the previous section it is assumed that the antenna positions are known exactly; now the case of uncertainty in the position estimates is treated. Unknown errors in the antenna position estimate may be classified into two categories: absolute errors and relative errors. Absolute errors are translations of the entire set of position estimates (e.g., GPS reporting an incorrect, fixed offset in altitude across all data). Relative errors, on the other hand, are dynamic errors that change over time (e.g., measurement noise or drift).

(a) No phase-center offset, $\sigma_{\text{ant}} = 1\lambda$ (b) Maximum phase-center offset, $\sigma_{\text{ant}} = 1\lambda$

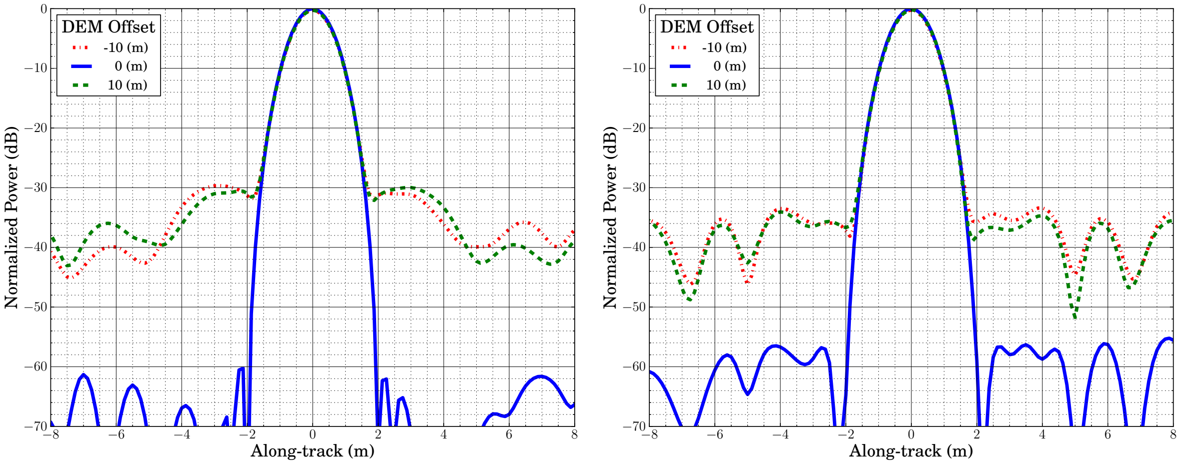

(c) No phase-center offset, $\sigma_{\text{ant}} = 5\lambda$ (d) Maximum phase-center offset, $\sigma_{\text{ant}} = 5\lambda$

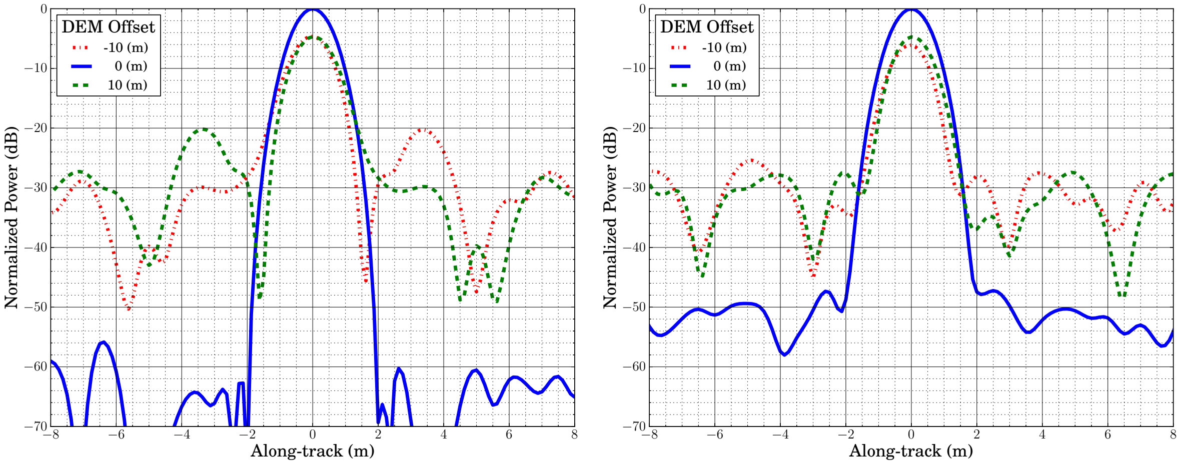

(e) No phase-center offset, $\sigma_{\text{ant}} = 10\lambda$ (f) Maximum phase-center offset, $\sigma_{\text{ant}} = 10\lambda$

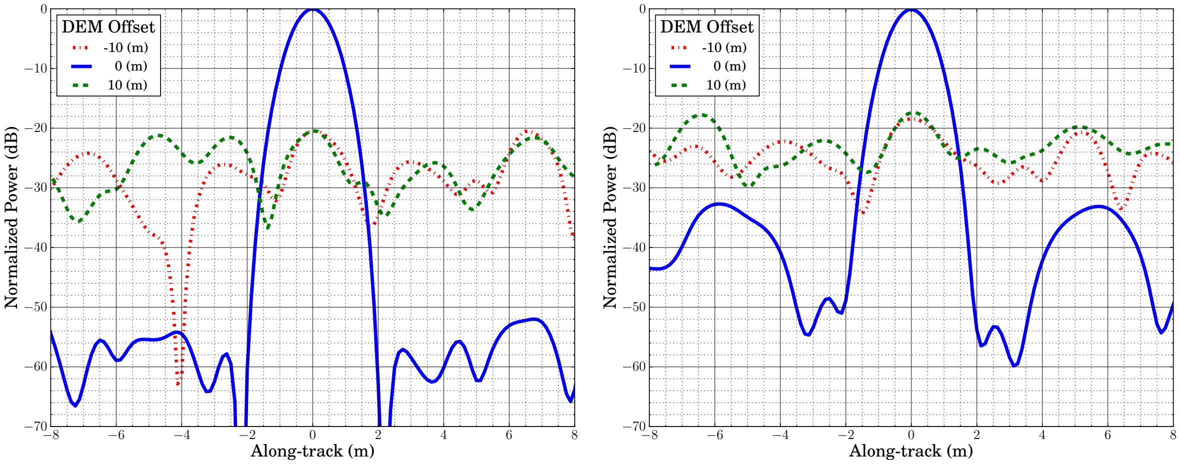

Figure 3.4: Azimuth impulse response with Gaussian position variance of σ^2_{ant} in elevation. The antenna positions are known exactly. Three curves are shown representing DEM height offsets. The phase-center offset mostly affects the sidelobes, not the main lobe.

Absolute position errors are functionally similar to DEM errors. This is because fixed altitude errors behave identically to a vertical offset in the DEM and horizontal position errors behave like lateral translations of the DEM. Depending on the scene topography, a lateral translation of the DEM may have no effect (e.g., perfectly flat terrain) or a very large one (e.g., terrain with high relief). Because vertical translation is the same as vertical DEM offset and horizontal translation is scene dependent, no example figures are given here. In general, however, absolute position errors do not present a great reduction in image quality given that the magnitude of error is bounded by those common to GPS (e.g., absolute position errors less than 10 m). Since absolute position errors add roughly the same residual phase to each backprojection summation term, their effect is nearly the same as a DEM offset described in the previous subsection.

Relative position errors, on the other hand, are more problematic because they add a different phase at each term in backprojection summation. Even for minor errors, the consequence is possibly dramatic both on the target impulse response and its peak location. The remainder of this subsection explores the effect of two types of relative position error: Gaussian random noise and drift.

Gaussian Random Noise

Figure 3.5 demonstrates the effect of uncertainty in the antenna position. Here, an ideal, linear flight track is assumed during processing using the same parameters as the subsections above, except that noise is added to the antenna positions. The noise is zero-mean, Gaussian distributed with standard deviations $\eta_{\text{ant}} = \frac{1}{1000}\lambda$, $\frac{1}{100}\lambda$, and $\frac{1}{10}\lambda$, shown in Fig. 3.5(b)-(d), respectively. Figure 3.5(a) provides the baseline for comparison. Even with only $\frac{1}{1000}\lambda$ of added noise, and although the mainlobe is unaffected, there is a significant raising of the sidelobes. At $\frac{1}{100}\lambda$ there is another noticeable jump in sidelobe level and the peak also drops by 3.5 dB. At $\frac{1}{10}\lambda$ the mainlobe is indistinguishable from the sidelobes.

These plots illustrate the importance of knowledge of the relative positions of the antenna (the absolute positions are not as critical for the reasons previously stated). Even tiny levels of uncertainty have a strong effect on impulse response. It is interesting to note that

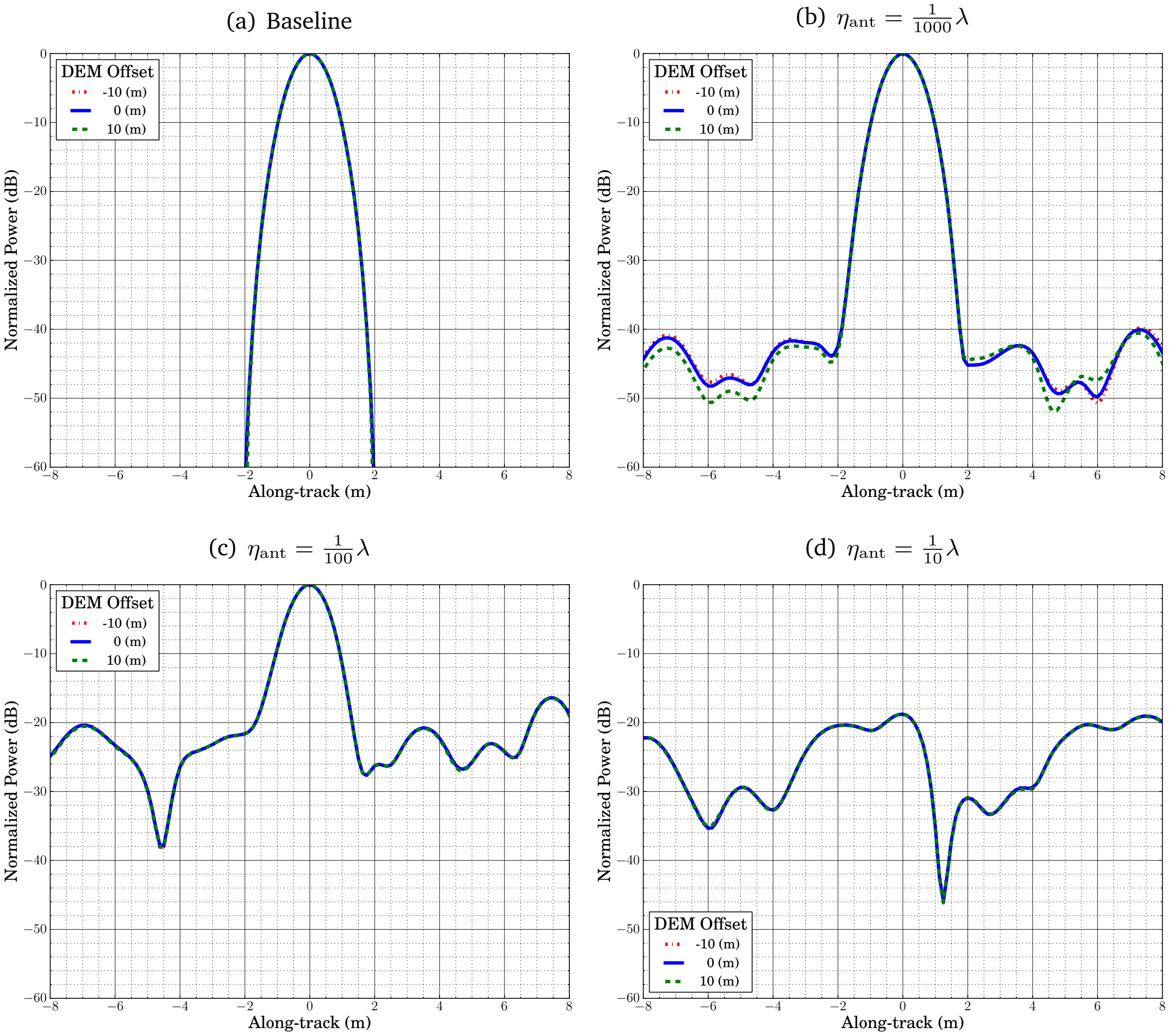

Figure 3.5: Azimuth impulse response with Gaussian position noise variance of η_{ant}^2 in elevation. The antenna positions are assumed to lie on an ideal, linear path (corrupted by unknown noise). Three curves are shown representing DEM height offsets. No phase-center displacement is present.

since the antenna position errors dominate, a DEM offset in these cases is almost unnoticeable. Although not shown, this is also the case with an offset phase-center: the effect of scattering-cell phase-center displacement is imperceptible.

Position Drift

Another form of position error is drift. Navigation systems typically employ an Inertial Measurement Unit (IMU). As these sensors generate estimates by performing integration of

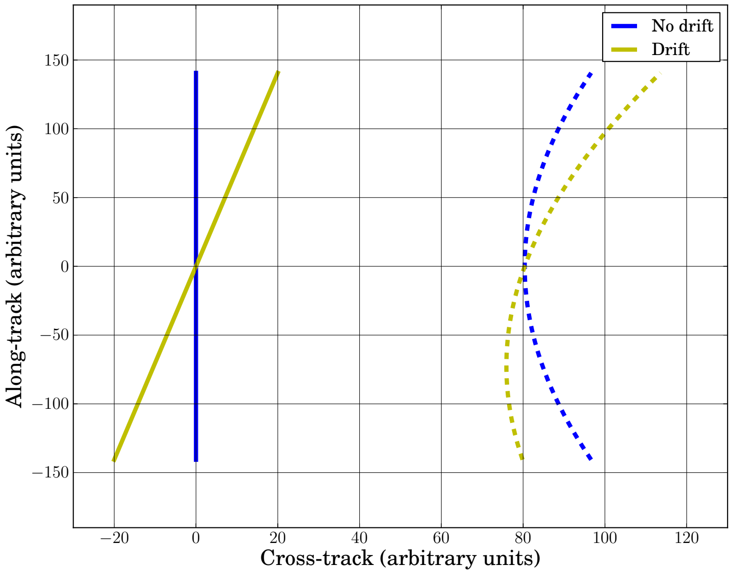

Figure 3.6: Illustration of the effect of drift on range cell migration. The figure presents a top-down view of the imaging geometry with the solid lines on the left representing the path the platform travels along and the dashed curves on the right representing the range to a given target for each along-track position of the platform. Units are arbitrary. The curve without drift is hyperbolic and symmetric about the point of closest approach, exemplifying an ideal range cell migration curve (RCMC). When platform drift is present (albeit exaggerated in this figure), the range curve is skewed. Not only does this present a residual range problem for the matched filter, but if the skew is large enough then incorrect contributions are chosen during backprojection summation.

accelerometer measurements, drift is almost unavoidable. Drift result in an incorrect estimate of the range to target. Additionally, since the magnitude of the errors changes across the synthetic aperture, an incorrect range migration curve results (i.e., the wrong contributions are used in backprojection summation). The magnitude of the effect corresponds to the magnitude of the drift.

Antenna beamwidth is an important factor in determining vulnerability to drift error because a wider beamwidth leads to a longer synthetic aperture and therefore more drift across the aperture. Particularly troublesome is drift in the along-track direction as it leads to larger errors in estimation of the range-to-target than drift in the lateral directions. An example of the effect of cross-track drift is illustrated in Fig. 3.6.

The effects of antenna position drift are shown in Fig. 3.7. The antenna positions are assumed to be linear (ideal) in the processing, while in actuality there is a drift component (i.e., time-varying position error). The fundamental simulation parameters are the same as before. The slant-range/azimuth resolutions are each 1 m. Subfigure (a) shows the baseline where no drift is present. Subfigures (b) and (c) show drift in different dimensions as a function of total magnitude of drift in wavelengths across the synthetic aperture. In (b), 10 wavelengths of position drift in the elevation dimension has a small effect on azimuth IPR: a slight raising of the sidelobes and an imperceptible broadening of the mainlobe. Although not shown, the same magnitude of drift in the ground-range dimension as elevation dimension has an identical effect (for a 45° incidence angle).

The effect of drift in the along-track dimension is greater than the other two dimensions. As stated previously, this is due to error in selecting the phase history of the target, thus diminishing the utilized azimuth chirp bandwidth for the target and coarsening the resolution. As in the previous figure showing random noise on position estimates, displacement of the phase-center appears insignificant as it is dominated by errors in the antenna position estimate.

Subfigure 3.7(d) shows the effect of elevation drift on the azimuth position of the target. Rather than specifying drift in wavelengths, it is specified in meters where the slant-range and azimuth resolutions are both 1 m. At 20 m of elevation drift across the synthetic aperture, the target is displaced nearly 100 m along-track. Subfigures (e) and (f) show various amounts of drift where the curves have been centered in order to compare their shape. As indicated previously, the same magnitude of drift causes substantially more effect when it is in the azimuth dimension as opposed to the range or elevation. (Notice the difference in horizontal axis scales between (e) and (f).)

3.4.3 Azimuth Beamwidth

This subsection develops an the upper-bound on the usable azimuth beamwidth due to the effects of the unknown location offset of the scattering-cell phase-center. As shown earlier, a residual phase results when the phase-center is not collocated with the physical center. This induces a phase error that grows as the platform moves away from the point of nominal residual phase (i.e., the point of closest approach). When the phase error grows sufficiently large, the pulses may sum destructively.

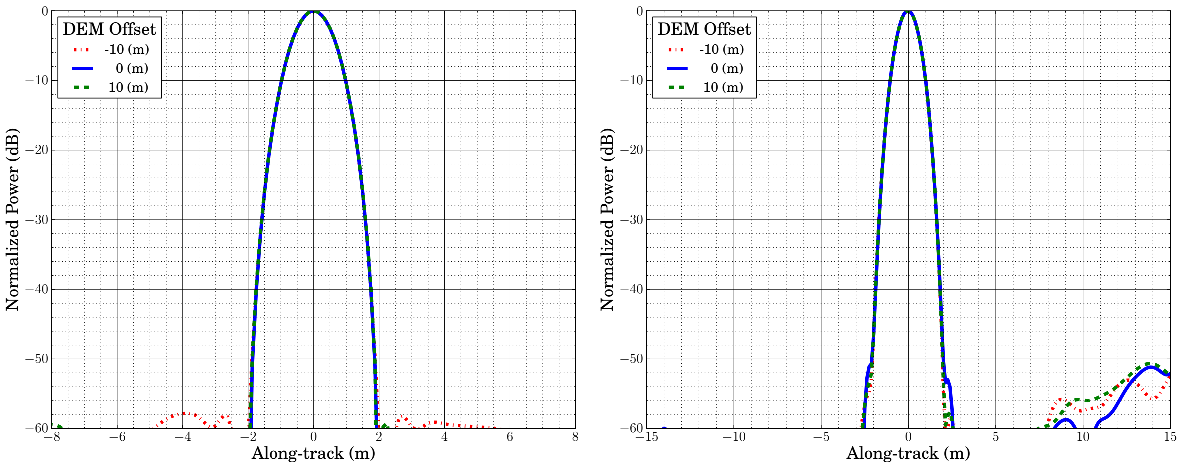

(a) No drift

(b) Elevation drift $\hat{z}_{\text{drift}} = 10\lambda$

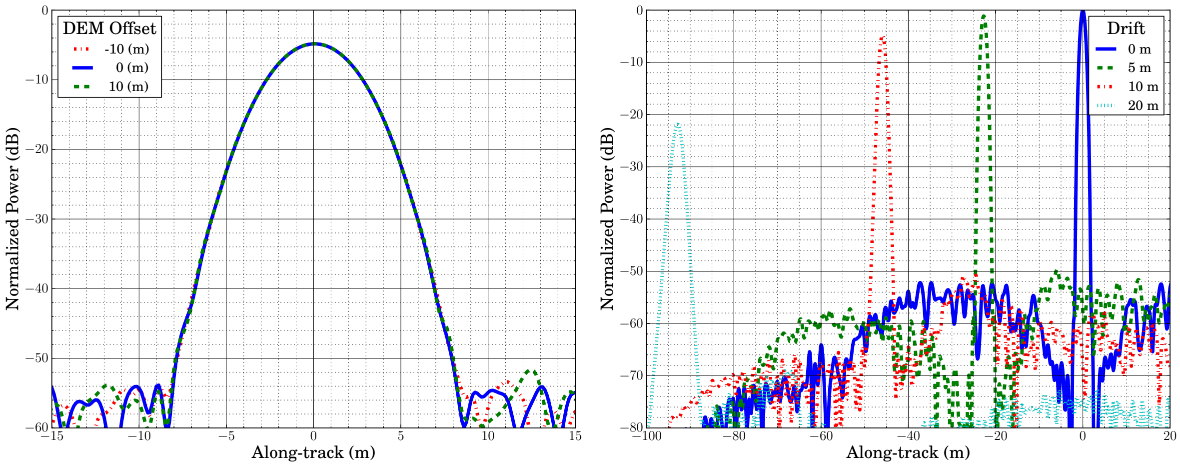

(c) Azimuth drift $\hat{x}_{\text{drift}} = 10\lambda$

(d) Azimuth position shift with elevaiton drift

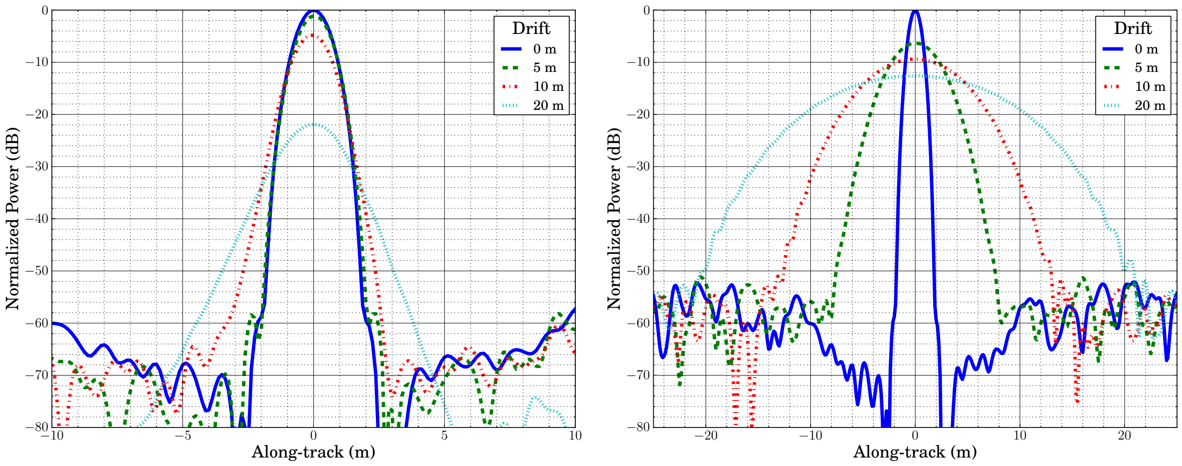

(e) Various elevation drifts

(f) Various azimuth drifts

Figure 3.7: Azimuth impulse response where the antenna positions are assumed to be lie on an ideal linear path, but the actual positions have drifted in the given dimension. Plot (a) has no drift. In (b) and (c), a drift of 10λ per second is present in elevation and azimuth, respectively. In (d)-(f), drift is in total meters across the synthetic aperture.

Derivation

To analyze this, let the slow-time index $n = 0$ be the pulse index when the platform is located at the synthetic aperture mean (for the particular target). ϕ_0 then is the nominal residual phase corresponding to $n = 0$. Destructive summation occurs for a contribution ϕ_n at $n \neq 0$ when

$$|\phi_n - \phi_0| = \phi_{\text{err}} = \frac{\pi}{2}. \tag{3.45}$$

In range, this corresponds to

$$\Delta r_{\text{err}} = \frac{\phi_{\text{err}}}{k} = \frac{\lambda}{4}. \tag{3.46}$$

Because the residual range-induced phase error grows as the platform distance from the mean increases, there exists an azimuth beamwidth wide enough to include target returns that sum destructively if the phase-center of the cell is is sufficiently displaced. Using the approximations of Section 3.3 it is possible to derive an analytic solution for this maximum azimuth beamwidth.

From Eq. 3.39 on page 39, $\gamma_0 = 0$ at the mean. Substituting this in Eq. 3.38, the nominal residual range Δr_0 is

$$\begin{aligned}
\Delta r_0 &\approx \frac{\beta_0}{2\bar{r}} + \frac{\beta_0^2}{4\bar{r}\left(2\bar{r}^2 - \beta_0\right)} \\
&= \frac{2\beta_0\left(2\bar{r}^2 - \beta_0\right) + \beta_0^2}{4\bar{r}\left(2\bar{r}^2 - \beta_0\right)} \\
&= \frac{4\beta_0\bar{r}^2 - \beta_0^2}{4\bar{r}\left(2\bar{r}^2 - \beta_0\right)} \\
&= \frac{\beta_0\left(\bar{r}^2 - \frac{\beta_0}{4}\right)}{2\bar{r}\left(\bar{r}^2 - \frac{\beta_0}{2}\right)}.
\end{aligned} \tag{3.47}$$

This leads to the value $\phi_0 = k\Delta r_0$, which is the phase at the mean. If β_0 is small compared to $\bar{r}^2$ then

$$\Delta r_0 \approx \frac{\beta_0}{2\bar{r}}, \tag{3.48}$$

which is the same as that given by the first-order Taylor series approximation. This confirms the validity of the Taylor series approximation near the point of closest approach.

Per Eq. 3.46, for contributions away from the nominal (i.e., $n \neq 0$), the interesting point is the maximum residual range $\Delta r_{\max}$ that is a quarter wavelength away from the residual at the point of closest approach:

$$\Delta r_{\max} = \Delta r_0 + \frac{\lambda}{4}. \tag{3.49}$$

Using Eq. 3.38, we are thus interested in finding the point where

$$\Delta r_{\max} = \Delta r_0 + \frac{\lambda}{4} = \frac{\beta_{\max}}{2\bar{r}} - \frac{\gamma_{\max}^2}{4\bar{r}\left(2\bar{r}^2 + \gamma_{\max}\right)} + \frac{\left(\gamma_{\max} - \beta_{\max}\right)^2}{4\bar{r}\left(2\bar{r}^2 + \gamma_{\max} - \beta_{\max}\right)}. \tag{3.50}$$

If the motion is ideal (i.e., all motion is in the along-track direction) then

$$\gamma_n = \zeta_{\mathrm{x},n}^2. \tag{3.51}$$

Likewise, if the geometry is non-squinted and there is little phase-center displacement in azimuth then β_n is approximately constant:

$$\beta_n \approx \beta_0 = 2\left(\delta_{\mathrm{y}}\bar{y} + \delta_{\mathrm{z}}\bar{z}\right) - \delta_{\mathrm{y}}^2 - \delta_{\mathrm{z}}^2. \tag{3.52}$$

Using these two assumptions it is possible to obtain an analytic expression for the maximum azimuth distance away from the mean. Solving for γ_n in Eq. 3.38 leads to

$$\gamma_n = \frac{\beta_n}{2} - 2\bar{r}^2 \pm \frac{\sqrt{\beta_n\left(\beta_n - 4\bar{r}\Delta r_n\right)\left(16\bar{r}^4 + 4\beta_n\bar{r}\Delta r_n - \beta_n^2\right)}}{2\left(4\bar{r}\Delta r_n - \beta_n\right)} \tag{3.53}$$

$$= \frac{\beta_n}{2} - 2\bar{r}^2 \pm \left(\frac{\beta_n^2}{4} + \frac{4\beta_n\bar{r}^4}{4\bar{r}\Delta r_n - \beta_n}\right). \tag{3.54}$$

Substituting this result into Eqs. 3.51 and 3.52 yields

$$\zeta_{\mathrm{x},\max}^2 = \frac{\beta_0}{2} - 2\bar{r}^2 + \frac{\beta_0^2}{4} + \frac{4\beta_0\bar{r}^4}{4\bar{r}\left(\Delta r_0 + \lambda/4\right) - \beta_0}. \tag{3.55}$$

The minus sign in ± is dropped since it leads to a non-physical solution. For a given phase-center displacement, this can be used to find the maximum distance the antenna may be from the point of closest approach before the pulses sum destructively. This gives a limit for the maximum azimuth beamwidth of the antenna.

Analysis

An example of the maximum azimuth beamwidth is illustrated in Fig. 3.8. In subfigure (a), the maximum azimuth beamwidth is plotted as a function of incidence angle to the scattering-cell where the platform motion is ideal. Multiple curves are shown, each depicting a different slant-range resolution in wavelengths. The phase-center displacement is the maximum distance from the physical center of the scattering-cell (from Eqs. 3.21 and 3.22). For finer range resolutions (i.e., the upper curves), a wider azimuth beamwidth is permitted than at coarser resolutions. This is because finer range resolutions limit the maximum phase-center displacement and thus decrease the maximum residual phase. It is interesting to note that since a wide azimuth beamwidth corresponds to fine azimuth resolution, it may not be possible to obtain fine azimuth resolution simultaneously with coarse range-resolution.

As stated previously, in many imaging scenarios, scattering-cells are treated as being distributed targets whose phase-center is near the physical center. This means that in practice scattering-cells may not have the “worst case” phase-center offset depicted here. It is important to keep in mind, however, that for discrete targets, an individual point target (e.g., a corner reflector) may be located anywhere within the scattering-cell and thus may cause a maximum residual phase.

The examination above assumes ideal, linear motion of the antenna platform. When non-ideal motion is present, the fluctuation from the linear path increases the magnitude of the range residuals. This in turn further constrains the azimuth beamwidth. Small incidence angles (those near nadir) are affected more significantly by non-ideal motion. This is shown in Fig. 3.8(b)-(d), which illustrate the effect of non-ideal motion for varying degrees of slant-range deviation.

In Fig. 3.8(b), where the displacement is 0.1% of the height above the surface, there is little difference except at low incidence angles (less than 10°) or very coarse range resolutions ($\sim 200\lambda$). When the non-ideal motion is 1% of the height, as in Fig 3.8(c), the effect of non-

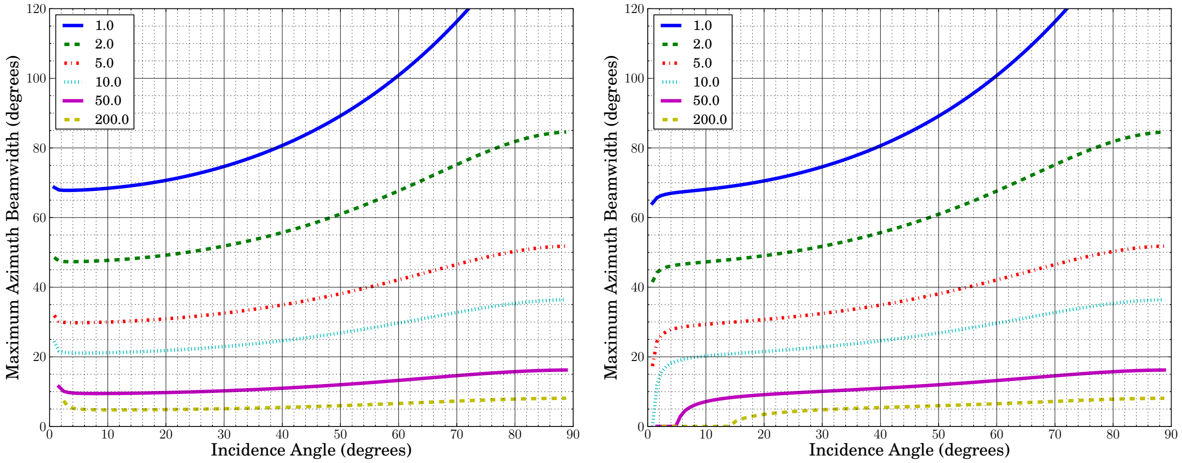

(a) Ideal motion

(b) 0.1% non-ideal motion

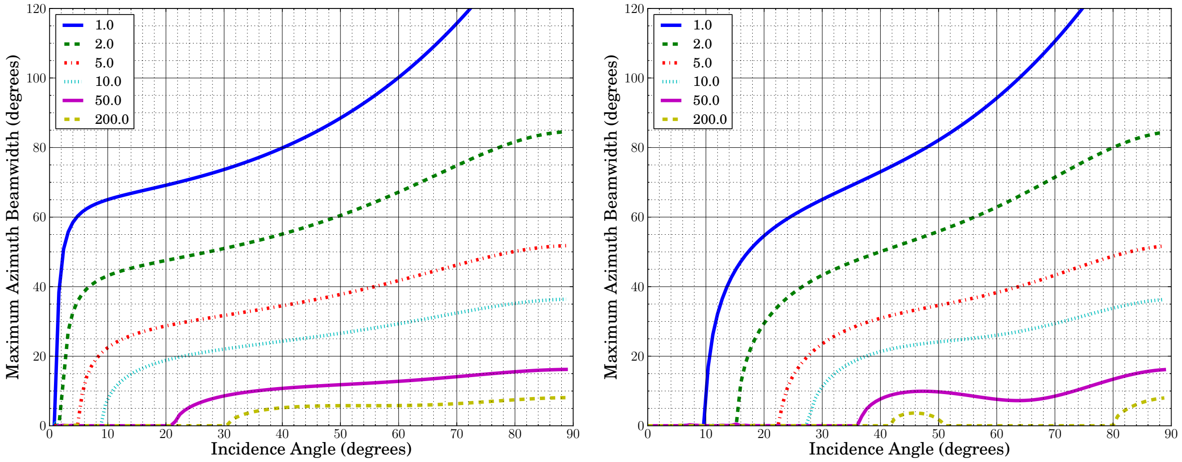

(c) 1% non-ideal motion

(d) 10% non-ideal motion

Figure 3.8: Maximum azimuth beamwidth as a function of incidence angle. In each subfigure, the various curves indicate slant-range resolution in multiples of wavelengths. In all cases, the phase-center of the scattering-cell is located in the corner away from the physical center. Subfigure (a) shows ideal motion. The remaining subfigures show non-ideal motion in slant-range as a percentage of range to the scattering-cell.

ideal motion is more pronounced: the minimum incidence angle with non-zero beamwidth is 20°, with the exception of the 200λ resolution which has a minimum acceptable incidence angle of 30°. By 30° incidence the maximum beamwidth is as it is without non-ideal motion for all but the 200λ case.

Figure 3.8(d) shows curves similar to the previous cases when there is 10% height-to-lateral/elevation random path deviation. With this amount of motion the results are very dependent on the incidence angle. Incidence angles smaller than 10° are unacceptable at any resolution. At phase-center displacements of 200λ only a very narrow beamwidth is allowed over a small range of incidence angles.

In most imaging situations the limit on azimuth beamwidth is not an issue. However, there are certainly cases where this issue could arise, especially in low altitude SAR. For example, if a SAR platform is 500 m above the ground and is imaging at 40° incidence with a 20° beamwidth antenna, then the aperture is 230 m wide. If the platform is traveling in the along-track direction at 25 m/s, then a 10 m/s cross-track velocity causes a residual phase error large enough that the pulses on the edge of the aperture add destructively for any cells whose phase-center is 20 or more wavelengths away from the center of the cell. While the effect may not be dramatic (as it may only affect a relatively small percentage of pulses) it does limit the effective maximum azimuth resolution and introduces artifacts.

3.4.4 Squint

Squint-mode SAR is where the antenna pointing angle is not coincident with the zero Doppler plane. Where the squint is zero, the antenna points directly at a target when at the point of closest approach (i.e., when the target is in the zero Doppler plane).

As cited previously, frequency domain algorithms typically require special processing in order to form images from squinted raw data. This arises for two main reasons. First, squint shifts the azimuth chirp spectrum so that it is no longer centered at 0 Hz. This necessitates modification of the azimuth matched filter. Second, the range and azimuth dimensions begin to couple and are no longer orthogonal, which has differing effects on the algorithms depending on the nature of their assumptions of orthogonality. The effects become especially pronounced at larger squint angles ($>30^\circ$).

Because backprojection models the propagation phase of the expected received signal as part of the matched filter, squint-mode operation does not require any special processing. In other words, backprojection natively forms images from even highly squinted geometries; Doppler-centroid shift needs no special handling. This is an important point because of the constraints placed on frequency domain algorithms which are taken care of by backprojection without any modification. This point is detailed further in the appendix Sec. 3.6.

Examples illustrating the impulse response of a squinted point target are shown in the contour plots of Fig. 3.9. The subfigures show squint angles of $0°$, $15°$, $30°$, $45°$, $60°$, and $75°$, respectively. The processing parameters are a $45°$ incidence angle, a 30 cm wavelength, and 1 m range/azimuth resolutions. The target is maximally displaced from the physical center of the scattering-cell, as described previously. In subfigure (a), notice the orthogonal sinc-like pattern in the range (cross-track) and azimuth (along-track). As the squint angle increases, the range and azimuth responses are no longer orthogonal. While the range response stays roughly the same (though the exact sidelobe structure changes and it is rotated by approximately the squint angle), the azimuth sidelobes diminish as the squint angle increases. The azimuth sidelobes diminish because of the increased number of pulses summed in backprojection. Additionally, the shape of the main lobe goes from circular to ovular, though the area remains the same. At higher squint angles the azimuth sidelobes all but disappear. This is due to the increased dwell time at higher squint angles. Examining each of the plots, it is apparent that backprojection handles squinted geometry without special handling requirements.

There is a small limitation on the maximum squint that SAR may accept. In the previous subsection, limits on the usable azimuth beamwidth are developed. For the same reasons described there, for high squint cases, if the phase-center of the scattering-cell is too far displaced from the physical center then the phase errors may grow too large and sum destructively. This, however, is not an issue for typical SAR antenna azimuth beamwidths (which are less than $20°$).

3.4.5 Range-compressed Signal Interpolation

As discussed in Sec. 3.2.1, the time-domain backprojection algorithm is usually expressed with the range-compressed signal as a function of continuous fast-time. This implicitly provides the range-compressed value corresponding to the exact propagation delay to the target. In practice, however, the range-compressed signal is composed of discrete samples. Because the available sample point may not actually correspond to the time-delay to the phase-center of the cell, the signal must be interpolated to the desired range otherwise a small error results (even though the signal is properly sampled at or above the Nyquist rate).

(a) 0° squint

(b) 15° squint

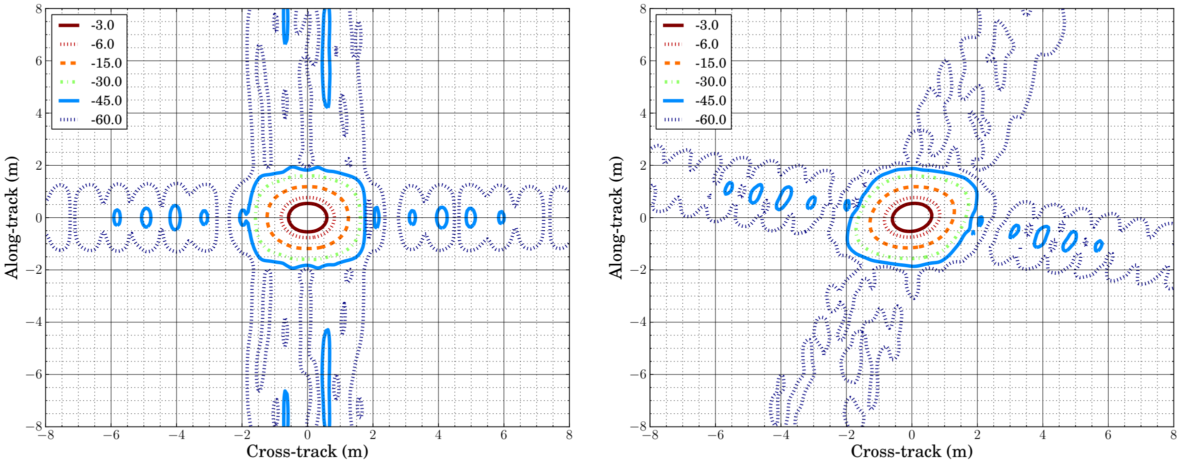

(c) 30° squint

(d) 45° squint

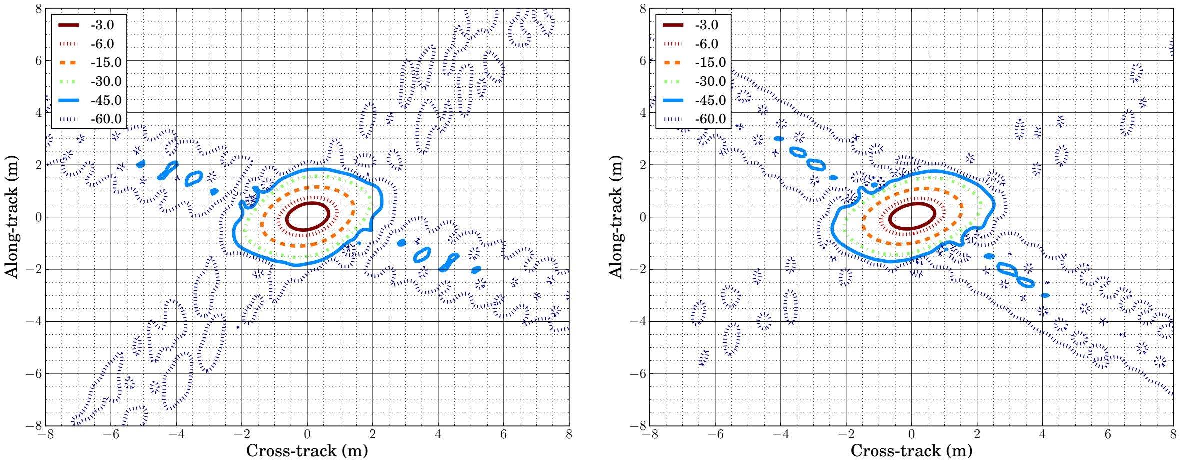

(e) 60° squint

(f) 75° squint

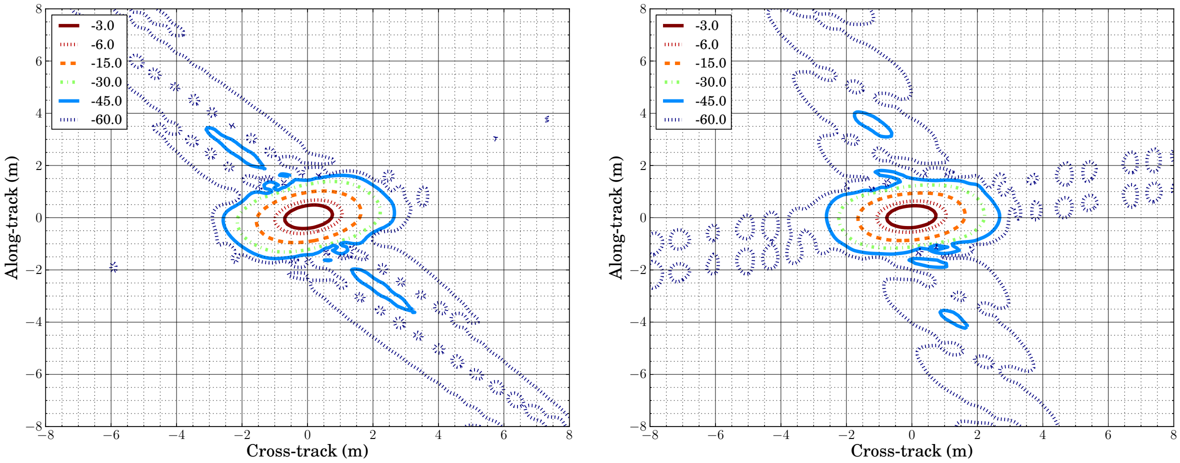

Figure 3.9: Point target impulse response in range and azimuth for varying levels of squint. The flight track is ideal and the antenna positions are known exactly. With zero squint, the range and azimuth responses are orthogonal. As squint is introduced, this is no longer true. The direction of both responses turns with the direction of the range response approaching the squint angle.

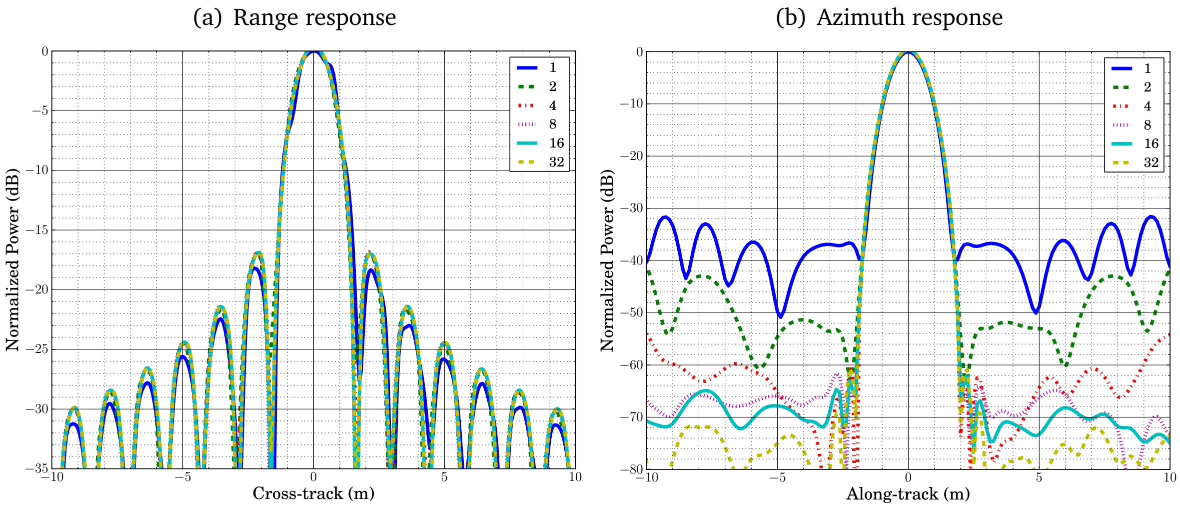

Figure 3.10: Range and azimuth impulse responses for varying factors of upsampling. The range response is misshapen without upsampling, but at an upsampling factor of 2 is the same as an upsampling factor of 32. The azimuth response shows the varying sidelobe levels depending on the upsampling factor. All have the same peak magnitude.

Several interpolation methods are available: nearest neighbor, upsampling nearest neighbor, linear, spline, etc. The upsampling nearest neighbor is performed by upsampling the signal and then choosing the sample closest to the desired point. This approach has the advantages of providing good results, being computationally efficient, and simple.

The effects of range-compressed pulse upsampling are shown in Fig. 3.10. The simulation parameters are the same as given in Sec. 3.4.4 on page 60. Each subfigure shows upsampling factors from 1 (no upsampling) to 32. Subfigure (a) gives the range impulse response of a point target and (b) gives the azimuth response. Notice in all of the cases (both range and azimuth response), upsampling has minimal effect on mainlobe peak power and width; the upsampling effects are primarily related to sidelobe structure. The minor exception to this is that the range response of the mainlobe is slightly misshapen without upsampling. Upsampling factors of 2 through 32 show practically identical range sidelobe structure.

In azimuth, just an upsampling factor of 2 dramatically lowers the sidelobes near the peak, however, the sidelobes eventually return to nearly the same levels as without upsampling. It is not until an upsampling factor of 8 that the sidelobes are significantly reduced across the entire width of the response. Upsampling factors of 16 and 32 also show marginal improvement in sidelobe reduction. In practice, sidelobe performance may be dominated by other factors such as DEM or antenna position estimate errors.

3.5 Discussion

This section discusses the results of the chapter and summarizes its contributions. First, the questions of where backprojection is advantageous and when is it applicable are answered. Following that, a summary of the contributions of each section is presented.

Examining the list of backprojection advantages in Section 3.1, many are not particularly applicable to spaceborne use (e.g., motion compensation, ground-plane imaging, highly parameterizable matched filter). This is because the spacecraft motion is very regular (i.e., nearly ideal). Additionally, a spaceborne platform has very far range-to-target and generally has a narrow enough range swath that the change in incidence angle across the swath is minor. It is at lower altitudes where the backprojection advantages become consequential due to significant non-ideal motion, high range-migration, dynamic imaging modes, etc.

Backprojection may be seen as an ideal two-dimensional, spatially-varying matched filter. If the imaging geometry is known exactly then backprojection is exact. Unfortunately, this is rarely the case since the phase-center of the scattering-cells is unknown and there is inaccuracy in the measurement of the platform position. As discussed in previous sections, the phase-center of the scattering-cell may be offset from the physical center of the cell, the DEM height may not be exact, and the INS measuring the SAR platform positions may have errors in the measurements. These uncertainties lead to phase errors that distort the backprojection solution. Fortunately, however, these errors are often small.

As shown in Sec. 3.4.1, for common slant-range resolutions, the effect of having the phase-center located away from the physical center of the scattering-cell is minimal as long as there is little DEM error. Since high quality DEMs are available over many parts of the Earth, this requirement can often be met. Additionally, considering that many imaging scenarios involve distributed targets whose phase-center is near the physical center of the cell, this issue is further moderated for such targets (though discrete targets may still be affected).

Table 3.2: Inertial Measurement Units (IMUs)

Grade	**Cost**	**Weight**	**Accelerometer Bias Error**	**Horizontal Position Error** (m)			
Units		(lbs)	(mg)	1s	10s	60s	1hr
Automotive	$1 - $500	< 0.5	125	620 mm	60 m	2.2 km	7900 km
Industrial	$500 - $3k	< 1	3	15 mm	1.5 m	53 m	190 km
Tactical	$5 - $30k	2.5	0.3	1.5 mm	150 mm	5.3 m	19 km
Navigation	> $100k	> 6	0.025	0.12 mm	12 mm	0.44 m	1.6 km

The requirement of precise antenna position knowledge necessitates use of a high quality INS. An INS typically incorporates an inertial measurement unit (IMU) and global position system (GPS). The combination allows for accurate measurement of both relative and absolute motion. The GPS also mitigates drift in the IMU. Table 3.2 provides general specifications for typical grades of IMU.[1] While lower cost automotive and industrial grade IMUs are available, their performance is not suitable for SAR image formation.

One factor constraining the specification of required IMU precision is the amount of drift that accumulates during a given synthetic aperture. For example, recall from Sec. 3.4.2 that along-track drift of one resolution length may occur across the synthetic aperture before significant degradation occurs. If a tactical grade IMU is used and the azimuth resolution is 15 cm, then the synthetic aperture length is constrained to be no longer than approximately 10 seconds. Consider two examples of platform height:

- If the azimuth beamwidth is $8°$, the incidence angle is $45°$, and the platform elevation is 300 m above the ground, then the synthetic aperture length is 60 m. If the platform travels at 30 m/s then the synthetic aperture length is 2 sec so the tactical grade IMU is acceptable.
- If, however, the altitude is 3000 m above the ground, with all other specifications the same as before then the synthetic aperture length is 600 m (20 seconds) and an unacceptable amount of drift may occur during during a single aperture.

---

[1] As used here, tactical grade means an accelerometer bias error less than 1 mg.

Thus, a given imaging geometry constrains the choice of IMU. This requirement may be relaxed through the use of an autofocus algorithm. Autofocus algorithms are commonly used in SAR to remove phase errors due to uncompensated motion, hardware limitations, or other non-ideal effects [4, 32, 33, 34, 35, 36, 37]. Appendix A on page 145 discusses autofocus in more detail.

In addition to showing situations that are well suited to the use of backprojection, the analysis presented in this chapter presents several novel concepts. In Section 3.2, a general expression for time domain backprojection from first principles is derived. This general derivation does not assume separability of the along-track/cross-track dimensions nor does it assume a homogeneous point spread function across range and azimuth. Because the general formulation is very computationally expensive, it is shown when approximations may be made to separate the range and azimuth compression steps which greatly aids computational efficiency.

In Section 3.3 the Bakhshali square root approximation is used to derive an expression for the range residual across very wide azimuth angles. This allows for a more accurate analysis of the effects of residual range/phase. It is also shown that the first-order Taylor series approximation is generally sufficient for the case of narrow-beam antennas. The residual range derivation is used as a basis for describing the sensitivity of backprojection to various imaging parameters. For example, the sensitivity to motion, range, etc. in a given dimension is higher the more the phase-center is displaced in that dimension. Increasing the slant-range-to-target desensitizes the residuals with respect to motion and phase-center displacement. Also, narrow-beamed antennas are not sensitive to small along-track phase-center displacement.

In Section 3.4, the performance characteristics of backprojection are described. While all possible geometries are not tested as there are too many degrees of freedom to exhaustively show them all, important cases are given and the concepts necessary to calculate the performance specifications for a given geometry are provided. Beyond these position accuracy considerations discussed above, an expression for the maximum azimuth antenna beamwidth for a SAR based on its resolution is derived. This derivation assumes the scattering-cells phase-center is maximally displaced (i.e., at the edge of the cell). It is shown that squint and

Doppler-centroid shift are not problematic for backprojection and require no special treatment. Finally, the effects of upsampling the range-compressed signal are shown.

3.6 Chapter Appendix: Doppler Centroid

For ideal, linear motion, the Doppler frequency of a given target monotonically decreases as the platform approaches and then passes that target. The Doppler frequency begins at a positive value, goes through zero at the point of closest approach, and then decreases to its minimum. This leads to a bijective (one-to-one) relationship between slow-time and the Doppler (azimuth) frequency. An excellent treatment of Doppler centroid and squint as it relates to frequency domain algorithms is presented in [3]. From [3], the relationship between slow-time η and Doppler frequency f_η is

$$f_\eta = -\frac{2V_r^2\eta}{\lambda\sqrt{R_0^2+V_r^2\eta^2}}, \tag{3.56}$$

$$\eta = -\frac{\lambda R_0 f_\eta}{2V_r^2\sqrt{1-\frac{\lambda^2 f_\eta^2}{4V_r^2}}}, \tag{3.57}$$

where V_r is the relative along-track velocity between the platform and the target, λ is the carrier wavelength, and R_0 is the distance at the point of closest approach. The range cell migration (RCM) in the range-Doppler domain is

$$R_{\mathrm{rd}}\left(f_\eta\right) = \frac{R_0}{\sqrt{1-\frac{\lambda^2 f_\eta^2}{4V_r^2}}}. \tag{3.58}$$

The Doppler centroid frequency is

$$f_{\eta_c} = \frac{2V_r \sin\theta_{\mathrm{sq,c}}}{\lambda}, \tag{3.59}$$

where $\theta_{\mathrm{sq,c}}$ is the slant-range squint angle to the target. Note that this angle may change as a function of ground-range; thus the Doppler centroid frequency may vary across the range swath.

When a narrow-beam antenna with zero squint is used, the relationship between frequency and time is approximately linear in the main lobe since the range function may be approximated as parabolic. However, for a wide beam antenna or for the case of squint, the relationship is more non-linear and the hyperbolic form must be used. Because the relationship between slow-time and azimuth frequency is non-linear, image formation using the range-Doppler algorithm requires two modifications: (1) RCM compensation and the azimuth matched filter must use the hyperbolic form for range. (2) The coupling between range and azimuth necessitates secondary range compression (SRC). SRC is a filter that corrects the effects of target blurring due to the range/azimuth coupling. There are several methods of performing SRC, but for the case of high squint, it should be performed in the 2D frequency domain so that the azimuth frequency dependence of the coupling may be taken into account. When performed in this manner, SRC is computationally expensive–more computationally expensive than either the chirp-scaling algorithm or the omega-K algorithm. Note that SRC is assumed to be independent of range-to-target and V_r, which may be inaccurate for some geometries [3].

Squint and Doppler Centroid

In order to illustrate the effects of squint on the spectrum of a target, Fig. 3.11 shows the two-dimensional spectrum of a range-compressed point target for varying levels of squint. The azimuth sampling rate is the Nyquist rate at the point of closest approach, and the carrier wavelength is 0.3 m. At 0° squint the along-track spectrum is centered at zero and is symmetric about zero with no skew. As the squint angle increases, the along-track spectrum shifts according to the cross-track frequency. This has the effect of translating and skewing the spectral envelope of the target. By 10°, the envelope has made one complete wrap. At higher squint angles, the decrease in the bandwidth of the Doppler chirp becomes apparent. Without modification, the spectrum of the matched filter of the range-Doppler algorithm matches the envelope in subfigure (a). The backprojection spectrum for a given pixel natively matches the spectrum of the target, whatever the squint angle may be.

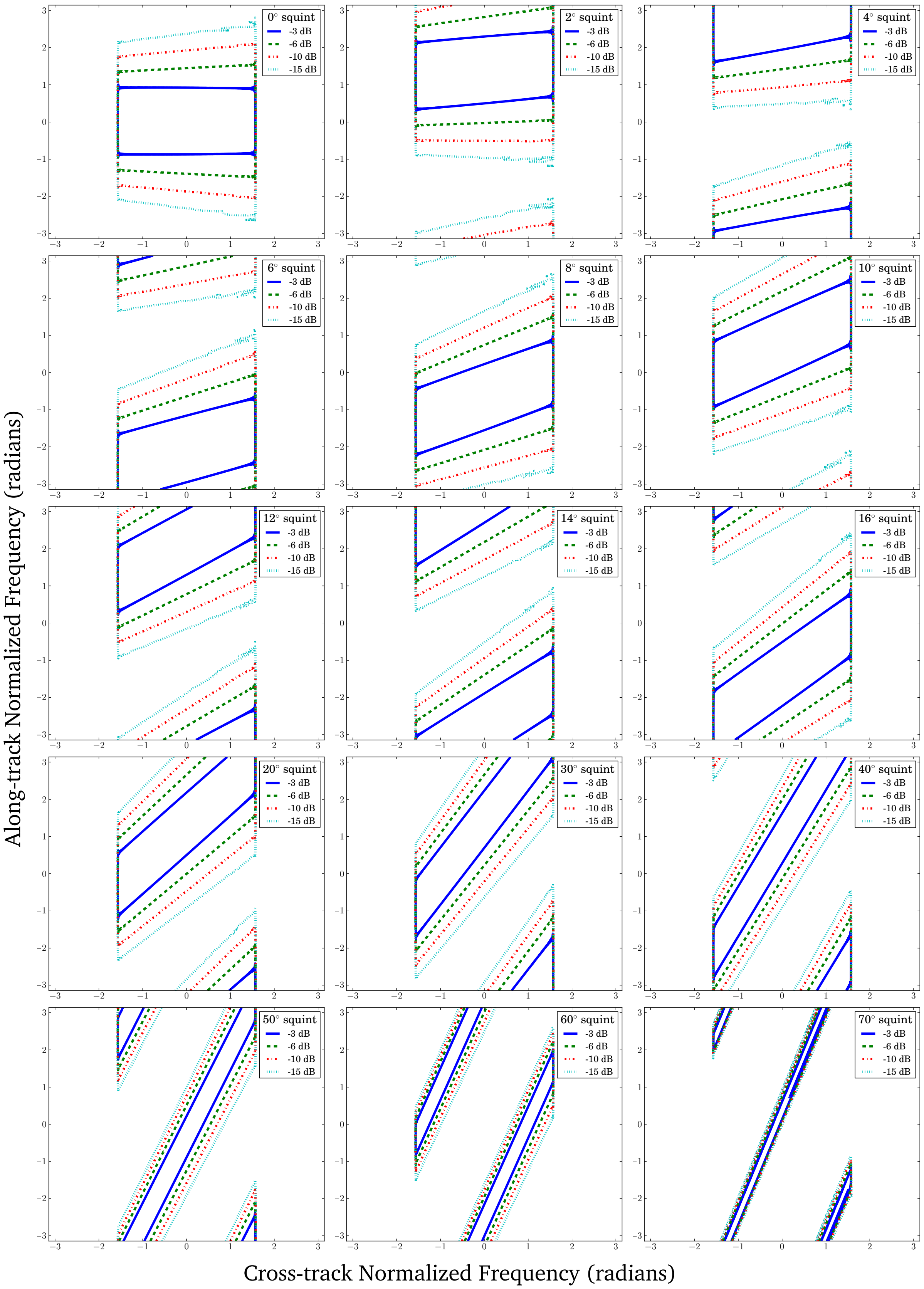

Figure 3.11: 2-D spectrum of a range-compressed point target for various squint angles. The envelope wraps approximately every 9°.

Chapter 4

Multistatic Geometric Correlation

4.1 Introduction

In order to motivate the analysis of multistatic geometric correlation, some background is necessary. As stated in Chapter 2, multistatic radar denotes the use of multiple combinations of monostatic and bistatic data. Multistatic radar may be considered a type of multiple-input and multiple-output (MIMO) technology [38] (in this chapter, the terms *multistatic* and *MIMO* are used interchangeably). In wireless communications, use of MIMO techniques can significantly increase channel capacity and link range [39]. Because of the advances MIMO has brought to communications, researchers have sought to apply MIMO techniques to radars, which have traditionally been single-input and single-output (SISO) only.

Current research divides MIMO radar into two categories: collocated (or coherent) and distributed (or statistical) [38]. With a collocated multistatic radar, transmit/receive antennas are placed close together, while a distributed multistatic system has antennas separated over a wide area. In both cases, many agree that despite the disadvantages of cost and complexity, there are potential advantages in surveillance radar for MIMO over conventional SISO [38, 40, 41, 42, 43, 44, 45, 46, 47, 48]. There are, however, critics who doubt the merits of MIMO radar [49]. In either case, MIMO radar is currently a heavily researched area.

Because of the potential advantages multistatic techniques bring to radar, researchers have sought to bring similar advantages to SAR. The advantages, however, of MIMO SAR over traditional SAR are vague and few papers have been published on the topic. Of those papers that have explored MIMO SAR, each presents a specific method using MIMO techniques, but none adequately motivates the use of MIMO for SAR, especially given the additional cost and complexity incurred with such a system. For example, one such paper discusses MIMO interferometry waveform techniques, but doesn't show or cite any advantages or performance analysis [50]. Another paper shows how to lower the minimum required pulse repetition frequency (PRF) [51], but this could be achieved without MIMO through the use of multiple receive-only antennas in azimuth. Several papers discuss using a specific constellation of distributed MIMO SARs with varying incidence angles to obtain somewhat higher range resolution than given by the transmit bandwidth [52]. Another paper claims lengthened range swath via orthogonal frequency-division multiplexing (OFDM) [53], but without any underlying improvement in resolution. A few other papers present signal synthesis and hardware design, but neglect any treatment of why MIMO SAR would be useful in practice [54, 55, 56, 57].

A key consideration in determining the utility of MIMO as applied to SAR is whether a particular MIMO SAR configuration operates in the collocated or the distributed regime. This can be determined by evaluating the signal correlation between the MIMO SAR channels. In order to develop the necessary tools for this evaluation, this chapter examines MIMO SAR signal correlation from first principles for various multi-static imaging geometries. This allows us to determine which regime a MIMO SAR utilizes and therefore its merits. Operating in the collocated regime is desirable for coherent processing whereas operating in the distributed regime is desirable for obtaining independent looks. The correlation analysis also becomes useful in the next chapter on interferometry.

Section 4.2 begins with a development of the correlation model, including an explanation of how this analysis is being performed and why it is different from previous analyses. Next, Section 4.3 derives an analytic expression for the correlation of MIMO signals in various geometric configurations. The section then presents a numerical analysis that allows for more complicated situations. Section 4.4 concludes with an analysis of various imaging scenarios and determine whether a given MIMO geometry is considered collocated or distributed.

4.2 Correlation Development

In multistatic imaging, multiple antennas are located at different positions in space. Because of this, each transmit/receive antenna pair has a different signal. The antenna separation leads to decorrelation of the signals of the antenna pairs. The extent to which signals from different geometries are decorrelated determines the degree to which various MIMO techniques are valid or meaningful. Therefore, it is critical to quantify the signal correlation for an assumed MIMO geometry in order to analyze its effects on a given processing regime.

This section begins with an explanation of how this analysis differs from analyses that have been performed previously. Following that is a discussion of how different geometries affect signal correlation. Finally, the section provides some geometric approximations to facilitate the solutions for signal correlation.

4.2.1 Motivation

Previous authors [58, 59, 60, 61, 62, 63] have investigated geometric correlation of SAR pixels for analyzing the correlated signal needs of interferometry. Despite starting with similar assumptions, at least four different models for geometric correlation have been developed [58, 59, 60, 61]. Each make the same first-order assumptions, but diverge in higher-order assumptions as well as specific methodology. It is not immediately obvious which is most accurate or most applicable in a given situation.

The previous methods share a common feature in that image formation is in the slant-plane. Performing the correlation analysis in the slant-plane leads to assumptions that are sufficient for cases where the antenna baseline separation is relatively small (i.e., interferometry), but may not be appropriate for general multi-static SAR.

An important assumption in deriving the correlation for distributed target pixels is that the individual scattering targets are uncorrelated between each other and are uniformly distributed over the surface, i.e., they are uniformly distributed in the ground-plane. When viewed in the slant-plane, the density of scatters are biased toward one end of a scattering-cell, where the bias depends on the incidence angle of the antenna to the cell. Figure 4.1 demonstrates this point by showing the scatterer probability distribution in the ground and slant

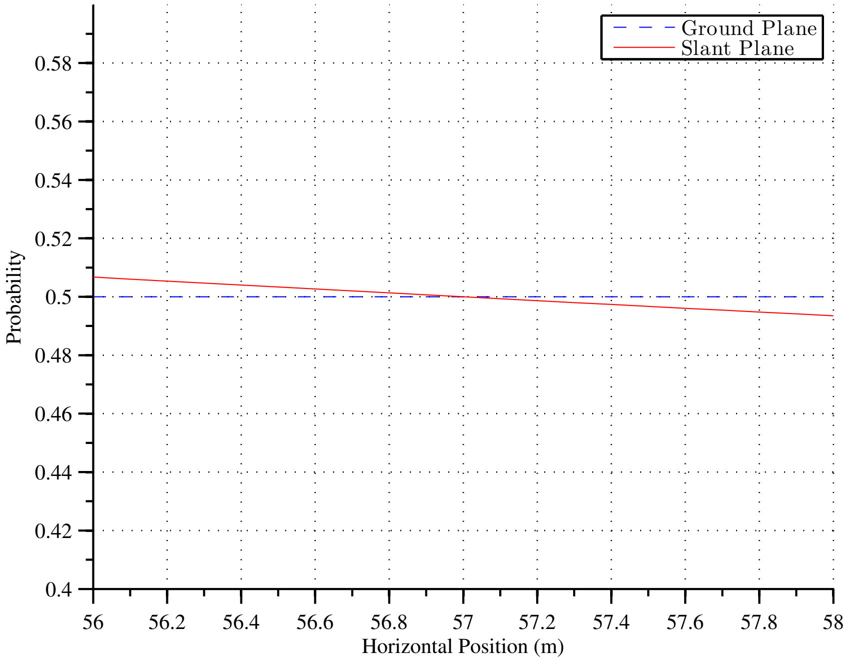

Figure 4.1: Comparison of scatterer distribution in the ground and slant planes for a 30° incidence angle. The scatterers are uniformly distributed in the ground plane inside a cell of length 2 meters in range.

planes for a 30° incidence angle. In other words, when viewed in the slant-plane the targets do not have a uniform distribution. In addition to this, the slant-plane image formation does not account for differences in the effective size of the scattering-cell (i.e., ground-plane range resolution) of the two antennas as a function of incidence angle and the corresponding effect on correlation. These issues lead to inaccuracy as antenna separation increases. As MIMO antennas are potentially widely separated, a more general correlation model is necessary.

The correlation model presented here is based on the phase-center displacement from the physical center of a scattering-cell. As shown in Chapter 3, if the imaging geometry (including scattering-cell phase-centers) were known exactly and used to parameterize the matched filter, then the residual backprojection pixel phase is zero. As will be shown later, this implies that no matter the antenna separation, multistatic backprojected pixels would be perfectly correlated. It is therefore the unknown precise location of the phase-center that leads to geometric decorrelation.

Because backprojection is an ideal matched filter, it is a natural choice for performing the correlation analysis. Backprojection has the advantage that images are formed in the ground-plane which explicitly handles ground-plane resolution difference and accurately reflects the target model of uniformly distributed scatterers in the ground-plane. As in the previous chapter, throughout the analysis the term *pixel* refers to the imaged signal and *scattering-cell* refers to the physical location being imaged.

4.2.2 Signal Pairs

Previous authors have modeled geometric decorrelation in SAR based on certain assumptions, including slant-plane image formation or approximations for the ground-range wavenumber. As mentioned earlier, accuracy can be improved upon using a ground-plane analysis. Because of this, I perform a new analysis of the geometric decorrelation using the pixels resulting from a ground-plane (i.e., backprojection) image formation algorithm.

Consider a general two transmit/receive channel case (see Fig. 4.2). Two antennas A and B illuminate a scattering-cell with dimensions equal to one range resolution bin by one azimuth resolution bin. The two antennas are placed in separate locations and observe the scattering-cell center C and an individual scatterer D. Because the antennas are not collocated, the antenna-to-cell-center and antenna-to-scatter propagation lengths differ. As the relative path lengths are different, the antennas each observe a different residual phase after matched filtering. This phase difference leads to geometric decorrelation. Recall from Section 3.2.1 that if a single isotropic scatterer is located at the center of the cell, there is no residual phase and thus no geometric decorrelation.

The correlation metric I use is the Pearson product-moment correlation coefficient (PPMCC) given by Rodgers and Nicewander [64]

$$\begin{aligned}\rho_{A,B} &= \frac{\mathrm{cov}(A,B)}{\sigma_A\,\sigma_B} \\ &= \frac{\mathrm{E}\left[AB^*\right]-\mathrm{E}\left[A\right]\mathrm{E}\left[B\right]}{\sqrt{\mathrm{E}\left[|A|^2\right]-|\mathrm{E}\left[A\right]|^2}\sqrt{\mathrm{E}\left[|B|^2\right]-|\mathrm{E}\left[B\right]|^2}},\end{aligned} \tag{4.1}$$

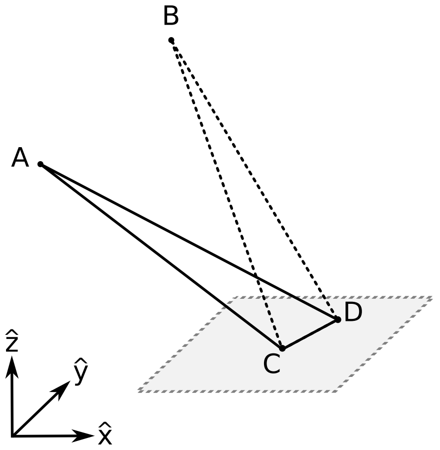

Figure 4.2: Scattering geometry for two antennas. Points A and B are the locations of the antennas, point D is the location of the scatterer, and point C is the center of the resolution-cell (image pixel).

where A and B are two random variables representing the complex pixel values and $\mathrm{E}\left[\cdot\right]$ is the expectation operator. The PPMCC may also be written using samples instead:

$$\rho_{A,B} = \frac{\sum_{i=1}^{n}(A_i - \bar{A})(B_i - \bar{B})}{\sqrt{\sum_{i=1}^{n}(A_i - \bar{A})^2}\sqrt{\sum_{i=1}^{n}(B_i - \bar{B})^2}}, \tag{4.2}$$

where A_n and B_n are the sample sets and $\bar{A}$ and $\bar{B}$ are the sample means. The PPMCC is a measure of the linear dependence between two random variables. Its absolute value produces a scalar between 0 and 1 where a value of 0 implies no linear correlation while a value of 1 implies a linear (or nonlinear bijective) equation perfectly represents the relationship of both random variables. An important property of the PPMCC is that it is invariant to affine transformations (i.e., $X \rightarrow mX + b$ produces the same correlation coefficient). These qualities make the PPMCC well-suited for comparing the coherence of two signals.

The signals of interest are the complex-valued pixels. These pixels come from separate backprojected images resulting from distinct transmit/receive antenna pairs. For convenience, the range-compressed signal $g_n(l)$ of Eq. 3.23 is transformed to $g(x, y)$, where (x, y) is the relative displacement of a scatterer from the cell center. From Eq. 3.25, a single pixel value I

from an individual point scatterer is given by

$$I = g(x,y) = \sum_{n\in\mathcal{N}} \Gamma_n \, R(\Delta d_n) \, \exp\left(jk\Delta d_n\right), \tag{4.3}$$

where $\mathcal{N}$ is the set of all pulses contributing to the scattering-cell, Γ_n is a pulse dependent term that captures the gain terms $A_n(l)$ and $G_n(l)$ from Eq. 3.4, $R(l)$ is the range-compressed impulse response, and Δd_n is the (two-way) difference in distance from the antenna-to-cell-center and the antenna-to-scatterer (for each pulse).

For targets sufficiently displaced from the cell center (i.e., large Δd_n), the range response $R(\Delta d_n)$ vanishes and the sum becomes insignificant. Contrariwise, if the target's displacement from the ideal position is small, the magnitude of the range response mismatch can be neglected. In the same way, a small deviation in position has a negligible effect on the gain terms. Eq. 4.3 may then be approximated by factoring the amplitude terms Γ_n and $R(\Delta d_n)$ out of the sum. Therefore, because the PPMCC performs normalization and mean removal, from a geometric decorrelation standpoint the dominating term in calculating the PPMCC comes from the term $\sum_n \exp\left(jk\Delta d_n\right)$. This describes the phase difference in the two pixels formed with different imaging geometries and is a direct result of the difference in path lengths for A and B.

Let an individual antenna be located at point A, a cell centered at point C, and a scatterer at point D. This geometry is shown in Figure 4.3. The distance from the antenna to the cell center is d, the distance from the antenna to the scatterer is c, and the distance from the cell center to the scatterer is a. The angle between segments a and d is θ.

For the moment, assume that for any given antenna the difference in propagation length from the antenna-to-cell-center d and antenna-to-scatterer c is known. This quantity $c - d$ is designated $\Delta d_{\mathrm{A},n}$, where the subscript indicates antenna A and n is the pulse index which is often suppressed for notational simplicity. In the following analysis, the receive antennas are designated A and B and the transmit antennas are designated T and U. This is illustrated in Fig. 4.4. Where a transmit antenna is collocated with the receive antenna, it uses the receive antenna nomenclature. A propagation path is the combination of the distance for an individual transmitter and an individual receiver. The propagation differential distance

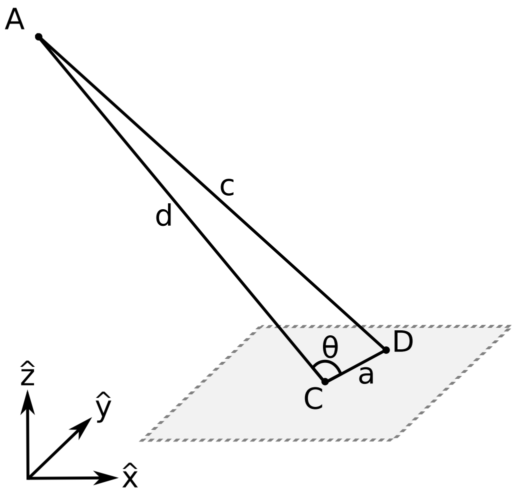

Figure 4.3: Scattering geometry at a single pulse for one antenna. Point A is the location of the antenna, point D is the location of the scatterer, and point C is the center of the resolution-cell (image pixel).

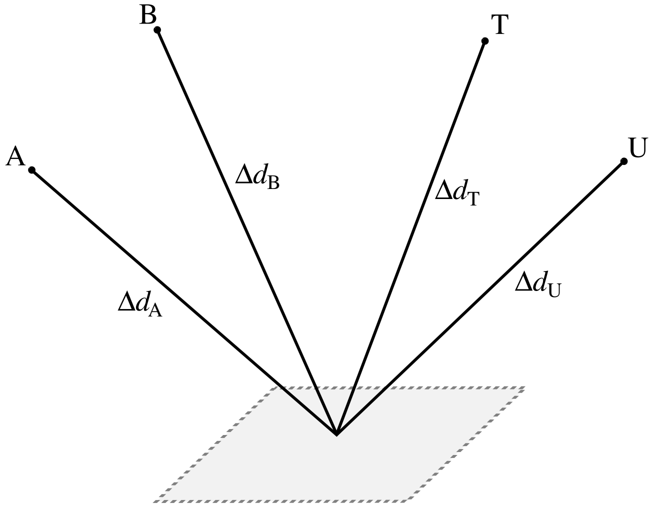

Figure 4.4: Illustration of MIMO scattering geometry. Points A and B represent receive antennas and points T and U represent transmit antennas. The residual propagation distance for each antenna to the scattering-cell is Δd, with a subscript distinguishing the respective antenna.

Table 4.1: Four Imaging Geometry Cases

Case	Type	Description	Propagation Difference $\Delta\Delta d$	μ
1	SIMO	1 Tx + 2 Rx	$\Delta d_A - \Delta d_B$	1
2	MISO	2 Tx + 1 Rx	$\Delta d_T - \Delta d_U$	1
3	Monostatic MIMO	2 Collocated Tx/Rx	$2\left(\Delta d_A - \Delta d_B\right)$	2
4	General MIMO	2 Tx + 2 Rx	$(\Delta d_A + \Delta d_T) -$ $(\Delta d_B + \Delta d_U)$	-

between two paths (e.g., channels AT to BU) is designated $\Delta\Delta d$. We now consider four antenna placement geometries summarized in Table 4.1 and described below.

1) *A single transmitter and two receivers*. This is the single-input and multiple-output (SIMO) case. The propagation differential between the two channels is

$$\begin{aligned}\Delta\Delta d &= [(\Delta d_{\mathrm{T}} + \Delta d_{\mathrm{A}}) - (\Delta d_{\mathrm{T}} + \Delta d_{\mathrm{B}})] \\ &= \Delta d_{\mathrm{A}} - \Delta d_{\mathrm{B}}. \end{aligned} \tag{4.4}$$

The propagation difference is dependent only on the receiver positions, not the transmitter position. Thus, the transmit antenna may be collocated with one of the receive antennas (i.e., monostatic) without any change in effect.

2) *Two transmitters and a single receiver*. This is the multiple-input and single-output (MISO) case. Here,

$$\begin{aligned}\Delta\Delta d &= [(\Delta d_{\mathrm{T}} + \Delta d_{\mathrm{A}}) - (\Delta d_{\mathrm{U}} + \Delta d_{\mathrm{A}})] \\ &= \Delta d_{\mathrm{T}} - \Delta d_{\mathrm{U}}. \end{aligned} \tag{4.5}$$

This result is similar to case 1: the propagation difference is only dependent on the transmitter locations, not the individual receiver. For quantitative correlation analysis, this can be considered the same as case 1.

3) *Two monostatic radars*. As there are multiple transmitters and multiple receivers, this can be considered a special case of MIMO.

$$\begin{aligned}\Delta\Delta d &= \left[\left(\Delta d_{\mathrm{A}} + \Delta d_{\mathrm{A}}\right) - \left(\Delta d_{\mathrm{B}} + \Delta d_{\mathrm{B}}\right)\right] \\ &= 2\left(\Delta d_{\mathrm{A}} - \Delta d_{\mathrm{B}}\right). \end{aligned} \tag{4.6}$$

In this case, the propagation difference is double those in the previous cases and can be treated similarly in analysis with only slight modification.

4) *Two bistatic radars*. This is the general MIMO case where neither receiver nor transmitter is collocated.

$$\Delta\Delta d = \left(\Delta d_{\mathrm{T}} + \Delta d_{\mathrm{A}}\right) - \left(\Delta d_{\mathrm{U}} + \Delta d_{\mathrm{B}}\right). \tag{4.7}$$

For this case, no simplification can be made and the full geometry must be used to determine decorrelation effects.

4.3 Pixel Correlation

With the correlation background developed the correlation solutions may be found. The first subsection presents an analytic solution for the case of an individual isotropic scatter inside a scattering-cell. The second subsection presents a numerical analysis which allows for more sophisticated scattering situations. The final subsection ends with an analysis of decorrelation due to volumetric scattering.

4.3.1 Analytic Solution

For isotropic scattering, the geometric correlation depends on the propagation differential $\Delta\Delta d$ at the pixels of interest. Recall the geometry given in Figure 4.3. As stated previously, if a scatterer is not located at the cell's center, there is a residual phase $\tilde{\phi}_n$ contributed for every pulse n summed:

$$\tilde{\phi}_n = k\ \left(\Delta d_{\mathrm{T},n} + \Delta d_{\mathrm{A},n}\right),$$

where subscripts T and A refer to the transmit and receive antennas, respectively, and n is the pulse index. From this, Eq. 4.3 (a single pixel with an individual point scatterer) can be rewritten as

$$I = \Gamma \sum_{n} \exp\left[jk\left(\Delta d_{\mathrm{T},n} + \Delta d_{\mathrm{A},n}\right)\right], \tag{4.8}$$

where Γ captures all of the amplitude terms (e.g., antenna gain, radar system gain, propagation loss, etc).

I now provide an analytic solution to the PPMCC of Eq. 4.1 for an individual scatterer contained in a resolution-cell. The expected value of the pixel I is

$$\mathrm{E}\left[I\right] = \iint f(x,y)p(x,y)\mathrm{d}x\mathrm{d}y, \tag{4.9}$$

where $f(x, y)$ is the backprojected value and $p(x, y)$ is the (pdf), with x and y the scatterer displacements from the physical center of the scattering-cell. The expected value of the product of two perfectly registered pixels received by different antennas is

$$\mathrm{E}\left[I_A I_B^*\right] = \iint f_A(x,y) f_B^*(x,y) p(x,y)\mathrm{d}x\mathrm{d}y. \tag{4.10}$$

As shown earlier, f has, in general, non-zero response away from its peak. For the purpose of finding a simple analytic solution, the limits of integration are constrained to be bounded by the resolution of the cell. Further, a flat response across the resolution-cell is assumed. These assumptions are relaxed in the numerical solution later.

Substituting Eq. 4.8 into this result yields

$$\mathrm{E}\left[I_A I_B^*\right] = \iint \sum_{n} \left|\Gamma_n\right|^2 \exp\left[jk\left(\Delta d_{A,n} - \Delta d_{B,n}\right)\right] p\left(x,y\right) \mathrm{d}x\mathrm{d}y, \tag{4.11}$$

assuming identical antennas and gain. For the moment, let the scatterer vertical displacement z be 0. Additionally, let us assume that the relative position of the scatterer at x and y are each uniformly and independently distributed across a cell bounded by the azimuth resolution R_x

and the range resolution R_y of the radar. Eq. 4.11 then becomes

$$\mathrm{E}\left[I_A I_B^*\right] = \frac{1}{R_x R_y} \int_{-R_y/2}^{R_y/2} \int_{-R_x/2}^{R_x/2} \sum_n \left|\Gamma_n\right|^2 \exp\left[jk\left(\Delta d_{A,n} - \Delta d_{B,n}\right)\right] \mathrm{d}x \mathrm{d}y. \tag{4.12}$$

The sum in this expression poses a problem in finding an analytic solution to $\mathrm{E}\left[I_A I_B^*\right]$ (i.e., in general no closed form solution exists). However, the sum may be simplified under certain conditions. For a side-looking SAR in strip-map mode with zero squint, the pulses near the point of closest approach contribute the most to this sum (similar to those discussed in Chapter 3). Furthermore, as long as the resolution size of the scattering-cell is not excessively large (e.g., $R_y < 100\lambda$), the propagation difference Δd does not vary widely across the pulses. Therefore, Eq. 4.12 may be approximated as

$$\mathrm{E}\left[I_A I_B^*\right] \approx \frac{\Gamma}{R_x R_y} \int_{-R_y/2}^{R_y/2} \int_{-R_x/2}^{R_x/2} \exp\left[jk\left(\Delta d_A - \Delta d_B\right)\right] \mathrm{d}x \mathrm{d}y, \tag{4.13}$$

where Δd_A and Δd_B are the differences at the pulse occurring at the point of closest approach and $\Gamma \approx \sum_n \left|\Gamma_n\right|^2$. In simulation, this leads to a net phase error generally less than 10%. However, the difference between the approximated phase and the actual phase resulting from the approximation is similar for both A and B. Hence, the resulting correlation error is small and Eq. 4.13 is a good approximation for the purposes of collapsing the sum to obtain an analytic expression of the pixel correlation. The full sum is used in the numerical calculations of the next section.

After some manipulation, Eq. 4.13 can be written as

$$\mathrm{E}\left[I_A I_B^*\right] = -\frac{r_A^2 r_B^2 V_X V_Y}{\mu^2 k^2 R_x R_y W_A W_B Q}, \tag{4.14}$$

where r_A and r_B are the one-way distances from the target to antennas A and B, respectively,

$$\begin{aligned}
V_X &= \xi_A \xi_{CB} - \xi_B \xi_{CA}\,, \\
V_Y &= \psi_A \psi_{CB} - \psi_B \psi_{CA}\,, \\
W_A &= \sqrt{\xi_A \xi_{CA} \psi_A \psi_{CA}}\,, \\
W_B &= \sqrt{\xi_B \xi_{CB} \psi_B \psi_{CB}}\,, \\
Q &= \left(r_A\left(x_B - x_C\right) + r_B\left(x_C - x_A\right)\right) \\
&\quad \cdot \left(r_A\left(y_B - y_C\right) + r_B\left(y_C - y_A\right)\right)
\end{aligned}$$

and

$$\begin{aligned}
\xi_A &= \exp\left(\frac{j\mu k R_x x_A}{r_A}\right), & \xi_{CA} &= \exp\left(\frac{j\mu k R_x x_C}{r_A}\right), \\
\xi_B &= \exp\left(\frac{j\mu k R_x x_B}{r_B}\right), & \xi_{CB} &= \exp\left(\frac{j\mu k R_x x_C}{r_B}\right), \\
\psi_A &= \exp\left(\frac{j\mu k R_y y_A}{r_A}\right), & \psi_{CA} &= \exp\left(\frac{j\mu k R_y y_C}{r_A}\right), \\
\psi_B &= \exp\left(\frac{j\mu k R_y y_B}{r_B}\right), & \psi_{CB} &= \exp\left(\frac{j\mu k R_y y_C}{r_B}\right).
\end{aligned}$$

Solving for the remaining pieces of Eq. 4.1, we obtain

$$\mathrm{E}\left[I_A\right] = -\frac{r_A^2\left(\xi_A - \xi_{CA}\right)\left(\psi_A - \psi_{CA}\right)}{\mu^2 k^2 R_x R_y W_A\,\left(x_A - x_C\right)\left(y_A - y_C\right)}, \tag{4.15}$$

$$\mathrm{E}\left[I_B\right] = -\frac{r_B^2\left(\xi_B - \xi_{CB}\right)\left(\psi_B - \psi_{CB}\right)}{\mu^2 k^2 R_x R_y W_B\,\left(x_B - x_C\right)\left(y_B - y_C\right)}, \tag{4.16}$$

$$\mathrm{E}\left[I_A I_A^*\right] = 1, \tag{4.17}$$

$$\mathrm{E}\left[I_B I_B^*\right] = 1. \tag{4.18}$$

Substituting Eq. 4.14 - 4.18 into Eq. 4.1 yields the analytic solution for geometric correlation.

In the equations above, the constant μ is 1 in the SIMO and MISO cases (cases 1 and 2 from Section 4.2.2) and μ is 2 for the special MIMO case of correlating pixels from two monostatic radars (case 3). An analytic solution for case 4 exists, but is significantly more complicated and doesn't lend any more intuition than examination of the formulas above.

Figure 4.5 shows plots of the single pixel correlation ρ_{AB} for cases $\mu = 1$ and $\mu = 2$ for side-looking SAR with zero squint. Each curve in the plots corresponds to a scattering-cell where the length in range (i.e., range resolution) is a multiple of the radar wavelength (i.e., $R_y \propto \lambda$). The along-track cell size (azimuth resolution) is constant. There reference antenna A, corresponding to the reference signal I_{AA}, is located at an incidence angle of 45 degrees at the point of closest approach. The second antenna B is placed at the same range-to-target as Antenna A but the incidence angle is varied from 0 to 90 degrees.

As expected, the signal correlation is 100% when the incidence angles are identical (i.e., the antennas are physically collocated). This result holds true for scattering-cells of any size. As the angular separation between the two receive antennas widens, the signals decorrelate in roughly a sinc-like manner. Note that the signals decorrelate more rapidly as the range resolution increases with respect to the wavelength. Also, notice that the curves for $\mu = 2$ (two monostatic radars) in Fig. 4.5(b) are the same as those for the $\mu = 1$ case in Fig. 4.5(a) when the range resolution R_y is doubled. This provides the reasoning for designating the cases as $\mu = 1$ and $\mu = 2$, referring to the coefficient μ in Eqs. 4.14 - 4.18.

Figure 4.6 shows correlation plots for the $\mu = 1$ cases when the elevation angle is kept constant but the azimuth angle is varied. Subfigures (a), (b), and (c) correspond to antennas with azimuth beamwidth 10, 20, and 40 degrees, respectively. As in the previous examples, several curves are presented at various range resolutions. The azimuth resolution is constant for each plot as it is implicitly a function of the antenna's effective azimuth beamwidth. The reference antenna is placed at the point of closest approach (0° azimuth). Both the reference antenna and the secondary antenna are placed at a constant height corresponding to an incidence angle of 45° at the point of closest approach.

These plots provide information on how correlated individual pulses are across a synthetic aperture. For radars with a range resolution on the same order of magnitude as the wavelength, decorrelation is low across the synthetic aperture. Notice, however, that as the beamwidth becomes wider, which corresponds to finer azimuth resolution, it becomes critical to have fine range resolution also in order to maintain coherence across the synthetic aperture.

(a) Case $\mu = 1$

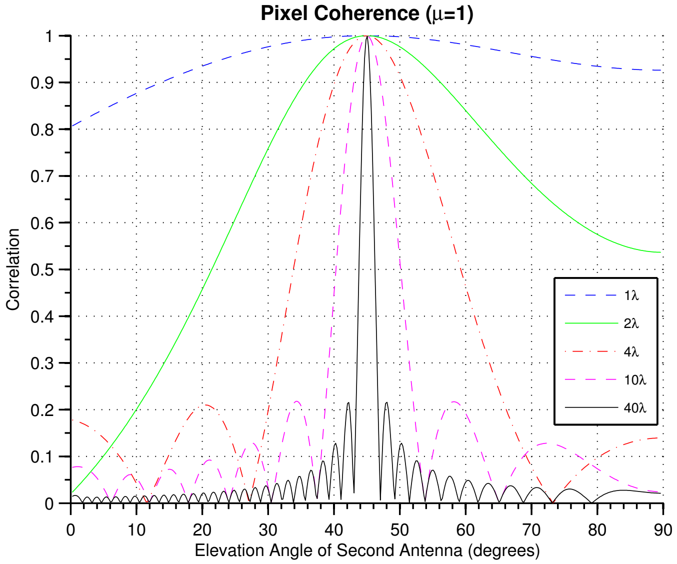

(b) Case $\mu = 2$

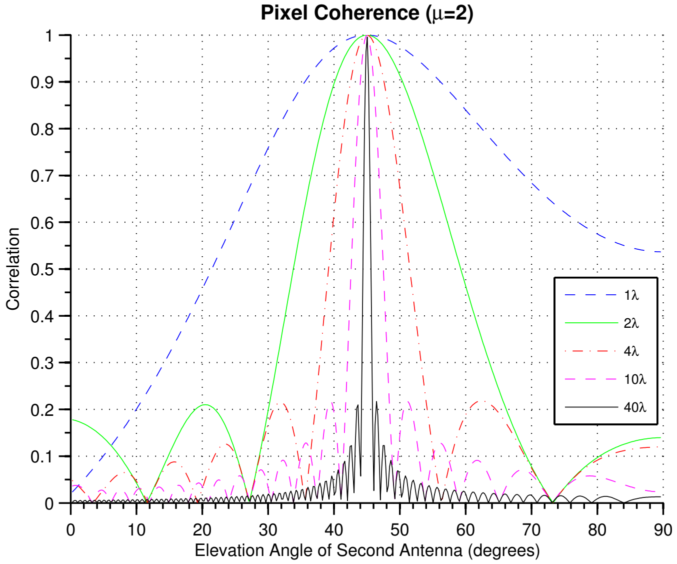

Figure 4.5: Analytic solution of pixel correlation for a single point target. (a) shows geometry cases 1 and 2 ($\mu = 1$) and (b) shows geometry case 3 ($\mu = 2$). The reference antenna is placed at an incidence angle of $45°$ and the second antenna is rotated from incidence angles $0°$ to $90°$ at a fixed range from the target. Multiple curves are shown, where each represents a different range resolution. The range resolution is a function radar wavelength (i.e., $R_y \propto \lambda$).

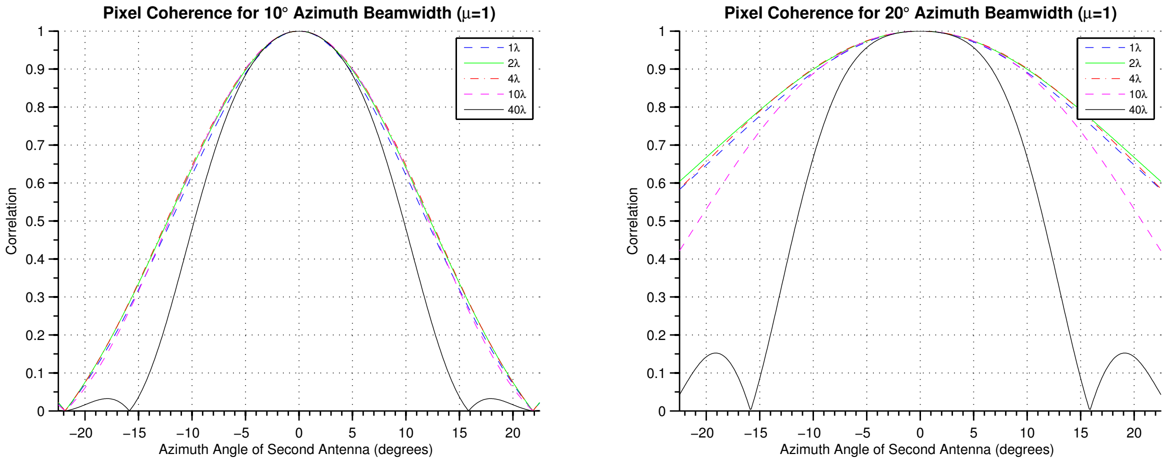
(a) 10° Azimuth Beamwidth

(b) 20° Azimuth Beamwidth

(c) 40° Azimuth Beamwidth

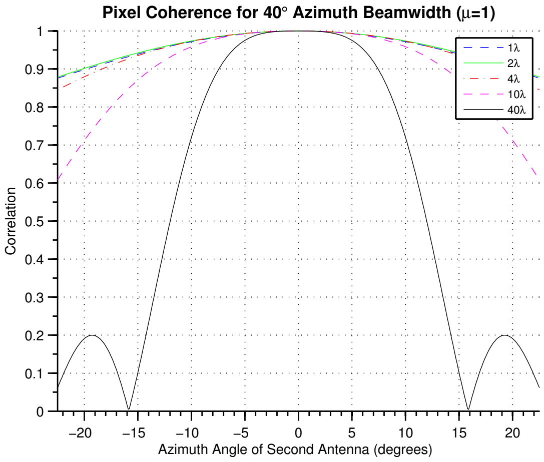

Figure 4.6: Pixel correlation for $\mu = 1$ cases of antennas separated in azimuth. Each subfigures shows a different azimuth beamwidth. The curves represent range-resolution as a multiple of wavelength. As the azimuth beamwidth increases, the along-track size of the scattering-cell narrows. The shortening of the cell improves pixel correlation.

The analytic solution provides useful insight for understanding signal correlation at various imaging geometries and radar parameters. However, this analytic solution is limited to a single scatterer. A numeric solution is required for more complicated situations.

4.3.2 Numeric Solution

All of the analysis to this point has been for a single scatterer displaced from the geometric center of the scattering-cell. When there is more than one scatterer, solving Eq. 4.1

analytically becomes intractable. However, an estimate of the correlation coefficient can be obtained numerically by replacing the expected value operator in Eq. 4.1 with ensemble averages[1]. The averages are performed over random realization of target location within the scattering-cell.

Using ensemble averages, the calculation of the correlation coefficient is repeated for the single scatterer case. In performing the ensemble averaging, a very smooth curve is obtained using 10^4 samples, although the general shape is visible with 10^3. Numeric analysis for a single scatterer confirms the results of the analytic analysis of the previous section. A figure showing the comparison of the analytic result with the numeric result (albeit for a variable width cell) appears later in Sec. 4.4.

Next, the numeric analysis is performed for multiple uniformly distributed (in the ground-plane) random scatterers. Interestingly, adding scatterers does not change the averaged correlation results computed for a single scatterer: using just one scatterer in the analysis produces the same decorrelation model as using many thousand. This is because adding scatterers does not change the relative distribution of cell phase. This is seen in Fig. 4.7. The figure shows a grid containing the probability distribution of a cell's phase for various sized cells and with a different number of scatterers. Notice the image in the upper-left corner for a cell with one scatterer and a range-resolution equal to the wavelength. At low incidence angles the phase is distributed from just over $-\pi$ to just under π (i.e., a phase distribution width slightly under 2π). As the incidence angle increases, the width of the phase distribution also increases. At around 17° the distribution reaches $\pm\pi$ and begins to wrap around. Moving down to the next image in the column, the cell length is increased to two wavelengths. The same trend is visible but the rate of change in phase distribution (i.e., the frequency of phase wrapping) increases. The phase distribution has already wrapped at 0°, and wraps again around 50°. This phenomenon continues as the cell size is increased further. Moving to the other columns, while the exact distribution of phase angles changes, the shape is quite similar: the transition regions and phase wrap frequency are identical. Because the expected value of the relative distribution of phase angles does not significantly change as scatterers are added, the corre-

---

[1] The expected value of random variable X can be approximated by the sample (or ensemble) average $\mathrm{E}\left[X\right] = \frac{1}{N}\sum_{n=1}^{N} x_n$, where x_n are the samples.

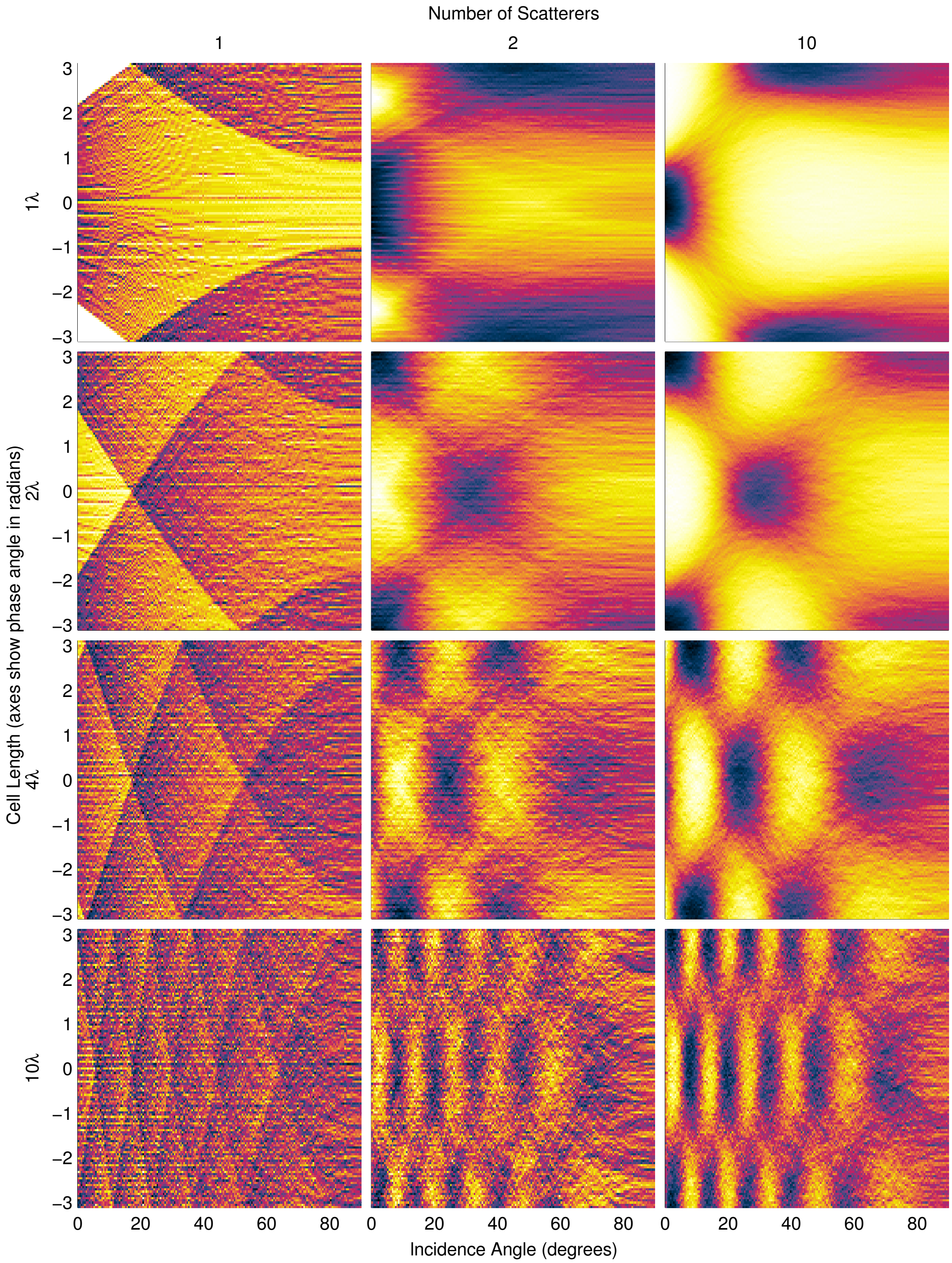

Figure 4.7: Plot showing normalized histograms (probability distribution) of cell phase at various incidence angles. For each plot, the vertical axis gives the distribution of phase angles from $-\pi$ to $+\pi$. Each vertical slice in a plot represents a particular incidence angle (given by the horizontal axis). Columns correspond to different numbers of scatterers within a cell. Rows correspond to different cell lengths (denoted as a multiple of the wavelength). The color white represents low probability and black represents high probability.

lation remains the same. Thus, the precise number of uniformly distributed scatterers is not critical.

Until this point, the analysis has used the simplifying assumption that the ground resolution is identical at every elevation angle. However, in reality, the ground-range resolution is a function of incidence angle. Given a radar with a slant-range resolution $R_{y,\mathrm{slant}}$, the ground-range resolution R_y is commonly approximated (assumption of plane-wave propagation) by the equation

$$R_y = \frac{R_{y,\mathrm{slant}}}{\sin\theta_0}, \tag{4.19}$$

where θ_0 is the incidence angle. Fig. 4.8 illustrates this concept. The figure shows a range slice of a scattering-cell as viewed from antennas at points A and B. Concentric arcs with equal radial separation are used to demarcate the areas that fall within one resolution-cell, where the cells are registered to share the same center point. Antenna A, at a larger incidence angle than B, has a narrower ground-range patch α than the ground patch β of antenna B. As the ground patch α is narrower than β, it contains only a subset of the scatterers contained by the patch that antenna B "sees."

Because the effective cell size changes as a function of incidence angle, antennas placed at different elevation angles contain a different set of scatterers. This causes decorrelation in addition to that seen previously. Thus, decorrelation is not only due to the difference in path length to each scatterer because of variations in imaging geometry, but decorrelation is also due to a different set of scatterers falling within the same resolution-cell.

While accounting for this phenomenon analytically is complicated, accounting for it numerically is straightforward. A larger field of scatterers is produced, and only those scatterers that are within the resolution-cell for each antenna for a particular geometry are included. Further, in a numeric computation we can avoid the approximations used in deriving the analytic expression and calculate Eq. 4.3 exactly. Using this more accurate model, Figure 4.9 shows an updated correlation coefficient ρ_{AB} for the $\mu = 1$ cases.

Comparing Fig. 4.9 to that of Fig. 4.5, the correlation is more sensitive to separation in incidence angle, especially for the smaller incidence angles at the left-hand side of the plot. As the incidence angle approaches zero, the ground-range resolution becomes larger and leads

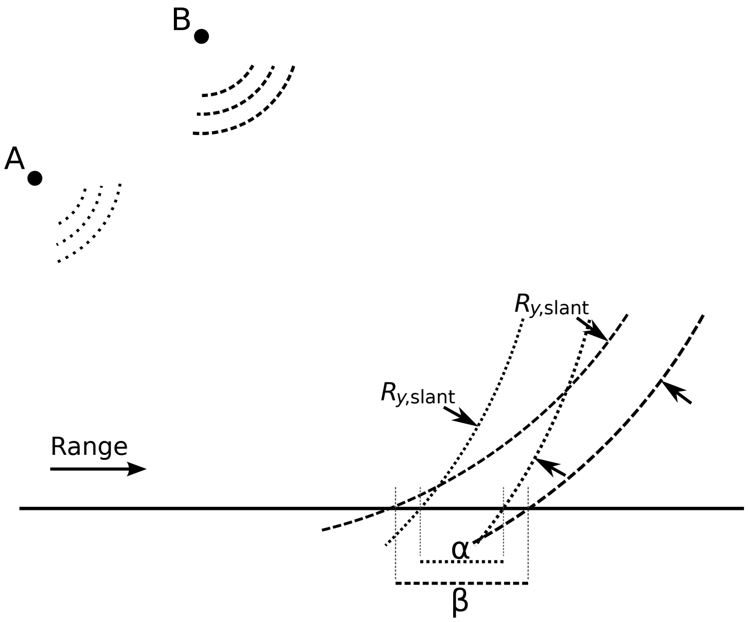

Figure 4.8: Diagram illustrating how incidence angle affects cross-track ground-range resolution. Antennas A and B have the same slant-range resolution $R_{y,\text{slant}}$. However, a larger incidence angle corresponds to a narrower ground-range resolution R_y. Therefore, the cross-track footprint α corresponding to antenna A is narrower than footprint β for antenna B.

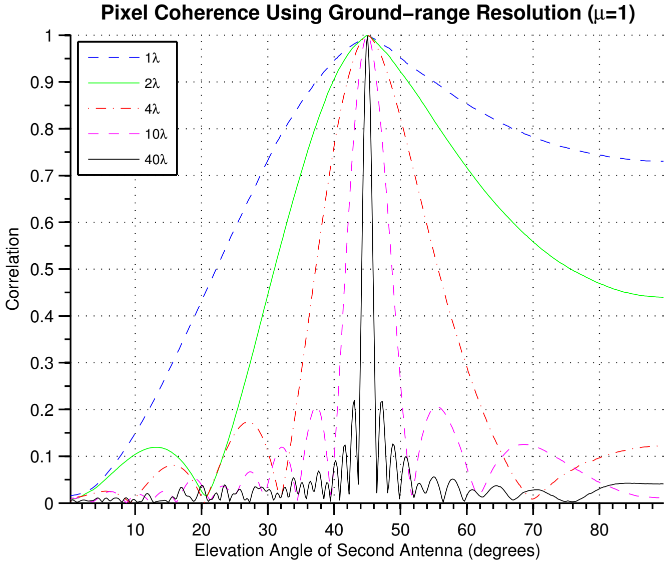

Figure 4.9: Pixel correlation for antennas of cases $\mu = 1$ with a swath of scatterers representing actual ground-range resolution by including only those scatterers contained within the resolution-cell.

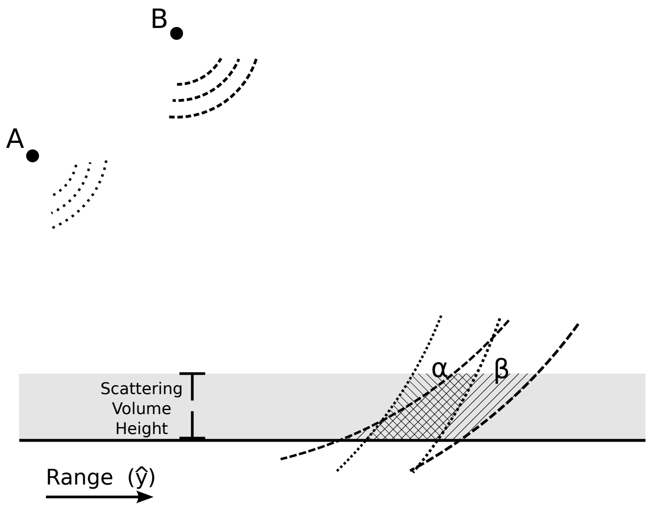

Figure 4.10: Diagram illustrating volume scattering. The gray area contains a volume of scatterers. As seen by antennas A and B, the volumes α and β contain common scatterers and both also contain scatterers not included by the other. Compare to Fig. 4.8.

to complete decorrelation. While only a single example using this ground-range resolution is provided here, the behavior is similar for other cases.

4.3.3 Volumetric Scattering

The analysis of the previous subsections is based on the assumption of a scattering surface (i.e., two-dimensional topological manifold). By introducing distributed displacement of height within the same cell, volumetric scattering results. Each "pixel" effectively becomes a voxel representing the scattered signal from a three-dimensional volume. This is illustrated by Fig. 4.10. The gray area in the figure represents a volume of scatterers.

Volumetric scattering is included by distributing the scatterers uniformly in the vertical direction (as well as horizontally), where the volume height is a multiple of the range resolution of the cell. Multipath effects among the scatterers is ignored (i.e, this analysis assumes the first Born approximation). Figure 4.11(a) shows an example of the case where the height of the cell is equal to the length of the cell in slant-range. In this case, the correlation is similar to that of the flat surface in Figure 4.9 for incidence angles corresponding to the "main lobe."

As the volume height of the scatterers is increased beyond the length of the cell in slant-range, decorrelation begins to occur. At a height of two times the slant-range length,

(a) 20° Azimuth Beamwidth

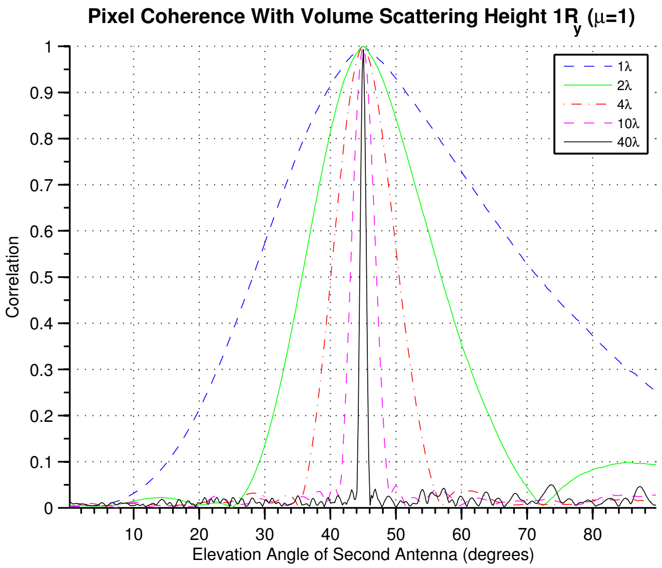

(b) 20° Azimuth Beamwidth

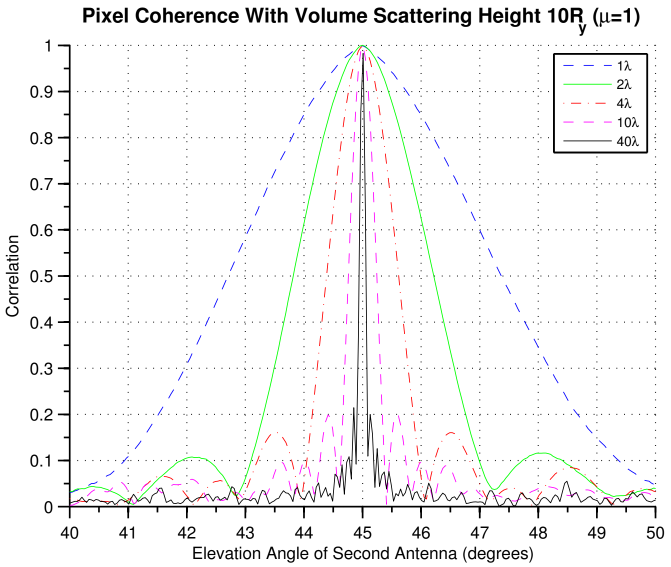

Figure 4.11: Pixel correlation with volumetric scattering-cells. In (a) the volumetric height is equal to the length of the cell in slant-range. In (b) the volumetric height is 10 times the length of the cell in slant-range. Note the narrowed horizontal axis in (b).

the decorrelation is increased slightly. However, at ten times the cell length in slant-range, decorrelation occurs rapidly. Figure 4.11(b) shows curves of this case. The correlation width is dramatically reduced and is only a few degrees wide even at fine resolutions. Thus we see that volumetric scattering significantly affects geometric correlation.

4.4 Discussion

I now compare my results to those found in literature. Figure 4.12 provides a comparison of correlation models using antennas in a geometric configuration corresponding to $\mu = 1$ and a slant-range resolution of 4λ. Four models from literature are shown. In the figure they are represented by: line 1 is Gatelli/et. al. [61], line 2 is Zebker/Villasenor [60], line 3 is Rodriguez/Martin [59], and line 4 is Li/Goldstein [58]. Though not visible in the figures, at 30° incidence angle, line 2 is identical to line 3; at 45° incidence angle line 2 is identical to line 4. Curves are also shown representing the analytic solution (line 5) and the numeric solution (line 6).

Note that for the analytic plots of Section 4.3.1, *ground-range resolution* is used, whereas this figure shows the analytic result converted to *slant-range resolution* via Eq. 4.19. In this way, the analytic results may be directly compared to the numeric models and the models from literature.

The models from literature are linear functions of incidence angle. As mentioned previously, this is a result of the assumptions made in modeling the correlation. These results show that geometric correlation has more of a “lobe-like” shape when a rect response function is used. This difference is most pronounced in the near coincident separation angles, where the correlation rolls off slowly before achieving a more linear descent. The sinc response is still rounded at the peak but has a more linear descent, though it rolls off at higher incidence angles. My analysis also shows that at higher incidence angles the correlation main lobe width is wider than that predicted by the other models.

In Fig. 4.13 the 80% correlation width is shown as a function of incidence angle. The model numbers are the same as those above in Fig. 4.12. The numeric solution is not shown as it is nearly identical to the analytic. The cusps on the right of the plots are caused when the

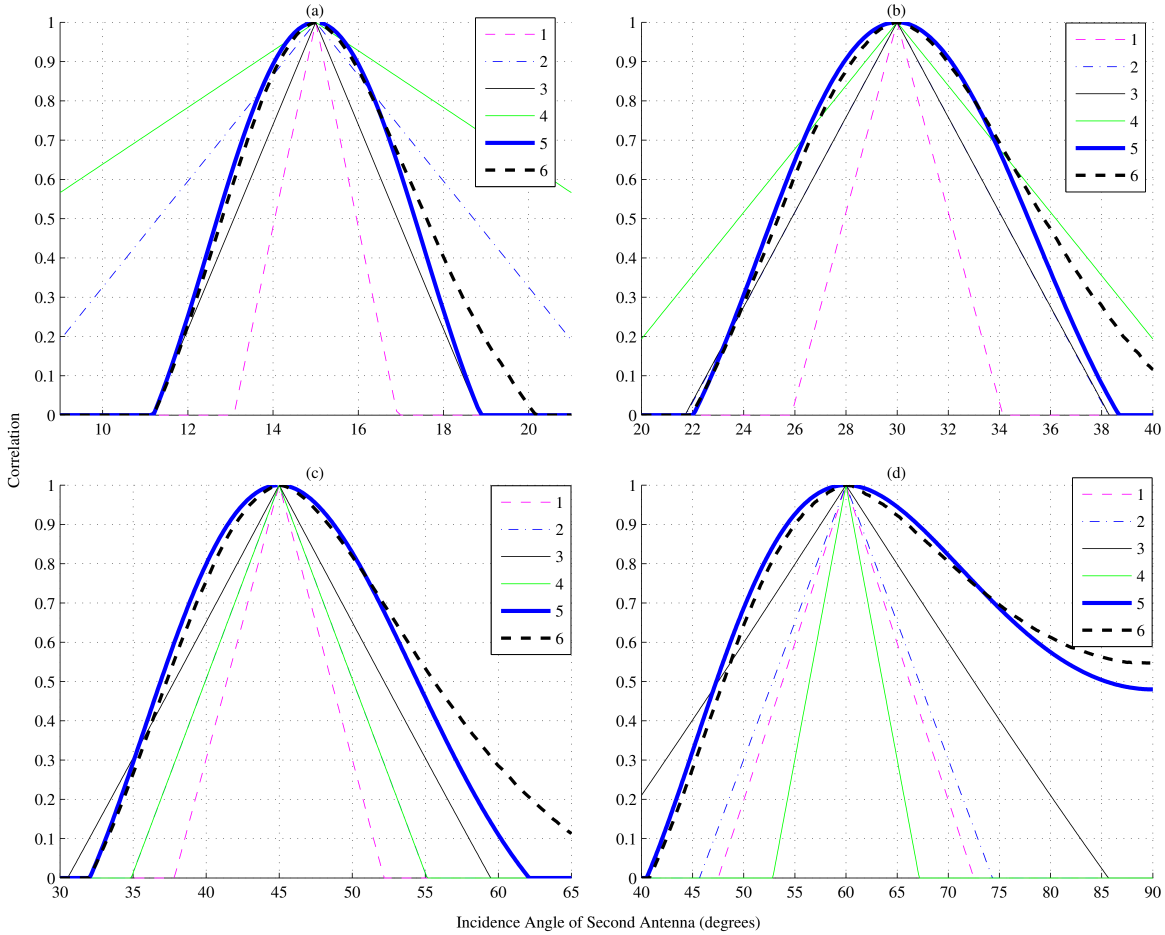

Figure 4.12: Comparison of pixel correlation for antennas (cases $\mu = 1$) using various models with a slant-range resolution of 4λ. Reference incidence angles by panel are (a) $15°$, (b) $30°$, (c) $45°$, and (d) $60°$. Model numbers are 1. Gatelli/et. al. [61], 2. Zebker/Villasenor [60], 3. Rodriguez/Martin [59], 4. Li/Goldstein [58], 5. analytic solution, and 6. numeric solution.

right-hand side of the correlation lobe hits $90°$ and thus cannot increase any farther. Notice that all but one of the models from literature become unstable at high incidence angles.

Note that there are several assumptions and limitations of this analysis. First, both models presented here and those found in literature are performed under the assumption that resolution-cells are made up of isotropic scatterers. While no scatter is truly isotropic, this assumption is commonly used for distributed targets. If, however, a resolution-cell is dominated by anisotropic scattering (e.g. man-made targets) then the correlation plots narrow according to the radiation beam-pattern created by the distribution of dominant scatterers within the cell.

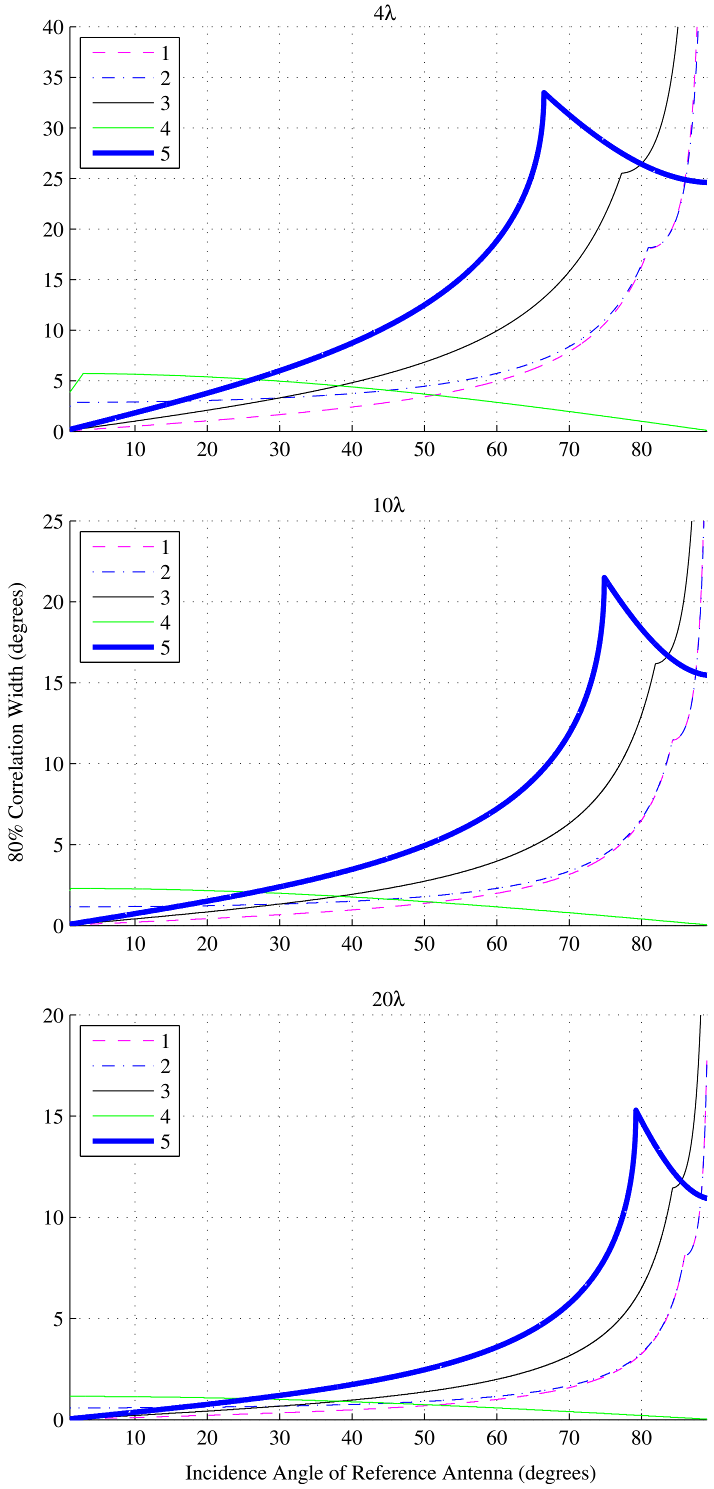

Figure 4.13: Comparison of 80% correlation width for antennas (cases $\mu = 1$) using various models. Slant-range resolutions are 4λ, 10λ, and 20λ. Model numbers are 1. Gatelli/et. al. [61], 2. Zebker/Villasenor [60], 3. Rodriguez/Martin [59], 4. Li/Goldstein [58], 5. analytic solution.

Second, there is no ground-slope parameter used in the analysis. However, because the analysis is performed using zero slope, an arbitrary slope can be added trivially by altering the relative incidence angle to the sloped surface.

Finally, this coherence analysis considers only geometric and volume decorrelation. It does not represent temporal decorrelation nor decorrelation due to noise. Use of a MIMO array usually implies concurrent imaging, and thus no temporal decorrelation. Decorrelation due to noise is well understood and typically represented as [60]

$$\rho = \rho_0 \frac{1}{1 + \mathrm{SNR}^{-1}}, \tag{4.20}$$

where ρ_0 is the correlation due to all non-noise factors and ρ is the total correlation.

4.4.1 Results

MIMO radar techniques may be categorized into two groups: collocated (or coherent) and distributed (or statistical). The baseline angle between each element of the MIMO array determines which group a particular geometric configuration falls into. Certain applications require a lower level of correlation in order to obtain independent looks. On the other hand, having highly correlated signals is necessary if coherent processing is desirable.

In order to provide a physical sense of how correlated various geometries are, the results of my analysis and several example geometries are given with the resulting effect on correlation. The example geometries are presented in Table 4.2. The first column shows the geometric configuration: slant-range resolution $R_{y,\mathrm{slant}}$, and reference incidence angle. The final three columns show the horizontal displacement required to reduce correlation to 75% for the stated platform altitudes. The horizontal baseline separation is given by

$$B = h \left(\tan\theta_1 - \tan\theta_2 \right), \tag{4.21}$$

where B is the horizontal baseline, h is the height above ground, θ_1 is the reference incidence angle, and θ_2 is the incidence angle resulting in the given level of decorrelation. This baseline represents a possible maximum separation for the collocated case, and a possible minimum for

Table 4.2: Horizontal Displacement for 75% Correlation (m)

Geometry (resolution, incidence angle, volume height)	100 m Height	1000 m Height	10,000 m Height
4λ, $45°$, flat	16.8	167.6	1675.7
10λ, $45°$, flat	7.2	72.4	723.7
20λ, $45°$, flat	3.8	37.7	376.8
10λ, $30°$, flat	2.9	29.3	293.0
10λ, $60°$, flat	23.4	234.0	2340.0
10λ, $45°$, $1R_y$	4.6	46.1	460.5
10λ, $45°$, $2R_y$	2.6	25.5	255.0
10λ, $45°$, $10R_y$	0.6	5.6	55.7

the distributed case. Note that this is the theoretical maximum baseline required to achieve a certain level of decorrelation. As mentioned earlier, other sources may lead to the same level of decorrelation at shorter baselines.

If all MIMO transmitters and receivers are required to be located on the same platform, these results suggest that most SAR imaging scenarios result in highly correlated signals. For the spaceborne case, this is all but guaranteed. For most airborne cases, signals are still highly correlated when produced from the same platform. As most of the traditional multi-channel SAR imaging has been performed from the same platform, the highly correlated nature of the multiple signals implies that MIMO SAR research should focus on the highly correlated MIMO regime. However, there are several exceptions to this.

As seen previously, if the radar system has very coarse range resolution then decorrelation occurs rapidly with antenna separation. The majority of modern SAR systems have a range resolution that is no coarser than 20 times the wavelength. Higher levels of decorrelation may be achieved via coarser resolutions, although degrading image resolution is not generally a desirable effect.

When the ground clutter contains significant volume scattering, decorrelation increases. Even fine-resolution systems at higher altitudes are very sensitive to changes in incidence angle when significant volumetric scattering is present. This suggests that MIMO SAR may provide advantages in foliage penetration and highly urbanized areas.

As altitude decreases, a given horizontal displacement corresponds to a wider change in incidence angle. Thus, if a platform is able to fly at low altitudes then the correlation baseline decreases. For typical range resolutions, this means an altitude somewhere in the vicinity of hundreds of meters or lower. This may not be feasible for manned aircraft but perhaps is more so for unmanned aerial vehicles (UAVs).

If a coordinated group of platforms is used (which is historically atypical of SAR), the bi-static baseline may be increased, which can provide increased levels of decorrelation. This may become more viable with smaller, low-cost SARs aboard UAVs.

4.4.2 Conclusion

In this chapter, the geometric decorrelation for multi-static SAR is derived for several classes of imaging geometries. This includes both an analytic result assuming fixed scattering-cell sizes as well as a numeric result for scattering-cells with size as a function of incidence angle. These developments are compared to previous models of geometric decorrelation, with the result that pixels formed in the ground-plane show lower levels of geometric decorrelation for the same imaging geometry.

Using these results, it is possible to determine when a group of multi-static signals may be considered correlated enough to perform coherent processing, or when they are decorrelated enough to perform statistical processing. These results imply that most single-platform MIMO SAR systems would operate in the coherent MIMO regime. To operate in the decorrelated regime, antennas must be more widely separated.

Chapter 5

Backprojection Interferometry

5.1 Introduction

Interferometry is a class of techniques that uses superimposed waves to derive information about the waves. In synthetic aperture radar (SAR), interferometry may be divided into two categories: along-track interferometry and cross-track interferometry [65]. Along-track interferometry uses multiple receive antennas separated in the along-track dimension in order to extract information about target motion in the imaged scene. Cross-track interferometry utilizes multiple receive antennas separated in the cross-track dimension (i.e., elevation and/or ground-range) in order to obtain the height of the imaged terrain [5]. Cross-track interferometry is exercised in the generation of digital elevation maps (DEMs). This chapter examines cross-track interferometry and from this point refers to it simply as *interferometry*.

Interferometric radars were first used in the remote sensing of Venus and the Moon to separate the received signals from the northern and southern hemispheres of the celestial bodies [66, 67]. The first interferometric airborne SAR was developed by the Goodyear Aerospace Corporation for the United States Air Force Charting and Geodetic Squadron [68]. Later, the principles of interferometric SAR were analyzed in detail at Jet Propulsion Laboratory (JPL) [58, 59, 60, 62, 69].

Traditional SAR interferometry uses coherent images formed by frequency domain methods to produce a height map of the imaged surface. Because frequency domain methods are used, traditional interferometry is subject to two implicit assumptions: (1) imaging is in the slant-plane, and (2) the interferometric phase difference between the images is due to the propagation path length difference. The time-domain backprojection algorithm, however, produces images in the ground-plane and the resulting pixels have a phase equal to the difference between the expected propagation path length and the actual length. Thus, backprojected interferometric phase is a difference of differences (this point is clarified later). Because of the distinction in pixel phase of backprojection versus frequency domain algorithms, a new, backprojection oriented interferometric method is required.

This chapter describes SAR interferometry for the time-domain backprojection algorithm. The chapter seeks to explore the difference between traditional interferometry and backprojection interferometry, and the strengths and weaknesses of both. Backprojection interferometry is derived, followed by an analysis of its characteristics and a comparison to traditional interferometry.

The chapter is organized as follows. Section 5.2 derives backprojection interferometry for squint-less, side-looking SAR. Using these results, Section 5.3 compares the input parameter sensitivity of traditional interferometry to backprojection interferometry. Specific performance characteristics of backprojection interferometry are given in Section 5.4. Finally, Section 5.5 concludes with analysis of the results and recommendation of when backprojection interferometry is advantageous.

5.2 Backprojection Interferometry Derivation

For brevity's sake, a derivation of traditional interferometry is not given here, but an excellent derivation is given in [62]. The following derivation of time-domain backprojection interferometry assumes a side-looking, squint-less geometry with a narrow-beam antenna as defined in Chapter 3. As shown in that chapter, under these assumptions the phase of each backprojected pixel can be estimated as the residual phase at the point of closest approach. This makes a derivation of backprojection interferometry tractable.

The phase of a received coherent radar signal lends insight into the length of the propagation path the signal traveled. Given a monostatic antenna A, the phase is a 2π wrapped equivalent of the distance times the carrier wavenumber ($k = 2\pi/\lambda$),

$$\phi = 2kr_a \bmod 2\pi, \tag{5.1}$$

where r_a is the one-way range from the antenna to a given target. Unfortunately, because of the phase wrapping, the range-resolution of the radar is typically not fine enough to unambiguously recover the exact distance the wave traveled. However, through the use of two receive antennas A and B, the *difference* in path length $(r_a - r_b)$ between the two can be determined with great precision. Interferometry makes use of this fact in order to obtain the height of a pixel's scattering-cell.

The backprojection interferometric phase difference $\Delta\Phi$ of two backprojected pixels (registered to be the same physical location) is

$$\Delta\Phi = k\left(\Delta r_a - \Delta r_b\right), \tag{5.2}$$

where k is the radar carrier wavenumber, and Δr is the backprojection residual range described in Chapter 3, with the subscripts a and b referring to the *receive* antennas A and B, respectively. The quantity $(\Delta r_a - \Delta r_b)$ is the "difference of differences" mentioned earlier. Note that any contribution due to the transmit antenna is explicitly neglected so long as the receive antennas share a common transmitter. If the scattering-cell can be assumed to have no receive antenna-specific polarimetric phase component then the propagation phase from the transmitter to the scattering-cell is common to both receive paths and is removed by the interferometric difference.

As stated in Chapter 3, backprojection removes the known phase component to the scattering-cell, leaving a residual phase due to the unknown exact range to the phase-center of the scattering-cell. However, because the receive antennas are not collocated they do not observe the same scattering-cell. Fig. 5.1(a) illustrates this in an exaggerated manner. Vectors $\mathbf{A}$ and $\mathbf{B}$ are the receive antenna locations, $\mathbf{C}$ is the estimated scattering-cell phase-center (for the pixel of interest), and $\mathbf{D}$ and $\mathbf{E}$ are the actual phase-centers of the scattering-cell as observed from antennas A and B, respectively. The dashed concentric arcs show the areas that

(a) Illustration of scattering-cells with non-overlapping areas

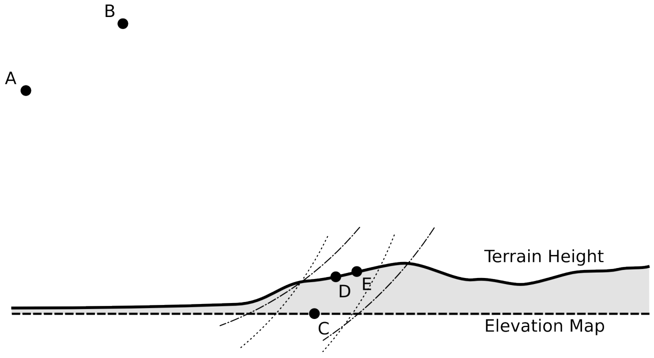

(b) Geometry of backprojection interferometry

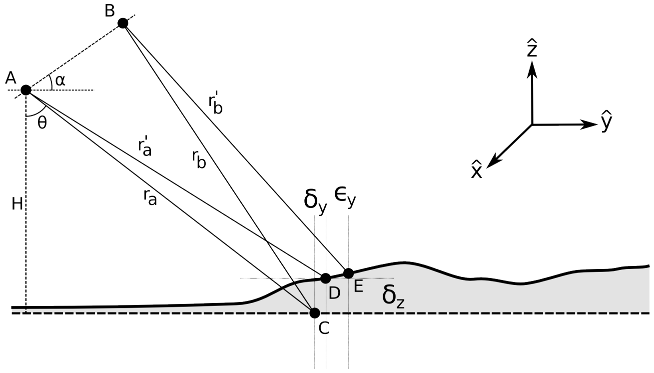

Figure 5.1: Exaggerated illustration of scattering-cell phase-center differences in interferometry. Receive antennas are located at points **A** and **B**. Point **C** is the estimated phase-center of the scattering-cell given coarse knowledge of the topography (e.g., a digital elevation map). Points **D** and **E** are the actual phase-centers of the scattering-cell observed by antennas at **A** and **B**, respectively. Notice that because the two antennas are not collocated, they observe a slightly different set of scatterers within the resolution cell.

fall within a given slant-range bin (i.e., the pixel of interest). Because the two receive antennas observe the ground-plane from slightly different angles, they do not necessarily simultaneously illuminate the same set of scatterers. This can cause the phase-center of the scattering-cell to differ as observed from each antenna. The level to which they differ is a measure of geometric decorrelation examined in the previous chapter.

Given that the two antennas may observe slightly different locations for the phase-center of the scattering-cell, this chapter proceeds with a derivation of the interferometric height resulting from backprojected residual phase. The interferometer geometry is given in Fig. 5.1(b). Here, r is the estimated range from the receive antenna to the scattering-cell phase-center and $r^{'}$ is the actual range to the scattering-cell phase-center. The three-dimensional displacement vector $\boldsymbol{\delta}$ $(\delta_\mathrm{x}, \delta_\mathrm{y}, \delta_\mathrm{z})$ is the offset from $\mathbf{C}$ to $\mathbf{D}$ and vector $\boldsymbol{\epsilon}$ is the displacement from $\mathbf{D}$ to $\mathbf{E}$. Hence,

$$\mathbf{D} = \mathbf{C} - \boldsymbol{\delta}, \tag{5.3}$$

$$\mathbf{E} = \mathbf{C} - (\boldsymbol{\delta} + \boldsymbol{\epsilon})\,. \tag{5.4}$$

In this derivation, $\boldsymbol{\delta}$ is the interferometric displacement from which height information is obtained. Although not used here, θ is the incidence angle to the scattering-cell and α is the interferometric angular baseline. These variables become important later in this section to parameterize traditional interferometry.

The backprojected residual ranges Δr are defined as

$$\Delta r_a = r_a - r_a^{'}, \tag{5.5}$$

$$\Delta r_b = r_b - r_b^{'}. \tag{5.6}$$

These ranges are given by the distances to the various points:

$$r_a = \|\mathbf{C} - \mathbf{A}\| = \sqrt{(x_a - x_c)^2 + (y_a - y_c)^2 + (z_a - z_c)^2}\,, \tag{5.7}$$

$$r_a^{'} = \|\mathbf{D} - \mathbf{A}\| = \sqrt{(x_a - x_d)^2 + (y_a - y_d)^2 + (z_a - z_d)^2}\,, \tag{5.8}$$

$$r_b = \|\mathbf{C} - \mathbf{B}\| = \sqrt{(x_b - x_c)^2 + (y_b - y_c)^2 + (z_b - z_c)^2}\,, \tag{5.9}$$

$$r_b^{'} = \|\mathbf{E} - \mathbf{B}\| = \sqrt{(x_b - x_e)^2 + (y_b - y_e)^2 + (z_b - z_e)^2}\,, \tag{5.10}$$

with x in along-track, y in ground-range, and z in elevation. The actual range from receive antenna A to the phase-center of the scatter-cell is

$$
\begin{aligned}
r_a^{'} &= \sqrt{(x_a - x_c - \delta_x)^2 + (y_a - y_c - \delta_y)^2 + (z_a - z_c - \delta_z)^2} \qquad (5.11)\\
&= \Big((x_a - x_c)^2 + (y_a - y_c)^2 + (z_a - z_c)^2 - \\
&\qquad \delta_x \left(2\left(x_a - x_c\right) - \delta_x\right) - \delta_y \left(2\left(y_a - y_c\right) - \delta_y\right) - \delta_z \left(2\left(z_a - z_c\right) - \delta_z\right) \Big)^{1/2} \\
&= \sqrt{r_a^2 - \delta_x \left(2\left(x_a - x_c\right) - \delta_x\right) - \delta_y \left(2\left(y_a - y_c\right) - \delta_y\right) - \delta_z \left(2\left(z_a - z_c\right) - \delta_z\right)}\,. \qquad (5.12)
\end{aligned}
$$

Using the first-order Taylor series approximation for the square root $\sqrt{m^2 + n} \approx m + n/(2m)$, this becomes

$$
r_a^{'} \approx r_a - \frac{\delta_x \left(2\left(x_a - x_c\right) + \delta_x\right) + \delta_y \left(2\left(y_a - y_c\right) + \delta_y\right) + \delta_z \left(2\left(z_a - z_c\right) + \delta_z\right)}{2\, r_a}. \qquad (5.13)
$$

The first-order Taylor series approximation is highly accurate near the point of closest approach, therefore it works well for a non-squinted geometry (see Section 3.3). For a squinted geometry this approximation is inaccurate. However, squinted geometry is beyond the scope of this derivation since there is no closed form solution for the squinted residual phase.

As the range from the receive antennas to the scattering-cell is presumed to be much larger than the phase-center displacement, Eq. 5.13 can be reduced further to

$$
r_a^{'} \approx r_a - \frac{\delta_x \left(x_a - x_c\right) + \delta_y \left(y_a - y_c\right) + \delta_z \left(z_a - z_c\right)}{r_a}. \qquad (5.14)
$$

Likewise, for antenna B,

$$
r_b^{'} \approx r_b - \frac{\left(\delta_x + \epsilon_x\right)\left(x_b - x_c\right) + \left(\delta_y + \epsilon_y\right)\left(y_b - y_c\right) + \left(\delta_z + \epsilon_z\right)\left(z_b - z_c\right)}{r_b}. \qquad (5.15)
$$

Substituting these into the range residuals yields

$$\begin{aligned}\Delta r_a &= r_a - r_a^{'} \\ &= \frac{\delta_x\left(x_a - x_c\right) + \delta_y\left(y_a - y_c\right) + \delta_z\left(z_a - z_c\right)}{r_a},\end{aligned} \tag{5.16}$$

$$\begin{aligned}\Delta r_b &= r_b - r_b^{'} \\ &= \frac{\left(\delta_x + \epsilon_x\right)\left(x_b - x_c\right) + \left(\delta_y + \epsilon_y\right)\left(y_b - y_c\right)}{r_b} + \\ &\quad \frac{\left(\delta_z + \epsilon_z\right)\left(z_b - z_c\right)}{r_b}.\end{aligned} \tag{5.17}$$

Unfortunately, this leads to an under-determined system of equations. Inserting Δr_a and Δr_b into Eq. 5.2 results in one equation with six unknowns (the $\boldsymbol{\delta}$ and $\boldsymbol{\epsilon}$ phase-center displacements). Under some simplifying assumptions this may be reduced to one unknown.

A key assumption in interferometry is that the pixels, as imaged from the two antennas, are highly correlated. In general, as discussed in Chapter 4, this requires that the baseline separation not be too great. The assumption that the pixel correlation is high requires that the scattering-cell phase-center be nearly the same when viewed from both receive antennas. In other words, the $\boldsymbol{\epsilon}$ terms are approximately zero. When $\boldsymbol{\epsilon} \approx 0$, the interferometric phase reduces to

$$\begin{aligned}\frac{\Delta\Phi}{k} &= \frac{\delta_x\left(x_a - x_c\right) + \delta_y\left(y_a - y_c\right) + \delta_z\left(z_a - z_c\right)}{r_a} - \frac{\delta_x\left(x_b - x_c\right) + \delta_y\left(y_b - y_c\right) + \delta_z\left(z_b - z_c\right)}{r_b} \\ &= \delta_x\left(\frac{x_a - x_c}{r_a} - \frac{x_b - x_c}{r_b}\right) + \delta_y\left(\frac{y_a - y_c}{r_a} - \frac{y_b - y_c}{r_b}\right) + \delta_z\left(\frac{z_a - z_c}{r_a} - \frac{z_b - z_c}{r_b}\right).\end{aligned} \tag{5.18}$$

Solving for the height displacement δ_z results in

$$\delta_z = \frac{\frac{\Delta\Phi}{k} - \delta_x\left(\frac{x_a-x_c}{r_a} - \frac{x_b-x_c}{r_b}\right) - \delta_y\left(\frac{y_a-y_c}{r_a} - \frac{y_b-y_c}{r_b}\right)}{\left(\frac{z_a-z_c}{r_a} - \frac{z_b-z_c}{r_b}\right)} \tag{5.19}$$

$$\begin{aligned} &= \frac{\Delta\Phi\, r_a\, r_b}{k\left(r_b\left(z_a-z_c\right) - r_a\left(z_b-z_c\right)\right)} - \\ &\quad \delta_x \frac{r_b\left(x_a-x_c\right) - r_a\left(x_b-x_c\right)}{r_b\left(z_a-z_c\right) - r_a\left(z_b-z_c\right)} - \\ &\quad \delta_y \frac{r_b\left(y_a-y_c\right) - r_a\left(y_b-y_c\right)}{r_b\left(z_a-z_c\right) - r_a\left(z_b-z_c\right)}, \end{aligned} \tag{5.20}$$

which is one equation with three unknowns (δ_x, δ_y, and δ_z).

For now, assume that $\delta_x \approx 0$ and $\delta_y \approx 0$. The consequences of this assumption are discussed in Section 5.4.2. With this assumption, the remaining degrees of freedom vanish and the estimate of height offset for the scattering-cell is

$$\boxed{\widetilde{\delta_z} = \frac{\Delta\Phi\, r_a\, r_b}{k\big(r_b\left(z_a-z_c\right) - r_a\left(z_b-z_c\right)\big)}}\,. \tag{5.21}$$

Note that in this case the height displacement may be computed without the use of trigonometric functions. However, recognizing that with incidence angle θ, $r_a \cos\theta_a = (z_a - z_c)$ and $r_b \cos\theta_b = (z_b - z_c)$, the height estimate may also be written as

$$\widetilde{\delta_z} = \frac{\Delta\Phi\, r_a\, r_b}{k\left(r_b\, r_a \cos\theta_a - r_a\, r_b \cos\theta_b\right)} \tag{5.22}$$

$$= \frac{\Delta\Phi}{k\left(\cos\theta_a - \cos\theta_b\right)}. \tag{5.23}$$

Recall that the interferometer geometry is shown in Fig. 5.1(b).

The traditional interferometric result for single-pass, fixed-baseline SAR is [62, 70]

$$\Phi = kB\sin\left(\theta - \alpha\right), \tag{5.24}$$

$$\theta = \arccos\left(\frac{H - \delta_z}{r}\right), \tag{5.25}$$

where Φ is the traditional interferometric phase difference, B is the baseline distance between the receive antennas, α is the angular difference between the antennas with respect to the horizontal plane, and H is the interferometer height above the reference plane. This leads to the height estimate

$$\boxed{\begin{aligned}\widetilde{\delta}_z &= H - r\cos\theta \\ &= H - r\cos\left(\alpha + \arcsin\frac{\Phi}{kB}\right)\end{aligned}}\ . \tag{5.26}$$

A cursory examination of Eqs. 5.21 and 5.26 reveals that the interferometric height estimate from backprojection is linear with phase, while the traditional method is quite non-linear. Other fundamental differences exist as well. The following section closely compares both interferometric methods and presents their respective sensitivities.

5.3 Sensitivity Comparison

This section examines the height estimate sensitivity of backprojection and traditional interferometry. Assaying the sensitivity to the input parameters of the estimate provides a basis for comparison of the two methods. First, the range bias in traditional interferometry is briefly discussed. Next, the parameter sensitivity of both methods is derived. Finally, this section concludes with an examination of baseline and phase errors, which are of specific concern when using interferometry.

5.3.1 Range Bias

Traditional interferometry is inaccurate due to a range bias indroduced in the derivation. As part of the derivation, the following approximation is made:

$$r_a - r_b \approx B\sin(\theta - \alpha)\,. \tag{5.27}$$

While this is a good approximation for $B \ll r_a$, it nevertheless has a range bias error specific to a given interferometric geometry (i.e, a constant offset in the estimate that is a function of baseline angle, baseline length, and range-to-target). Figure 5.2 shows this range bias for various baseline angles across all incidence angles. Even though the maximum range bias is only 5×10^{-4} times the interferometric baseline length, the bias error may become significant

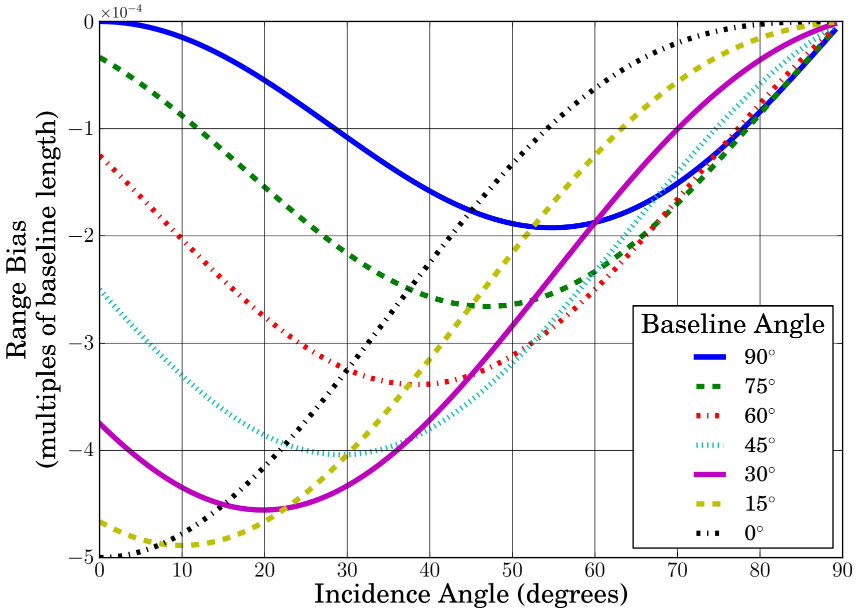

Figure 5.2: Slant-range bias in the range difference $r_a - r_b$ that exists in traditional interferometry. The range bias leads to a height estimate bias. Each curve shows a given baseline angle. The vertical axis is in multiples of a 10 m baseline length.

when height is estimated. For example, with a 10 m baseline length, a 45° baseline angle, and a 45° incidence angle, the approximation in Eq. 5.27 has a range bias that leads to a 2.5 m error in the interferometry height estimate. The bias is removed by changing Eq. 5.26 to

$$\widetilde{\delta}_z = H - r\cos\left[\alpha + \arcsin\left(\frac{\Phi/k - r_{\text{bias}}}{B}\right)\right], \tag{5.28}$$

where

$$r_{\text{bias}} = (r_a - r_b) - B\sin(\theta - \alpha)\,. \tag{5.29}$$

Throughout the rest of this chapter, the height estimate for conventional interferometry has been corrected to Eq. 5.28.

5.3.2 Sensitivity Derivation

The sensitivity of the interferometry method to its parameters is found by taking the partial derivative of the height estimate $\widetilde{\delta}_z$ with respect to each variable of interest. For simplicity of notation, the $\sim$ on $\widetilde{\delta}_z$ is discarded below. For traditional SAR interferometry, computing the partial of Eq. 5.26 results in

$$\begin{aligned}\frac{\partial \delta_z}{\partial \Phi} &= \frac{r \sin \theta}{kB\sqrt{1-\left(\frac{\Phi}{kB}\right)^2}} \\ &= \frac{r \sin \theta}{kB \cos\left(\theta - \alpha\right)},\end{aligned} \tag{5.30}$$

$$\begin{aligned}\frac{\partial \delta_z}{\partial B} &= -\frac{\Phi r \sin\left(\alpha + \arcsin \frac{\Phi}{kB}\right)}{kB^2\sqrt{1-\left(\frac{\Phi}{kB}\right)^2}} \\ &= -\frac{r}{B} \tan\left(\theta - \alpha\right) \sin \theta,\end{aligned} \tag{5.31}$$

$$\begin{aligned}\frac{\partial \delta_z}{\partial \alpha} &= r \sin\left(\alpha + \arcsin \frac{\Phi}{kB}\right) \\ &= r \sin \theta,\end{aligned} \tag{5.32}$$

$$\frac{\partial \delta_z}{\partial \theta} = r \sin \theta, \tag{5.33}$$

$$\frac{\partial \delta_z}{\partial r} = -\cos \theta, \tag{5.34}$$

through the use of the formulas

$$\frac{\mathrm{d}}{\mathrm{d}x} \arcsin x = \frac{1}{\sqrt{(1-x^2)}}, \tag{5.35}$$

$$\begin{aligned}\sqrt{1-\left(\frac{\Phi}{kB}\right)^2} &= \sqrt{1-\left(\frac{kB \sin\left(\theta-\alpha\right)}{kB}\right)^2} \\ &= \cos\left(\theta - \alpha\right),\end{aligned} \tag{5.36}$$

$$\begin{aligned}\arcsin\frac{\Phi}{kB} &= \arcsin\frac{kB\sin(\theta-\alpha)}{kB} \\ &= \theta-\alpha, && (5.37) \\ \frac{\Phi}{kB\sqrt{1-\left(\frac{\Phi}{kB}\right)^2}} &= \tan(\theta-\alpha), && (5.38) \\ \sin\left(\alpha+\arcsin\left(\frac{\Phi}{kB}\right)\right) &= \sin\theta. && (5.39)\end{aligned}$$

Notice that the height sensitivity to baseline angle $\frac{\partial\delta_z}{\partial\alpha}$ and incidence angle $\frac{\partial\delta_z}{\partial\theta}$ is identical.

In order to compare the traditional sensitivity results to those of backprojection, Eq. 5.23 must be rewritten in terms of baseline length and angle. From Fig. 5.1 on page 100, the paths from antennas to cell-center **C** and to each other form a triangle. Using the law of sines,

$$\begin{aligned}\frac{r_a}{\sin\left(\frac{\pi}{2}-\alpha+\theta_b\right)} &= \frac{B}{\sin(\theta_a-\theta_b)}, && (5.40) \\ \sin(\theta_a-\theta_b) &= \frac{B}{r_a}\cos(\theta_b-\alpha), \\ \theta_a &= \theta_b+\arcsin\left(\frac{B}{r_a}\cos(\theta_b-\alpha)\right). && (5.41)\end{aligned}$$

Let γ be the incidence angle difference between the two antennas, i.e.,

$$\begin{aligned}\gamma &= \theta_a-\theta_b && (5.42) \\ &= \arcsin\left(\frac{B}{r_a}\cos(\theta_b-\alpha)\right), && (5.43)\end{aligned}$$

then Eq. 5.23 may be rewritten as

$$\delta_z = \frac{\Delta\Phi}{k\left[\cos(\theta_b+\gamma)-\cos\theta_b\right]}. \tag{5.44}$$

The backprojection sensitivities are found by taking the partial derivatives of Eq. 5.44 with respect to each variable:

$$\frac{\partial\delta_z}{\partial\Delta\Phi} = \frac{1}{k(\cos\theta_a-\cos\theta_b)}, \tag{5.45}$$

$$\begin{aligned}\frac{\partial \delta_z}{\partial B} &= \frac{\Delta\Phi \, \sin\left(\theta_b + \gamma\right)}{k\left(\cos\left(\theta_b + \gamma\right) - \cos\theta_b\right)^2} \, \frac{\cos\left(\theta_b - \alpha\right)}{r_a \, \sqrt{1 - \sin^2\gamma}} \\ &= \frac{\delta_z k \left(\cos\theta_a - \cos\theta_b\right)\sin\theta_a \cos\left(\theta_b - \alpha\right)}{k \, r_a \left(\cos\theta_a - \cos\theta_b\right)^2 \cos\gamma} \\ &= \delta_z \frac{\sin\theta_a \cos\left(\theta_b - \alpha\right)}{r_a \cos\gamma \left(\cos\theta_a - \cos\theta_b\right)}, \end{aligned} \tag{5.46}$$

$$\begin{aligned}\frac{\partial \delta_z}{\partial \alpha} &= \frac{\Delta\Phi \, \sin\left(\theta_b + \gamma\right)}{k\left(\cos\left(\theta_b + \gamma\right) - \cos\theta_b\right)^2} \, \frac{B \sin\left(\theta_b - \alpha\right)}{r_a \sqrt{1 - \sin^2\gamma}} \\ &= \delta_z \frac{B \sin\theta_a \sin\left(\theta_b - \alpha\right)}{r_a \cos\gamma \left(\cos\theta_a - \cos\theta_b\right)}, \end{aligned} \tag{5.47}$$

$$\begin{aligned}\frac{\partial \delta_z}{\partial r_a} &= -\frac{\Delta\Phi \, \sin\left(\theta_b + \gamma\right)}{k\left(\cos\left(\theta_b + \gamma\right) - \cos\theta_b\right)^2} \, \frac{B \cos\left(\theta_b - \alpha\right)}{r_a^2 \sqrt{1 - \sin^2\gamma}} \\ &= -\delta_z \frac{B \sin\theta_a \cos\left(\theta_b - \alpha\right)}{r_a^2 \cos\gamma \left(\cos\theta_a - \cos\theta_b\right)}, \end{aligned} \tag{5.48}$$

$$\begin{aligned}\frac{\partial \delta_z}{\partial \theta_b} &= -\frac{\Delta\Phi \left(\sin\left(\theta_b + \gamma\right)\left(\frac{B \sin(\theta_b - \alpha)}{r_a \, \sqrt{1 - \sin^2\gamma}} - 1\right) + \sin\theta_b\right)}{k\left(\cos\left(\theta_b + \gamma\right) - \cos\theta_b\right)^2} \\ &= -\delta_z \frac{\left(\frac{B \sin(\theta_b - \alpha)}{r_a \cos\gamma} - 1\right)\sin\theta_a + \sin\theta_b}{\cos\theta_a - \cos\theta_b}. \end{aligned} \tag{5.49}$$

We observe that the sensitivity equations for backprojection are more complicated than the traditional approach.

The sensitivities of both methods are given side-by-side in Table 5.1.

5.3.3 Sensitivity Analysis

The backprojection sensitivity equations are more complicated than those of the traditional method which makes a direct comparison of the sensitivities difficult. However, two observations may be made in general: (1) In all but phase, backprojection sensitivity is directly proportional to target displacement. This implies that if the target displacement is small (i.e., the DEM is highly accurate), then backprojection sensitivity to these parameters is likewise small. This is a critical insight as traditional interferometry is extremely sensitive to these (i.e., baseline length and angle). (2) In the cases where range appears in the sensitivity

Table 5.1: Interferometric Sensitivities

	Traditional	Backprojection
$\frac{\partial \delta_z}{\partial \Phi}$	$\frac{r \sin\theta}{kB\cos(\theta-\alpha)}$	-
$\frac{\partial \delta_z}{\partial \Delta\Phi}$	-	$\frac{1}{k(\cos\theta_a-\cos\theta_b)}$
$\frac{\partial \delta_z}{\partial B}$	$-\frac{r}{B}\tan(\theta-\alpha)\sin\theta$	$\delta_z \frac{\sin\theta_a\cos(\theta_b-\alpha)}{r_a\cos\gamma(\cos\theta_a-\cos\theta_b)}$
$\frac{\partial \delta_z}{\partial \alpha}$	$r\sin\theta$	$\delta_z \frac{B\sin\theta_a\sin(\theta_b-\alpha)}{r_a\cos\gamma(\cos\theta_a-\cos\theta_b)}$
$\frac{\partial \delta_z}{\partial r_a}$	$-\cos\theta$	$-\delta_z \frac{B\sin\theta_a\cos(\theta_b-\alpha)}{r_a^2\cos\gamma(\cos\theta_a-\cos\theta_b)}$
$\frac{\partial \delta_z}{\partial \theta_b}$	$r\sin\theta$	$-\delta_z \frac{\left(\frac{B\sin(\theta_b-\alpha)}{r_a\cos\gamma}-1\right)\sin\theta_a+\sin\theta_b}{\cos\theta_a-\cos\theta_b}$

equations, for traditional interferometry it always appears in the numerator and in backprojection it always appears in the denominator. Therefore, as range increases, the sensitivity of backprojection interferometry to the other parameters decreases.

For these two reasons, it is evident that backprojection is less sensitive than traditional interferometry to physical errors: baseline length, baseline angle, range-to-target, and incidence angle. However, backprojection is sensitive to phase errors. Because $\cos\theta_a - \cos\theta_b$ is very small in general, $\partial\delta_z/\partial\Delta\Phi$ is large. As shown later, for most imaging scenarios backprojection is more sensitive to phase errors than traditional interferometry, and indeed phase error is the primary limiting factor in the accuracy of backprojection height estimation.

A detailed comparison of sensitivities is somewhat tedious, but appears later in Sec. 5.6. For brevity, only the highlights and key observations are given here. The example figures referenced come from that section.

- *Sweet spots* are incidence angles that perform particularly well for a given method. The sweet spot for traditional interferometry lies in the baseline length sensitivity when the baseline angle matches the incidence angle. It comes from Eq. 5.31 as the term $\partial\delta_z/\partial B = 0$ when $\tan(\theta-\alpha) = 0 \implies \theta = \alpha$. An example of this appears later in Fig. 5.10(a) on page 130. For backprojection interferometry, the sweet spot lies in the baseline angle sensitivity itself. This comes from the term $\sin(\theta_b - \alpha)$ in Eq. 5.47, which implies that $\theta = \alpha$. An example of this is shown in Fig. 5.10(c).

- The sweet spot in incidence angle sensitivity for backprojection does not occur when the baseline angle equals the incidence angle, but rather a larger incidence angle [e.g., Fig. 5.10(d)] from Eq. 5.49 given by the non-linear equation

$$\theta_a = \arcsin\left[-\left(\frac{B\sin(\theta_b - \alpha)}{r_a\cos(\theta_a - \theta_b)} - 1\right)^{-1}\sin(\theta_b)\right]. \tag{5.50}$$

- The sensitivity of backprojection to the physical parameters (baseline length, baseline angle, range-to-target) is much lower, sometimes four or five orders of magnitude lower than traditional [e.g., Fig. 5.13(e) on page 133]. However, for typical SAR incidence angles, backprojection is about twice as sensitive to interferometric phase [e.g., Fig. 5.13(b)].

- Regarding height estimation error, traditional interferometry performs comparatively better at shallow incidence angles (near $0°$), and backprojection interferometry performs better at large incidence angles (near $90°$). See Fig. 5.12(f) as an example.

- Backprojection interferometry sees the biggest improvement in height estimate accuracy when the range is increased and when the height offset is small (i.e., the DEM is accurate). See Fig. 5.12(f) and 5.13(f) as examples. If the DEM is accurate, then backprojection provides a better estimate, sometimes by several orders of magnitude.

Errors in phase or baseline measurement severely affect interferometry performance, so they are discussed in more depth in the following subsections.

5.3.4 Baseline Error Comparison

The previous subsection summarized the individual sensitivity components of both interferometric methods to their input parameters. While analyzing the individual components provides insight, in order to gain understanding of how the components fit together, this section investigates the error in height estimate for both interferometric approaches. For purposes of performance comparison, this subsection specifically examines the effects of errors in the

(a) Baseline Angle Error: 0.0001 rad

(b) Baseline Angle Error: 0.001 rad

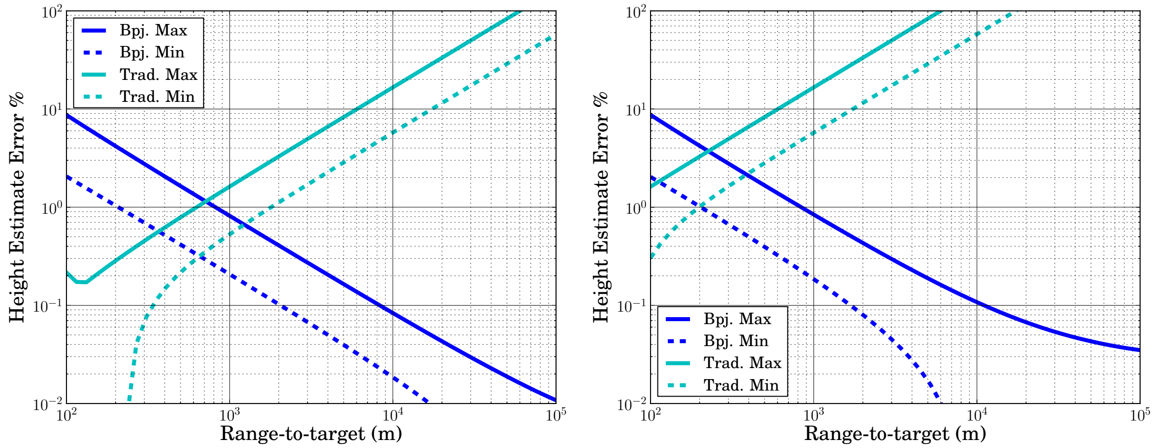

(c) Baseline Length Error: 1 mm

(d) Baseline Length Error: 1 cm

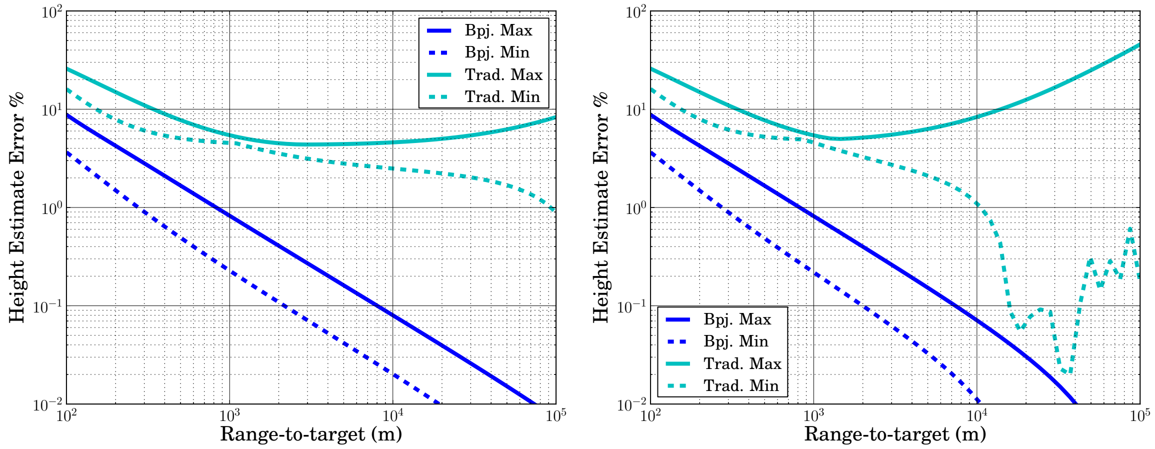

Figure 5.3: Comparison of the effects of baseline errors on the interferometric height estimate as a function of range-to-target. Plots (a) and (b) show the effect of angular baseline error with a baseline of length 1 m. Plots (c) and (d) show the effect of baseline length error with a baseline length of 100 m. The nominal baseline angle is $45°$. The maximum and minimum are taken across the range of incidence angles $30°$ to $60°$.

measurement of baseline length and baseline angle. It is seen that traditional interferometry is extremely sensitive to baseline errors.

Figure 5.3 gives the height estimation error for both interferometric methods as a function of range-to-target. Rather than examine one particular incidence angle, the minimum and maximum of each method is retained from $30°$ to $60°$. Showing only one incidence angle would disadvantage one of the methods if the incidence angle coincided with a given sweet spot. Showing a variety of incidence angles would result in a multiplicity of plots. In the figures, it may be assumed that the minimum curves represent the performance at the sweet spot of the method, and the maximum curves more closely represent the performance away from the sweet spot.

The model parameters are $\lambda = 3\,\mathrm{cm}$, baseline angle $\alpha = 45^\circ$, and a target displacement of 10 m from the DEM. Subfigures (a) and (b) illustrate the effects of error in the measurement of the interferometric baseline angle for a baseline of 1 m. The baseline angle error in (a) is 0.0001 rad and in (b) is 0.001 rad. This example is suggestive of a low-altitude platform where a combination of non-ideal motion and errors in attitude measurement lead to errors in the measurement of the baseline angle. For a small range-to-target, the traditional method has lower error than the backprojection method; however, the error increases as the range-to-target increases, and between 200-700 m backprojection begins to outperform it. If the baseline length is increased then backprojection surpasses the traditional method in performance even at smaller ranges. It is important to note that for conventional interferometry, if there is significant uncertainty in measurement of the baseline angle, then the sweet spot might go un-utilized and the performance would be closer to the maximum error than to the minimum error.

Subfigures (c) and (d) show the effects of error in measurement of the interferometric baseline length for a nominal baseline length of 100 m. This geometry is more suggestive of a high-altitude interferometer. In (c), the error in measurement of the baseline length is 1 mm and in (d) is 1 cm. Because of the large baseline, even at near ranges the maximum backprojection error is less than the traditional method's error. The maximum error in the traditional method decreases until an inflection point where it begins to grow large again. For a large range-to-target, the minimum goes to zero (i.e., no error) at the sweet-spot of $\alpha = \theta$. In the high altitude case, it may be realistic for most of the range swath to fall within this sweet-spot.

Notice that in all the cases, the error in backprojection height estimate decreases as the range-to-target increases. Notice also that in each case, the performance of backprojection is almost identical even though the performance of the traditional method varies widely. This reinforces the conclusion of the previous subsection that backprojection is less sensitive to errors in measurement of the interferometric baseline, while the opposite is true for the traditional method.

5.3.5 Phase-noise Comparison

This subsection compares how errors in the interferometric phase measurement affect both methods. It is somewhat difficult to do a direct comparison since traditional interferometry measures Φ, while backprojection interferometry measures $\Delta\Phi$. However, under certain assumptions a comparison may be made. If the phase error is due to zero-mean Gaussian distributed random noise, then with random variables X and Y,

$$X \sim \mathcal{N}\left(0,\, \sigma_X^2\right), \tag{5.51}$$

$$Y \sim \mathcal{N}\left(0,\, \sigma_Y^2\right). \tag{5.52}$$

If

$$\sigma_{XY} = \operatorname{cov}\left(X, Y\right), \tag{5.53}$$

then the multivariate difference is distributed as

$$(X - Y) \sim \mathcal{N}\left(0,\, \sigma_X^2 + \sigma_Y^2 - 2\sigma_{XY}\right). \tag{5.54}$$

Assuming that X and Y are independently and identically distributed, then

$$(X - Y) \sim \mathcal{N}\left(0,\, 2\sigma_X^2\right). \tag{5.55}$$

This is the variance of the backprojection interferometric phase error used below.

Figure 5.4 compares the effects of interferometric phase error on both methods. In each, the wavelength $\lambda = 3\,\mathrm{cm}$, the baseline angle $\alpha = 45^\circ$, and the height from the DEM $\delta_\mathrm{z} = 10\,\mathrm{m}$. As before, the minimum and maximum of each method is taken from 30° to 60°. Subfigures (a)-(c) have 10° of phase error, while (d) has 1°. The baseline lengths in (a)-(d) are 1 m, 10 m, 100 m, and 10 m, respectively.

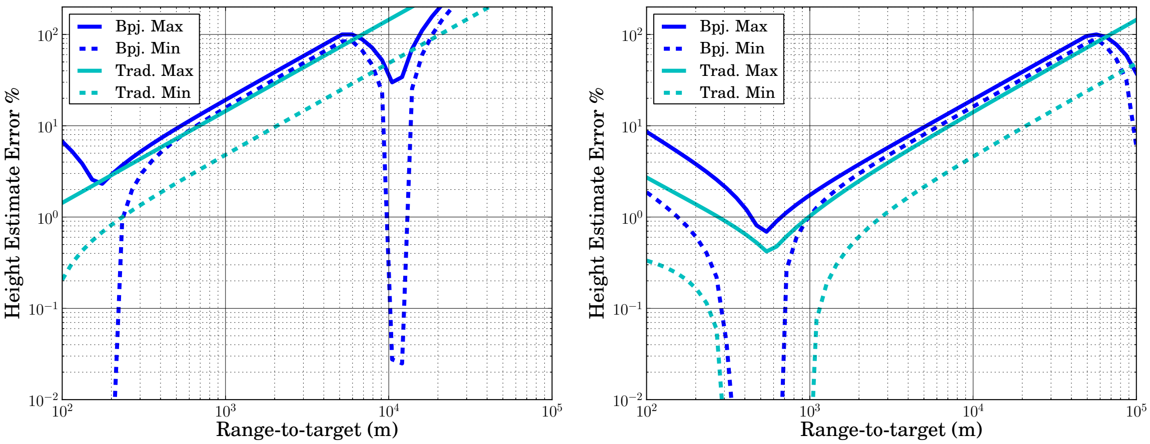

(a) Baseline: 1 m, Phase Error: 10°

(b) Baseline: 10 m, Phase Error: 10°

(c) Baseline: 100 m, Phase Error: 10°

(d) Baseline: 10 m, Phase Error: 1°

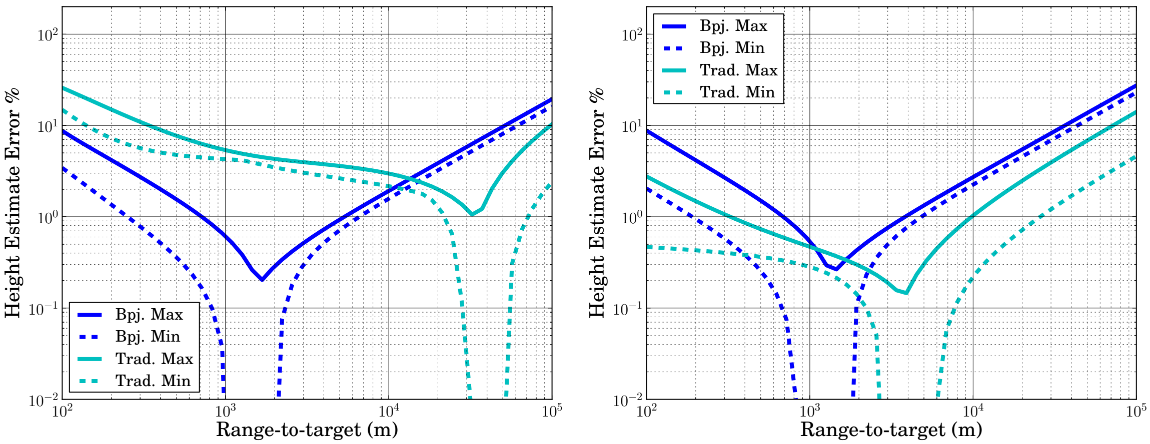

Figure 5.4: Comparison of the effects of phase error for both interferometric methods as a function of range-to-target. The minimum and maximum error percentage are computed from incidence angles $30°$ to $60°$. The model parameters are $\lambda = 3\,\mathrm{cm}$, $\alpha = 45°$, and $\delta_{\mathrm{z}} = 10\,\mathrm{m}$. Subfigures (a)-(c) have $10°$ of phase error, while (d) has $1°$. The baseline lengths in (a)-(d) are 1 m, 10 m, 100 m, and 10 m, respectively.

In (a), (b) and (d) (i.e, 10 m baseline and shorter) the maximum backprojection height estimate error is worse than the traditional method. At a 100 m baseline, the performance of backprojection exceeds the traditional method for smaller ranges to target (where the approximations in traditional interferometry are invalid), but at larger ranges the traditional method again performs better than backprojection. Whereas with baseline errors where backprojection's estimate improved with increasing range, here the backprojection estimate gets worse with range for large ranges. Even in (d) where the phase error is quite small, the traditional method attains a better estimate than backprojection.

It is evident that while both interferometry methods are sensitive to phase errors, backprojection is more so. This is intuitive as it is a difference of differences (i.e., derivatives amplify noise).

5.4 Interferometry Performance

The following subsections describe specific performance aspects of time domain backprojection interferometry. The previous section showed that backprojection interferometry may require a longer baseline than conventional interferometry in order to maintain the same level of accuracy. With that in mind, in Subsection 5.4.1 the concept of the *transition baseline* is introduced. This is the minimum interferometric baseline length for which the performance of backprojection interferometry surpasses conventional interferometry. In Subsection 5.4.2, the effects of phase-center shift in each of the dimensions, azimuth, range, and elevation is described. In the final subsections, 5.4.3 and 5.4.4, the effects of DEM accuracy are discussed.

5.4.1 Transition Baseline

Derivation

Backprojection interferometry can perform better than traditional interferometry for a sufficiently long baseline. It is possible to approximate the minimum baseline length where the height estimation accuracy of backprojection exceeds that of traditional interferometry. Both methods suffer from height estimation errors due to phase measurement errors. The height estimate of conventional interferometry also has errors due to baseline length and baseline angle measurement errors.

To estimate the transition baseline, I find the baseline length B where the major contributing errors of both interferometric methods are equal. Thus, setting $\partial\delta_z$ from Eq. 5.45 on page 108 (the backprojection phase sensitivity) equal to the sum of $\partial\delta_z$ from Eqs. 5.30

through 5.32 on page 107 (the phase and geometric sensitivities of the traditional method),

$$\begin{aligned}\frac{\partial\Delta\Phi}{k\left(\cos\theta_a-\cos\theta_b\right)} &= \partial\Phi\frac{r\sin\theta}{kB\cos\left(\theta_a-\alpha\right)}-\partial B\frac{r}{B}\tan\left(\theta_a-\alpha\right)\sin\theta+\partial\alpha\left(r\sin\theta_a\right) \qquad (5.56)\\ &= r\sin\theta_a\left[\frac{\partial\Phi}{kB\cos\left(\theta_a-\alpha\right)}-\frac{\partial B}{B}\tan\left(\theta_a-\alpha\right)+\partial\alpha\right],\\ 0 &= \frac{k\left(\cos\theta_a-\cos\theta_b\right)}{\partial\Delta\Phi}r\sin\theta_a\left(\frac{\partial\Phi}{kB\cos\left(\theta_a-\alpha\right)}-\frac{\partial B}{B}\tan\left(\theta_a-\alpha\right)+\partial\alpha\right)-1. \qquad (5.57)\end{aligned}$$

The transition baseline length B may be found through use of a numerical root solver.

This expression may be simplified if the interferometric angular baseline $\alpha\approx 45°$. Assuming this to be the case,

$$\theta_b\approx\arccos\left(\cos\theta_a+\frac{B\cos\alpha}{r_a}\right). \qquad (5.58)$$

Additionally, let

$$\Gamma\,\partial\Phi=\partial\Delta\Phi, \qquad (5.59)$$

where the constant Γ represents the ratio of phase difference error to phase error. Substituting these into Eq. (5.57),

$$\begin{aligned}\Gamma &= \frac{k}{\partial\Phi}\left(\frac{-B\cos\alpha}{r_a}\right)r_a\sin\theta_a\left(\frac{\partial\Phi}{kB\cos\left(\theta_a-\alpha\right)}-\frac{\partial B}{B}\tan\left(\theta_a-\alpha\right)+\partial\alpha\right)\\ &= -kB\cos\alpha\sin\theta_a\left(\frac{1}{kB\cos\left(\theta_a-\alpha\right)}-\frac{\partial B}{\partial\Phi}\frac{1}{B}\tan\left(\theta_a-\alpha\right)+\frac{\partial\alpha}{\partial\Phi}\right)\\ &= -\frac{\cos\alpha\sin\theta_a}{\cos\left(\theta_a-\alpha\right)}+\frac{\partial B}{\partial\Phi}k\cos\alpha\sin\theta_a\tan\left(\theta_a-\alpha\right)-\frac{\partial\alpha}{\partial\Phi}kB\cos\alpha\sin\theta_a.\end{aligned}$$

Rearranging,

$$\begin{aligned}\frac{\partial\alpha}{\partial\Phi}kB\cos\alpha\sin\theta_a &= \frac{\partial B}{\partial\Phi}k\cos\alpha\sin\theta_a\tan\left(\theta_a-\alpha\right)-\frac{\cos\alpha\sin\theta_a}{\cos\left(\theta_a-\alpha\right)}-\Gamma,\\ B &= \frac{\partial\Phi}{\partial\alpha}\frac{1}{k\cos\alpha\sin\theta_a}\left[\frac{\partial B}{\partial\Phi}k\cos\alpha\sin\theta_a\tan\left(\theta_a-\alpha\right)-\frac{\cos\alpha\sin\theta_a}{\cos\left(\theta_a-\alpha\right)}-\Gamma\right],\\ B &= \frac{\partial B}{\partial\alpha}\tan\left(\theta_a-\alpha\right)-\frac{\partial\Phi}{k\,\partial\alpha}\left(\frac{1}{\cos\left(\theta_a-\alpha\right)}+\frac{\Gamma}{\cos\alpha\sin\theta_a}\right). \qquad (5.60)\end{aligned}$$

Recall that this expression is only valid near $\alpha = 45°$. As the angular baseline approaches the two extremes of $0°$ and $90°$, Eq. 5.57 must be solved directly. Since the sensitivity of the traditional method to errors in range has been neglected, if it becomes a significant source of error then the transition baseline is actually shorter than that given by this expression. Note that while the ratios $\partial B/\partial\Phi$ and $\partial\alpha/\partial\Phi$ look like partial derivatives, they are better thought of as ratios of errors (i.e., the ratio of baseline-length error to baseline-angle error and phase error to baseline-angle error, respectively).

It is important to note that, as the name implies, the transition baseline length is only near the center of a "transition region". Baseline lengths near that given by Eq. 5.60 may have interferometric height estimates that are approximately equal for either method. Therefore, the transition baseline is not a hard and fast rule, but rather a guideline for determining which interferometric method performs better in a given situation. Also note that the transition baseline is a mathematical construct, and is not readily described by a diagram.

The paragraphs below demonstrate the transition baseline for various geometries and magnitudes of error.

Geometry Comparison

Figure 5.5 shows the transition baseline for several prevalent geometries at various frequency bands through computing Eq. 5.57. The carrier frequency for the bands used are UHF: 650 MHz, L: 1.5 GHz, C: 6 GHz, X: 10 GHz, $\mathrm{K_u}$: 15 GHz, and $\mathrm{K_a}$: 35 GHz. The geometries in subfigures (a)-(d) represent item numbers (1), (3), (4), and (5) in Table 5.2, respectively. The errors used in each model are also given in the table. Note that the values for these errors do not necessarily represent the error in the given systems, but rather indicate reasonable values for purposes of comparison. For a given frequency, a baseline length above the corresponding curve indicates favorability of backprojection interferometry and those below favor traditional interferometry. From these examples, several observations may be made:

- Notice the apparent sweet-spot in subfigures (c) and (d) at $45°$. The peak here suggests that a larger baseline is required before backprojection becomes advantageous.

---

[1] These error values are deemed suitable for purposes of illustration based on common SAR systems. The error values do not necessarily represent the exact values in the given systems.

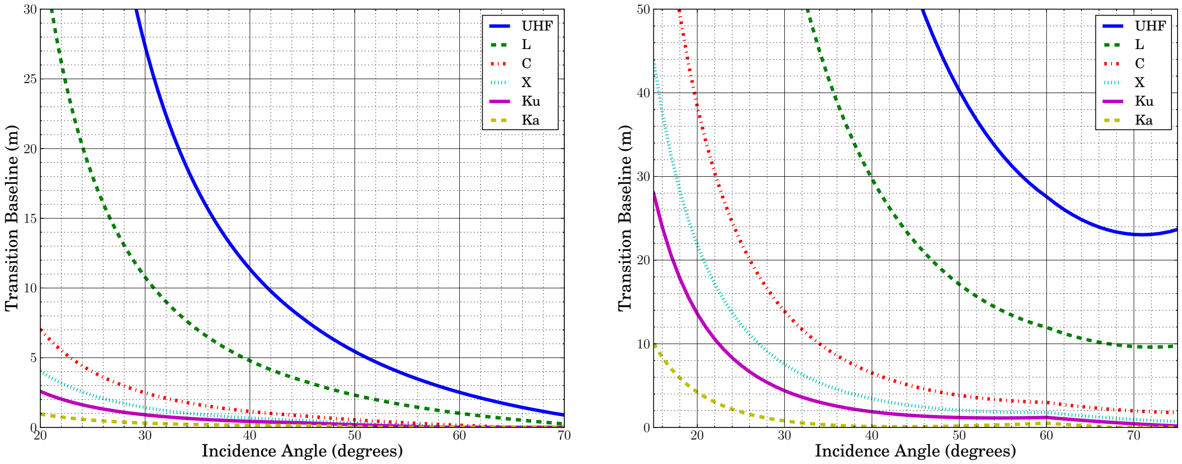

(a) $H = 250$ m, $\alpha = 45^\circ$

(b) $H = 9000$ m, $\alpha = 63^\circ$

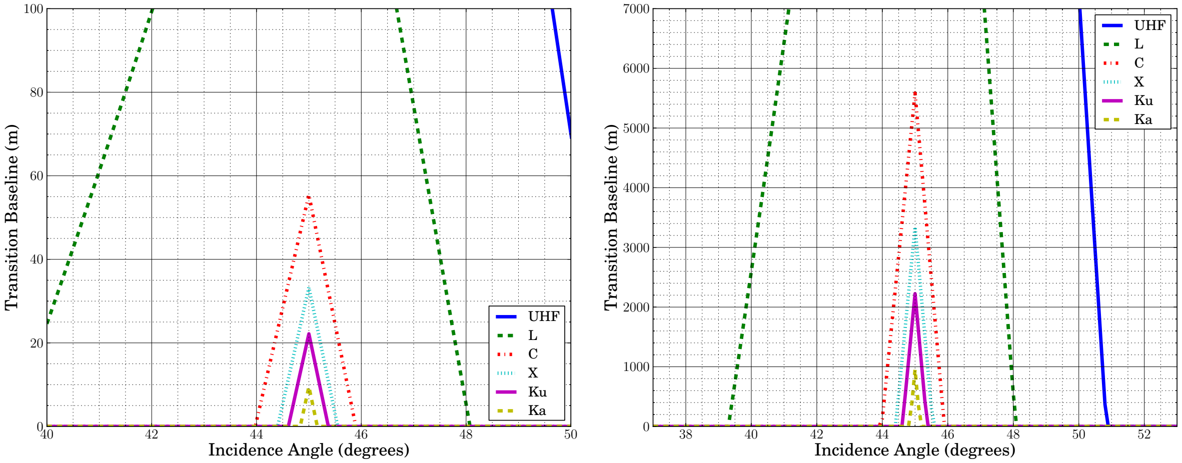

(c) $H = 233$ km, $\alpha = 45^\circ$

(d) $H = 514$ km, $\alpha = 45^\circ$

Figure 5.5: Comparison of baseline transition region for several geometries across various frequency bands.

Table 5.2: Example Geometries

#	Example	Cite	Height	Baseline Length	Baseline Angle	$\partial\Phi$[1]	∂B[1]	$\partial\alpha$[1]
1	Small UAV	-	250 m	0.16 m	45°	0.21	.001	2e-3
2	Medium UAV	-	500 m	2 m	90°	0.21	.001	2e-3
3	TOPSAR	[71]	8500 m	2.6 m	62°	0.21	.001	3e-4
4	SRTM	[72]	233 km	60 m	45°	0.21	0.1	3e-5
5	TanDEM-X	[73]	514 km	400 m	45°	0.21	0.1	3e-7

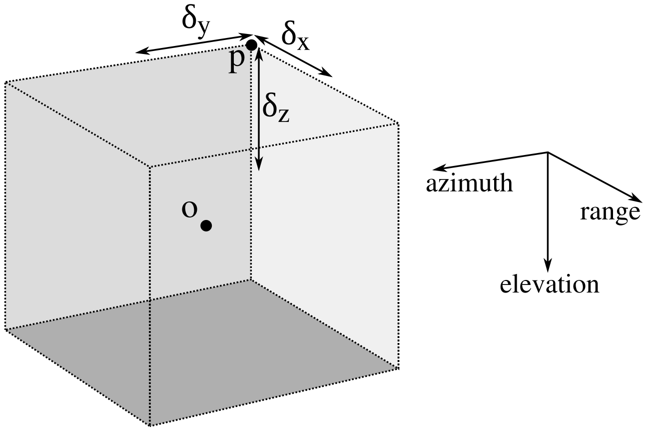

Figure 5.6: Illustration of phase-center displacement in a scattering-cell. Point o is the physical center of the cell and point p is the phase-center. In this diagram, the phase-center is maximally displaced from the physical center of the cell. δ_x, δ_y, and δ_z represent the phase-center displacement in azimuth, range, and elevation, respectively.

- As the carrier frequency increases, the transition baseline becomes smaller. This implies that backprojection interferometry is better suited to high-frequency usage and traditional interferometry is better suited to low-frequency.
- Subfigures (a) and (c) are more likely candidates for backprojection interferometry than (b) and (d). This is because the geometric uncertainties are large enough to push the transition baseline low enough for the required baseline to be practical. Notice in (c) that this is true for C-band and higher, even at the sweet spot of 45° incidence.

5.4.2 Phase-center Displacement

In Sec. 5.2 on page 104, in order to eliminate the unknown degrees of freedom in the derivation of backprojection interferometry, it was assumed that the phase-center displacement is solely in the vertical dimension (i.e., $\delta_x = \delta_y = 0$). This subsection explores the consequences of that assumption. In other words, this subsection shows the effect of phase-center displacement on the interferometric height estimate. Figure 5.6 illustrates maximal phase-center displacement.

Figure 5.7 demonstrates the computed height estimate for phase-center displacement solely in a given dimension, represented by the three curves. The receive antennas are placed in a horizontal baseline (i.e., $\alpha = 0$), separated by 100 wavelengths, and the incidence angle to

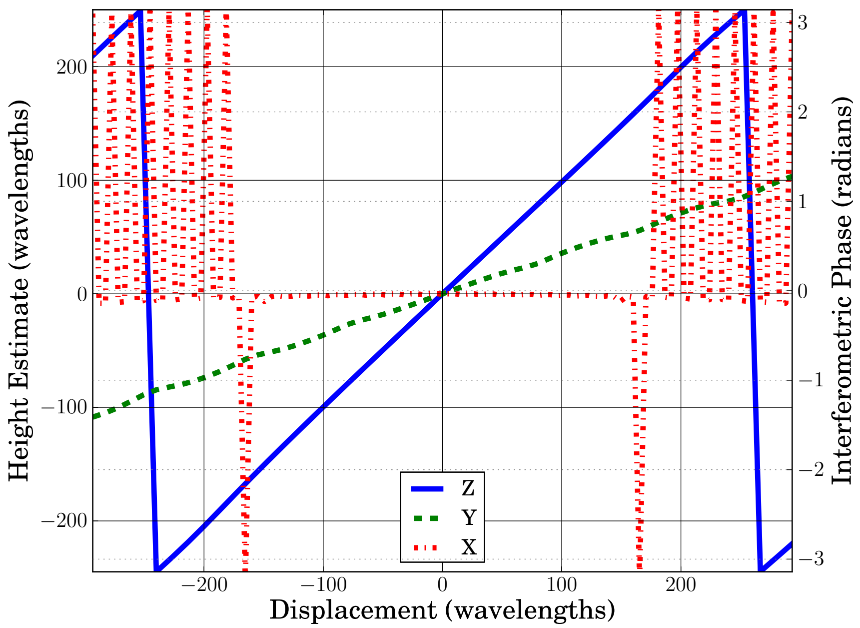

Figure 5.7: Height estimate resulting from displacement solely in each given dimension for a horizontal baseline of 100 wavelengths. The reference height 0 represents no displacement from the physical center of the scattering-cell.

the scattering-cell is 45°. The vertical axis on the left gives the height estimate in wavelengths and the vertical axis on the right gives the equivalent interferometric phase. As expected, when the displacement is strictly in the vertical dimension, the height estimate equals the vertical phase-center displacement.

When the displacement is in the ground-range dimension, the height estimate is still linear with displacement, but at a reduced slope. When the displacement is in the along-track dimension, it has negligible effect, even at distances greater than the length of the baseline itself. This implies that while phase-center displacement in azimuth may be ignored, displacement in ground-range causes errors in the height estimate of the cell. As previously mentioned, for distributed targets the phase-center is likely near the physical-center of the cell so the effect of ground-range displacement is typically be small. However, as point targets may be physically located anywhere within the scattering-cell, they are subject to the greatest uncertainty in height estimation.

One possible way to mitigate the effect of ground-range displacement is by assuming that the vertical offset δ_z is matched by a ground-range offset to keep the phase-center at the physical center of the scattering-cell (i.e., the same slant-range to the assumed scattering-cell center as the slant-range to the actual scattering-cell center as seen by antenna A). Assuming zero azimuth displacement, this implies the following two equations simultaneously

$$
\begin{aligned}
r_a^2 &= (x_a - x_c)^2 + (y_a - y_c)^2 + (z_a - z_c)^2 , \\
r_a^2 &= (x_a - x_c)^2 + (y_a - y_c - \delta_y)^2 + (z_a - z_c - \delta_z)^2 .
\end{aligned}
\tag{5.61}
$$

This leads to

$$
\begin{aligned}
r_a^2 &= (x_a - x_c)^2 + (y_a - y_c)^2 + (z_a - z_c)^2 - 2\left(\delta_y (y_a - y_c) + \delta_z (z_a - z_c)\right) + \delta_y^2 + \delta_z^2, \\
0 &= -2\left(\delta_y (y_a - y_c) + \delta_z (z_a - z_c)\right) + \delta_y^2 + \delta_z^2 \\
&= \delta_y^2 - 2(y_a - y_c)\,\delta_y + \left(\delta_z^2 - 2\delta_z (z_a - z_c)\right), \\
\delta_y &= \frac{2(y_a - y_c) \pm \sqrt{4(y_a - y_c)^2 - 4\left(\delta_z^2 - 2\delta_z (z_a - z_c)\right)}}{2} \\
&= (y_a - y_c) \pm \sqrt{(y_a - y_c)^2 - \left(\delta_z^2 - 2\delta_z (z_a - z_c)\right)} \\
&\approx (y_a - y_c) \pm \left[(y_a - y_c) - \frac{\delta_z^2 - 2\delta_z (z_a - z_c)}{2(y_a - y_c)}\right] \\
&= \mp \frac{\delta_z^2 - 2\delta_z (z_a - z_c)}{2(y_a - y_c)},
\end{aligned}
\tag{5.62}
$$

where the ± sign takes the opposite value of the sign of $(y_a - y_c)$ (since the other solution is above the platform) and the approximation is the Taylor series square root approximation. As improving the height estimate δ_z is of greater importance than the precise value of δ_y, Eq. 5.62 is substituted directly into Eq. 5.20 on page 104. Assuming $\left|\delta_z^2\right| \ll \left|2\delta_z (z_a - z_c)\right|$ then

$$
\begin{aligned}
\frac{\Delta\Phi}{k} &= \delta_y \left(\frac{y_a - y_c}{r_a} - \frac{y_b - y_c}{r_b}\right) + \delta_z \left(\frac{z_a - z_c}{r_a} - \frac{z_b - z_c}{r_b}\right) \\
&\approx \delta_z \left(\frac{z_a - z_c}{y_a - y_c}\right)\left(\frac{y_a - y_c}{r_a} - \frac{y_b - y_c}{r_b}\right) + \delta_z \left(\frac{z_a - z_c}{r_a} - \frac{z_b - z_c}{r_b}\right), \\
\delta_z &= \frac{\Delta\Phi}{k}\left[\left(\frac{z_a - z_c}{y_a - y_c}\right)\left(\frac{y_a - y_c}{r_a} - \frac{y_b - y_c}{r_b}\right) + \frac{z_a - z_c}{r_a} - \frac{z_b - z_c}{r_b}\right]^{-1} .
\end{aligned}
\tag{5.63}
$$

Whether or not Eq. 5.63 gives a better estimate than Eq. 5.21 depends on the nature of the scattering-cell and the amount of lateral phase-center displacement. If the scattering-cell may be treated as distributed with the phase-center near the physical center then, Eq. 5.63 should provide a better estimate than Eq. 5.21.

5.4.3 DEM Accuracy

This section characterizes the performance of backprojection interferometry with respect to DEM accuracy for various geometries. In doing so, this analysis assumes that the DEM inaccuracy does not significantly affect pixel focus, as discussed in Sec. 3.4.1 on page 44. If the focus is significantly affected then there may be a drop in signal-to-noise ratio (SNR) or signal-to-clutter ratio (SCR). This may adversely affect the pixel phase and lead to poor interferometry results.

Figure 5.8 shows plots of normalized interferometric phase $\Delta\Phi/k$ from Eq. 5.21 for vertical height displacement from 0.1 m to 100 m across all incidence angles. Since the phase is normalized by the carrier wavenumber, horizontal dashed lines are placed in the plot to mark the point where the first phase-wrap occurs ($\pm\pi$) for a given frequency. The frequencies corresponding to the named bands are as before: UHF: 650 MHz, L: 1.5 GHz, C: 6 GHz, X: 10 GHz, $\mathrm{K_u}$: 15 GHz, and $\mathrm{K_a}$: 35 GHz. Subfigures (a)-(e) coincide respectively with rows (1)-(5) in Table 5.2. Subfigure (f) compares the normalized phase Φ/k of traditional interferometry.

Examining the plots, the same general curved shape is seen in each where the normalized phase peaks near 45° incidence and tapers off towards 0° and 90°. As evident in the plots, a given magnitude of increase in vertical offset increases the phase by the same magnitude. Interestingly, in these examples, even for highly displaced targets ($\sim$100 m), a single phase wrap does not occur except at higher frequency bands. This highlights one of the primary advantages of backprojection interferometry: for many geometries the need for phase unwrapping is either eliminated or trivialized. This may be compared to traditional interferometry in subfigure (f), where all the offset curves appear to overlap (they are in fact separate, but indistinguishable on this scale). Notice the large magnitude of normalized phase. The phase so great that even small changes in incidence angle across the range swath cause rapid phase wrapping. Indeed, phase-unwrapping is a primary concern of traditional interferometry [62].

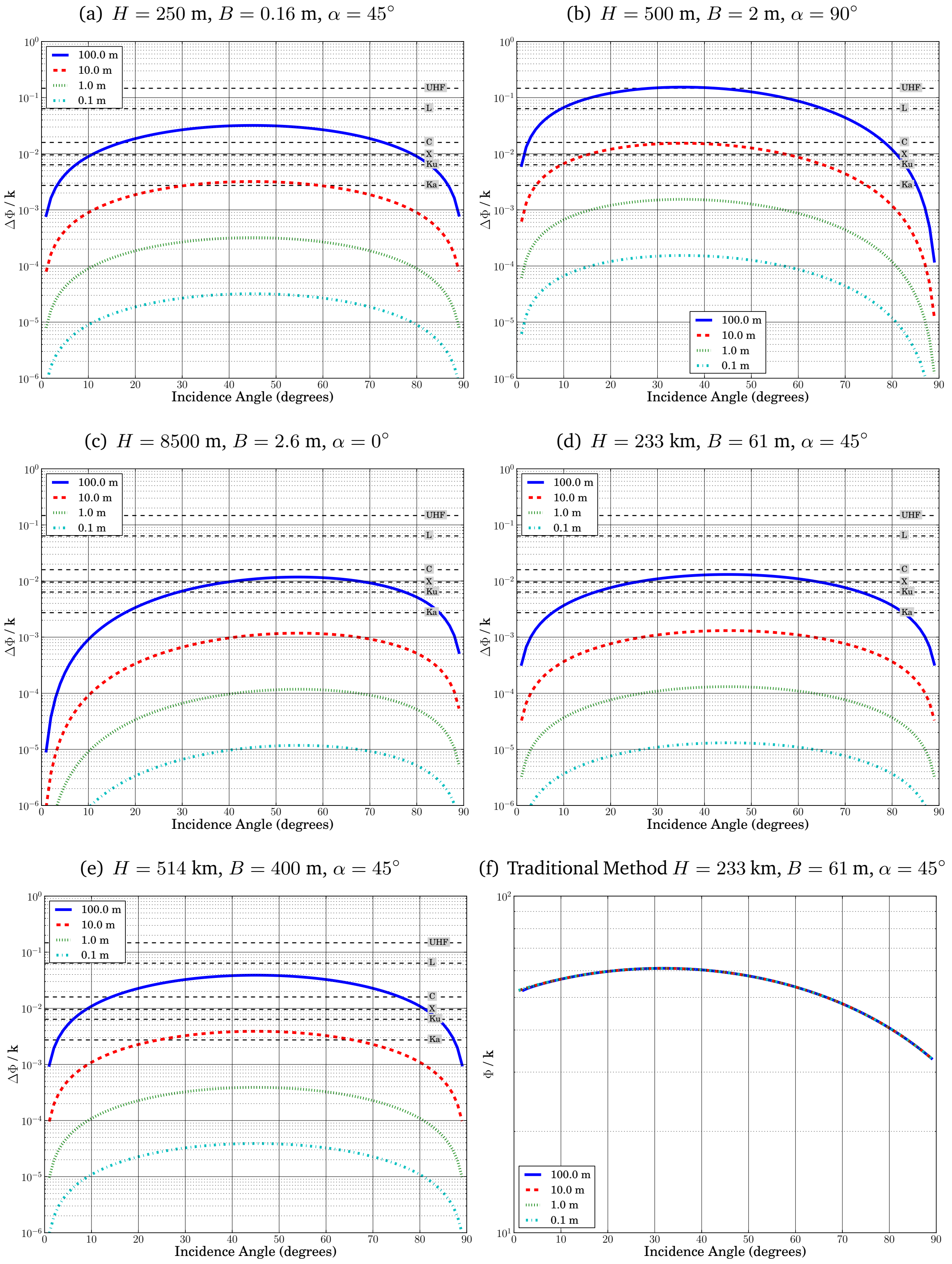
(a) $H = 250$ m, $B = 0.16$ m, $\alpha = 45^\circ$

(b) $H = 500$ m, $B = 2$ m, $\alpha = 90^\circ$

(c) $H = 8500$ m, $B = 2.6$ m, $\alpha = 0^\circ$

(d) $H = 233$ km, $B = 61$ m, $\alpha = 45^\circ$

(e) $H = 514$ km, $B = 400$ m, $\alpha = 45^\circ$

(f) Traditional Method $H = 233$ km, $B = 61$ m, $\alpha = 45^\circ$

Figure 5.8: Comparison of normalized interferometric phase Φ/k for various imaging geometries. Subfigures (a)-(e) represent backprojection interferometry and (f) represents traditional. The subfigure geometries are (a) & (b) low-altitude cases for baselines compatible with small UAVs; (c) similar to TOPSAR; (d) similar to SRTM; (e) similar to TanDEM-X; (f) similar to SRTM using traditional interferometric methods. In (f) the curves are so close they appear to overlap.

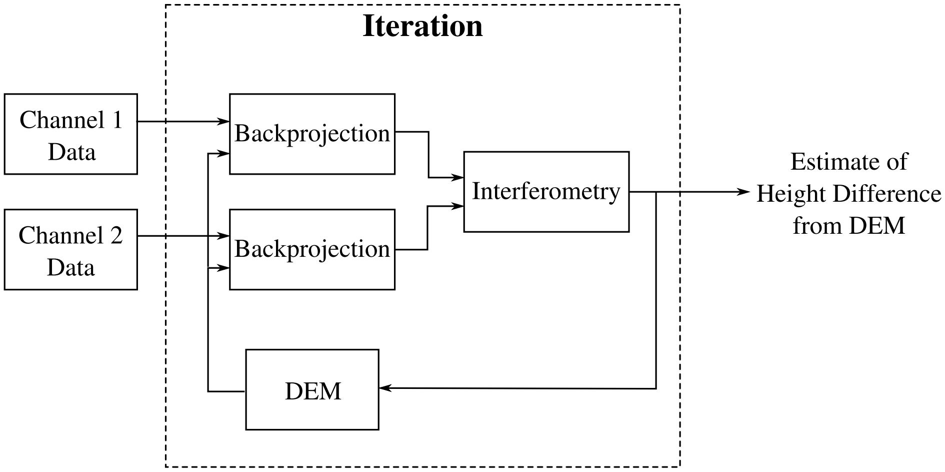

Figure 5.9: Block diagram of iteration of backprojection interferometry height estimate.

As discussed in the previous section, phase noise places a fundamental limit on the accuracy of height estimates. For high coherence areas and with independent looks (around $n = 4$) it is very reasonable to have a phase standard deviation of 10° [74]. To get an idea of what that means for height estimate accuracy, from the plots in Fig. 5.8 first choose a frequency band. Since the Φ/k wrap lines for that band represent 180°, divide by 10° (the phase standard deviation). That means the minimum distinguishable height lies 18 times (or $10^{1.25}$) lower than the wrap line for the given band. For example, given the geometry in (b), at $\mathrm{K_u}$-band, the minimum discernible height is in the 10s of centimeters.

5.4.4 DEM Iteration

One subtle aspect of backprojection interferometry is the height-offset induced ground-range translation mentioned in Sec. 3.4.1. As a large height offset leads to the apparent shifting of targets in the output image, the estimated height is erroneously attributed to the wrong physical location on the ground. This effect may be mitigated by iteratively reforming backprojected images after updating the DEM to account for the measured height offset for each pixel. Figure 5.9 shows a block diagram of the iteration of backprojection interferometry. The height estimate is used to update the DEM and then reform backprojected images for input to interferometry. While this process may be repeated many times, in practice phase noise may cause the solution to converge at a value other than the true height.

5.5 Discussion

This section discusses the results of the chapter and summarizes its contributions. First, the question of where backprojection interferometry is advantageous compared to traditional interferometry is answered. Following that, a summary of the contributions of each section is presented.

Ideally, the use of backprojection implies that an initial DEM is available. This could have been performed with traditional interferometry. As DEMs are available over most of the surface of the Earth, this is a reasonable assumption. The purpose in performing backprojection interferometry is to either refine the DEM or to measure changes in height that have occurred since the DEM was generated (e.g., landslide, earthquake, etc.). Assuming that a sufficiently accurate DEM is available to generate a focused backprojected image, there are four key advantages to backprojection interferometry:

1. Backprojection trivializes the need for phase unwrapping. As shown at the end of the previous section, the backprojection interferometric phase varies slowly as the cells are displaced from the DEM. Not only does this help eliminate height estimate inaccuracies due to errors in phase unwrapping, but may also lead to the ability to resolve heights of very steep terrain (e.g., urban environments). This is also notably advantageous in low-altitude interferometry where the rapid change in incidence angle across the range swath leads to especially rapid phase wrapping. Additionally, this is advantageous at higher frequency bands where phase wrapping likewise occurs more rapidly.

2. As seen in Sec. 5.3, backprojection is highly insensitive to errors in the measurement of the interferometry baseline length and angle. This is particularly advantageous at lower altitude applications on an aircraft where turbulence and non-ideal motion lead to errors in the measurement of baseline angle. Additionally, at lower altitudes, the potentially wide change in incidence angles across the range swath means that portions of the swath are possibly outside the sweet-spot, and therefore present larger height estimate errors. Where attitude measurement error is pronounced, traditional interferometry can be inaccurate.

3. Sec. 5.3 shows that errors in the height estimate for traditional interferometry grow as the baseline grows. Given that an interferometric baseline length is not so large that geometric decorrelation becomes significant, backprojection interferometry yields greater accuracy in height estimates for longer baselines. The results of Chapter 4 may be used to quantitatively determine the decorrelation for a given geometry. As the baseline length increases, the frequency of phase wrapping in the interferogram does as well. Despite this increase, however, the wrapping still remains much lower than traditional interferometry and can be removed using simple methods.

4. Backprojection explicitly forms images in the ground-plane, making orthorectification unnecessary. As topography can be explicitly included, image artifacts due to terrain relief may be reduced, which may also lead to improved accuracy in image analysis and identifying the height of a given location.

It is seen that while backprojection interferometry may be advantageous in spaceborne applications, it is especially advantageous at lower altitudes where phase wrapping and errors in baseline measurement are important issues.

To summarize the contributions of this chapter, Section 5.2 provides the derivation of backprojection interferometry. In Section 5.3, the sensitivities of both interferometry methods are derived and a detailed comparison if each is made. This analysis shows that traditional interferometry is highly sensitive to errors in the measurement of the interferometric baseline while backprojection interferometry is rather insensitive to this. This section also shows that while both methods are sensitive to their respective interferometric phase, backprojection is more sensitive.

A key contribution of this chapter is the analysis showing that traditional interferometry and backprojection interferometry yield different results and have different sensitivity. Perhaps some may think that “removal of the DEM phase” before image formation has the same result as removal after image formation. This chapter shows, perhaps counter-intuitively, that this is not the case and the two are, in fact, quite different.

Finally, Section 5.4 gives analysis of three specific performance considerations of backprojection interferometry. First, the transition baseline is derived which shows the minimum

Table 5.3: Sensitivity Parameters for Examples Given

	Nominal	Fig. 5.10	Fig. 5.11	Fig. 5.12	Fig. 5.13
θ	$53°$				
B	2 m	2 m → 200 m			
α	$45°$		$30° \to 60°$		
r_a	10 km			1 km → 10 km	
δ_z	500λ				$5\lambda \to 500\lambda$
λ	1.9 cm				

baseline region for which backprojection interferometry performs better than traditional interferometry. Second, the effects of phase-center displacement on the height estimate in all dimensions are shown: almost no change for displacement in azimuth, but a somewhat significant change displacement in ground-range. Third, the effects of DEM accuracy on backprojection interferometry are shown.

5.6 Chapter Appendix: Detailed Sensitivity Comparison

5.6.1 Individual Parameters

These observations deal with the sensitivity of the two methods in a broad sense. In order to gain a better understanding of the methods' behavior for each parameter across all incidence angles, four examples are presented. Figures 5.10 through 5.13 compare the changes in baseline length, baseline angle, range-to-target, and target displacement where there is no error in any of the parameters. Observations from these sensitivities directly follows. The nominal geometry parameters used are an incidence angle $\theta = 53°$, antenna baseline length of $B = 2$ m, a baseline angle of $\alpha = 45°$, $r_a = 10$ km range-to-target and a $\delta_z = 500\lambda$ vertical displacement. Phase sensitivity is evaluated at Ku-band ($\lambda = 1.9$ cm). Table 5.3 shows the nominal parameters, along with those changed in each example.

For each example, sensitivity plots are computed directly from the equations in Table 5.1. The height estimate error is computed by comparing Eqs. 5.21 and 5.26 to the actual height offset when no phase noise nor geometry errors are present. Note that although the sensitivity of traditional interferometry to baseline angle and incidence angle is identical, both are shown below since they are not identical for backprojection.

Change In Baseline Length

Figure 5.10 provides an example of the difference in sensitivity when the baseline length is changed from 2 m to 200 m. Examining subfigures (c) the baseline angle, (d) incidence angle, and (e) range sensitivity, none are affected by changing the baseline length. In each case backprojection interferometry is orders of magnitude less sensitive than the traditional method.

For subfigures (a) the baseline length and (b) the phase sensitivity, both decrease in sensitivity by 100 times when the baseline length is increased by the same magnitude. Backprojection is less sensitive to baseline length, even near the “sweet spot” of $45°$ incidence. (Sweet spots are incidence angles that perform particularly well for a given method.) Notice that the incidence angle sweet spot for traditional interferometry is in the baseline length but for backprojection interferometry is in the baseline angle.

Backprojection is slightly more sensitive to phase than the traditional method. Despite this, the backprojection interferometry height estimate of the scattering-cell is much more accurate than the traditional (several orders of magnitude in most places).

Change In Baseline Angle

In Figure 5.11 on page 131, the baseline angle is changed from $30°$ to $60°$. Traditional interferometry shows the previously mentioned incidence angle sweet spot at $30°$ and $60°$ in the baseline length sensitivity, and backprojection interferometry shows it in the baseline angle. The magnitude of sensitivity remains roughly the same except for the shift in sweet spot. All other sensitivities remain nearly the same when the baseline angle is changed.

(a) Baseline Length Sensitivity

(b) Phase Sensitivity

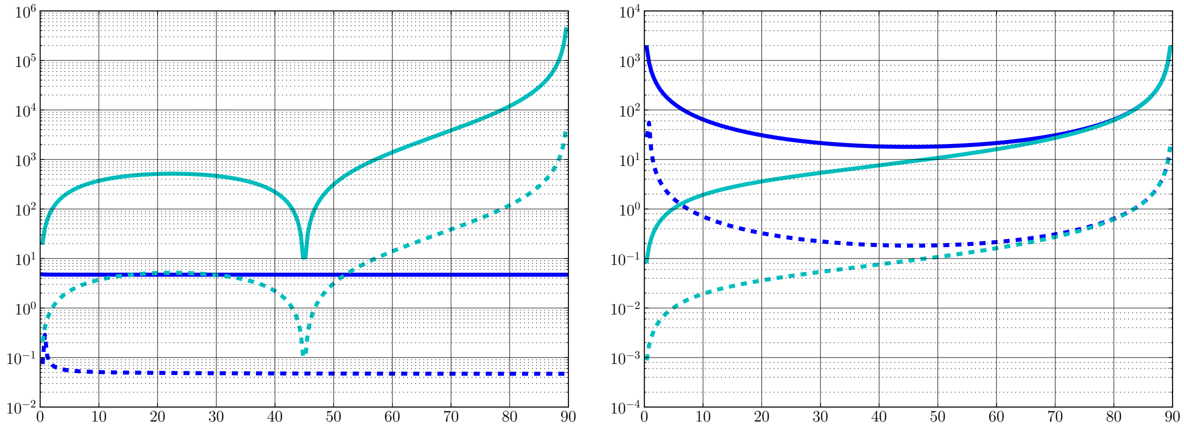

(c) Baseline Angle Sensitivity

(d) Incidence Angle Sensitivity

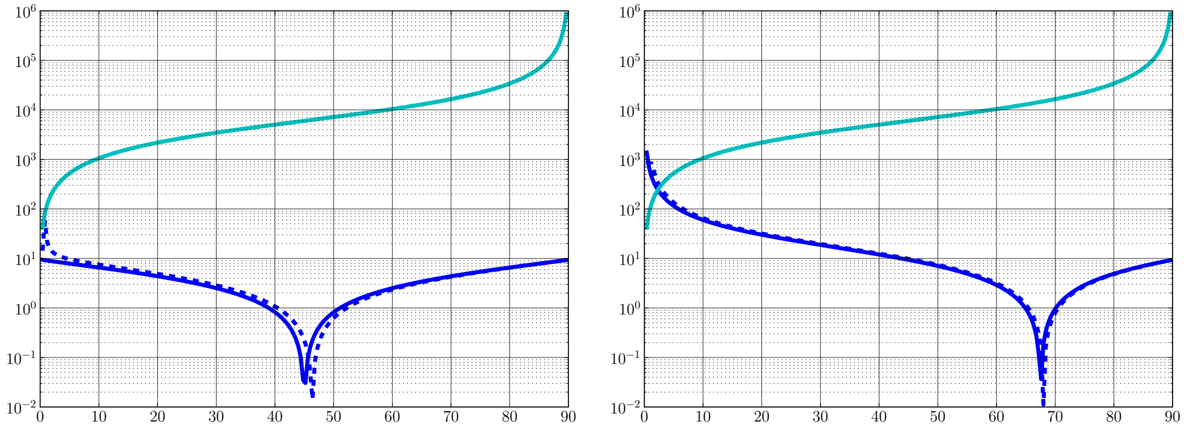

(e) Range Sensitivity

(f) Height Estimate Error %

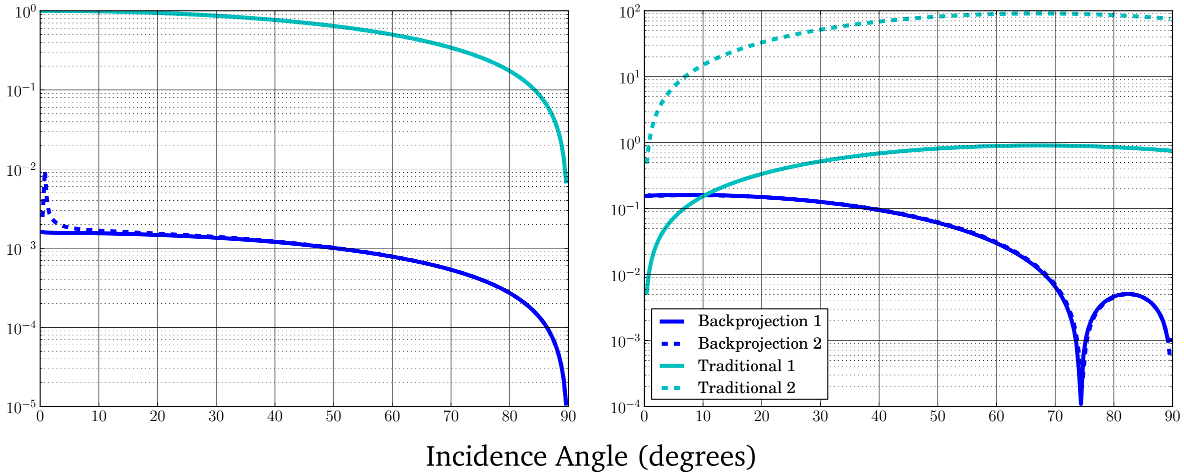

Figure 5.10: Sensitivity comparison of traditional and backprojection interferometry when the baseline length is changed. The solid lines correspond to a baseline length of 1.4 meters and the dashed lines correspond to 141 meters. Where there is no change the dashed lines are not visible.

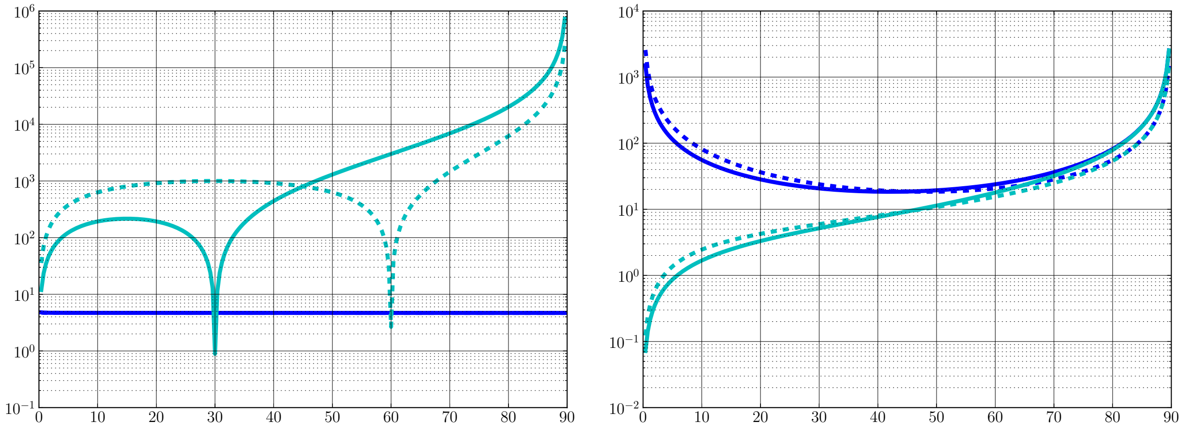

(a) Baseline Length Sensitivity

(b) Phase Sensitivity

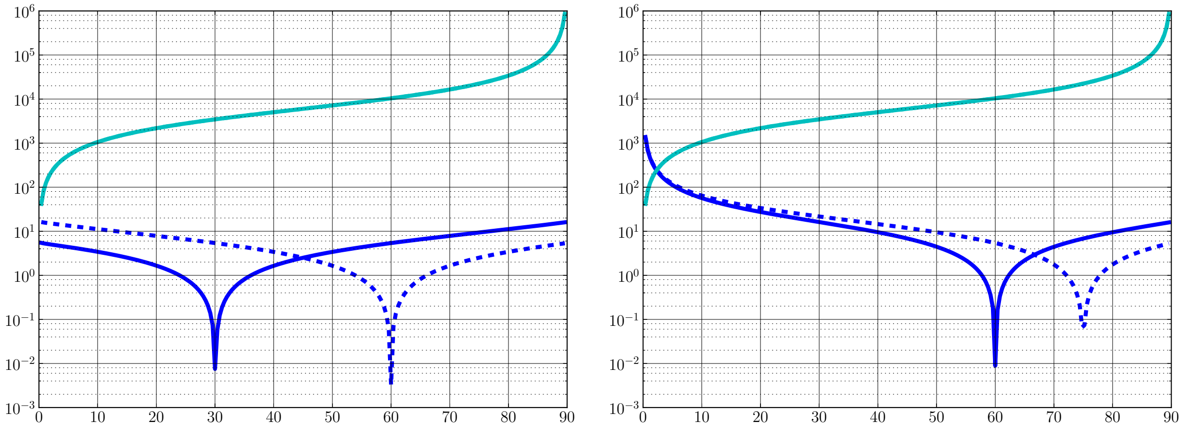

(c) Baseline Angle Sensitivity

(d) Incidence Angle Sensitivity

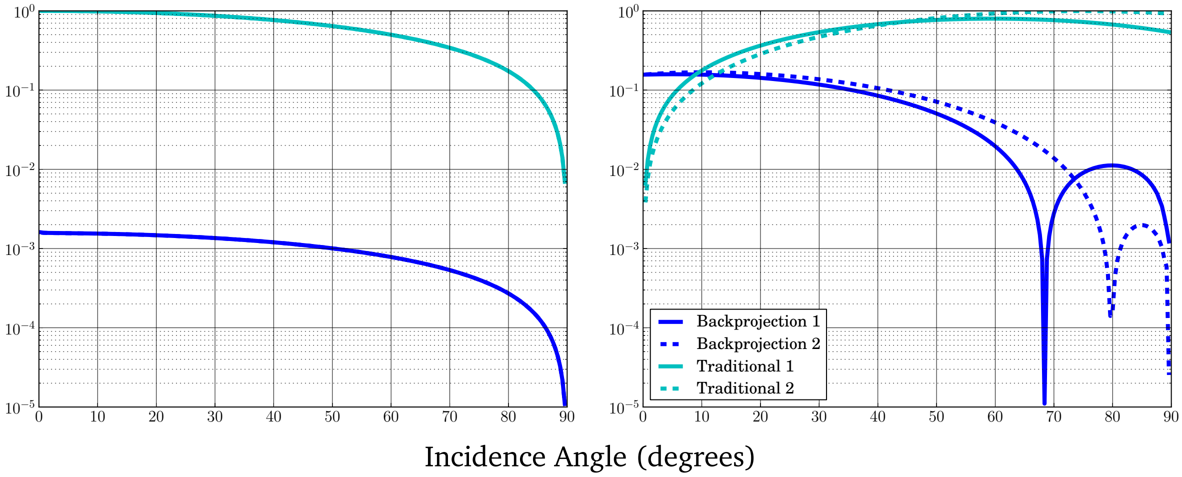

(e) Range Sensitivity

(f) Height Estimate Error %

Figure 5.11: Sensitivity comparison of traditional and backprojection interferometry when the baseline angle is changed. The solid lines correspond to a 30° baseline and the dashed lines correspond to 60° baseline. Where there is no change the dashed lines are not visible.

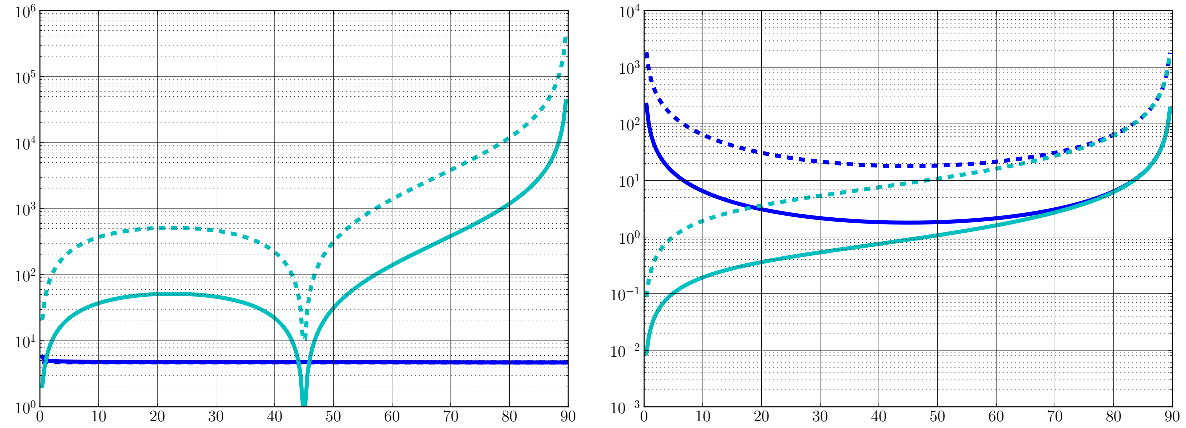
(a) Baseline Length Sensitivity

(b) Phase Sensitivity

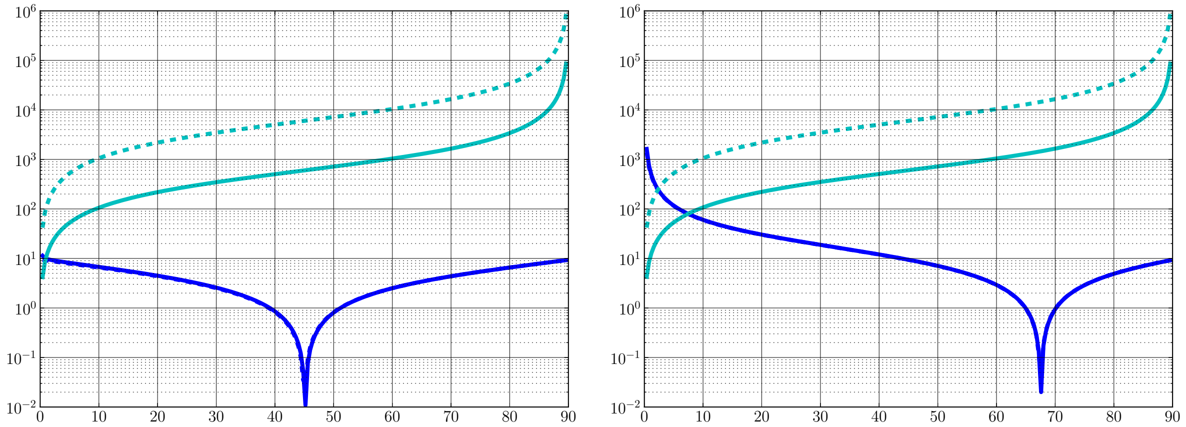
(c) Baseline Angle Sensitivity

(d) Incidence Angle Sensitivity

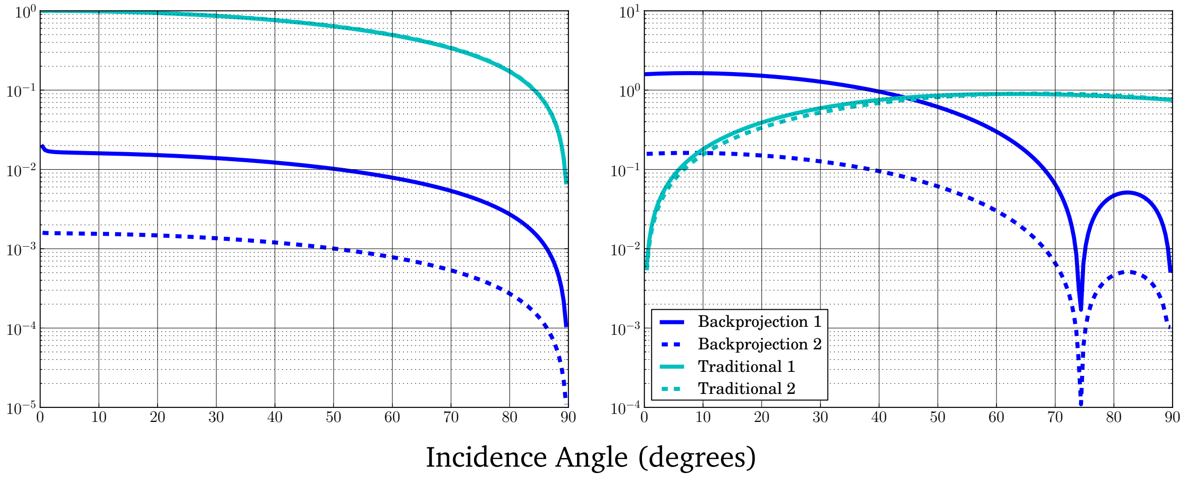
(e) Range Sensitivity

(f) Height Estimate Error %

Figure 5.12: Sensitivity comparison of traditional and backprojection interferometry when the range from the antenna-to-target is changed. The solid lines correspond to a range of 1,160 meters and the dashed lines correspond to range of 116,600 meters. Where there is no change the dashed lines are not visible.

(a) Baseline Length Sensitivity (b) Phase Sensitivity

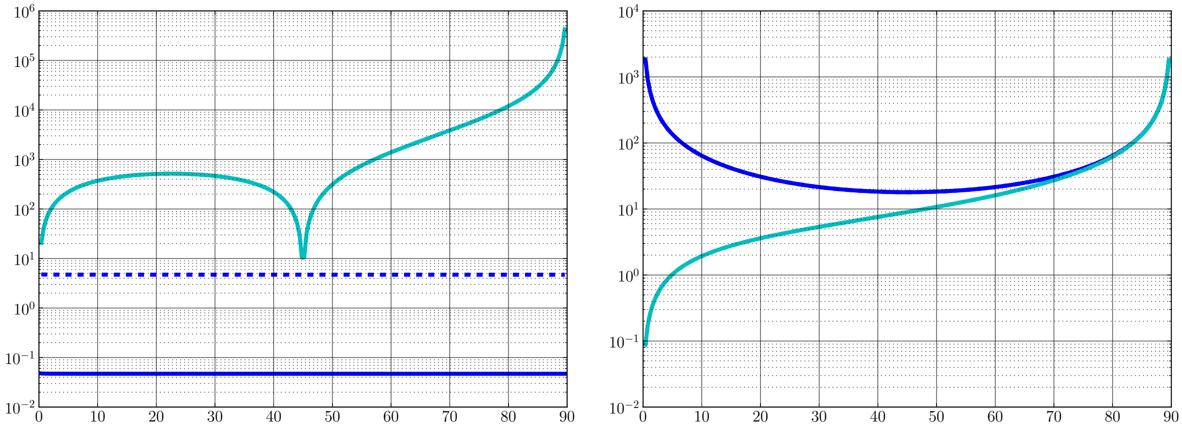

(c) Baseline Angle Sensitivity (d) Incidence Angle Sensitivity

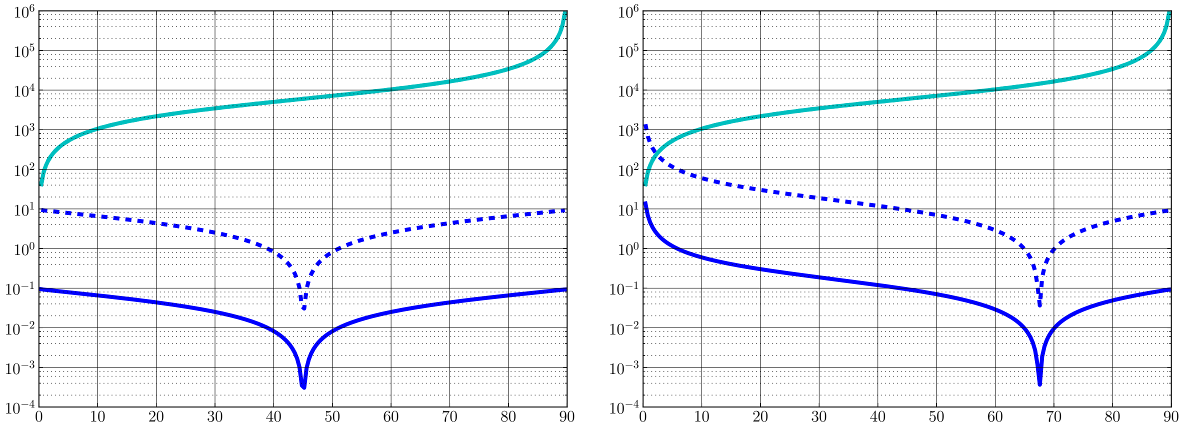

(e) Range Sensitivity (f) Height Estimate Error %

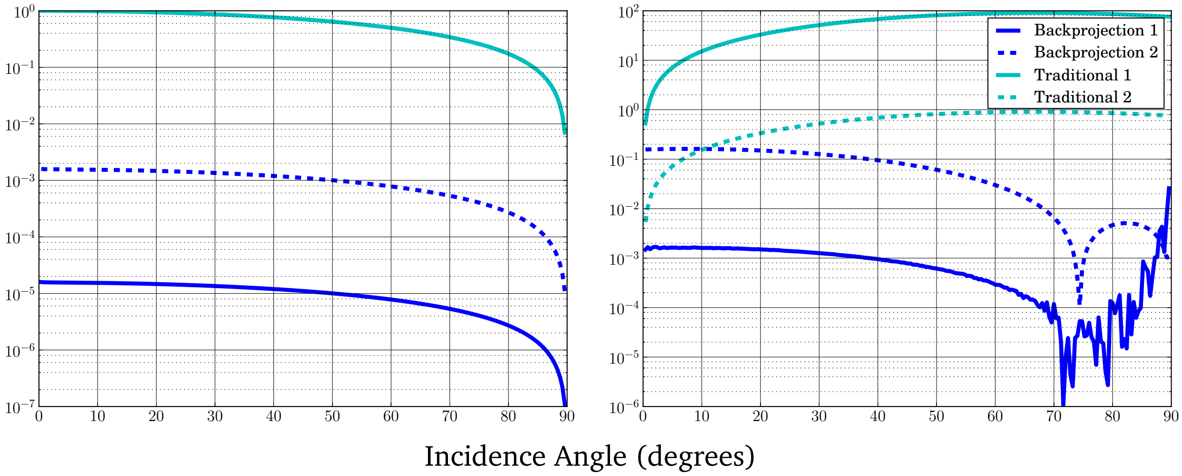

Figure 5.13: Sensitivity comparison of traditional and backprojection interferometry when the height of the target is changed. The solid lines correspond to a height offset of 5 wavelengths from the reference height, and the dashed lines correspond to a 500 wavelength offset. Where there is no change the dashed lines are not visible.

In this case the height estimate error percentage of both traditional and backprojection interferometry changes little as the baseline angle changes. Backprojection is more accurate than traditional except at very shallow incidence angles.

Change In Range-to-target

Figure 5.12 demonstrates the effect of changing the range from the antenna to a target. Here, the slant-range is changed from 1 km to 10 km. With the increase in range, both methods become more sensitive to interferometric phase by the same magnitude.

Backprojection becomes less sensitive to range while the traditional remains the same. The backprojection method stays the same in baseline length, baseline angle, and incidence angle, but the traditional method becomes more sensitive in all of these as the range increases. In fact, even at at altitude of a thousand meters, backprojection is still less sensitive in each of these areas.

The height estimate error for traditional interferometry remains unchanged as the range is increased. On the other hand, backprojection sees an improvement in height estimate accuracy by two orders of magnitude.

Change In Target Displacement

In Figure 5.13, the target height displacement is changed from 5λ to 500λ. The interferometric phase sensitivity remains unchanged for both. For the traditional approach, the baseline length, baseline angle, and baseline sensitivity stay the same while backprojection grows more sensitive (this is opposite of the previous example where backprojection stayed the same). In each of these, the sensitivity of the backprojection method increases by the same magnitude as the change in height displacement. The range sensitivity of backprojection also increases by the same amount.

In this example, when the height displacement of the target increases, the height estimate error of the traditional method decreases. Contrariwise, increasing the height displacement causes the estimation error of backprojection to increase. Despite this, however, even with a height displacement of 500λ, backprojection still has a lower error for most incidence angles than the traditional method.

5.6.2 Combined Comparison

The following two paragraphs describe the ratio of baseline-length error to phase error $\partial B/\partial \Phi$ and baseline-angle error to phase error $\partial \alpha/\partial \Phi$. Recall from Sec. 5.4 that while these ratios appear to be partial derivatives, they are ratios of errors and have no physical meaning of themselves.

Analysis of $\partial B/\partial \Phi$

In the previous paragraph, the error sources are held constant for a given geometry. In order to gain insight into how the error values affect the transition baseline, the effects of variable error are now shown. In order to simplify the analysis, rather than directly comparing all three error sources ($\partial \Phi$, ∂B, $\partial \alpha$), which has three degrees of freedom, the ratios $\partial B/\partial \Phi$ and $\partial \alpha/\partial \Phi$ are compared, which has only two. Figure 5.14 gives plots where the curves compare the transition baseline length for various values of $\partial B/\partial \Phi$ (0.001, 0.1, 0.1, 1). The height used is 1000 m, the center frequency is 6 GHz, and the baseline angle is $45°$. The subfigures display a fixed value of $\partial \alpha/\partial \Phi$ (0, 10^{-5}, 10^{-4}, 10^{-3}). Backprojection is better suited when the baseline length lies in the region above the transition curve. Subfigure (a) shows that the traditional method is better suited in situations where there is no angular error in baseline. In the remaining subfigures, for small values of error in baseline length, the traditional method is better suited across the whole range of incidence angles. As the $\partial B/\partial \Phi$ grows large (i.e., approaches 1) backprojection becomes better suited outside the $45° \pm 1°$ sweet spot. As the error in baseline angle grows, backprojection becomes much more feasible, even near the sweet spot. (Notice the change in scale on the vertical axes.)

Analysis of $\partial \alpha/\partial \Phi$

Figure 5.15 on page 137 shows the case where the curves in each plot compare the baseline transition length for various values of $\partial \alpha/\partial \Phi$ (10^{-5}, 10^{-4}, 10^{-3}, 10^{-2}). Backprojec-

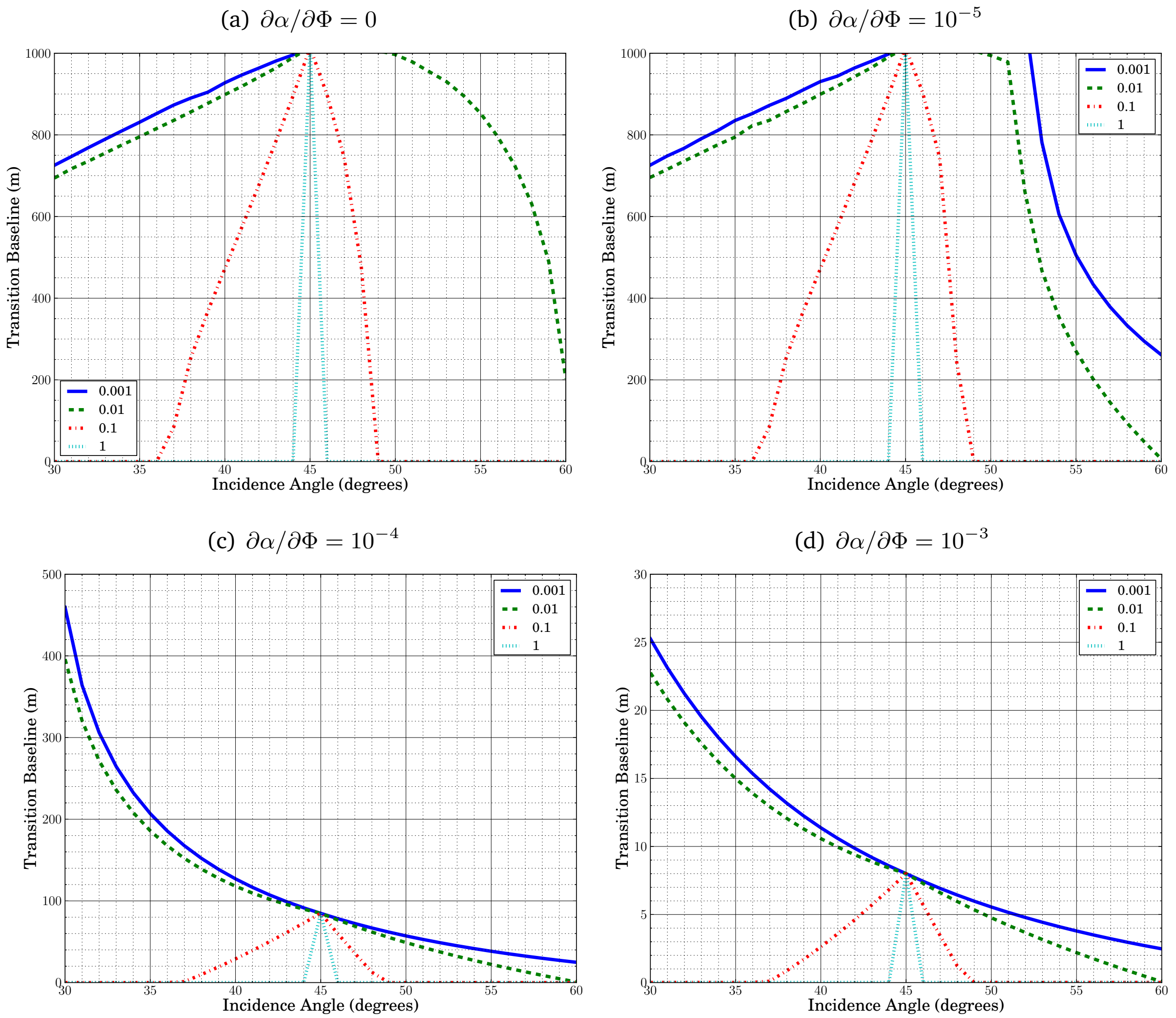
(a) $\partial\alpha/\partial\Phi = 0$

(b) $\partial\alpha/\partial\Phi = 10^{-5}$

(c) $\partial\alpha/\partial\Phi = 10^{-4}$

(d) $\partial\alpha/\partial\Phi = 10^{-3}$

Figure 5.14: Comparison of baseline transition length for various values of $\partial B/\partial\Phi$, with $f_0 =$ 6 GHz, $H = 1000$, and $\alpha = 45°$.

tion is better suited when the baseline length lies in the region above the transition curve. Each subfigure compares heights 0.1, 1, 10, and 100 km, where the baseline error $\partial B/\partial\Phi = 0$ throughout. The purpose of this figure is to show not only what magnitudes of baseline angular error yield a given transition baseline, but also that the transition baseline length decreases as the platform altitude increases, until approximately 10 km, after which increasing altitude has a negligible effect. As before, backprojection is best suited to scenarios with large errors in angular baseline.

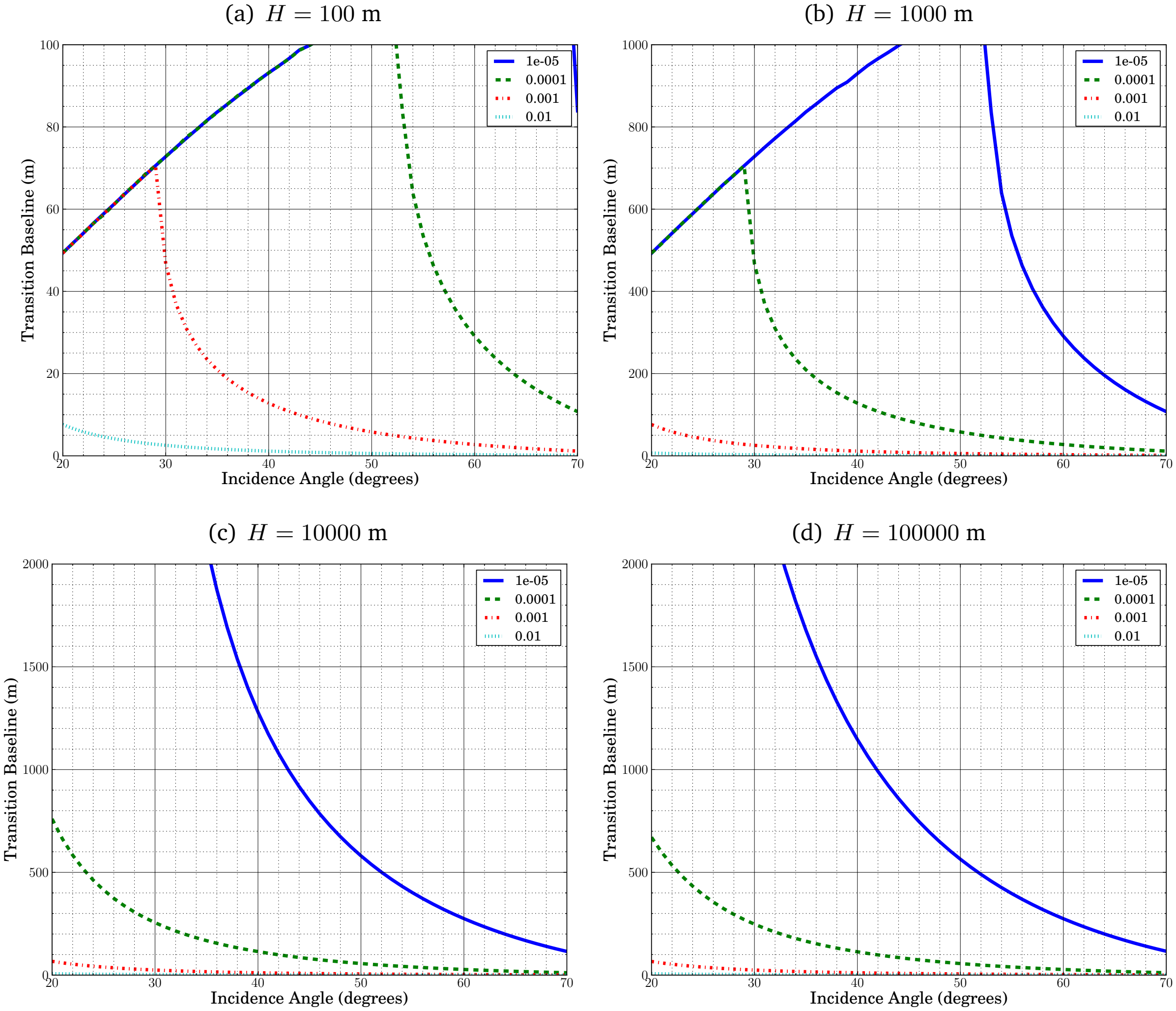
(a) $H = 100$ m

(b) $H = 1000$ m

(c) $H = 10000$ m

(d) $H = 100000$ m

Figure 5.15: Comparison of baseline transition length for various values of $\partial\alpha/\partial\Phi$, with $f_0 = 6$ GHz, $\alpha = 45°$, and $\partial B/\partial\Phi = 0$.

Chapter 6

Conclusion

This dissertation increases the body of knowledge in synthetic aperture radar for time-domain backprojection. The increase comes in three main areas: the backprojection algorithm in general, geometric correlation for MIMO SAR, and interferometry using backprojected imagery. The specific contributions in each area are enumerated in Section 6.1.

An important finding of the dissertation is that time-domain backprojection is particularly well-suited to airborne, low-altitude SAR. This happens for at least two main reasons: a high level of non-ideal motion (i.e., turbulence) and a wide range of incidence angles in the ground-range swath.

Rapidly changing atmospheric effects (e.g., variable wind-speed) have a significant effect on low-altitude SAR. Additionally, implied in low-altitude SAR is smaller platforms (e.g., unmanned aerial vehicles or UAVs), which fly at slower velocities and are more susceptible to turbulence. These issues result in a high level of non-ideal motion that may present problems for traditional motion compensation. Backprojection, however, implicitly handles non-ideal motion. This means that backprojection often produces higher quality images in low-altitude situations. Nevertheless, image quality isn't the only item affected by non-ideal motion. Interferometry is notoriously difficult in low-altitude SAR because any inaccuracy in measurement of the interferometric baseline leads to large errors in height estimates. As shown in Chapter 5, backprojection interferometry is insensitive to these types of errors.

The second reason for backprojection's advantage at low-altitudes is the large range of incidence angles from the near edge of the range swath to the far edge. For low-altitude

SAR, the range of incidence angles in the illumination footprint may exceed $75°$. This leads to considerable range migration of targets and may be difficult for frequency domain algorithms and result in reduced image quality. The wide range of incidence angles also affects traditional interferometry (through the use of frequency domain algorithms) because the imaged swath extends outside the angular sweet spot seen in Chapter 5. Leaving the sweet spot subjects traditional interferometry to inaccuracy because of baseline measurement errors. Backprojection interferometry isn't subject to this limitation. At higher altitudes, leaving the sweet spot becomes less of an issue because the imaged swath is often narrow enough that most of it falls within the sweet spot.

For these reasons, backprojection is often superior to traditional frequency-domain methods, both in quality of imagery and accuracy of interferometry at low altitudes. Backprojection is more computationally expensive, but this downside is nearly eliminated by modern computers which are capable of thousands of parallel computations. At high altitudes, while backprojection still performs well, it may have little advantage over traditional frequency domain methods.

6.1 Contributions

This dissertation makes novel contributions to the field of synthetic aperture radar, particularly in regard to the time-domain backprojection algorithm. These contributions are organized into three primary categories: generalized time-domain backprojection fundamentals, multistatic geometric correlation, and interferometry:

1. **Generalized Backprojection**
    - The dissertation derives generalized time-domain backprojection from first principles. This derivation is novel because it is more straightforward than any currently in literature.
    - The backprojection matched filter is typically parameterized as the physical center of the scattering-cell. If the phase-center of the cell is at the physical center (or similarly, if the exact location of the phase-center is known), then in principle it

is possible to achieve perfect imaging. However, the phase-center is generally unknown so there is image degradation (the degree to which depends on the amount of phase-center displacement, cell resolution, squint, elevation map accuracy, and non-ideal motion). The dissertation introduces the notion that these image focusing errors result from lack of knowledge of the phase-center of the scattering-cell.

- The derivation introduces the idea of nominal residual phase. This is the average phase difference between the matched filter and the received signal. If the residual phase is constant across the synthetic aperture then there is no defocusing. Variations in residual phase from the nominal lead to defocusing.
- The analysis introduces an approximation for the hyperbolic range from the antennas to the target based on the Bakhshali approximation, which is novel for SAR.
- The dissertation performs an analysis of the various sensitivities of the backprojection algorithm to the radar and geometric parameters as well as an analysis of several performance characteristics of backprojection. Specifically, contributions are made showing the effects of errors in the digital elevation map used in image formation.
- The analysis shows there is a maximum useful azimuth antenna beamwidth for SAR due to the unknown phase-center of the scattering-cells, and how to determine it.
- Backprojection does not require modification based on antenna squint, a problem that particularly troubles frequency domain methods.

2. **Multistatic-static / MIMO Correlation**
    - The dissertation creates a new model for multistatic geometric correlation of SAR pixels from first principles, based on backprojection. The new model of geometric correlation makes fewer assumptions than previous models from literature.
    - A comparison is made of the existing models from literature to the new backprojection based model. It is seen that the existing models do not perform well near 0° and 90° incidence, and some are more accurate than others depending on the exact imaging geometry.

- I show that the total number of scatterers inside a scattering-cell does not affect the correlation statistics: one random target behaves the same way as many.
- The dissertation finds that for practical imaging situations, when all antennas are placed on the same imaging platform, the resulting images are highly correlated, even for low-altitude SAR.

3. **Backprojection Interferometry**
    - The dissertation derives a new method of SAR interferometry based on backprojected imagery. The matched filter of backprojection makes backprojected images unsuited to traditional SAR interferometric methods. The new interferometric method makes use of the fact that the phase difference of two backprojected images is, in fact, a difference of differences.
    - A comparison is made of traditional interferometry to backprojection interferometry, including a comparison of their respective sensitivities. The comparison shows that despite both being based on the phase difference of two images, both perform quite differently. A key observation is that backprojection interferometry is insensitive to errors in measurement of the interferometric baseline, which is critical in traditional interferometry.
    - I derive the minimum baseline length for which backprojection interferometry outperforms traditional interferometry. This is termed the transition baseline.

6.2 Future Work

The research presented in this dissertation may be extended in a variety of ways. Following is a list of some possible avenues:

- **Backprojection pixel phase**. It was shown in Chapter 3 and then used in Chapters 4 and 5 that the phase of the backprojection sum for a given pixel is approximately equal to the residual phase at the point of closest approach. While this is a reasonable approximation for low squint (i.e., less than half the azimuth beamwidth), it is not reasonable for squinted data in general. It is also somewhat inaccurate when there is a high level of non-ideal motion. A model that produces the expected residual phase for an arbitrary geometry would aid several other research areas.

- **Squinted interferometry**. The interferometry derivation in Chapter 5 uses the assumption just mentioned in its derivation. By modeling the expected phase of the backprojection sum for squinted data, it may be possible to derive a model for squinted interferometry.
- **Variable baseline interferometry**. Chapter 5 is concerned with single-pass interferometry, where two antennas with a fixed baseline are used simultaneously. It is also theoretically possible to use repeat passes of a single antenna or antennas on separate airborne platforms to perform interferometry, given that the pixel correlation remains sufficiently high. The difficulty here is that, in general, the baseline is no longer fixed. This means that, as mentioned above, the phase approximation at the point of closest approach may no longer be valid and a more sophisticated approach is required.
- **Precise phase-center location**. In Chapter 5, the interferometry derivation assumes that the bulk of the interferometric phase is due to the height offset of the phase-center of a scattering-cell. This assumption is reasonable for distributed targets, but not all targets in general. It should be possible to specifically locate the azimuth position of the phase-center by forming multiple sub-apertures of the received data. However, in order to unambiguously resolve the difference between ground-range and height, more than two observations (i.e., receive antennas) are required. A more general derivation and analysis of cross-track interferometry using more than two antennas could provide more accurate height/position estimates.
- **Comparison of image spectra**. Backprojection and frequency domain methods produce images with mostly overlapping but slightly different frequency spectra. It would be interesting to investigate these differences and any resulting implications.
- **Hybrid interferometry**. In principle, it is possible to add back the flat-earth phase after forming backprojected images and then perform traditional interferometry. This

suggests that it may be possible to create a hybrid interferometric method that combines both forms and perhaps has the advantages of each.

Appendix A

Autofocus

A.1 Introduction

Due to uncompensated or unmeasured motion, atmospheric propagation effects, hardware limitations, or processing approximations, there may be phase errors in raw synthetic aperture radar (SAR) data. Autofocus algorithms are commonly employed in SAR to remove phase errors. These errors have varying effects on image quality depending on the nature of the errors. All share the commonality that they reduce image focus.

Autofocus techniques typically fall into two categories: model based and estimation based [4]. Model based autofocus methods estimate a set of coefficients that parameterize a model which is used to compensate for phase errors. Estimation based methods estimate a phase function which is used to compensate for phase errors.

Many autofocus methods have been developed for SAR. Some of the more common methods are map-drift autofocus (MDA) [32], phase-gradient autofocus (PGA) [33, 35], and prominent point processing (PPP) [34].

The map-drift autofocus methods are model based and operate by forming two or more subaperture images for a given scene. The necessary translation required to register the images is used to estimate coefficients in the phase correction model. If a scene is divided into two subapertures then a quadratic phase error estimate results. Increasing the number of subapertures yields higher order estimates. MDA is thus able to provide an accurate compensation but only for low-order phase errors since it is limited to estimating a small number of parameters.

Phase-gradient autofocus is an estimation based method. In it, an isolated bright target is taken at each range gate. The phase characteristics of each target are examined and averaged together from which the phase correction function is estimated. PGA has the advantage that it is able to accurately estimate high-order phase errors. However, it also has restrictions on imaging geometry and requires isolated, bright targets in the scene at various ranges. Targets with low SNR or that are too close together can present difficulties.

Prominent point processing is an estimation method that measures the pulse-to-pulse range and phase variations of several prominent point targets in a scene. Thus, it is able to accurately estimate low and high-order phase errors. It is also able to measure rotational motion in SAR/inverse-SAR (ISAR) collections. Its drawbacks are the requirement of prominent, uninterrupted point targets for phase and range estimation, as well as being potentially interactive (i.e., not strictly automatic).

Most autofocus methods assume spotlight-mode imaging where, after polar formatting, an inverse Fourier transform of the output image in azimuth yields the original range-compressed data. For stripmap SAR data, a simple inverse transform does not provide this. For example, to apply traditional autofocus methods to a stripmap image requires deconvolving with the azimuth matched filter (i.e., Doppler chirp). This is not well posed as it would be better to operate on each pulse of the range-compressed phase history data prior to image formation.

An additional limitation of most autofocus methods is the requirement of linear platform motion. This arises because of the assumption of a linear FM Doppler chirp in the range-compressed data to estimate phase errors. Large, uncompensated motion or more exotic flight geometries (i.e., circular SAR) pose problems for traditional autofocus algorithms.

These constraints on autofocus have not previously been prohibitive because the imaging scenario is already constrained, that is, use of frequency domain methods already poses limitations on the SAR mode and geometry. However, with backprojection, having comparatively few constraints on platform motion (e.g. a roughly elliptical shaped flight track is acceptable), it is desirable to obtain a more general autofocusing algorithm that is similarly unconstrained.

This appendix presents a type of autofocus method which has previously been used in optics [37] and may be adapted to synthetic aperture radar. Section A.2 gives some common sources of phase error in SAR. Section A.3 introduces the autofocus methodology. Finally, Section A.4 shows preliminary results for simulated and experimental data.

A.2 Phase Error

In traditional SAR imaging there are three common sources of phase error: (1) radar system timing errors (including "signal propagation through media with unknown spatially varying propagation velocity" [75]), (2) antenna position measurement errors, and (3) approximations in motion compensation and image formation. In backprojection, we exchange the third error source for an alternate: target location errors. The following discusses each error source for backprojection.

Radar System Phase Error

As the radar system is dependent on a clock (e.g. local oscillator) that is subject to drift and other effects, the result is small inaccuracies in the measurement of time-of-flight of the pulse. Usually this difference is within a small fraction of a second, but as the period of a wave at the carrier frequency may be nanoseconds or less, any uncertainty may lead to phase errors. For high-altitude SARs, variations in propagation velocity through the atmosphere cause a similar effect. These errors can often be approximated as constant across a given pulse. When this is the case, a single scalar estimate of the phase error is sufficient to compensate for this.

Position Measurement Errors

As already shown in Chapter 3, the backprojection algorithm operates by calculating the ideal azimuth matched filter from knowledge of the range to scattering-cell at every pixel in the output image. This dependence on knowledge of range-to-target is common for all SAR image formation algorithms. However, as most others form images in the slant-plane, the range-to-target is implicit in the radar data itself and is sufficient for image formation. The backprojection algorithm requires explicit knowledge of the range-to-target at every pulse. This makes the backprojection process highly sensitive to errors in antenna position. Thus, as shown in the aforementioned chapter, precise antenna position measurements are required. This places limitations on the acceptable inertial navigation system (INS) for a given collection geometry. In SAR, this usually calls for use of a high-grade inertial measurement unit (IMU).

As shown in the Section 3.2.1 on page 29, the backprojection matched filter is a function of the range-to-target (pixel or cell) at each slow-time sample. This range may be obtained given the scattering-cell location and phase-center of the antenna according. Thus, errors in the position estimate of the phase-center of the antenna lead to phase errors in the backprojected image. The phase error ϕ_e for a specific antenna and target position as a function of position estimate error is

$$\phi_e \quad = \quad \exp\left[j\,2k\sqrt{\left(x+x'\right)^2+(y+y')^2+(z+z')^2}\right], \tag{A.1}$$

where (x, y, z) are the true coordinates of the the antenna phase-center relative to the pixel center and $(x^{'}, y^{'}, z^{'})$ are the measurement errors. This may be approximated as

$$\phi_e \approx \exp\left[j\frac{2k}{r}\left(x^{'}x+y^{'}y+z^{'}z\right)\right], \tag{A.2}$$

if the measurement errors are small and the azimuth coordinate $x \ll r$ where $r = \sqrt{y^2+z^2}$, the range at the point of closest approach.

Figure A.1 shows the magnitude of the phase error for various geometries as a function of the lateral position error to wavelength ratio (e.g. $y^{'}/\lambda$) . Multiple lines are plotted, each representing a different incidence angle to the target. A horizontal line is placed at $\pi/8$, which serves as a reminder that any phase error above this becomes a source of significant phase error in the backprojection sum.

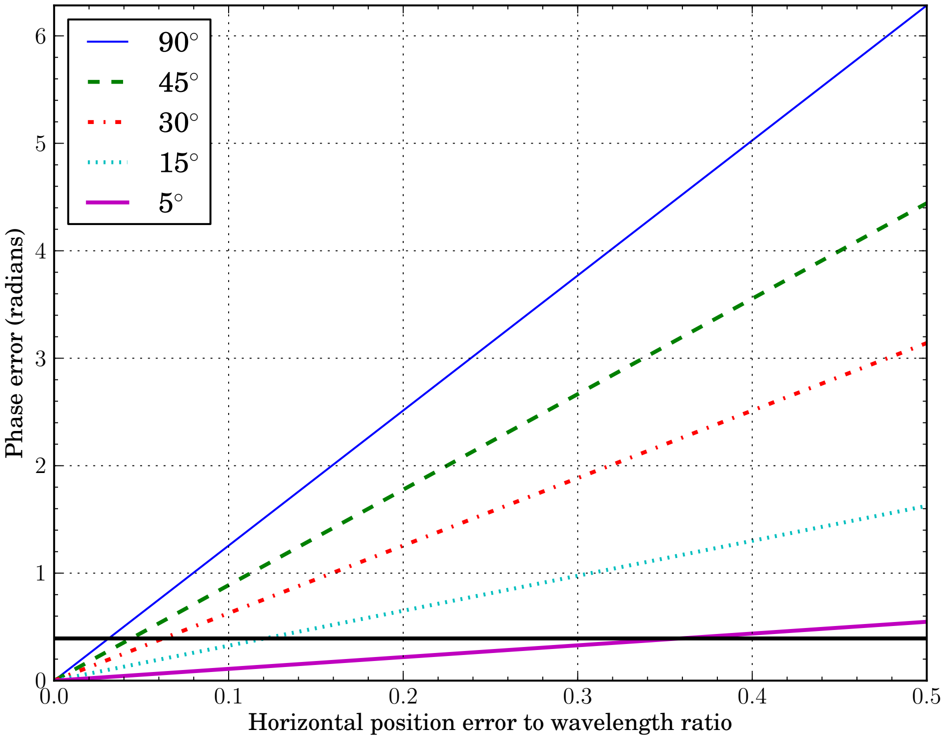

Figure A.1: Estimate of the phase error for various position estimate errors as a function of the ratio of position error magnitude to wavelength. Multiple lines are shown for various coordinate to slant-range ratios. The horizontal line marks the phase $\pi/8$, above which phase errors become significant.

DEM Errors

The backprojection formula requires knowledge of the position in three-space of every scattering-cell calculated. To aid the backprojection process, a priori knowledge of the cell's vertical position is usually provided via a digital elevation map (DEM) of the imaged terrain. A bias error (i.e., a height offset) in the elevation map results in varying effects in the output image depending on the SAR collection geometry and the exact steps performed in backprojection processing. As seen in Sec. 3.4, DEM errors become significant if they are large, if there is significant shift in the phase-center of the antenna, or if there is a high degree of non-ideal motion. These become sources of phase error that reduce the quality of the output image.

A.3 Autofocus

A.3.1 Methodology

As indicated previously, most autofocus methods involve analysis of the formed image (i.e., range- and azimuth-compressed) in order to estimate proper correction factors. This method differs in that the autofocus adjustment is calculated on a per-pulse basis prior to image formation. Recall that the maximum pixel magnitude is obtained when the backprojection matched filter uses the exact range-to-target at every pulse in the summation; a distance error reduces the pixel magnitude. This distance error may instead be considered a corresponding phase error. In fact, any and all phase error terms present at each pulse may be lumped into a single value.

The effect of this may be described in an intuitive manner. Each sample from a range-compressed pulse is a complex value with contributions from a group of illuminated targets and also contributes to a group of pixels in the output image. This complex value is a vector representing magnitude and phase. Azimuth matched filtering represents a rotation of that sample at a given pulse. When perfect matched filtering occurs, all of the sample vectors are rotated to the same direction such that when they are summed, all sum constructively yielding a result with large magnitude and phase equal to the intrinsic phase of the target cell. The errors described earlier distort this process so that each sample no longer adds in phase and a degraded pixel sum results.

Because the matched filtered pulses with phase error do not sum in phase, the backprojection sum yields a lower pixel magnitude. This suggests the simple solution of applying a phase correction to each pulse that maximizes the magnitude of the pixel sum. While this approach works well with isolated, prominent targets, it may not work in general. If multiple “bright” targets are located near the target of interest, their returns may overlay at some pulses. If all the samples are assumed to come from a single source (i.e., the target of interest), then the samples containing the bright returns of nearby objects are erroneously rotated to maximize the pixel magnitude of the target of interest. This can result in target “ghosting” in the output image. In addition, because of noise and clutter this may not perform well with lower SNR pixels. It is therefore advantageous to simultaneously focus a group $\mathcal{M}$ of pixels

$\left(a_1, a_2, \ldots, a_{|\mathcal{M}|}\right)$. Here, $|\mathcal{M}|$ indicates the cardinality of set $\mathcal{M}$ (i.e., the number of elements in the set).

In order to focus a group of pixels, some kind of optimization method utilizing an objective function is required. The proposed autofocus technique estimates the phase error at each pulse using coordinate descent optimization. A similar approach is taken by [76] for convolution backprojection. The coordinate descent method performs a *line search* at a point along a single coordinate direction for each iteration [77]. In other words, the function $F(\mathbf{x})$ with $\mathbf{x} = \left(x_1, x_2, \ldots, x_{|\mathcal{P}|}\right)$ is minimized one component x_p at a time. After all coordinates have been searched, a single descent iteration $\mathbf{x}^k$ (with iteration index k) is complete. Therefore, beginning with an initial guess $\mathbf{x}^0$ for a local minimum of F, one can iteratively obtain the sequence $\mathbf{x}^0,\ \mathbf{x}^1,\ \mathbf{x}^2,\ \ldots$. This guarantees that at each iteration

$$F(\mathbf{x}^0) \geq F(\mathbf{x}^1) \geq F(\mathbf{x}^2) \geq \ldots . \tag{A.3}$$

The function minimization for each component in $\mathbf{x}$ proceeds as follows. Given the kth iteration $\mathbf{x}^k$, the ith coordinate of $\mathbf{x}^{k+1}$ is

$$x_i^{k+1} = \arg\min_{y \in \Omega} F(x_1^{k+1}, \ldots, x_{i-1}^{k+1}, y, x_{i+1}^{k}, \ldots, x_n^{k}), \tag{A.4}$$

where Ω is the domain of possible values y can take. A given iteration is complete when this minimization has been performed for all coordinates i. Note in the equation above, the coordinates are minimized in ascending order beginning with x_1, however, any ordering that traverses all coordinates may be used.

In this optimization scheme, each coordinate of $\mathbf{x}$ corresponds to the phase correction of a single pulse. The optimization is performed by minimizing some objective function F for each coordinate/contribution. The objective functions examined are given below. One descent iteration consists of performing this process at each coordinate to minimize the objective function.

The coordinate descent method differs from a *gradient descent* method (also known as *steepest descent*) where optimization is performed by steps proportional to the negative of the gradient at each point. Because $\mathbf{x}$ has cardinality equal to the number of pulses contributing to the backprojected pixel sums (i.e., a large number), a gradient descent method could be computationally prohibitive. However, it can be shown that the sequence of Eq. A.3 has similar convergence properties to the gradient descent method [78].

An important note when optimizing a group of pixels is that the same phase correction is applied to every sample at a given pulse. This means that a given group of pixels, termed a "tile," must be kept small enough that the same approximate phase error can be removed from each. For per-pulse radar system phase errors, this is the case for all samples in a given pules. For motion related phase errors, the tile size is a function of the slant-range to the tile and the expected magnitude of the motion errors. The result is tiles that are wide in azimuth (to examine the range migration curve of many targets with overlapping range migration curves) but possibly narrow in range (to obtain an accurate phase error estimate where the phase error is approximately the same across the given range swath).

This autofocus method is advantageous because it requires no general assumptions of platform motion in order to operate. Other methods of autofocus typically only operate on spotlight mode data. This is because of underlying assumptions made in the derivation of the autofocus algorithm. For example, many methods examine the azimuth spectrum of the formed image in order to determine the phase correction that should be applied. However, this assumes that the azimuth direction and the along-track direction are equivalent (i.e., orthogonal to the range or cross-track dimensions). This is certainly true for many flight geometries, but is not true in the case of an aircraft circling around a stationary point on the ground. For this case, a more general autofocusing method is required.

A.3.2 Objective Functions

Although there are many reasonable objective functions that may be used for the purpose of optimization, this analysis is limited to three cases: maximum contrast, minimum entropy, and elliptic projection maximum contrast.

The maximum contrast method takes the form

$$F = -\sum_{m\in\mathcal{M}} a_m^2. \tag{A.5}$$

This method maximizes the L^2-norm of the pixel or tile.

Maximum contrast methods have previously been shown to be particularly well suited for use in SAR because they maintain a good balance between high and low return areas [37]. "Furthermore, this metric has been shown to produce phase error estimates equivalent to maximum likelihood estimates under particular conditions" [79].

The minimum entropy method has the form

$$F = -\sum_{m\in\mathcal{M}} a_m \log a_m. \tag{A.6}$$

Finally, the elliptic projection method is given as an analytic solution to an elliptic projection of the solution space to also maximize contrast. It is based on the work of [76]. This method is termed the elliptic or Ash method.

A.3.3 Drift Compensation

The previous analysis for estimating phase error assumes that the correct range compressed sample contributing to a given target / pixel is chosen for every pulse in the backprojection summation. This requires aircraft position measurements to be accurate to at least the same order of magnitude as the resolution cell. If the measurement errors are zero-mean with low variance then the correct samples are still chosen on average (resulting in good autofocus performance). Problems occur when the zero-mean/low-variance assumption is violated. An example of this is drift in the position measurement.

Position drift is common in measurements made by IMUs. As these sensors integrate measurements from accelerometers, drift is almost unavoidable. A key figure of merit in judging the quality of IMUs is the amount of drift a given IMU will present over a given period of time. If the drift over a given azimuth aperture is small then the correct range samples are still chosen, but if it grows larger then incorrect samples are used in the backprojection sum. Particularly troublesome is drift in the along-track direction as it leads to larger errors in estimation of the range-to-target than drift in the lateral directions.

One method for removing these problems is to estimate the position measurement drift. This can be performed similarly to the maximum contrast coordinate descent method described above. A bounded optimization is performed on the drift estimate, calculating the amount of drift that maximizes the L^2 norm of a given pixel or group of pixels. Note that drift is a first order effect, but a similar approach could be used to estimate higher-order motion errors if *a priori* knowledge of the presence such errors exists.

In general, several iterations may be required in order to descend on the optimal drift values. As shown previously, if the true platform motion is perfectly straight in range and elevation then there is no unique solution providing the position of the target (i.e., the optimization may converge to a drift in elevation / azimuth that is not correct). However, perfect platform motion is not generally the case for airborne imagery.

After the position drift is estimated, the antenna positions are updated accordingly. Note that this only removes the linear trend in the estimate error. Other motion errors are still present but are now zero mean. This means that on the average the correct range-to-target is used for every pulse and thus the correct range samples are selected in the backprojection sum. The aforementioned autofocus method may now be used to remove any remaining phase errors.

A.4 Results

The elliptic method provides an analytic estimate of the phase error for each pulse throughout a coordinate descent iteration. However, the maximum contrast and minimum entropy methods require a numerical method to estimate the phase error at each pulse. To do this, a scalar bounded minimization is performed from $-\pi \leq \hat{\phi}_e \leq \pi$ using Brent's method [80]. Brent's method is a root-finding algorithm which combines several methods (bisection method, secant method, and inverse quadratic interpolation). It is as reliable as the bisection method but can be as computationally efficient as the less reliable methods.

Table A.1: Simulation Parameters

Parameter	Value
Wavelength	0.3 m
Azimuth beamwidth	0.3 rad
Along-track velocity	50 m/s
PRF	200 Hz
TX bandwidth	300 MHz

The drift compensating algorithm, on the other hand, must find a vector of three coordinates, not a scalar value. An attempt was made to use Brent's method on each coordinate individually, but resulted in poor convergence. Instead, a modification of Powell's method [81, 82] is used, which is a conjugate direction method. I have found that it has the best convergence results of any method examined. Other methods tested include sequential least squares, the Nelder-Mead method [83, 84] (uses the Simplex algorithm), the Polak-Ribiere [85] (a nonlinear conjugate gradient algorithm), and the Broyden, Fletcher, Goldfarb, and Shanno method [86] (a quasi-Newton method using only first derivatives).

Simulated data sets are created using the specifications in Table A.1. For results requiring zero mean Gaussian noise be added to the position estimates, a standard deviation of 0.1 m at every pulse was used. For results requiring drift, 1.5 m/s in the along-track direction (1/50 the forward velocity) and 2 cm/s in the cross-track direction were used. These values were arbitrarily chosen and represent drift values well beyond those expected with a reasonable IMU/GPS combined INS.

Figure A.2 compares the performance of the various autofocus objective functions on a simulated stripmap data set, where the antenna positions have random Gaussian noise added. Only one iteration of autofocusing is performed. A range cell migration curve of a range-compressed point target is selected from the simulation and plot the backprojected phase error (in radians) at every pulse. The original backprojected data without autofocus exhibits a large amount of phase error. After autofocusing using the elliptic/Ash method, the phase error is reduced significantly. The maximum contrast and minimum entropy methods both show even more reduction in phase error, with the minimum entropy solution performing slightly better.

Figure A.3 shows the backprojected images of the simulated data set using a single iteration with each of the autofocusing methods. Two targets are present at this location in the

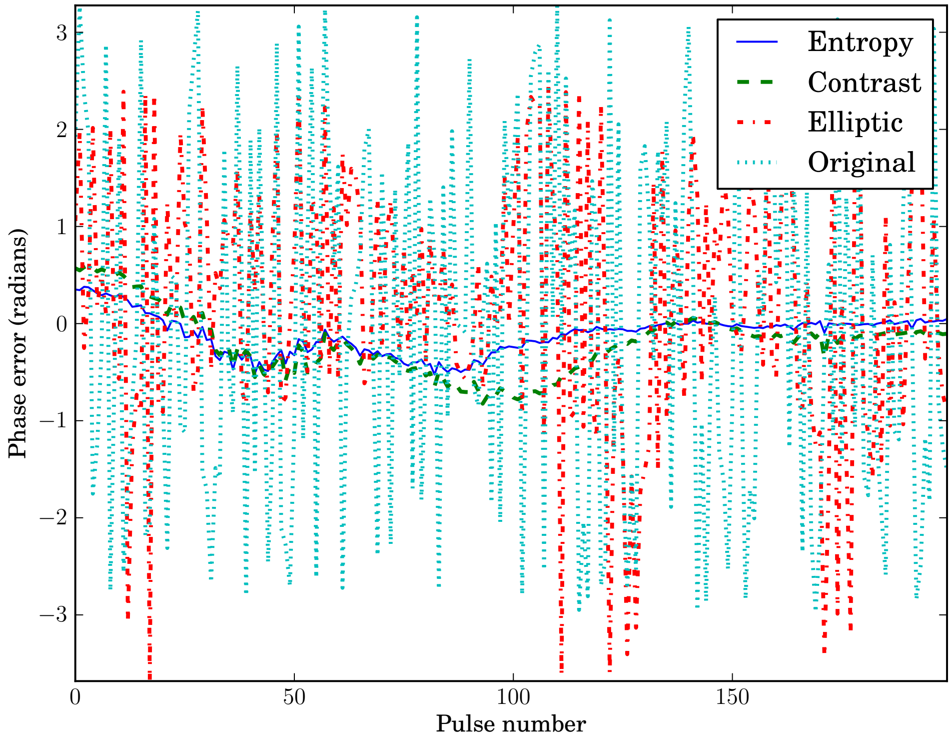

Figure A.2: Phase error for each pulse at the target's peak

data. Plot (a) shows the original backprojected image without any autofocusing. Because of the large phase error present, the targets are blurred in range and particularly in azimuth. Plot (b) shows the result of autofocusing using the Ash/elliptic method. The blurring is significantly reduced and the individual point targets are now distinguishable, however some spreading of the azimuth energy is still noticeable. This corresponds to the phase error remaining after autofocusing as seen in the previous figure. The plot in (c) demonstrates focusing using the maximum contrast method and (d) demonstrates the minimum entropy method. Note that the axes have been zoomed on these two images to show more detail. These methods show similar levels of performance, although the side lobes are lower with the minimum entropy method.

These features are more easily seen in Figure A.4 which contains an azimuth slice through one of the point targets. In (a) the three autofocus methods are plotted together and

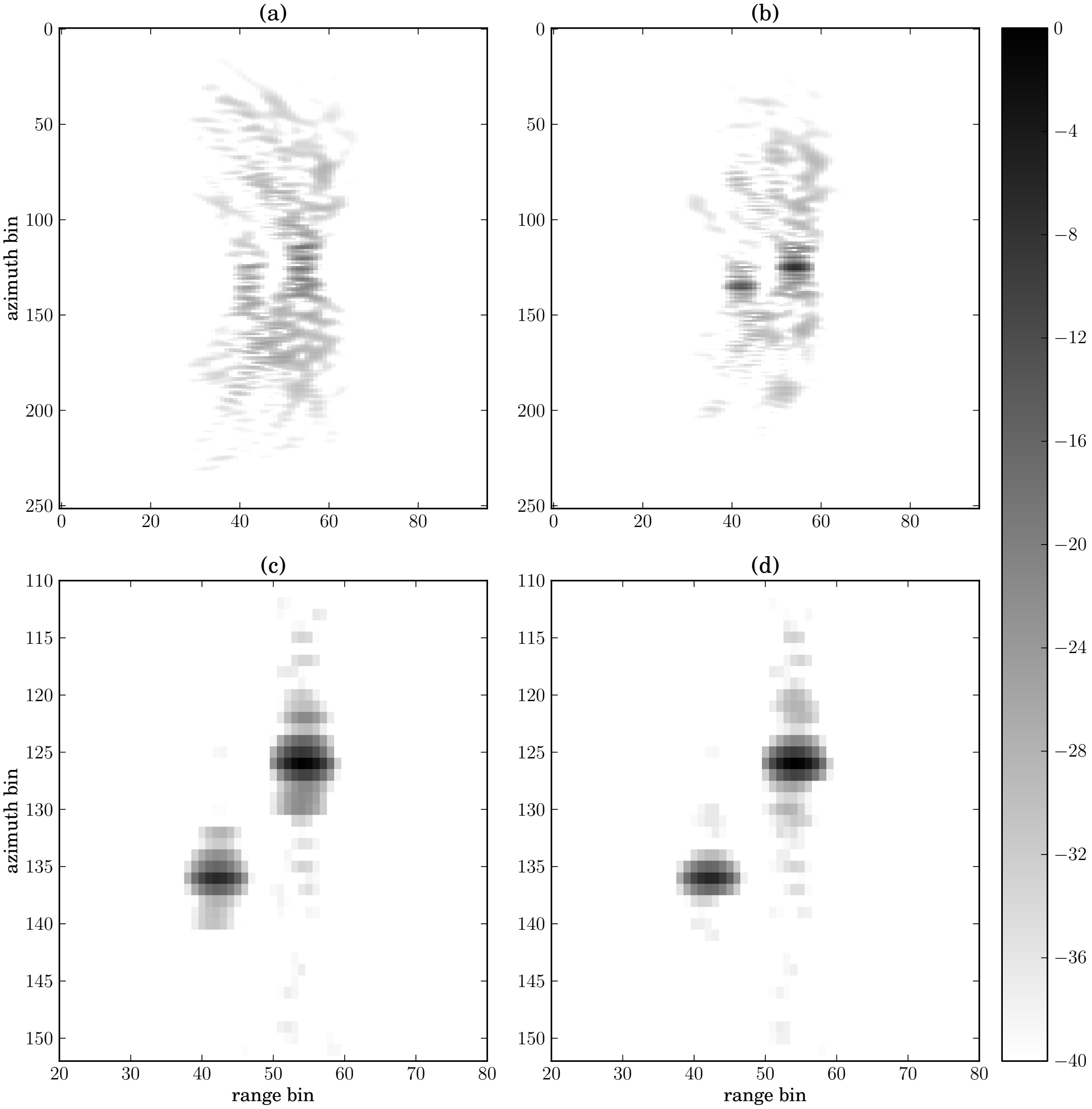

Figure A.3: Backprojected images in dB of simulated data with two point targets. (a) shows the original image and (b-d) show autofocused results for various objective functions: (b) elliptic, (c) maximum contrast, and (d) minimum entropy.

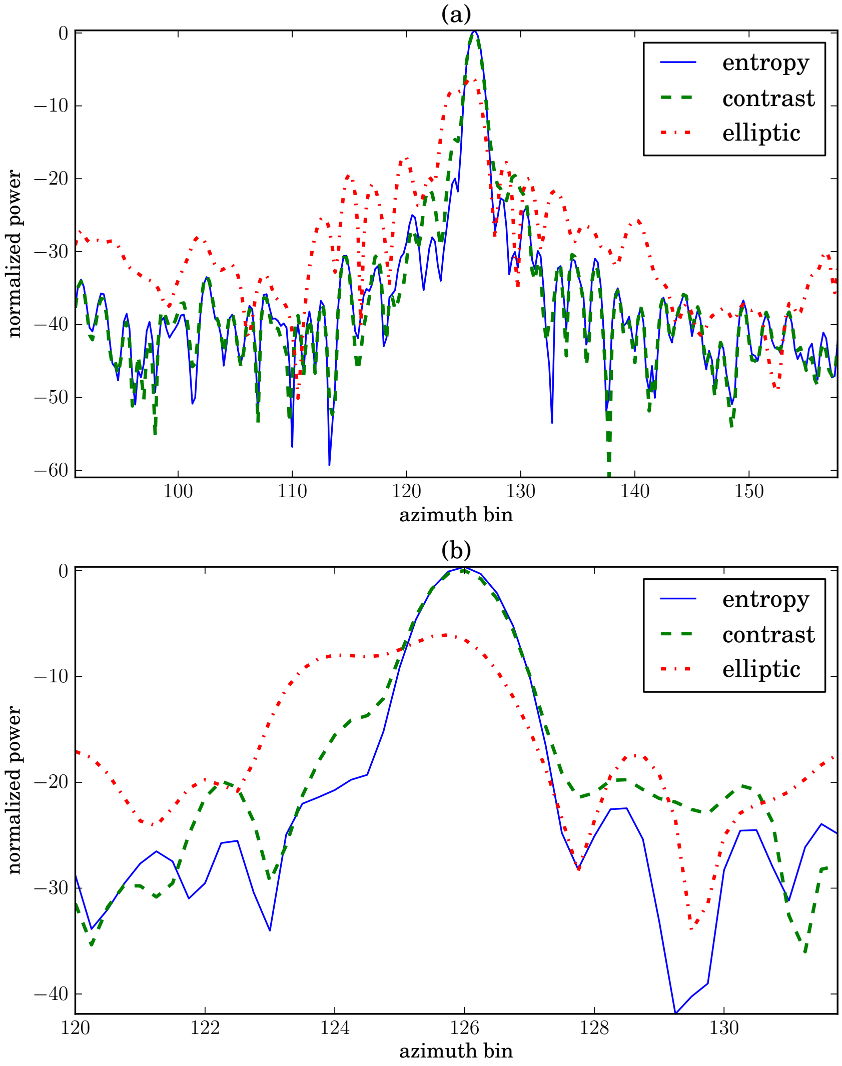

Figure A.4: Azimuth slices through one of the autofocused point targets from Fig. A.3 for each autofocus objective function. The lower plot (b) shows a zoomed-in region around the central peak.

in (b) the central region around the main lobe is zoomed. The lobe peak and width is nearly identical for both the maximum contrast and minimum entropy methods.

The performance of the autofocus algorithm is examined using actual SAR data collected aboard a low-altitude aircraft. The sensor is a generic SAR at Ku-band with 1.5 GHz bandwidth. A particular data set was chosen where the backprojected image suffers from tar-

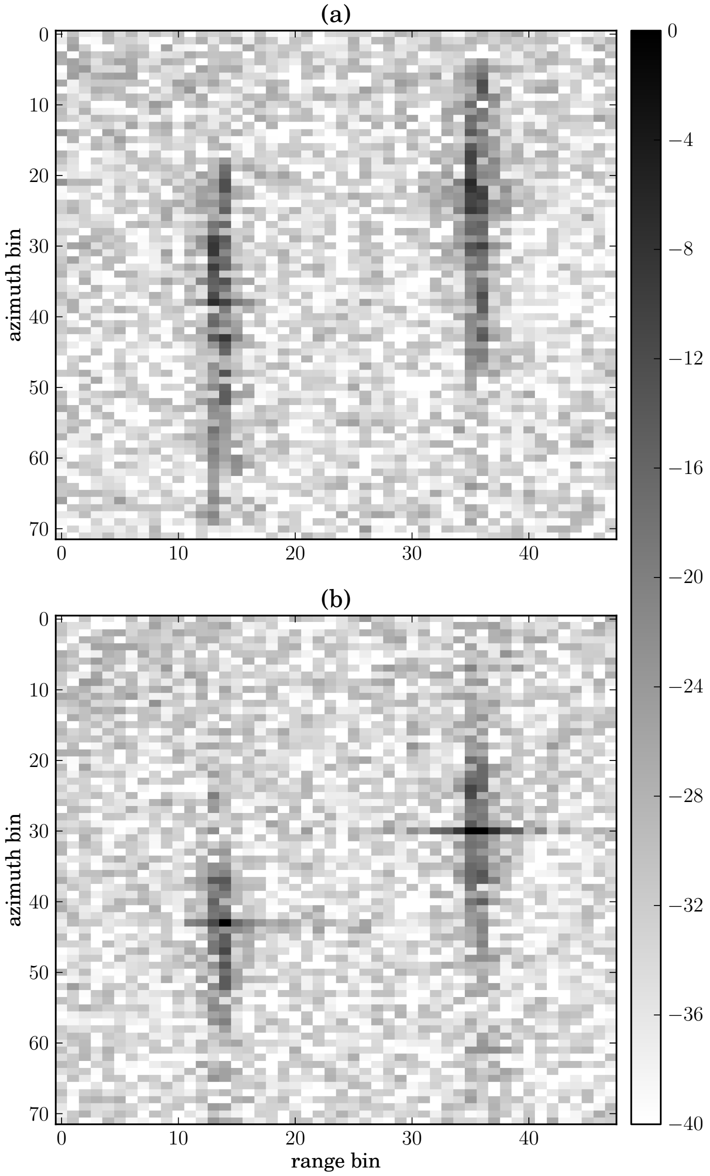

Figure A.5: Performance comparison of actual SAR data (a) before and (b) after autofocus. The two targets are corner reflectors lying on bare earth.

get smearing in azimuth. The original image and the autofocused image are given in Figure A.5. Here, two corner reflectors are present, lying on bare earth.

Although these results are preliminary, they show that under certain circumstances this is a viable method of autofocus for backprojected data.

Appendix B

Compression

This appendix provides a derivation of pulsed/continuous-wave range compression and azimuth compression. These two steps constitute a simple form of the range-Doppler image formation algorithm. This derivation is similar to that given in [87].

B.1 LFM Pulse Compression

B.1.1 Pulsed

For simplicity, this derivation ignores azimuth effects and assumes that a reflected target's signal is a time delay, t_o, of the original signal. It also assumes that the signal is single-side band as opposed to double-side band (a full derivation of double-side band SAR is developed by Robertson [12]). These assumptions simplify the derivation but still provide an accurate model of range compression [88].

The transmit and received signals are modeled by

$$x_{\mathrm{Tx}}(t) = \frac{1}{2}\cos\left(\omega_c t + \beta t^2\right) \qquad \text{and} \tag{B.1}$$

$$x_{\mathrm{Rx}}(t, t_o) = \frac{1}{2}\cos\left(\omega_c (t - t_o) + \beta (t - t_o)^2\right), \tag{B.2}$$

respectively, where $\beta = \pi\,\mathrm{BW}/T$ represents the slope of the linear frequency vs time. We note here that t is in "fast time." Hardware mixes the signal down to an intermediate frequency,

w_d, and then low-pass filters it,

$$\begin{aligned}
m_{\text{if}}(t) =& x_r(t) \otimes \cos(w_d t) \\
=& \frac{1}{2} \cos\left(w_c(t-t_o) + \beta(t-t_o)^2\right) \cos(w_d t) \\
=& \frac{1}{4} \cos\left(w_c(t-t_o) + \beta(t-t_o)^2 - w_d t\right) + \frac{1}{4} \cos\left(w_c(t-t_o) + \beta(t-t_o)^2 + w_d t\right) \\
\overset{LPF}{\Longrightarrow}& \frac{1}{4} \cos\left(w_c(t-t_o) + \beta(t-t_o)^2 - w_d t\right). \qquad \text{(B.3)}
\end{aligned}$$

This is the signal that is digitized by the hardware and recorded. Next, substituting $\omega_o = \omega_c - \omega_d$ and taking the Hilbert Transform yields

$$\begin{aligned}
m_{\text{if}}(t) &= \frac{1}{4} \exp\left[j\left(\omega_c(t-t_o) + \beta(t-t_o)^2 - (\omega_c - \omega_o)t\right)\right] \\
&= \frac{1}{4} \exp\left[j\left(\omega_o t + \beta(t-t_o)^2 - \omega_c t_o\right)\right]. \qquad \text{(B.4)}
\end{aligned}$$

At this point, it is useful to calculate the minimum Nyquist sampling rate. By examining the phase, $\phi(t)$, it can be seen that the phase derivative, $\dot{\phi}(t)$ is

$$\begin{aligned}
\phi(t) &= \omega_o t + \beta(t-t_o)^2 - \omega_c t_o, \\
\dot{\phi}(t) &= \omega_o + 2\beta(t-t_o). \qquad \text{(B.5)}
\end{aligned}$$

$\dot{\phi}(t)$ represents frequency, whose maximum occurs for every $t - t_o = T$. Thus, based on the Nyquist criterion the minimum sampling rate is

$$S_{\text{min-rate}} = 2(f_o + BW). \qquad \text{(B.6)}$$

The matched filter is given by

$$h(t) = \exp\left[j\left(\omega_o t + \beta t^2\right)\right]. \qquad \text{(B.7)}$$

Although $h(t)$ is infinite in length, for a finite-length matched filter with large T, this simplifying assumption is valid. *Pulse compression* or *range compression* is then performed by matched filtering, i.e., correlating $m_{\text{if}}(t)$ and $h(t)$:

$$\begin{aligned}
m(t) &= m_{\text{if}} \otimes h^*(t) \\
&= \int m_{\text{if}}(t+\tau)h^*(\tau)d\tau \\
&= \frac{1}{4}\int e^{j\left(\omega_o(t+\tau)+\beta(t-t_o+\tau)^2-\omega_c t_o\right)} e^{-j(\omega_o\tau+\beta\tau^2)}d\tau \\
&= \frac{1}{4}e^{j\left(\omega_o t+\beta({}^{-}2t_o t+t_o^2+t^2)-\omega_c t_o\right)} \int e^{j\beta(2t\tau-2t_o\tau)}d\tau.
\end{aligned}$$

Applying the limits of integration,

$$\begin{aligned}
m(t) &= \frac{1}{4}e^{j\left(\omega_o t+\beta(t-t_o)^2-\omega_c t_o\right)} \int_{-t+t_o}^{T-t+t_o} e^{j\beta(2t\tau-2t_o\tau)}d\tau \\
&= \frac{1}{4}\frac{e^{j\left(\omega_o t+\beta(t-t_o)^2-\omega_c t_o\right)}}{2j\beta(t-t_o)}\left(e^{2j\beta(T-t+t_o)(t-t_o)} - e^{2j\beta(-t+t_o)(t-t_o)}\right) \\
&= \frac{1}{4}\frac{e^{j\omega_o t-j\omega_c t_o}}{2j\beta(t-t_o)}\left(e^{2j\beta T(t-t_o)}e^{-j\beta(t-t_o)} - e^{-j\beta(t-t_o)}\right) \\
&= \frac{1}{4}\frac{e^{j\omega_o t-j\omega_c t_o}}{\beta(t-t_o)}e^{j\beta T(t-t_o)}\sin\left(\beta T(t-t_o)\right)e^{-j\beta(t-t_o)} \\
&= \frac{T}{4}e^{j\omega_o t-j\omega_c t_o}e^{j\beta(t-t_o)(T-1)}\text{sinc}\left(\beta T(t-t_o)\right).
\end{aligned} \tag{B.8}$$

Examining Eq. B.8 leads to some important points. The $\frac{T}{4}$ amplitude term shows that the SNR is a function of the chirp period—thus a longer chirp leads to higher SNR. The sinc effect resulting from autocorrelation is also visible. The width of the sinc is inversely proportional to the bandwidth of the chirp. This suggests that the resolution in range is a function of chirp bandwidth and not period. Resolution is treated in Appendix C.

B.1.2 Continuous-wave

Figure B.1 shows the LFM-CW transmit/receive model of frequency versus fast-time. The LFM transmit up-ramp begins at frequency f_{min} and continues to f_{max}. Received returns off point targets are delayed by times t_0, t_1, ..., t_n from the transmit signal. T represents the duration of one up-ramp. Notice that at any given time, targets farther in range correspond to a greater frequency difference from the transmit signal.

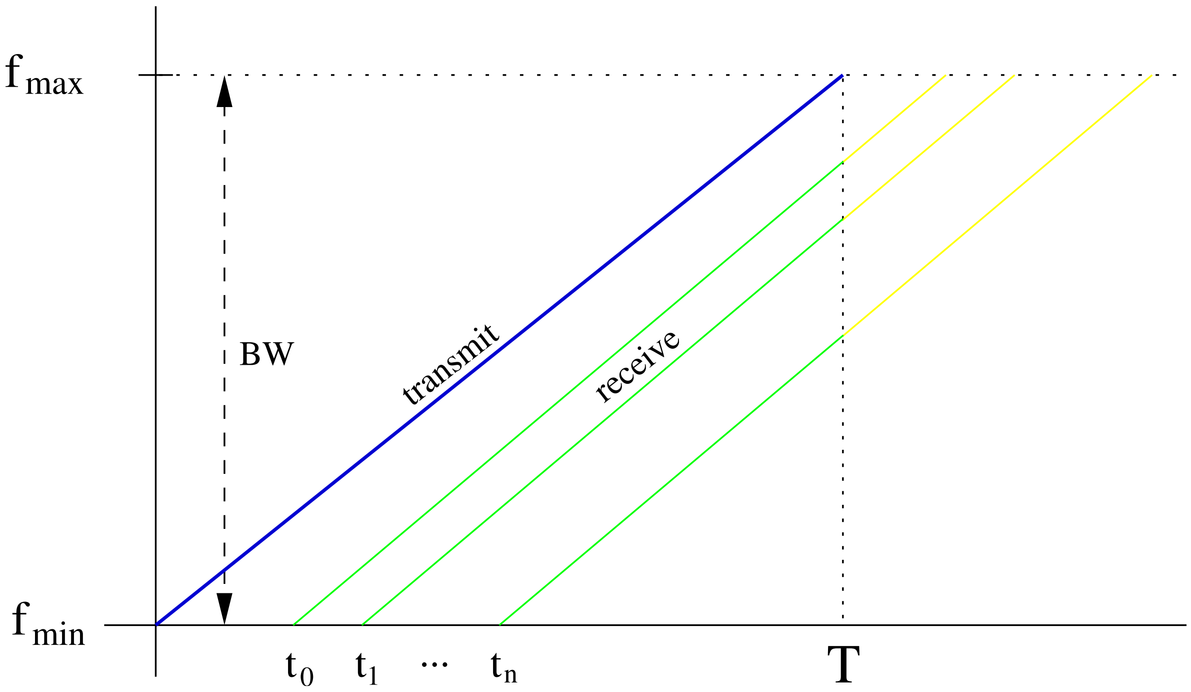

Figure B.1: Illustration of a scattered LFM-CW signal. The horizontal axis represents fast-time and the vertical axis represents frequency. The transmit signal displays the linear frequency up-ramp, after which delayed copies are received from point scatterers at times t_0, t_1, … , t_n. The up-ramp interval is T.

The derivation of LFM-CW range compression follows as similar development as [88]. The derivation begins with models for the transmitted and received signals as in the pulsed case, except the signals are expressed in exponential form for convenience:

$$x_{\mathrm{Tx}}(t) = \exp\left[j\left(\omega_o t + \frac{\beta t^2}{2} + \psi\right)\right] \qquad \text{and} \tag{B.9}$$

$$x_{\mathrm{Rx}}(t, t_o) = \exp\left[j\left(\omega_o (t - t_o) + \frac{\beta (t - t_o)^2}{2} + \psi\right)\right]. \tag{B.10}$$

The difference in amplitude between the transmitted signal and received is ignored here, and ψ represents an arbitrary phase present in the signal. The hardware mixes these two signals together and low-pass filters:

$$\begin{aligned} m(t) &= x_t(t) \otimes x_r^*(t, t_o) \\ &= \exp\left[j\left(\omega_o t + \frac{\beta t^2}{2} + \psi\right)\right] \exp\left[-j\left(\omega_o (t - t_o) + \frac{\beta (t - t_o)^2}{2} + \psi\right)\right] \\ &= \exp\left[j(\omega_o t_o + \beta t_o t - \frac{\beta t_o^2}{2})\right]. \end{aligned} \tag{B.11}$$

This is the signal that is digitized and recorded. As shown above, by examining the phase, $\phi(t)$, it can be seen that

$$\begin{aligned} \phi(t) &= \omega_o t_o + \beta t_o t - \frac{\beta t_o^2}{2}, \\ \dot{\phi}(t) &= \beta t_o. \end{aligned} \tag{B.12}$$

$\dot{\phi}(t)$ represents the frequency difference between the transmitting chirp and received chirp, whose maximum is the frequency difference corresponding to the farthest target in range, represented by time t_n. Thus, the minimum sampling rate is

$$S_{\text{min−rate}} = 2\beta t_n. \tag{B.13}$$

Comparing this result with Eq. B.6, LFM-CW has a much lower minimum sampling rate requirement than pulsed chirp radar.

Range compression is performed by taking the Fourier transform. The limits of integration are ignored here but are retained below.

$$\begin{aligned} I(w) &= \int \exp\left[j\left(\omega_o t_o + \beta t_o t - \frac{\beta t_o^2}{2}\right)\right] \exp\left[-j\omega t\right] \mathrm{d}t \\ &= \exp\left[j\left(\omega_o t_o - \frac{\beta t_o^2}{2}\right)\right] \int \exp\left[\beta t_o t\right] \exp\left[-j\omega t\right] \mathrm{d}t \\ &= 2\pi\delta(\beta t_o - \omega) \exp\left[j\left(\omega_o t_o - \frac{\beta t_o^2}{2}\right)\right], \end{aligned} \tag{B.14}$$

resulting in the compressed signal $I(\omega)$. It is important to note that $I(\omega)$ is in the spatial domain due to the frequency-domain nature of the dechirped signal.

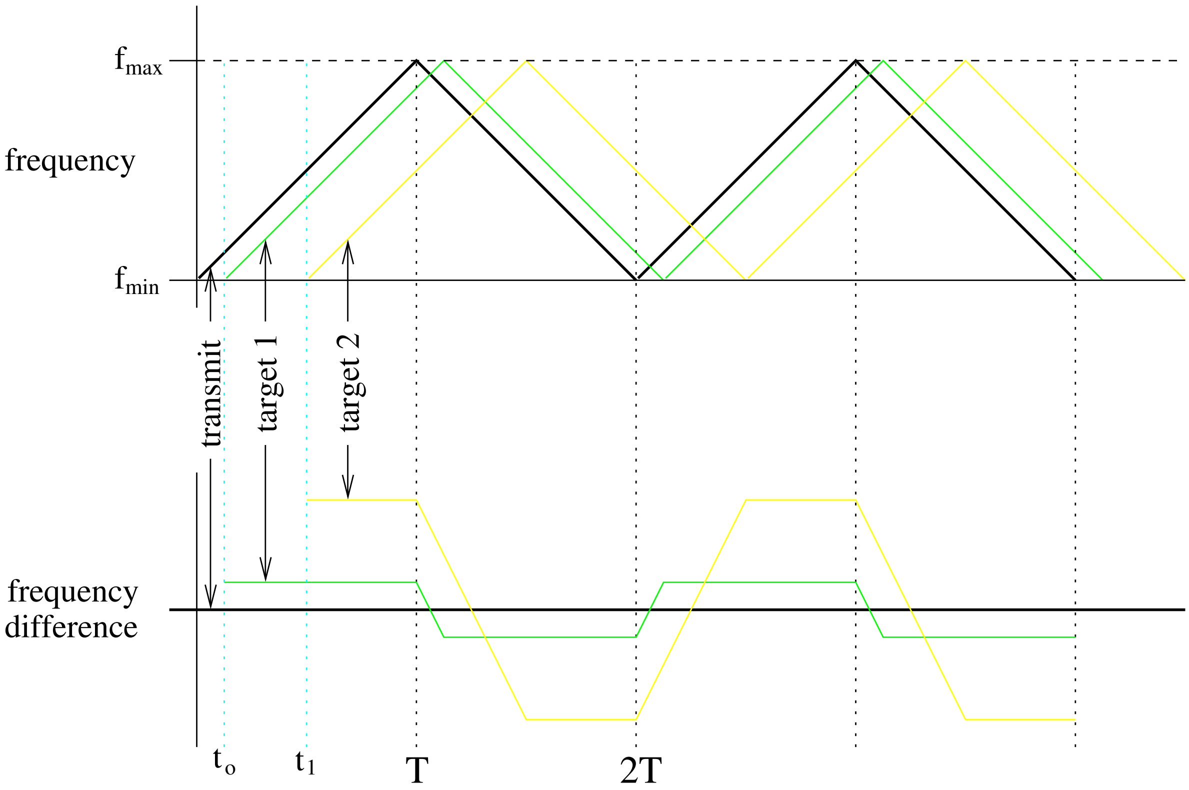

Figure B.2: Sketch showing dechirping LFM-CW frequency difference of two point targets.

As shown in Fig. B.2, the signal for the first target is only present from time t_o to time T. This results in a window, which can be represented in frequency as

$$W_{CW}(\omega) = \begin{cases} (T-t_o)\exp\left[-j\omega\frac{T-t_o}{2}\right]\operatorname{sinc}\left(\frac{\omega(T-t_o)}{2}\right), & \text{if } t_o < T \\ 0, & \text{if } 0 > t_o \text{ or } t_o > T. \end{cases} \tag{B.15}$$

Equation B.14 is convolved with Eq. B.15, resulting in the complete range compressed LFM-CW signal

$$\begin{aligned} I_{CW} &= \int_T I(\omega-\rho)W_{CW}(\rho)\mathrm{d}\rho \\ &= \int_T e^{j(\omega_o t_o - \frac{\beta t_o^2}{2})} 2\pi\delta(\beta t_o - \omega - \rho)(T-t_o)e^{-j\rho\frac{T-t_o}{2}}\operatorname{sinc}\left(\rho\frac{T-t_o}{2}\right)\mathrm{d}\rho \\ &= 2\pi(T-t_o)e^{j(\omega_o t_o - \frac{\beta t_o T}{2} + \frac{\omega(T-t_o)}{2})}\operatorname{sinc}\left((\beta t_o - \omega)\frac{T-t_o}{2}\right)\mathrm{d}\rho. \end{aligned} \tag{B.16}$$

There are several important points from this result. The first is that the amplitude for each target is proportional to $(T - t_o)$, showing that the SNR improves with increased pulse length. Thus, because an LFM-CW period is longer than a conventional pulse, less transmit power is required in LFM-CW to maintain the same SNR. However, targets farther away in range have shorter integration time and therefore suffer from reduced power compared to closer targets.

The argument $(\beta t_o - \omega)\frac{T-t_o}{2}$ of the sinc function is also worthy of notice. Since

$$\beta = \frac{\pi BW}{T},$$

we see that

$$\mathrm{sinc}\left((\beta t_o - \omega)\frac{T-t_o}{2}\right) = \mathrm{sinc}\left((\pi BW - \omega T)\frac{T-t_o}{2T}\right).$$

This shows that the width of the sinc function decreases as the bandwidth increases. As expected, resolution becomes finer for increased bandwidth.

B.2 Azimuth Compression

Returning to the range compressed form of Eq. B.8 and setting $t = t_o$ (note that t now represents slow-time and the difference between t and t_o is inconsequential), the result is

$$m(t) = \frac{T}{4}\exp\left[j\omega_o t_o - j\omega_c t_o\right]. \tag{B.17}$$

Because $\omega_c \gg \omega_o$, the $\omega_o t_o$ term may be assumed to be zero. It is the $\omega_c t_o$ term in Eq. B.8 and Eq. B.17 that is responsible for the azimuth chirp. Continuing,

$$s(t) \simeq \frac{T}{4}\exp\left[-j\omega_c t\right]. \tag{B.18}$$

Because the constant $\frac{T}{4}$ varies depending on the type of SAR model and is unimportant to the derivation, it is replaced with α for convenience. Let $R(t)$ be the range to target. The two-way time for the signal to target is given by

$$t = \frac{2R(t)}{c_o}. \tag{B.19}$$

Substituting this into Eq. B.18 yields

$$\begin{aligned} s(t) &= \alpha \exp\left[-j\omega_c t\right] \\ &= \alpha \exp\left[-j\frac{2\omega_c R(t)}{c_o}\right] \\ &= \alpha \exp\left[-j\frac{4\pi R(t)}{\lambda}\right]. \end{aligned} \tag{B.20}$$

$R(t)$ is of interest as it is responsible for the time varying phase shift of the signal. Returning to Eq. C.9,

$$\phi_D(t) = \frac{2\pi v^2 t^2}{\lambda r},$$

which yields the phase term used for $R(t)$. Combining the previous result with Eq. C.7,

$$\frac{4\pi R(t)}{\lambda} \simeq \frac{4\pi R_o}{\lambda} + \frac{2\pi v^2 t^2}{\lambda R_o}. \tag{B.21}$$

Substituting this result back into Eq. B.20, the final form of the signal used in azimuth compression can be written as

$$\begin{aligned} s(t) &= \alpha \exp\left(-j\frac{4\pi}{\lambda}R(t)\right) \\ &= \alpha \exp\left(-j\frac{4\pi R_o}{\lambda}\right) \exp\left(\frac{-j2\pi v^2 (t - t_o)^2}{\lambda R_o}\right). \end{aligned} \tag{B.22}$$

The final term contains the azimuth chirp, and becomes the basis for the matched filter

$$h_{az}(t) \triangleq \exp\left(\frac{-j2\pi v^2 t^2}{\lambda R_o}\right). \tag{B.23}$$

Performing correlation on the two signals from Eq. B.22 and Eq. B.23,

$$\begin{aligned}
v(t) &= s(t) \otimes h^*_{az}(t) \\
&= \int s(t+\tau)h^*(\tau)d\tau \qquad \frac{-T_a}{2} < \tau + t - t_o < \frac{T_a}{2} \\
&= \alpha\, e^{\frac{-j4\pi R_o}{\lambda}} \int e^{\frac{-j2\pi v^2}{\lambda R_o}(t-t_o+\tau)^2} e^{\frac{j2\pi v^2 \tau^2}{\lambda R_o}} \mathrm{d}\tau \\
&= \alpha\, e^{\frac{-j4\pi R_o}{\lambda}} \int e^{\frac{-j2\pi v^2}{\lambda R_o}\left((t-t_o)^2 + 2\tau(t-t_o)\right)} \mathrm{d}\tau.
\end{aligned}$$

Rearranging and applying the limits of integration,

$$\begin{aligned}
v(t) &= \alpha \, \exp\left[\frac{-j4\pi R_o}{\lambda} - \frac{j2\pi v^2 (t-t_o)^2}{\lambda R_o}\right] \int_{-\frac{T_a}{2}-(t-t_o)}^{\frac{T_a}{2}-(t-t_o)} \exp\left[\frac{-j4\pi v^2 \tau (t-t_o)}{\lambda R_o}\right] \mathrm{d}\tau \\
&= \frac{j\alpha c_a}{c_b} \exp\left[-jc_b\tau\right]\Bigg|_{\tau=-\frac{T_a}{2}-(t-t_o)}^{\tau=\frac{T_a}{2}-(t-t_o)}, \qquad \text{(B.24)}
\end{aligned}$$

where

$$\begin{aligned}
c_a &= \exp\left[\frac{-j4\pi R_o}{\lambda} - \frac{j2\pi v^2(t-t_o)^2}{\lambda R_o}\right], \qquad \text{(B.25)} \\
c_b &= \frac{4\pi v^2 \tau (t-t_o)}{\lambda R_o}. \qquad \text{(B.26)}
\end{aligned}$$

Evaluating Eq. B.24,

$$\begin{aligned}
v(t) &= \frac{j\alpha c_a}{c_b}\left\{\exp\left[-jc_b\left(\frac{T_a}{2} - (t-t_o)\right)\right] - \exp\left[-jc_b\left(\frac{-T_a}{2} - (t-t_o)\right)\right]\right\} \\
&= \frac{j\alpha c_a}{c_b}\exp\left[jc_b(t-t_o)\right]\left\{\exp\left[-jc_b\frac{T_a}{2}\right] - \exp\left[jc_b\frac{T_a}{2}\right]\right\} \\
&= \frac{-j\alpha c_a}{c_b}\exp\left[jc_b(t-t_o)\right]\, 2j\sin\left(\frac{c_b T_a}{2}\right) \\
&= \alpha T_a c_a \operatorname{sinc}\left(\frac{c_b T_a}{2}\right)\exp\left[jc_b(t-t_o)\right]. \qquad \text{(B.27)}
\end{aligned}$$

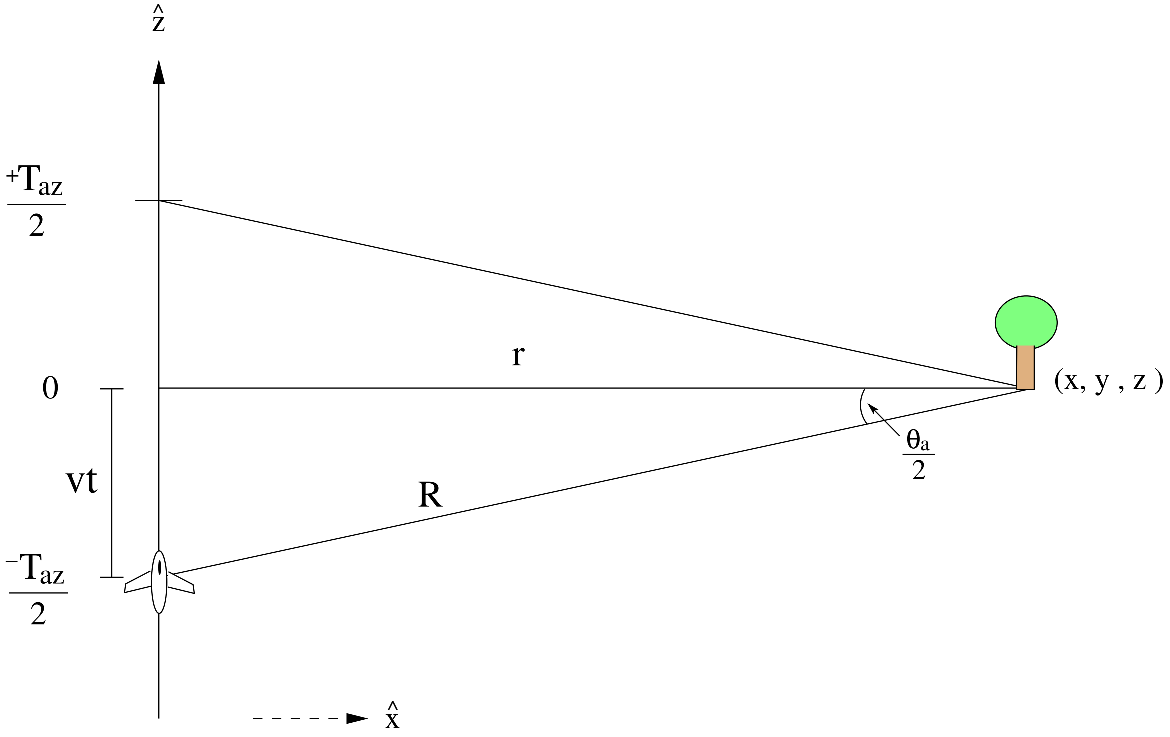

Figure B.3: Overhead view of time/distance relationship of moving platform.

Substituting c_a and c_b back in,

$$\begin{aligned} v(t) &= \alpha T_a \operatorname{sinc}\left(\frac{2\pi T_a v^2(t-t_o)}{\lambda R_o}\right) \exp\left[\frac{-j4\pi R_o}{\lambda} - \frac{j2\pi v^2(t-t_o)^2}{\lambda R_o} + \frac{j4\pi v^2(t-t_o)^2}{\lambda R_o}\right] \\ &= \alpha T_a \operatorname{sinc}\left(\frac{2\pi T_a v^2(t-t_o)}{\lambda R_o}\right) \exp\left[\frac{-j4\pi R_o}{\lambda}\right] \exp\left[\frac{j2\pi v^2(t-t_o)^2}{\lambda R_o}\right]. \end{aligned} \tag{B.28}$$

At this point, the function $v(t)$ is given in terms of target dependent variables T_a and R_o. Rearranging the terms, it is possible to obtain a solution where the only target dependent variable is R_o, thus simplifying $v(t)$. If L_z is defined as the distance the radar platform moves while the target is illuminated, and v is the velocity of the platform, then

$$T_a = \frac{L_z}{v}.$$

This geometry is shown in Fig. B.3. Continuing,

$$\begin{aligned}\tan\left(\frac{\theta_a}{2}\right) &= \frac{L/2}{R_o}\\ &= \frac{T_a v}{2R_o},\\ T_a &= \frac{2R_o}{v}\tan\left(\frac{\theta_a}{2}\right).\end{aligned} \tag{B.29}$$

Substituting back into Eq. B.28,

$$v(t) = \alpha T_a \operatorname{sinc}\left[\frac{4\pi v(t-t_o)}{\lambda}\tan\left(\frac{\theta_a}{2}\right)\right]\exp\left[\frac{-j4\pi R_o}{\lambda}\right]\exp\left[\frac{j2\pi v^2(t-t_o)^2}{\lambda R_o}\right]. \tag{B.30}$$

The sinc function is now independent of target parameters; however, the two exponential functions are still in terms of target-dependent R_o. The first is simply a constant phase, but the second is quadratic phase in time.

As seen in Eq. B.23, the matched filter is dependent on both target range, R_o, and platform velocity, v. This means that while range compression is performed using a single matched filter (i.e., the transmitted signal itself), azimuth compression must be performed on each range slice independently. While the range-to-target may be calculated from the range sample spacing, the velocity must be measured.

Appendix C

Figures of Merit

This appendix lists some of the key figures of merit for synthetic aperture radar: range resolution, azimuth resolution, radiometric resolution, signal-to-noise ratio, peak sidelobe ratio, integrated sidelobe ratio.

Range Resolution

Resolution is a measure of the resolvability of individual targets by a radar. SAR techniques lead to finer resolution than conventional real-aperture systems, thus making them desirable in radar imaging. The following subsections discuss resolution for real and synthetic aperture radar, in both the range and azimuth directions.

Range resolution may be obtained using a pulse of very short transmit duration. The resolution resulting from a simple square pulse shape with duration T_p is

$$\Delta r = \frac{c_o T_p}{2}, \tag{C.1}$$

in meters per pixel where c_o is the speed of light. Consequently, the shorter the pulse length, the finer the resolution in range. Taking this to the logical limit suggests a delta function as the pulse shape. Unfortunately, this ideal is impossible as the delta function has infinite magnitude. In practice, hardware designed to transmit pulses of very short length is very expensive and such systems suffer from low signal-to-noise ratio (SNR). To alleviate this, it is possible to obtain high resolution using longer pulses that are frequency modulated.

There are several different methods for deriving the range resolution of an LFM chip [12, 89, 5]; however, one simple approach is to recognize that radar bandwidth is approximately equal to $1/T_p$, so Eq. C.1 can be expressed as

$$\Delta r = \frac{c_o}{2\mathrm{BW}}\,, \tag{C.2}$$

where BW is the bandwidth of the transmitted signal. Increasing the transmit bandwidth thus improves the resolution. This result is consistent with various derivations, and is a common rule-of-thumb in radar processing.

Azimuth Resolution

In real aperture radar, the azimuth resolution is proportional to the azimuth beamwidth of the antenna while synthetic aperture resolution is inversely proportional to the azimuth beamwidth. It can be shown [90] that the azimuth resolution of a real aperture radar is

$$\Delta z_{\mathrm{rar}} = 2r\tan\left(\frac{\theta_a}{2}\right), \tag{C.3}$$

where r is the near range and θ_a is the azimuth beamwidth in radians. Substituting the approximation $\theta_a \approx \lambda/L_z$ into $\Delta z \approx r\theta_a$, the azimuth resolution for real aperture radar is

$$\Delta z_{\mathrm{rar}} \approx \frac{r\lambda}{L_z}, \tag{C.4}$$

where λ is the carrier wavelength, and L_z is the antenna length in azimuth [9]. As is apparent, an increase in the length of the antenna yields finer resolutions. In practice, the antenna length is limited by the length the platform can support. Thus, obtaining very fine azimuth resolution with real aperture radar is impractical due to the large antenna size required.

Synthetic aperture radar is based on the change in propagation phase of a target as the platform travels along its path (also called the apparent “Doppler shift”, though the true Doppler shift of the carrier wave is unrelated). The shift is positive as the platform approaches each target, is zero at boresight, and goes negative as the platform moves away from each target. It can be shown [91] that the achievable azimuth resolution for SAR is the velocity divided by azimuth bandwidth

$$\Delta z = \frac{v}{BW_z}. \tag{C.5}$$

The following derivation shows how the azimuth bandwidth can be approximated using the phase change of the radar return off each target. A more mathematically rigorous derivation can be found in [92]. The phase change ϕ_D of the received signal is related to the change in range δ_r from the platform to the target

$$\begin{aligned}\phi_D &= \frac{4\pi f \delta_r}{c_o} \\ &= \frac{4\pi\delta_r}{\lambda}.\end{aligned} \tag{C.6}$$

The variable δ_r can be estimated from the slant range R:

$$\begin{aligned}R &= \sqrt{(r)^2 + (vt)^2} \\ &\approx r + \frac{(vt)^2}{2r},\end{aligned} \tag{C.7}$$

$$\delta_r \approx \frac{(vt)^2}{2r}. \tag{C.8}$$

An example of this is shown in Fig. B.3 on page 170. Equation C.7 is found assuming $vt \ll R$ and with the Taylor expansion approximation

$$\sqrt{1+x} \approx 1 + \frac{x}{2}, \qquad \text{where} \qquad x \ll 1,$$

with error $x^2/4$. Substituting δ_r into Eq. C.6 gives

$$\phi_D(t) = \frac{2\pi v^2 t^2}{\lambda r}. \tag{C.9}$$

Noting that the phase changes quadratically with time, this phase change may be considered an azimuth chirp. The azimuth frequency f_z is found by differentiating the phase to obtain

$$f_z = \frac{2v^2 t}{\lambda r} \tag{C.10}$$

and the azimuth chirp rate is

$$\dot{f}_z = \frac{2v^2}{\lambda r}. \tag{C.11}$$

The azimuth bandwidth BW_z is found from the chirp rate $\dot{f} \triangleq BW/T$, where T is the period. Figure B.3 shows the geometric relation used to find the azimuth period T_z. It can be seen from the figure that

$$\tan\left(\frac{\theta_a}{2}\right) = \frac{vT_z}{2r}. \tag{C.12}$$

Applying the small angle approximation $\tan(\theta_a/2) \approx \theta_a/2$, the azimuth period is

$$T_z = \frac{\theta_a r}{v}. \tag{C.13}$$

This allows the azimuth bandwidth to be solved for in terms of the approximated azimuth period,

$$\begin{aligned} BW_z &= \dot{f}_z T_z \\ &= \frac{2v^2}{\lambda r}\frac{\theta_a r}{v} \\ &= \frac{2v\theta_a}{\lambda}. \end{aligned} \tag{C.14}$$

Finally, employing the previously used $\theta_a \approx \lambda/L_z$ and substituting this result into Eq. C.5 yields the SAR azimuth resolution, Δz,

$$\begin{aligned} \Delta z &= \frac{v}{BW_z} \\ &= \frac{\lambda}{2\theta_a}, \end{aligned}$$

which results in

$$\Delta z \approx \frac{L_z}{2}. \tag{C.15}$$

Comparing this result with Eq. C.4 shows the obvious advantage of synthetic aperture radar over real aperture radar. For the same size antenna, application of SAR processing leads to much finer azimuth resolutions and makes available high resolution radar imaging on aircraft.

This result suggests that an infinitely small antenna provides the best azimuth resolution. However, the pulse repetition frequency (PRF) must meet the minimum Nyquist criterion, which is twice the azimuth bandwidth:

$$\begin{aligned} PRF_{min} &= \frac{4v\theta_a}{\lambda}, \quad \text{or} \\ &\approx \frac{4v}{L_z}. \end{aligned}$$

Thus, PRF_{min} is inversely proportional to the length of the antenna. Conversely, the maximum allowable PRF is limited in practice by hardware restrictions and desirable data bandwidth. Therefore, a trade-off must be made between finer azimuth resolution and the minimum PRF.

Radiometric Resolution

The noise-equivalent sigma-naught (NES0 or σ_n) is the equivalent terrain radar backscatter coefficient that would produce a signal in the receiver equal to the receiver noise-only signal [4]. NES0 is a measure of radiometric resolution, i.e., how finely a SAR can distinguish varying levels of intensity in the backscatter. It is given by

$$\sigma_n = \frac{\sigma^0}{\mathrm{SNR}_{\mathrm{clutter}}}. \tag{C.16}$$

It is important to note that σ_n is a function of range since SNR is also.

SNR

A SAR has processing gain from both range and azimuth compression. The range compression gain is approximately the time-bandwidth product:

$$A_r \approx \beta_T \tau_p, \tag{C.17}$$

where β_T is the bandwidth of the signal and τ_p is its duration. The azimuth compression gain is simply the number of pulses contributing to the pixel:

$$A_a = \frac{d_a}{vt} \approx \frac{\lambda r}{L_a vt}, \tag{C.18}$$

where d_a is the aperture length, v is the platform velocity, t is the time period between successive pulses, and L_a is the antenna length. Thus, the SNR of a target in a SAR image is (neglecting receiver noise and propagation loss)

$$\mathrm{SNR}_{\mathrm{target}} = \frac{\mathrm{P_r}}{\mathrm{P_n}} \mathrm{A_r A_a}, \tag{C.19}$$

where P_r is the received signal power and P_n is the noise power.

Using the resolutions

$$\Delta_r = \frac{c}{2\beta_T}, \tag{C.20}$$

$$\Delta_a = \frac{L_a}{2}, \tag{C.21}$$

the processing gain becomes

$$A_r A_a = \frac{\beta_T \tau_p \lambda r}{L_a vt} \tag{C.22}$$

$$= \left(\frac{\tau_p}{t}\right)\left(\frac{c\lambda r}{4v\Delta_r\Delta_a}\right). \tag{C.23}$$

With the PRF f_{PRF} and peak transmit power P_T, the first term combines with the transmit power to obtain the average transmit power:

$$P_{\mathrm{av}} = \tau_p f_{\mathrm{PRF}} P_T. \tag{C.24}$$

The second term combines with the remaining portions of P_r to obtain the SNR for a target contained inside an individual resolution cell,

$$\mathrm{SNR}_{\mathrm{target}} = \frac{P_{\mathrm{av}} G^2 \lambda^3 c \sigma_t}{4\left(4\pi r\right)^3 P_n L v \Delta_r \Delta_a}, \tag{C.25}$$

with noise power

$$P_n = k_B T \beta_R F_n, \tag{C.26}$$

where σ_t is the radar cross-section of the target, k_B is Boltzmann's constant, T is the receiver temperature, and F_n is the receiver noise figure. The terms $k_B T \beta_R$ are the thermal noise of an ideal receiver, while F_n accounts for the extra noise added by the receiver as compared to the ideal.

Using distributed targets (e.g., ground clutter),

$$\mathrm{SNR}_{\mathrm{clutter}} = \frac{P_{\mathrm{ave}} G^2 \lambda^2 \sigma^0}{(4\pi)^3 R^4 P_n L} \left(\frac{R \lambda c}{4 v \sin \theta_i} \right), \tag{C.27}$$

where σ^0 is the normalized ground/clutter reflectivity and θ_i is the incidence angle. Note that Carrara [4] replaces bandwidth β_R (inside P_n) in the denominator with Δ_r in the numerator, as they are inversely proportional.

Signal-to-clutter Ratio

Usually, $\mathrm{SNR}_{\mathrm{target}}$ is not the limiting factor in target detection because background clutter limits detection first. Thus, signal-to-clutter ratio is a figure of merit limiting detection performance [5]:

$$\mathrm{SCR} = \frac{\sigma_t \sin \theta_i}{\sigma^0 \Delta_a \Delta_r}. \tag{C.28}$$

This gives a limit on detection performance regardless of receiver noise. In practice, a combination of total noise and clutter limits detection performance.

Sidelobe ratios

The impulse response (IPR) of a focused point target is another important quality of the SAR. It shows how well compressed the targets are as well as any spreading due to window tapers. Among the methods of measuring IPR is peak sidelobe ratio (PSLR) and integrated sidelobe ratio (ISLR). The PSLR is the ratio of the peak of the mainlobe to the peak sidelobe.

ISLR is a measure of the ratio of the integrated power of the mainlobe to the integrated power of the sidelobes. A good treatment of this subject appears in [4].

Bibliography

[1] F. T. Ulaby, R. K. Moore, and A. K. Fung, *Microwave Remote Sensing: Active and Passive, Volume I: Fundamentals and Radiometry*, F. T. Ulaby, Ed. Artech House Publishers, 1986.

[2] A. W. Doerry, D. F. Dubbert, M. Thompson, and V. D. Gutierrez, "A portfolio of fine resolution ka-band sar images: part i," in *Defense and Security*. International Society for Optics and Photonics, 2005, pp. 13–24.

[3] I. G. Cumming and F. H. Wong, *Digital Processing of Synthetic Aperture Radar Data*. Artech House, 2005.

[4] W. Carrara, R. Goodman, and R. Majewski, *Spotlight Synthetic Aperture Radar: Signal Processing Algorithms*. Norwood, MA: Artech House, 1995.

[5] G. Franceschetti and R. Lanari, *Synthetic aperture radar processing*, F. Shapiro, Ed. CRC, 1999.

[6] M. A. Richards, J. A. Scherr, and W. A. Holm, *Principles of Modern Radar: Basic Principles*, D. R. Kay, Ed. SciTech Publishing, 2010.

[7] E. Zaugg, "Generalized Image Formation for Pulsed and LFM-CW Synthetic Aperture Radar," Ph.D. dissertation, Brigham Young University, 2010.

[8] F. Rocca, "Synthetic aperture radar: A new application for wave equation techniques," *Stanford Exploration Project Rep.*, vol. SEP-56, pp. 167–189, 1987.

[9] D. P. Duncan, "Motion Compensation of Interferometric Synthetic Aperture Radar," Master's thesis, Brigham Young University, 2004.

[10] R. B. Lundgreen, "Method of Motion Compensation of YINSAR Data," Master's thesis, Brigham Young University, 2001.

[11] C. Stringham and D. G. Long, "Improved processing of the CASIE SAR data," in *Geoscience and Remote Sensing Symposium (IGARSS), 2011 IEEE International*, Jul. 2011.

[12] A. E. Robertson, "Multi-baseline Interferometric SAR for Iterative Height Estimation," Master's thesis, Brigham Young University, 1998.

[13] D. G. Thompson, "Innovative radar interferometry," Ph.D. dissertation, Brigham Young University, 2001.

[14] I. Cumming and J. Bennett, "Digital processing of seasat sar data," in *Acoustics, Speech, and Signal Processing, IEEE International Conference on ICASSP '79.*, vol. 4, 1979, pp. 710–718.

[15] M. Y. Jin and C. Wu, "A SAR correlation algorithm which accommodates large-range migration," *IEEE T. Geosci. Remote.*, vol. 22, pp. 592–597, 1984.

[16] R. K. Raney, H. Runge, R. Bamler, I. G. Cumming, and F. H. Wong, “Precision SAR processing using chirp scaling,” *IEEE T. Geosci. Remote.*, vol. 32, no. 4, pp. 786–799, 1994.

[17] K. Eldhuset, “A new fourth-order processing algorithm for spaceborne SAR,” *IEEE T. Aero. Elec. Sys.*, vol. 34, no. 3, pp. 824–835, 1998.

[18] A. Moreira, J. Mittermayer, and R. Scheiber, “Extended chirp scaling algorithm for air- and spaceborne SAR data processing in stripmap and ScanSAR imaging modes,” *IEEE T. Geosci. Remote.*, vol. 34, no. 5, pp. 1123–1136, 1996.

[19] J. Mittermayer, A. Moreira, and O. Loffeld, “Spotlight SAR data processing using the frequency scaling algorithm,” *IEEE T. Geosci. Remote.*, vol. 37, no. 5, pp. 2198–2214, 1999.

[20] R. Bamler, “A comparison of range-doppler and wavenumber domain SAR focusing algorithms,” *IEEE T. Geosci. Remote.*, vol. 30, no. 4, pp. 706–713, 1992.

[21] U. Benz, K. Strodl, and A. Moreira, “A comparison of several algorithms for SAR raw data compression,” *IEEE T. Geosci. Remote.*, vol. 33, no. 5, pp. 1266–1276, 1995.

[22] R. Caves, S. Quegan, and R. White, “Quantitative comparison of the performance of SAR segmentation algorithms,” *IEEE T. Image. Process.*, vol. 7, no. 11, pp. 1534–1546, 1998.

[23] C. Gilmore, I. Jeffrey, and J. LoVetri, “Derivation and comparison of sar and frequency-wavenumber migration within a common inverse scalar wave problem formulation,” *IEEE T. Geosci. Remote.*, vol. 44, no. 6, pp. 1454–1461, 2006.

[24] P. Prats, K. de Macedo, A. Reigber, R. Scheiber, and J. Mallorqui, “Comparison of topography- and aperture-dependent motion compensation algorithms for airborne SAR,” *Geoscience and Remote Sensing Letters, IEEE*, vol. 4, no. 3, pp. 349–353, 2007.

[25] E. Zaugg and D. Long, “Generalized frequency-domain SAR processing,” *IEEE T. Geosci. Remote.*, vol. 47, no. 11, pp. 3761–3773, 2009.

[26] M. Backues, U. Majumder, D. York, and M. Minardi, “Synthetic aperture radar backprojection on sony playstation 3 cell broadband engine and intel quad-core xeon,” High Performance Embedded Computing (HPEC), Tech. Rep., 2008.

[27] M. A. Richards, *Fundamentals of Radar Signal Processing*. McGraw-Hill, 2005.

[28] V. T. Vu, T. K. Sjogren, and M. I. Pettersson, “A comparison between fast factorized backprojection and frequency-domain algorithms in UWB lowfrequency SAR,” in *Proc. IEEE Int. Geoscience and Remote Sensing Symp. IGARSS 2008*, vol. 4, 2008.

[29] ——, “Fast backprojection algorithm for UWB bistatic SAR,” in *Proc. IEEE Radar Conf. (RADAR)*, 2011, pp. 431–434.

[30] A. Ribalta, “Time-domain reconstruction algorithms for FMCW-SAR,” *IEEE T. Geosci. Remote.*, vol. 8, no. 3, pp. 396–400, 2011.

[31] M. N. Channabasappa, “On the square root formula in the Bakhshali manuscript,” *Indian J. History Sci.*, vol. 2, pp. 112–124, 1976.

[32] C. Mancill and J. Swiger, "A map drift autofocus technique for correcting higher-order SAR phase errors," in *27th Annual Tri-Service Radar Symposium Record*, 1981, pp. 391–400.

[33] P. H. Eichel, D. C. Ghiglia, and C. V. Jakowatz Jr., "Speckle processing method for synthetic-aperture-radar phase correction," *Optics Letters*, vol. 14, no. 1, pp. 1–3, 1989.

[34] S. A. S. Werness, W. G. Carrara, L. S. Joyce, and D. B. Franczak, "Moving target imaging algorithm for SAR data," *IEEE T. Aero. Elec. Sys.*, vol. 26, no. 1, pp. 57–67, 1990.

[35] D. E. Wahl, P. H. Eichel, D. C. Ghiglia, and C. V. Jakowatz Jr., "Phase gradient autofocus-a robust tool for high resolution SAR phase correction," *IEEE T. Aero. Elec. Sys.*, vol. 30, no. 3, pp. 827–835, 1994.

[36] L. Xi, L. Guosui, and J. Ni, "Autofocusing of ISAR images based on entropy minimization," *IEEE T. Aero. Elec. Sys.*, vol. 35, no. 4, pp. 1240–1252, 1999.

[37] J. Fienup and J. Miller, "Aberration correction by maximizing generalized sharpness metrics," *J. Opt. Soc. Am.*, vol. 20, no. 4, pp. 609–620, 2003.

[38] J. Li and P. Stoica, *MIMO Radar Signal Processing*. John Wiley and Sons, Inc., 2009.

[39] J. Wallace, M. Jensen, A. Swindlehurst, and B. Jeffs, "Experimental characterization of the MIMO wireless channel: data acquisition and analysis," *IEEE T. Wirel. Commun.*, vol. 2, no. 2, pp. 335 – 343, March 2003.

[40] I. Bekkerman and J. Tabikian, "Target detection and localization using MIMO radars and sonars," *IEEE Trans. Signal Process.*, vol. 54, pp. 3873–3883, October 2006.

[41] P. Stoica, J. Li, and Y. Xie, "On probing signal design for MIMO radar," *IEEE Trans. Signal Process.*, vol. 55, no. 8, pp. 4151–4161, August 2007.

[42] T. Aittomäki and V. Koivunen, "Low-complexity method for transmit beamforming in MIMO radars," in *IEEE Int. Conf. Acuoustics, Speech, and Signal Processing*, April 2007.

[43] E. Fishler, A. Haimovich, R. Blum, L. Cimini, D. Chizhik, and R. Valenzuela, "Performance of MIMO radar systems: Advantages of angular diversity," in *Conference Record of the Thirty-Eighth Asilomar Conference on Signals, Systems and Computers.*, November 2004, pp. 305 – 309.

[44] ——, "Spatial diversity in radars–models and detection performance," *IEEE Trans. Signal Process.*, vol. 54, no. 3, pp. 823 – 837, March 2006.

[45] T. Aittomäki and V. Koivunen, "Exploiting correlation in target detection using MIMO radar with angular diversity," 2009, pp. 1191 – 1195.

[46] ——, "Performance of MIMO radar with angular diversity under Swerling scattering models," *IEEE Journal of Selected Topics in Signal Processing*, vol. 4, no. 1, pp. 101–114, February 2010.

[47] ——, "MIMO radar target detection with parametric scattering correlation model," in *Proceedings of the 4th International Symposium on Communications, Control and Signal Processing, ISCCSP*, March 2010.

[48] ——, "Target detection and positioning in correlated scattering using widely distributed MIMO radar," in *Proceedings of the 7th European Radar Conference*, 2010, pp. 403 – 406.

[49] F. Daum and J. Huang, "MIMO radar: snake oil or good idea?" in *42nd Asilomar Conference on Signals, Systems and Computers.* Raytheon, October 2008, pp. 183–187.

[50] J. H. Kim, A. Ossowska, and W. Wiesbeck, "Investigation of MIMO SAR for interferometry," in *Radar Conference, 2007. EuRAD 2007. European*, 2007, pp. 51 – 54.

[51] W. H. Y. W. Yueguan Lin, Bingchen Zhang and Y. Li, "MIMO SAR processing with azimuth nonuniform sampling," in *IGARSS*, 2010, pp. 4652–4655.

[52] D. P. Diego Cristallini and P. Lombardo, "Exploiting MIMO SAR potentialites with efficient cross-track constellation configurations for improved range resolution," *IEEE Trans. Geosci. Remote Sens.*, vol. 49, no. 1, pp. 38–52, Jan 2011.

[53] W. Q. Wang, "Space-time coding MIMO-OFDM SAR for high-resolution imaging," *IEEE T. Geosci. Remote.*, vol. 49, no. 99, pp. 3094–3104, 2011.

[54] J. Li, X. Zheng, and P. Stoica, "MIMO SAR imaging: Signal synthesis and receiver design," in *Computational Advances in Multi-Sensor Adaptive Processing, 2007. CAMPSAP 2007. 2nd IEEE International Workshop on*. IEEE, 2007, pp. 89 – 92.

[55] J. H. G. Ender and J. Klare, "System architectures and algorithms for radar imaging by MIMO-SAR," in *Radar Conference, 2009 IEEE*, 2009, pp. 1–6.

[56] W. Libao, X. Jia, P. Shibao, H. Kan, and P. Yingning, "Ground moving target indication for MIMO-SAR," in *Synthetic Aperture Radar, 2009. APSAR 2009. 2nd Asian-Pacific Conference on*. IEEE, 2009, pp. 173 – 176.

[57] W. Q. Wang, Q. Peng, and J. Cai, "Diversified MIMO SAR waveform analysis and generation," in *Synthetic Aperture Radar, 2009. APSAR 2009. 2nd Asian-Pacific Conference on*. IEEE, 2009, pp. 270 – 273.

[58] F. K. Li and R. M. Goldstein, "Studies of multibaseline spaceborne interferometric synthetic aperture radars," *IEEE T Geosci Remote*, vol. 28, no. 1, pp. 88–97, 1990.

[59] E. Rodriguez and J. M. Martin, "Theory and design of interferometric synthetic aperture radars," *IEE Proceedings F Radar and Signal Processing*, vol. 139, no. 2, pp. 147–159, 1992.

[60] H. A. Zebker and J. Villasenor, "Decorrelation in interferometric radar echoes," *IEEE T Geosci Remote*, vol. 30, no. 5, pp. 950–959, 1992.

[61] F. Gatelli, A. M. Guamieri, F. Parizzi, P. Pasquali, C. Prati, and F. Rocca, "The wavenumber shift in SAR interferometry," *IEEE T. Geosci. Remote.*, vol. 32, no. 4, pp. 855–865, 1994.

[62] P. A. Rosen, S. Hensley, I. R. Joughin, F. K. Li, S. N. Madsen, E. Rodriguez, and R. M. Goldstein, "Synthetic aperture radar interferometry," *Proc. IEEE*, vol. 88, no. 3, pp. 333–382, 2000.

[63] G. Krieger, H. Fiedler, J. Mittermayer, K. Papathanassiou, and A. Moreira, "Analysis of multistatic configurations for spaceborne SAR interferometry," *IEE Proceedings -Radar, Sonar and Navigation*, vol. 150, no. 3, pp. 87–96, 2003.

[64] J. Rodgers and W. Nicewander, “Thirteen ways to look at the correlation coefficient,” *American Statistician*, vol. 42, no. 1, pp. 59–66, Feb 1988.

[65] W. L. Melvin and J. A. Scheer, *Principles of Modern Radar: Advanced Techniques*, D. R. Kay, Ed. SciTech Publishing, 2013.

[66] A. Rogers and R. Ingalls, “Venus: Mapping the surface reflectivity by radar interferometry,” *Science*, vol. 165, no. 3895, pp. 797–799, 1969.

[67] S. Zisk, “A new, earth-based radar technique for the measurement of lunar topography,” *The moon*, vol. 4, no. 3-4, pp. 296–306, 1972.

[68] L. Graham, “Synthetic interferometer radar for topographic mapping,” *Proc. IEEE*, vol. 62, no. 6, pp. 763–768, 1974.

[69] H. A. Zebker and R. M. Goldstein, “Topographic mapping from interferometric synthetic aperture radar observations,” *Journal of Geophysical Research: Solid Earth*, vol. 91, no. B5, pp. 4993–4999, 1986.

[70] R. Bamler and D. Just, “Phase statistics and decorrelation in SAR interferograms,” in *Proc. Int. Geoscience and Remote Sensing Symp. IGARSS ’93. Better Understanding of Earth Environment*, 1993, pp. 980–984.

[71] H. Zebker, S. Madsen, J. Martin, K. Wheeler, T. Miller, Y. Lou, G. Alberti, S. Vetrella, and A. Cucci, “The topsar interferometric radar topographic mapping instrument,” *Geoscience and Remote Sensing, IEEE Transactions on*, vol. 30, no. 5, pp. 933–940, 1992.

[72] T. G. Farr, P. A. Rosen, E. Caro, R. Crippen, R. Duren, S. Hensley, M. Kobrick, M. Paller, E. Rodriguez, L. Roth, D. Seal, S. Shaffer, J. Shimada, J. Umland, M. Werner, M. Oskin, D. Burbank, and D. Alsdorf, “The shuttle radar topography mission,” *Reviews of Geophysics*, vol. 45, no. 2, pp. n/a–n/a, 2007.

[73] G. Krieger, A. Moreira, H. Fiedler, I. Hajnsek, M. Werner, M. Younis, and M. Zink, “Tandem-x: A satellite formation for high-resolution sar interferometry,” *Geoscience and Remote Sensing, IEEE Transactions on*, vol. 45, no. 11, pp. 3317–3341, 2007.

[74] R. Bamler and P. Hartl, “Synthetic aperture radar interferometry,” *Inverse Problems*, vol. 14, no. 4, p. R1, 1998.

[75] R. L. Morrison, M. N. Do, and D. C. Munson, “SAR image autofocus by sharpness optimization: A theoretical study,” *IEEE T Image Process*, vol. 16, no. 9, pp. 2309–2321, 2007.

[76] J. N. Ash, “An autofocus method for backprojection imagery in synthetic aperture radar,” *IEEE Geosci. Remote. S.*, vol. 9, no. 1, pp. 104–108, 2012.

[77] T. Moon and W. Stirling, *Mathematical methods and algorithms for signal processing*. Prentice hall, 2000, vol. 204.

[78] J. C. Bezdek, R. J. Hathaway, R. E. Howard, C. A. Wilson, and M. P. Windham, “Local convergence analysis of a grouped variable version of coordinate descent,” *Journal of Optimization Theory and Applications*, vol. 54, pp. 471–477, 1987.

[79] T. J. Schulz, "Optimal sharpness function for SAR autofocus," *IEEE Signal Proc Let*, vol. 14, no. 1, pp. 27–30, 2007.

[80] R. Brent, *Algorithms for Minimization Without Derivatives*. Englewood Cliffs, NJ: Prentice-Hall, 1973, ch. 3-4.

[81] M. Powell, "An efficient method for finding the minimum of a function of several variables without calculating derivatives," *The computer journal*, vol. 7, no. 2, pp. 155–162, 1964.

[82] W. Press, B. Flannery, S. Teukolsky, W. Vetterling *et al.*, *Numerical recipes*. Cambridge Univ Press, 1986.

[83] J. A. Nelder and R. Mead, "A simplex method for function minimization," *The Computer Journal*, vol. 7, no. 4, pp. 308–313, 1965.

[84] M. Wright, "Direct search methods: Once scorned, now respectable," *Pitman Research Notes in Mathematics Series*, pp. 191–208, 1996.

[85] E. Polak, *Computational Methods in Optimization: a Unified Approach*. Academic Press, 1971, vol. 77.

[86] J. Nocedal and S. Wright, *Numerical Optimization*. Springer, 2006.

[87] M. I. Duersch, "BYU micro-SAR: A Very Small, Low-power LFM-CW Synthetic Aperture Radar," Master's thesis, Brigham Young University. Department of Electrical and Computer Engineering, 2004.

[88] R. L. Smith, "Micro Synthetic Aperture Radar Using FM/CW Technology," Master's thesis, Brigham Young University, 2002.

[89] M. Soumekh, *Synthetic Aperture Radar Signal Processing with MATLAB Algorithms*. New York, NY: John Wiley & Sons, Inc., 1999.

[90] C. Elachi, *Spaceborne Radar Remote Sensing: Applications and Techniques*. New York, NY: IEEE, 1988.

[91] D. V. Arnold, "Vector Quantization of Synthetic Array Radar Data," Master's thesis, Brigham Young University, 1987.

[92] N. Levanon, *Radar Principles*. New York, NY: John Wiley & Sons, Inc., 1988.

Glossary

Acronyms

A/D	analog to digital
AWGN	additive white gaussian noise
DEM	digital elevation map
GPS	global positioning system
IMU	inertial measurement unit
INS	inertial navigation system
IPR	impulse response
ISAR	inverse synthetic aperture radar
ISLR	integrated sidelobe ratio
LFM	linear frequency modulation
MDA	map-drift autofocus
MIMO	multiple-input and multiple-output
MISO	multiple-input and single-output
OFDM	orthogonal frequency-division multiplexing
PCA	point of closest approach
PDF	probability density function
PGA	phase-gradient autofocus
PPMCC	Pearson product-moment correlation coefficient
PPP	prominent point processing
PRF	pulse repetition frequency
PRI	pulse repetition interval
PSLR	peak sidelobe ratio
RCM	range cell migration
RCMC	range cell migration curve
RDA	range-Doppler algorithm
SAR	synthetic aperture radar
SCR	signal-to-clutter ratio
SIMO	single-input and multiple-output
SISO	single-input and single-output
SLAR	side-looking airborne radar
SNR	signal-to-noise ratio
SRC	secondary range compression
UAV	unmanned aerial vehicle

Symbols

α	interferometric baseline angle, page 104
δ	phase-center displacement, page 35
$\widetilde{\delta}$	estimated phase-center displacement, page 104
ϵ	phase-center displacement observed from second antenna, page 101
Φ	interferometric phase (traditional), page 104
$\Delta\Phi$	interferometric phase difference (backprojection), page 99
ϕ	phase, page 29
λ	wavelength, page 34
μ	geometry case coefficient, page 81
η	additive noise
ρ	correlation coefficient, page 73
θ	incidence angle, page 35
ζ	antenna displacement, page 37
B	interferometric baseline length, page 104
c	speed of light, page 34
d	distance (usually two-way), page 34
$\tilde{d}$	distance parameterizing the matched filter, page 34
Δd	residual distance, page 34
$\Delta\Delta d$	differential residual distance between two propagation paths, page 77
f_0	center frequency, page 29
h	matched filter reference function, page 30
I	pixel value, page 31
K	LFM ramp-rate, page 29
k	wavenumber, page 34
n	slow-time pulse index (usually used as a subscript), page 30
r	slant-range distance (usually one-way), page 11
$r^{'}$	range to scattering-cell phase-center, page 101
r_0	range at the point of closest approach
Δr	residual range, page 37
$R()$	range-compressed impulse response, page 35
R_x	azimuth resolution, page 79
R_y	ground-range resolution, page 35
$R_{y,\text{slant}}$	slant-range resolution, page 35
T	pulse period, page 30
t	fast-time
$\tilde{t}$	fast-time parameterizing matched filter, page 30
$\hat{x}, \hat{y}, \hat{z}$	azimuth, range, and elevation dimensions, respectively, page 11
$\bar{x}, \bar{y}, \bar{z}$	mean range-to-target, page 37

Index